NATIONAL ENERGY TECHNOLOGY LABORATORY

# RECENT SOLID OXIDE FUEL CELL CATHODE STUDIES

## *TOOLS, RESULTS, AND NOVEL CONCEPTS FOR MAKING BETTER CELLS*

December 30, **2016**

**DOE/NETL-2017/1818**

U.S. DEPARTMENT OF ENERGY | NATIONAL ENERGY TECHNOLOGY LABORATORY

# DISCLAIMER

## Acknowledgments

This report was prepared by the Power Systems Division, National Energy Technology Laboratory (NETL), U.S. Department of Energy (DOE). The work shown in this report was funded by the DOE Office of Fossil Energy's Solid Oxide Fuel Cells Program, also known as the Solid State Energy Conversion Alliance (SECA) program. The Power Systems Division wishes to acknowledge the contributions and cooperation of the Primary Investigators (PIs) and their teams, particularly:

***Authors***

Argonne National Laboratory—Kee-Chul Chang, Paul Fuoss, Brian Ingram, and Hoydoo You

Boston University—Srikanth Gopalan

Georgia Technological University—Dong Ding and Meilin Liu

Massachusetts Institute of Technology—Bilge Yildiz

Carnegie Mellon University—Paul A. Salvador

National Energy Technology Laboratory—Kirk Gerdes

***Contributors***

Jeff Stevenson, Pacific Northwest National Laboratory

Yves Idzerda, Montana State University

Heather Quedenfeld (Power Systems Division Director) and Shailesh Vora (Fuel Cells Technology Manager) for guidance on this effort.

Jenny Bowman for thoroughly editing this report.

# Contents

## Executive Summary

In 2007, the SECA program began a focused effort to correlate the surface attributes of common SOFC cathodes (LSM, LSCF) with performance and stability. In parallel, various cathode infiltration techniques and material sets were investigated to assess the potential for improved performance and stability. This series of three integrated and five topical reports—written by SECA program researchers—provides a concise, portfolio-wide synopsis of this research. Included reports are as follows:

- Integrated Reports—Activity; Stability and Degradation; and Surface Chemistry and Microstructure
- Topical Reports—Oxygen Reduction; Degradation; Infiltration; In situ/Ex situ Correlations; In situ X-ray Techniques; Microstructural Characterization; Modeling Cathodes; and Thin Films

Highlights include:

- **New Surface Property Data—**The surface chemistry of the state-of-the-art cathode materials were characterized under SOFC operating conditions in situ. Results showed that both LSM and LSCF have Sr segregated to their surfaces under operating conditions.
- **Surface Chemistry Manipulation—**Surface compositions can be tailored by varying A-site dopants (Ba vs. Ca vs. Sr).
- **In situ/Ex situ Correlations—**The surface chemistry of LSM was characterized under near-in situ conditions (700 °C and air, no bias) and temperatures down to room temperature ex situ. The surface chemistry is approximately constant over the temperature range suggesting that using ex situ lab-based tools, such as XPS and TEM, are probably acceptable for LSM.
- **In situ Tools—**Synchrotron-based X-ray techniques were used heavily to study the surfaces of model thin-film cathode materials providing surface chemistries, crystallographies, and valence states. A laboratory X-ray diffractometer was modified to accept button cells that can provide the phase information of cathodes.
- **Infiltration—**A number of cathode infiltration architectures were investigated and tested at lab-scale, including LSM on LSCF (Georgia Tech) and LSC on LSCF/SDC (NETL). Data indicate that a broad array of infiltrated electro-catalysts improve short-term performance and stability relative to state-of-the-art cathodes, although mechanisms remain largely unknown. For promising architectures, evaluation of long-term stability and overall economics is needed.
- **Infiltrant Thickness and Activity—**Infiltrants of varying thicknesses showed different electronic properties; an insight that may be important for optimizing microstructures.
- **Interfaces Affect Performance—**A pulsed laser deposited ceria barrier layer strongly improved performance in LSCF-based cells over a sintered barrier layer. Also cathode materials deposited on various substrates showed massively different surface kinetics, suggesting that interface combinations can influence performance.

# Part I: Integrated Reports

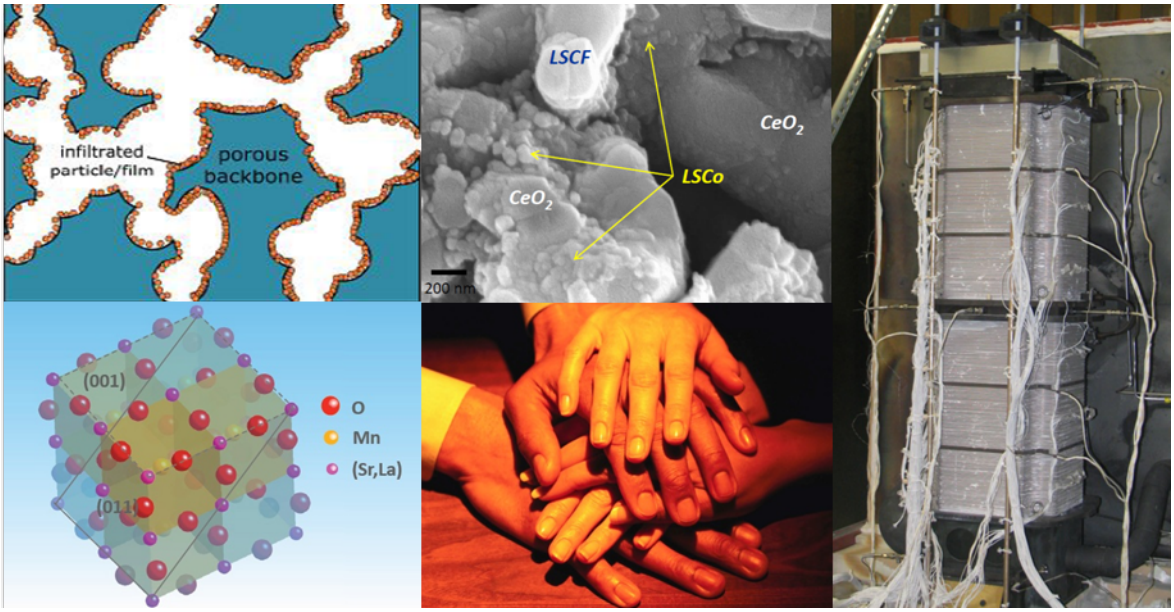

# **Cathode Surface Science for Solid Oxide Fuel Cells** *by Paul Fuoss (Argonne National Laboratory) & Bilge Yildiz (Massachusetts Institute of Technology)*


## Summary

The SECA core research program has performed systematic studies of the structure and chemical reactivity of solid oxide fuel cell (SOFC) cathodes under conditions that closely approximate operating conditions. These in situ and *in operando* studies have shown that SOFC cathodes are compositionally inhomogeneous on the nanoscale and that these inhomogeneities significantly modify the oxygen reduction reactivity of cathodes. These composition inhomogeneities are not an artifact of manufacturing processes but are intrinsic to the cathode materials, and are driven by surface induced electrochemical potentials and strain.

For the commonly used $La_xSr_{1-x}MnO_{3-\delta}$ (LSM) cathode materials, the key findings include:

- Strontium segregation to the surface of LSM is in thermodynamic equilibrium at SOFC operating temperatures and key thermodynamic parameters have been measured.
- While LSM is a semiconductor at room temperature, above 400 ˚C the band structure changes and a surface metallic-like state is formed.

SECA research into the mixed conductors $La_xSr_{1-x}CoO_{3-\delta}$ (LSC) and $La_xSr_{1-x}Co_yFe_{1-y}O_{3-\delta}$ (LSCF) have found these key results:

- There is significant segregation of Sr to the surface of LSCF but, unlike LSM, the segregation does not depend on oxygen partial pressure.
- There is segregation of Co to the surface of LSCF that is enhanced by cathodic potentials.
- There is significant lattice strain associated with the chemical capacitance of LSCF. These lattice strains can be used to map out local performance in cathodes.

The design and performance of simple cathodes made from a single material are increasingly well understood and this understanding may lead to more robust fuel cells. In addition, this understanding of single material cathodes points to approaches that may yield significantly higher cathode performance:

- Using infiltrants to improve cathode performance is promising, and a significant body of work indicates that a wide range of infiltrants improve cathode performance. Understanding the mechanism(s) of improvement and developing practical manufacturing processes is important.
- Post-fabrication modification of cathode surfaces may improve performance. Such modification may be accomplished by a chemical treatment, such as atomic layer deposition, to modify the surface properties (e.g., increase the surface Mn content).
- Research results indicate that engineering of surface electronic structure may significantly improve the oxygen reduction reaction kinetics. Translating these research concepts into a

design suitable for manufacturing is a challenge but also an opportunity for significantly improved cathodes.

## Overview

A solid oxide fuel cell (SOFC) has only three active components: 1) the anode where fuel is used to produce charged oxygen vacancies ($V_O^{\bullet\bullet}$), 2) the electrolyte that transfers the $V_O^{\bullet\bullet}$ to the cathode while preventing the transfer of electrons, and 3) a cathode that reduces oxygen to annihilate the $V_O^{\bullet\bullet}$. However, a detailed examination of these active components reveals surprisingly complex and dynamic processes, at least at the elevated temperature and near atmospheric pressure SOFC operating conditions. The important processes occur on a variety of length scales from atomic (e.g., electrocatalytic decomposition of oxygen) to many microns (e.g., the porous cathode microstructure), and on time scales that range from very fast (e.g., oxygen diffusion) to very slow (e.g., grain growth in components). This wide variety of length and time scales coupled with the high-temperature, reactive environment of an operating fuel cell make a detailed scientific understanding that enables predictive models very challenging to develop.

Currently, the performance of SOFCs is limited by effectiveness of the cathode at reducing oxygen, the oxygen reduction reaction (ORR), and by the transport of the resulting oxygen to the electrolyte. Thus, the SECA program has a strong effort aimed at developing the scientific basis to understand the underlying mechanisms of cathodes, to build predictive models of cathode performance, and to use these models to develop higher performance cathodes. An important step in the ORR is transfer of electrons and this transfer might be strongly impacted by local electronic properties of the surface including the availability of electrons at appropriate energies in the cathode. The transport of the oxygen to the electrolyte is strongly controlled by oxygen vacancy content of the cathode. Both the electronic properties and the oxygen vacancy concentration are strongly influenced by the local atomic structure of the cathode. Hence, this program has focused on determining the atomic structure, and the resultant chemical/electronic properties, of strontium-doped lanthanum-based perovskite cathodes under operating conditions.

This effort has revealed that the atomic level structure of cathode materials such as $La_{1-x}Sr_xO_{3-\delta}$ (LSM) and $La_{1-x}Sr_xCo_{1-y}Fe_yO_{3-\delta}$ (LSCF) are dynamic and respond rapidly to changes in oxygen chemical potential and electrochemical bias. These rapid responses are surprising since the LSM and LSCF are typically operated at less than half their melting points, temperatures where conventional materials science would predict relatively static structures. However, these structural changes highlight the strong driving forces necessary to drive oxygen through a SOFC at the desired current densities—densities that result in roughly 12,000 oxygen atoms being transported through every lattice site per second.

There have been a number of excellent review articles written on the subject of cathode design and performance (e.g., Adler[1]). This summary will build on that knowledge base of cathode science and

[1] Adler, S. B., Chem. Rev., *Factors governing oxygen reduction in solid oxide fuel cell cathodes*, **104**, 4791(2004)

will attempt to put the SECA program's new *in operando* measurements into context, to highlight what is known to be important for a high-performance cathode, and, perhaps more important, to highlight the gray (or even black) areas where understanding is currently lacking. While we are most comfortable discussing what is known, it is in this last area, the unknown, where cathode breakthroughs may be discovered.

## Current Understanding of SOFC Cathode Science

As discussed by Adler[1], the perovskite cathodes fall into two general categories. First is the commonly used LSM that is a good electronic conductor but does not have appreciable ionic conductivity under typical conditions. The broader range of cathodes including LSC and LSCF has appreciable electronic and ionic conductivities. While there is a clear difference in the underlying chemistry of these two classes of cathode materials, there are several general features they have in common including significant structural rearrangements, such as surface segregation, that occur under SOFC operating conditions.

## Inhomogeneity of SOFC Cathode Materials

The performance of cathodes is strongly influenced by the oxygen vacancy concentration of the cathode. Since the vacancy concentration is intimately connected with the cation stoichiometry and composition, understanding the nanoscale compositional distribution of a cathode under operating conditions is crucial for predicting and modeling cathode performance.

Many of the perovskite surfaces of materials such as LSM and LSCF are polar and, because of long-range electric fields, cannot be abruptly terminated.[2] That is, the material must eliminate the surface charge by a structural reconstruction (e.g., eliminating a portion of the surface atoms), changing the surface composition (e.g., by surface segregation), or by a chemical modification (e.g., changing the valence of surface atoms). There are many studies indicating that the surface composition of LSM and LSCF films can be significantly different than the bulk composition. For example, Kumigashira et al.[3] found significant Sr enrichment at the surface of LSM and van der Heide[4] found significant Sr enrichment in a variety of $La_{1-x}Sr_x$ films with the perovskite structure.

The Argonne team conducted a study of the equilibrium segregation of A- and B-site constituents in LSM and LSCF as a function of $pO_2$ and temperature.[5] They found that for relatively high Sr films of

---

[2] Tasker, P., *The stability of ionic crystal surfaces,* J. of Phys. C: Solid State Phys., 4977(1979).

[3] Kumigashira, H., et al., *In situ photoemission characterization of terminating-layer-controlled $La_{0.6}Sr_{0.4}MnO_3$ thin films*, Appl. Phys. Lett., **82**, 3430(2003).

[4] van der Heide, P.A.W., *Systematic X-ray photoelectron spectroscopic study of $La_{1-x}Sr_x$-based perovskite-type oxides,* Surf. and Interface Analysis, **33**, 414(2002).

[5] Fister, T.T., et al., *In situ characterization of strontium surface segregation in epitaxial $La_{0.7}Sr_{0.3}MnO_3$ thin films as a function of oxygen partial pressure,* Appl. Phys. Lett., **93**, 151904(2008).

LSM (x=0.3), there was significant Sr segregation that decreased with increasing oxygen partial pressure and operating temperature. However, under all of the examined conditions there was significant Sr segregation. The MIT team has correlated the presence of surface Sr with reduced ORR performance. However, their measurements were at relatively low $pO_2$ where Sr segregation is enhanced.[6] They also found that A-site deficiency reduced the Sr segregation in LSM with 20% Sr.[7] Finally, at low Sr compositions (15%), the Boston University group has found Sr surface *depletion*.[8]

The segregation behavior of LSCF is potentially more complicated for two reasons. First, segregation can occur on both the A site (La, Sr) and B site (Co, Fe). In addition, there can be rapid and significant changes in the bulk vacancy concentration that are not allowed in LSM because of its lack of ionic conductivity. Bauman and coworkers demonstrated significant bias-induced changes in the resistance of an LSCF film.[9] A cathodic treatment decreased the resistance while an anodic treatment increased the resistance. From ex situ XPS measurements on quenched sample, these resistance changes were correlated with an increase in Sr surface composition with cathodic treatment and a corresponding decrease with anodic treatment. However, it is not clear from XPS studies at very low $pO_2$ what the equilibrium state of the surface under SOFC operating conditions. Addressing this uncertainty, Fister and coworkers at Argonne determined that Sr segregation occurs in LSCF but, unlike the case of LSM, there is essentially no dependence on $pO_2$. Recent work by Cai et al. from MIT and Vienna University of Technology have found that there is a significant reduction in Sr segregation on a LSC film deposited at 450 °C versus a film deposited at 630 °C, and that the 450 °C film performed better (i.e., the opposite of the Bauman result).[10]

In agreement with Baumann, Chang and coworkers at Argonne have found that Co segregates to the surface of LSCF at elevated temperature under normal atmospheric conditions.[11] This segregation is slightly enhanced by a cathodic potential and is strongly suppressed by the application of an anodic

---

[6] Katsiev, K., et al., *Electron tunneling characteristics of La0.7Sr0.3MnO3 thin-film surfaces at high temperature*, Appl. Phys. Lett., **95,**092106 (2009).

[7] Lee, W., Z. Cai and B. Yildiz, R*ole of Chemical Heterogeneities on Oxygen Reduction Kinetics on the Surface of Thin Film Cathodes*, ECS Transactions, **45**, 405(2012).

[8] Gopalan, S. and Ludwig, K., Private Communication, 2012.

[9] Baumann, F. S., *Strong performance improvement of $La_{0.6}Sr_{0.4}Co_{0.8}Fe_{0.2}O_{3-\delta}$ SOFC cathodes by electrochemical activation*, J. Electrochem. Soc., **152**, A2074(2005).

[10] Cai, Z., et al., *Chemical heterogeneities on $La_{0.6}Sr_{0.4}CoO_{3-\delta}$ thin films – Correlations to cathode surface activity and stability*, Chem. of Mater., **24**, 1116(2012).

[11] Chang, K.C., et al., *Supporting R&D for Solid Oxide Fuel Cells*, Unpublished Work, Argonne

National Laboratory, Argonne, IL (2010).

potential. This result importantly signifies that the cation segregation problem is not limited to the A-site, but also the B-site cations can respond to the surrounding environment.

## Electronic Structure

Catalytic reduction of oxygen is the limiting factor of SOFC performance. Surface electronic structure provides a key indicator to charge transfer kinetics on the cathode surface, which is a critical step in the oxygen reduction process. In particular, the availability of electrons of the appropriate energy is a strong factor. Thus, it is important to measure the electronic properties of cathode surfaces under realistic conditions. The in situ capability to measure electron transfer on oxide films at intermediate temperatures (<600 °C) and oxygen gas at MIT has identified previously unknown properties of perovskite cathodes.

Table 1. A summary of the results of various in situ experiments measuring the surface composition of materials for SOFC cathodes.

| | System | Surface | | ORR |
|---|---|---|---|---|
| | | Strontium | Cobalt | |
| Fister[5] | $La_{0.7}Sr_{0.3}MnO_3$ | Enhanced | — | — |
| Katsiev[6] | $La_{0.7}Sr_{0.3}MnO_3$ | Enhanced | — | Reduced |
| Lee[7] | $(La_{0.8}Sr_{0.2})_yMnO_3$ | Enhanced | — | — |
| Gopolan[8] | $La_{0.85}Sr_{0.15}MnO_3$ | Reduced | — | — |
| Cai[10] | $La_{0.6}Sr_{0.4}CoO_{3-\delta}$ | Enhanced | — | — |
| Chang[11] | $La_{0.6}Sr_{0.4}Co_{0.8}Fe_{0.2}O_{3-\delta}$ | Enhanced | Enhanced | — |

Khabibulakh et al. have measured the electronic tunneling current of an LSM surface and found that LSM exhibited a semiconducting state with an energy gap at room temperature and a metallic-like state with no-gap at and above 400 °C.[6] In addition, the tunneling conductance decreased from 500 to 580 °C, which can result from the changes in the surface structure and composition of the LSM. A p-type conductivity in LSM arises as a result of hole-doping through the increase in $Mn^{4+}/Mn^{3+}$ ratio,[12] which depends on the A-site cation substitution and oxygen non-stoichiometry. They attributed the decreasing tunneling conductance to the evolution of Sr-rich phases accompanied by the relative decrease of Mn on the surface. This result suggests that the A-site rich and Mn-poor surfaces are less active for electron exchange in ORR kinetics on LSM film surfaces.

[12] Zener, C., *Interaction Between the d-shells in the transition metals.□II. Ferromagnetic compounds of manganese with perovskite structure*, Phys. Rev, **82**, 403(1951).

Correlation between the electronic and chemical state of the film surfaces and the electro-catalytic activity of SOFC cathodes has been further investigated under close to operating conditions of SOFC cathodes by Lee et al.[13] In particular, the energy gap of LSM films was systematically examined as a function of temperature and oxygen pressure. The surface electronic structure of LSM films on $SrTiO_3$ substrates showed a strong dependency on the temperature and oxygen pressure. At room temperature, the LSM/$SrTiO_3$ thin films showed a semiconducting state with an energy gap of 1.86±0.15 eV. As the temperature increased, the energy gap decreased and showed a metallic-like state with no-gap. This transition to a metallic-like state at elevated temperatures was observed in all oxygen pressures tested. Furthermore, the electronic transition occurred at different temperatures depending on the oxygen pressure; the transition occurred at the lower temperature with the lower oxygen pressure. After cooling to room temperature maintaining each oxygen pressure, LSM film surfaces recovered their semiconducting states with slightly lower values.

The MIT group's hypothesis is that the observed electronic transition originates mainly from the formation of oxygen vacancies on the surface. Formation of oxygen vacancies at the surface can induce additional defect states in the energy gap, resulting in the delocalization of the charge carriers at elevated temperatures.[14,15] This defect-induced transition was partially reversible within this range of temperature and oxygen pressure; the energy gaps were recovered to their initial values after cooling to room temperature, but slightly smaller than the initial ones. After cooling, the excess vacancies on the surface would be filled by the oxygen to reach an equilibrium state at room temperature. Since the surface electronic structure depends strongly on measurement conditions, the charge transfer kinetics based on room temperature results cannot be a good indicator of reactivity on these perovskite surfaces. Furthermore, these results show that oxygen vacancies on the film surface are important not only as reaction sites for oxygen exchange, but also that they have a significant effect on the surface electron transfer properties for ORR. These detailed studies of the atomic and electronic structure of surfaces under conditions that approximate those of operating SOFCs provide a basis for the design of cathode surfaces that achieve higher ORR rates and, thus, higher cathode performance.

## Electrochemical Dynamics

Studies of the lattice parameter of a cathode material like LSCF can reveal a great deal about the underlying mechanisms and dynamics because there is a well-defined correlation between the

---

[13] Lee, W., et al., *Reversible electronic structure transitions as a function of temperature and oxygen partial pressures on $La_{0.7}Sr_{0.3}MnO_3$ thin-film surfaces*, Manuscript in Preparation, 2012.

[14] Dulli, H., et al., *Surface segregation and restructuring of colossal-magnetoresistant manganese perovskites $La_{0.65}Sr_{0.35}MnO_3$*, Phys. Rev. B, **62**, R14629(2000).

[15] Bertacco, et al., *Evidence for strontium segregation in $La_{0.7}Sr_{0.3}MnO_3$ thin films grown by pulsed laser deposition: consequences for tunnelling junctions*, Surf. Sci., 511, 366(2002).

lattice parameter and oxygen vacancy concentration.[16] In particular, the concentration of oxygen vacancies, $V_O^{\bullet\bullet}$, in the LSCF layer is determined by concentration gradients across the LSCF surface (controlled primarily by the oxygen reduction reactions), and by the gradient across the buried interface between LSCF and the electrolyte (or buffer layer). For a given current through the structure, the LSCF vacancy concentration will reach equilibrium and the LSCF film will have a well-defined lattice parameter.[17] When the current is changed, there will be a period where the vacancy concentration is changing and reveals further information about the relative kinetics of the surface ORR and transport of $V_O^{\bullet\bullet}$ across the buried interface.

Ingram and coworkers at Argonne have made static and dynamic measurements of the lattice parameter of LSCF as functions of temperature, $pO_2$ and electrochemical bias. They found an increase in lattice parameter under cathodic potential that showed that not only is the surface ORR limiting the conduction, it is significantly slower than the vacancy transfer rate at the buried interface. Hardy et al. from Pacific Northwest National Laboratory have demonstrated that a laboratory X-ray source can be used to monitor the long-term evolution of cathodes in an operating fuel cell via lattice parameter measurements.[18] They demonstrated that the lattice parameter of LSCF slowly changes at operating conditions and is consistent with gradual loss of Sr under typical SOFC operating conditions.

## Outstanding Questions in SOFC Cathode Science

### Origin of Sr Segregation

Cation segregation on perovskite oxide surfaces affects SOFC cathode activity. The chemical complexity of cathode surfaces due to the dynamic nature of perovskite-type oxides in the surrounding environments and the harsh conditions for operating SOFCs have prohibited thus far development of fundamental principles that explain the origin of this phenomena for designing materials with optimal surface chemistry. This is important not only for the activity but also for the durability of the electrodes. Fister et al. found that the segregation of Sr to the surface of LSM was independent of the strain state by depositing films on three different substrates, $SrTiO_3$, $NdGaO_3$ and $DyScO_3$.[19] Fister et al. also searched extensively and unsuccessfully for a surface reconstruction that would compensate for the polar nature of the LSM (001) surface. In addition, they interpreted their results on the $pO_2$ dependency to be primarily an electrostatic effect since Sr segregation in LSCF (which doesn't support an oxygen vacancy gradient) does not exhibit a significant dependence

---

[16] Adler, S.B., *Chemical Expansivity of Electrochemical Ceramics*, J. Am. Ceram. Soc., **84**, 2117(2001).

[17] Ingram, B.J., et al., *In situ X-ray studies of oxygen surface exchange behavior in thin film* $La_{0.6}Sr_{0.4}Co_{0.2}Fe_{0.8}O_{3-\delta}$, Appl. Phys. Lett., **101**, 051603(2012).

[18] Hardy, J.S., et al., *Lattice expansion of LSCF-6428 cathodes measured by in situ XRD during SOFC operation,* J. of Power Sources, **198**, 76(2012).

[19] Fister, T. T., et al., Unpublished Work, 2008.

on $pO_2$. Therefore, consistent with calculations by Harrison,[20] they concluded that Sr segregation was driven primarily by electrostatic effects.

The MIT team, Lee et al., have quantitatively assessed the elastic and electrostatic interactions of the dopant with the surrounding lattice as the key driving forces for the segregation on model perovskite compounds, doped $LaMnO_3$, and found a significant electrostatic component to the segregation.[21] However, they also found a strong dependency of Sr surface segregation on the size mismatch between A-site cations (see Figure 1). Their data indicated that dopant-to-Mn ratios increased with the annealing temperaturen and the changes were larger with larger size mismatch. They argued that this dependency on the size mismatch substantiates that elastic energy minimization plays a key role in cation rearrangements as a driving force. They also found that oxygen content during annealing induced changes in the lattice parameters—higher oxygen pressure contracts the lattice and lower oxygen pressure expands the lattice—and argued that this directly affects the strain energy in the doped system and couples to the elastic energy as the driving force for cation rearrangements.

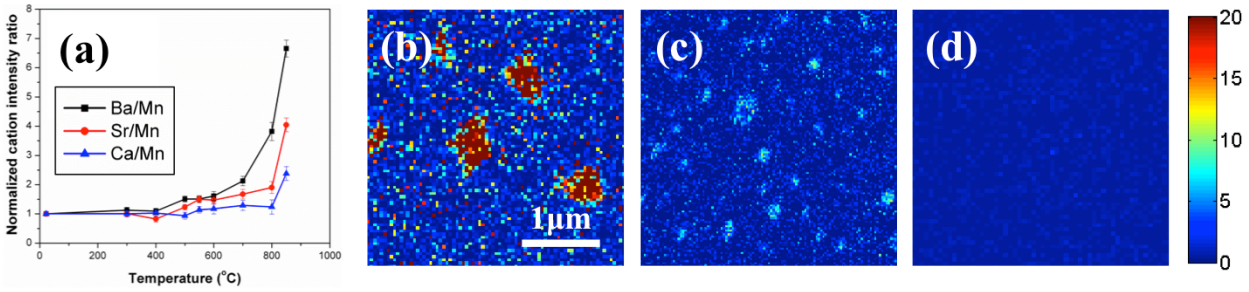


Figure 1. (a) Normalized cation intensity ratio (dopant/Mn) by angle-resolved XPS as a function of annealing temperature. (b–d) Cation intensity ratio maps of thin films after annealing at 800 °C for 1 hour by Auger electron spectroscopy: (b) Ba/Mn, (c) Sr/Mn, and (d) Ca/Mn.

**Role of Surface Structure on Cathode Performance**

The full impact of cathode surface (and near-surface) structure is not yet understood and cathode surface structure cannot be fully controlled at this time. A key question that needs to be answered is the role of Sr segregation on the electrochemical performance of a cathode since there are conflicting results in the literature. If, as concluded by Khabibulakh and coworkers, Mn termination improves the electrochemical performance of a cathode, can this surface be engineered for enhanced performance by stabilizing a Mn surface termination? The Argonne team is investigating this possibility through atomic layer deposition of Mn on LSM surfaces. However, it is also important to consider the particular structure and chemical state of the surface Mn.

---

[20] Harrison, W. A., *Origin of Sr segregation at $La_{1-x}Sr_xMnO_3$ surfaces*, Phys. Rev. B, **83**, 155437(2011).

[21] Lee, W., *Cation size mismatch and charge interactions drive dopant segregation on the surfaces of manganite perovskites*, Manuscript submitted, 2012.

**Engineered Multi-Component Cathodes**

Multi-component cathodes offer the opportunity to build enhanced chemical performance into SOFC cathodes. An important parameter is the strain state of the cathode. The role of lattice strain in improving ORR has been investigated in the context of low-temperature catalysis and electrocatalysis for more than a decade. However, SOFC cathodes operate in a complex environment with strains induced by cathode geometry and chemical capacitance that are not well understood. X-ray techniques are now being applied to understand the strain state in cathodes under *in operando* conditions.[17]

The findings of the SECA core research team studies on the effects of strain sheds light on how microstructural features affect surface chemistry and oxygen reduction kinetics on cathodes. Jalili et al. probed the strain-induced changes in the surface chemical and electronic states of LSM films, which are important to understand the mechanistic role of lattice strain in promoting the ORR activity.[22] Two key parameters were investigated as a function of strain state: 1) the chemical state of the LSM surface, in particular, the segregation of Sr cations and oxygen vacancy formation and 2) surface electronic structure. Based on their findings, tensile strain is expected to improve the ORR reactivity of LSM surfaces by increasing the oxygen vacancy concentration and by facilitating electron transfer from the surface. These results were later also confirmed for LSC films,[23] and significantly higher oxygen exchange (x4) and diffusion (x10) kinetics were found on the tensile strained LSC films.[24]

The Carnegie Mellon University group, Yan et al., investigated the substrate- and thickness-related effects on the oxygen surface exchange of LSM thin films.[25] A strong substrate effect on the oxygen surface exchange kinetics was observed, with a faster exchange on the tensile strained LSM films compared to the compressively strained ones. This observation is consistent with the findings from the MIT group summarized above. Two distinct activation energies were found for the surface exchange reaction. This was interpreted to arise from two parallel exchange processes—on the pristine surface of coherently strained films, and along the dislocations of the relaxed films.

---

[22] Jalili, H., et al., New insights into the strain coupling to surface chemistry, electronic structure and reactivity of $La_{0.7}Sr_{0.3}MnO_3$, J. Phys. Chem. Lett., **2**, 801(2011).

[23] Cai, Z., et al., *Surface Electronic Structure Transitions at High Temperature on Perovskite Oxides: The Case of Strained $La_{0.8}Sr_{0.2}CoO_3$ Thin Films*, J. Am. Chem. Soc., **133**, 17696(2011).

[24] Kubicek, M., et al., *Tensile lattice strain accelerates oxygen surface exchange and diffusion in $La_{1-x}Sr_xCoO_{3-\delta}$ Thin Films*, Submitted for publication, 2012.

[25] Yan, L. and Salvador, P.A., *Substrate and Thickness Effects on the Oxygen Surface Exchange of $La_{0.7}Sr_{0.3}MnO_3$ Thin Films*, Appl. Mater. & Inter., **4**, 2541(2012).

Recent studies have demonstrated that $La_{0.8}Sr_{0.2}CoO_3/(La_{0.5}Sr_{0.5})_2CoO_4$ ($LSC_{113/214}$) hetero-interfaces exhibit orders of magnitude faster ORR kinetics compared with either single phase at 500 °C.[26] To obtain a microscopic level understanding and control of such unusual enhancement, the MIT team implemented a novel combination of in situ scanning tunneling spectroscopy and focused ion beam milling to probe the local electronic structure at nanometer resolution in model multilayer superlattices.[27] At 200–300 °C, the $LSC_{214}$ layers are electronically activated via electron doping through an interfacial coupling with $LSC_{113}$. Such electronic activation is expected to facilitate charge transfer to oxygen, and concurrent with the anisotropically fast oxygen incorporation on $LSC_{214}$, quantitatively explains the vastly accelerated ORR kinetics near the $LSC_{113/214}$ interface. These results, from research conducted outside the SECA program, identify electronically coupled oxide structures as the basis of novel cathodes with exceptional performance.

## Conclusion

In situ and *in operando* studies have shown that SOFC cathodes are compositionally inhomogeneous on the nanoscale and that these inhomogeneities significantly modify the oxygen reduction reactivity of cathodes. These composition inhomogeneities are not an artifact of manufacturing processes but are intrinsic to the cathode materials, and are driven by surface induced electrochemical potentials and strain. Surface segregation, particularly of Sr and Co, is commonly found and strongly modifies the surface structure and electronic properties. These modifications may, in turn, impact the ORR rate and the performance of the cathode. The segregation of Sr can be reduced by either lowering the Sr composition in the film or by tuning the A-site stoichiometry. A robust correlation between these surface modifications and SOFC performance is not complete and experimental work is in progress.

The design and performance of simple cathodes made from a single material are increasingly well understood and this understanding may lead to more robust fuel cells. In addition, this understanding of single material cathodes points to approaches that may yield significantly higher cathode performance. Research results indicate that engineering of surface electronic structure may significantly improve the ORR kinetics. Translating these research concepts into a design suitable for manufacturing is a challenge but also an opportunity for significantly improved cathodes.

---

[26] Sase, M., et al., J. Electrochem. Soc., 155, B793(2008).

[27] Chen, Y., et al., *Electronic activation of cathode superlattices at elevated temperatures – source of markedly accelerated oxygen reduction kinetics*, Submitted for publication, 2012.

## **Degradation in State-of-the-Art Solid Oxide Fuel Cell Cathodes** *by Kirk Gerdes (National Energy Technology Laboratory) & Hoydoo You (Argonne National Laboratory)*


### Summary

Fuel cell degradation is considered to be any evolution of cell microstructure or chemistry that deviates from the initially constructed state, and which manifests as a time-dependent reduction in performance. Fuel cell degradation processes are influenced by both the contemporaneous operating condition and by the cumulative history of multi-modal degradation. Cathode materials in particular are subjected to *intrinsic* and *extrinsic* degradation processes, and both *primary* (direct) and *secondary* (multi-step or indirect) modes exist. A framework to categorize degradation processes is presented in Table 1, which distinguishes between modes on the basis of mechanistic complexity and the origin of the degradation-inducing thermodynamic potentials.

Broad modes of degradation are shared among all SOFC cathodes. Such modes include:

- Cation diffusion creating depressed activity phases and unwanted secondary phases;
- Agglomeration of grains resulting in diminished porosity and decreased triple phase boundary length;
- Accumulation of impurities at critical reaction interfaces, which depress or halt reaction kinetics; and
- Reaction between cathode and electrolyte to produce inactive phases.

Specific processes can be organized into these broad modes and the mathematical descriptions of specific modes within the broad divisions will be similar.

The specifically manifested degradation processes experienced by a particular cell construction and stack design are unique, and, consequently, a detailed analysis of degradation modes must be completed for each cell construction to categorize and quantify the expressed degradation. For example, Sr and Mn or Co are broadly known to respond to the applied conditions of operation (temperature, overpotential), but the specific degradation behavior appears to be strongly dependent upon the exact composition of the cathode. Some evidence even suggests that LSM 80/20 and LSM 70/30 will degrade in very different manners. Examples of modes that should be specifically examined in LSM and LSCF cathodes in all applications include:

- Segregation of Sr and Mn or Co towards the surface of cathode grains, and the impact on surface oxygen exchange;
- Agglomeration of cathode particle clusters and grain growth, principally at the cathode-air and cathode-electrolyte interfaces;
- Separation of YSZ into t-YSZ and c-YSZ domains as a function of applied overpotential; and

- Attack of cathode surfaces by $H_2O$, $CO_2$, and Cr.

Fortunately, a broad matrix of tests and analytical techniques has been leveraged to examine the common modes of degradation, and simple extrapolations may extend knowledge of a generalized mode to the specific degradation experienced by a certain cell/stack. Appropriate tests render definable and quantifiable degradation processes, and rational mitigation approaches can be advanced.

Table 1. Categories of principal cathode degradation modes.

| | **Intrinsic** |
|---|---|
| **Primary (direct or single step)** | *Degradation arises from relaxation of thermodynamic potentials within the cathode under intended, designed, or standard conditions of operation*<br>_____<br>Cathode cation diffusion forms an enriched phase<br>Crystallographic distortion results in phase breakdown<br>Sintering or grain coarsening results in microstructural evolution<br>Delamination arising from incompatible thermal expansion |
| **Secondary (indirect or multi-step)** | *Degradation arises from relaxation of thermodynamic potentials within the cathode in response to:*<br>*i) Operation of the cell beyond intended, designed, or standard conditions*<br>*ii) Multi-step degradation processes (cascading failure)*<br>_____<br>Activation or acceleration of primary modes at new conditions<br>Cathode delamination due to substantial secondary phase formation |
| | **Extrinsic** |
| **Primary (direct or single step)** | *Degradation arises from relaxation of cathode thermodynamic potentials influenced by external sources in response to:*<br>*i) Non-standard conditions of elemental exposure (gas phase)*<br>*ii) Cell fabrication outside of the design specifications*<br>_____<br>Diffusion of cations present as contaminants in cathode pre-cursor materials<br>Adsorption/reaction of contaminant molecules in gas feed (Cr, Si)<br>Operating point disruptions (load, fuel, etc.) |
| **Secondary (indirect or multi-step)** | *Degradation arises from relaxation of cathode thermodynamic potentials influenced by external sources. Degradation is characterized by a multi-step process (sequential or simultaneous), and at least one step includes a solid state degradation reaction of a cell component proximal to the cathode*<br>_____<br>Reaction of cathode with electrolyte/interconnect/seal<br>Overpotential variations arising from failure of current collecting mesh |

## Additional Details

This section of the report outlines the primary processes and modes, and illustrates the identified degradation with specific examples that have been documented in published literature.

*Intrinsic degradation* defines degradation occurring among engineered cathode components, which is inherent to the materials of construction or the engineered microstructure. Intrinsic degradation arises:

- in direct response to an applied thermodynamic potential step change or gradient, whether thermal, chemical, electrical, or other;
- from operation of the standard cathode outside of designed thermodynamic conditions; and
- in multi-step (cascading) degradation processes.

Specific modes of degradation related to intrinsic processes must be identified on the basis of the standard thermodynamic operating conditions for a given cell. Generally speaking however, many degradation modes are common among all cells, with variations in degradation intensity observed according to operating conditions. Common modes related to intrinsic processes include the following:

- **Cation diffusion affecting phase properties—**Specific cation diffusion mechanisms and rates are dependent upon the elements present [1–3], the conditions of cell operation [4], and the relative orientation of constitutive grains [5]. Cation diffusion is expected to result in alteration of the chemical compositions of cathodes. Because the compositions of active cathode materials are mostly at or near the boundaries of a metal-insulator transition, an impact on electronic properties of the cathode materials can be significant and often results in diminished activity of the oxygen reduction reaction. Sr segregation has been studied in detail and some generalized conclusions can be made regarding behavior [6]:
    - Segregation of Sr in LSM is dependent on $pO_2$, temperature, and crystal orientation
    - Sr segregation in LSC and LSCF occurs more readily and significantly at lower temperature than LSM and is dependent on temperature, $pO_2$, and the substrate crystal orientation.
    - Long-term annealing or operation leads to irreversible formation of Sr-enriched nanoparticles resulting in permanent or semi-permanent alteration of chemical compositions.
    - Sr segregation is independent of substrate strain and film thickness
- **Cation diffusion generating secondary phases—**Cation diffusion is often also a pre-cursor to secondary phase formation in the cathode, with the reaction of standard YSZ and LS[C]F to form reduced conductivity strontium zirconate phases being a well established example [7]. Secondary phase formation is generally expected to result in depressed cell performance. Other examples include:
    - Sr-enriched secondary phases are observed on the surface of LSM thin-films after annealing at 830 °C [8]

    - Among thin films composed of LSrM, LBaM, and LCaM, only the Ca-containing film does not generate an enriched surface phase after annealing at 830 °C [9]
- **Microstructural evolution of cathode backbone—**The cathode backbone is also subject to intrinsic morphological evolution potentially leading to degradation. Cathode morphological and microstructural evolution processes occur over thousands of hours of operation, and depend on the thermodynamic conditions to which the cathode is subjected [10].

Intrinsic degradation likely occurs most intensely through an initial operating period, though some background rate of intrinsic degradation is expected to occur throughout a cell's entire operational lifetime. Intrinsic degradation processes can be mitigated through judicious material selection, optimization of operating cathode microstructure, and strict control of cell/stack operating conditions.

*Extrinsic degradation* defines degradation of the cathode that is manifested through reactions with materials that are not inherently part of the cathode. Extrinsic degradation arises:

- from exposure of the cathode to foreign (often gas phase) materials;
- by operation of the cathode outside the standard thermodynamic conditions;
- from solid-state reaction processes involving other cell components.

Specific modes of degradation related to extrinsic processes are unique to the materials of construction and the design of a given cell and stack. Generally speaking however, many degradation modes are common among all stacks. Common modes related to extrinsic processes include the following:

- **Adsorption/reaction of contaminant molecules—**The elemental composition of some materials in direct contact with the cathode should be considered, since significant incompatibility will facilitate rapid degradation.
    - Materials containing elements such as Cr and Si should be avoided [3,6] unless precautions are made to immobilize such elements. In case any of these elements are present, cathodes and components in contact with the cathode should not contain Ag due to its reactivity [3] and its mobility/volatility [7].
    - The susceptibility of a cathode to elemental attack depends both on the mechanism of oxygen reduction for the particular cathode, and the location of the deposited attack element. As an example, experiments show that LSM cathodes are susceptible to boron-induced degradation while LSCF cathodes are not [4].
- **Phase separation induced by thermodynamic operating conditions—**Thermodynamic conditions and especially operating conditions at the edge of the operating envelope must be considered when evaluating cathode degradation, since the expressed degradation processes are principally dependent upon the thermodynamic state.
    - Critical thermodynamic parameters include the absolute magnitude of water present [4], the temperature of operation [10], exposure to $CO_2$, and steady potential differences between phases.

- **Cation diffusion from poor cell processing control—**Cation diffusion during cell fabrication could also induce cathode degradation. For example, nickel migration from the anode has been investigated during fabrication and is known to coarsen LSM cathodes [2].

Extrinsic cathode degradation processes can be suppressed by careful selection of cell construction materials, adoption of manufacturing quality control practices, restriction of the acceptable range of conditions in the operating envelope, and possibly through introduction of stabilizing materials. Cathode cation immobilization or pinning can be achieved through application of interlayers or dopants, with interlayers composed of doped Ce compounds being typical [9]. Careful control of cell processing conditions can eliminate as-fabricated compositional features that will result in more rapid degradation during cell operation. Examples of control include minimization of sintering temperatures and careful handling of materials to prevent cross-introduction of cations. Indirect degradation suppression methods may also exist, such as application of electrocatalytically active materials via infiltration, which could mitigate modes that are sensitive to local overpotentials.

## Time Dependent Degradation

The degradation processes occurring at a given operating time are influenced by the cumulative history of degradation. That is, degradation is a function of the total time of operation and the unique degradation path that the system has already traversed. The degradation rates that can be expected from cascading processes over long time scales are therefore imprecisely predictable. This fact complicates interpretation of any cathode-related cell failures observed following a step change in operating condition or a process upset, as the resulting degradation may not be directly correlated to the imposed condition. Even for two cells operated under identical initial conditions, the same cell performance (current density) will not necessarily be observed after the same elapsed time unless the exact temporal operating conditions were imposed identically on the cells. Therefore, cell failures must be subjected to root cause analysis, with an increase in analytical intensity that is proportional to the service time of the stack being analyzed.

## Conclusions and Postulated Mitigations of Cathode Degradation

Cathode degradation arises from diverse primary and secondary modes. Although the global problem of cathode degradation is complex, consideration of the topic provides some insight into general strategies to address the issue in a relatively simple fashion. Broadly considered, mitigation of cathode degradation can occur through a combination of best engineering practices and operating protocol. Best engineering practices can be used effectively to mitigate degradation through careful material selection, accurate specification of operating conditions, and verification of component compatibility. Operating protocols can be implemented to ensure limits and controls are in place for operating stacks to prevent activation of degradation modes that occur principally through deviation from standard operating conditions. Judicious use of cathode interlayers and infiltration of electrocatalytically active materials may also help to stabilize cathode performance.

Table 2. General approaches to mitigation of cathode degradation.

| | Intrinsic | Extrinsic |
|---|---|---|
| **Primary (direct or single step)** | *Best Engineering Practices* | *i) Best Engineering Practices*<br>*ii) Operating Protocols* |
| **Secondary (indirect or multi-step)** | *i) Operating Protocols*<br>*ii) Best Engineering Practices* | *Best Engineering Practices* |

## References


[1] Journal of Power Sources 198 (2012) 76– 82

[2] Journal of the Electrochemical Society, 157 (5) B643-B649 (2010)

[3] Journal of The Electrochemical Society, 157 (6) B964-B969 (2010)

[4]: Applied Physics Letters, 93, 151904 (2008)

[5]: Argonne National Laboratory Quarterly Progress letter, R&D for SECA, Jan-Mar 2009

[6]: Argonne National Laboratory Quarterly Progress letter, R&D for SECA, Jan-Mar 2010

[7] Solid State Ionics 161 (2003) 11–18

[8]: Journal of Power Sources 155 (2006) 246–252

[9]: Lee and Yildiz, 13th SECA Workshop, Pittsburgh, PA, USA , July 25, 2012

[10]: Applied Physics Letters, 101, 033909 (2012)

[11] J. Phys. Chem. C 2008, 112, 13299–13303

[12] Journal of The Electrochemical Society, 152 (4) A740-A745 (2005)

[13] Journal of The Electrochemical Society, 152 (9) A1851-A1859 (2005)

[14] Journal of The Electrochemical Society, 157 (7) B1019-B1023 (2010)

[15] Electrochemical and Solid State Letters, 9 (10) A478-81 (2006)

# Oxygen Reduction Reaction in Solid Oxide Fuel Cells: An Executive Summary of SECA Phase I Results *by Srikanth Gopalan (Boston University) & Meilin Liu (Georgia Institute of Technology)*


## Summary

The oxygen reduction reaction (ORR) in the cathode is to date a significant source of polarization and efficiency loss in a solid oxide fuel cell (SOFC), especially at lower operating temperatures in the 600–800 °C. Depending on the materials set employed, particularly the electrolyte, several cathode materials have been used. However, $La_{1-x}Sr_xMnO_3$ (LSM), a predominantly electronic conductor, and $La_{1-x}Sr_xCo_{1-y}Fe_yO_3$ (LSCF), an excellent mixed conductor, have been the principal candidates used as SOFC cathodes [1]. Many new materials continue to be investigated. It has been long recognized that the structural and compositional changes that occur at the surface of the cathode, i.e., gas-cathode interface, play a key role in the ORR. However, the specific details of the role that these factors play has not been clearly elucidated. Further, a detailed understanding of the relationship between the various kinetic parameters related to the ORR, namely, oxygen surface adsorption, bulk and surface diffusivities of oxygen to the sites of the electrochemical reduction reaction, and the relative importance of triple phase boundaries and gas exposed surfaces of the cathode is still emerging. Ultimately, research on cathode materials will need to provide the mechanistic link between the compositional and structural changes at the cathode surface to the measured kinetic parameters. Such a linkage is essential to design new cathode materials and cathode architectures.

We present the summary of work accomplished with respect to understanding the ORR and reducing cathode polarization losses in two parts. In part I we summarize the infiltration methodology developed at Georgia Tech to achieve high performance cathodes. In part II we summarize the patterned electrode methodology used at Boston University to study the kinetics of the ORR.


## Enhancing Cathode Performance through Infiltration

### Background

Polarization due to ORR on cathode still contributes significantly to efficiency loss of SOFC operation, more so at lower operating temperatures [2–5]. Our recent study suggests that the performance of LSCF cathodes can be enhanced through solution infiltration of a proper surface coating.

### Experimental

A solution infiltration process has recently been developed to introduce a catalyst coating to the surface of a pre-sintered LSCF cathode; the surface coating can be discontinuous (particles) or continuous (film) after a subsequent thermal treatment, depending on the specific infiltration processes and the catalysts infiltrated. The LSCF cathode is fired at high temperatures to ensure

excellent bonding between the electrode backbone and the electrolyte, excellent connectivity for effective conduction of electron and oxygen ion, and good structural stability of the cathode under operating conditions. The catalyst/electrode coating introduced by infiltration can be fired at temperatures much lower than that needed for the backbone to form the desired phases. The interfacial polarization resistance ($R_p$), long term stability, and cathodic polarization behavior of various catalysts-infiltrated LSCF cathodes were carefully characterized and compared with the performance of the LSCF cathode without catalyst infiltration. Further, a semi-empirical model has been developed to explain the performance enhancement of LSM-coated LSCF cathodes.

**Results and Discussion**

***Dense and Continuous LSM Coating on an LSCF Cathode***

When the surface of a porous LSCF cathode was covered with a dense and continuous LSM coating, both performance and stability were enhanced [6, 7]. As shown in Figure 1a, the cell with the LSM-coated LSCF model electrode experienced a gradual increase in cell current during the testing, which is consistent with the activation behavior of LSM cathode under cathodic polarization. In contrast, a continuous degradation in performance was observed for the cell with the LSCF cathode without LSM modification. Similarly, the same trend was observed for anode-supported cells with a LSM-coated LSCF cathode at a constant voltage of 0.7 V at 750 °C, as shown in Figure 1b.

To explain the effect of LSM infiltration, we developed a mathematical model for performance prediction of the LSM-coated LSCF cathodes. Figure 2a shows the trend of the area normalized interfacial resistance as a function of oxygen vacancy concentration at different cathodic bias. LSCF clearly has a different trend from LSM, as it is suspected that the trend of LSM leads to improved performance under large bias when the LSM is coated with LSCF. Figure 2b shows the trend of interfacial resistance as oxygen vacancy formation is made less favorable by modifying the free energy of reaction. The trend shows an increasing tendency toward larger activation at more severe cathodic bias. Figure 2c and 2d show how the trend of the area-specific resistance is affected by making adsorption and dissociation of oxygen more favorable. These results indicate that the LSM coating is less active at open circuit voltage because it has fewer oxygen vacancies, however its activation under large cathodic bias due to larger relative increase in vacancy concentration as well as its suspected more favorable adsorption properties make it more active at mild cathodic bias. These modeling trends agree with our experiments in both thin-films and porous, operational cathodes [6]. Further, the LSM coating has dramatically suppressed the tendency of Sr segregation toward LSCF surface, thus enhancing the long-term stability of the cathode [8].

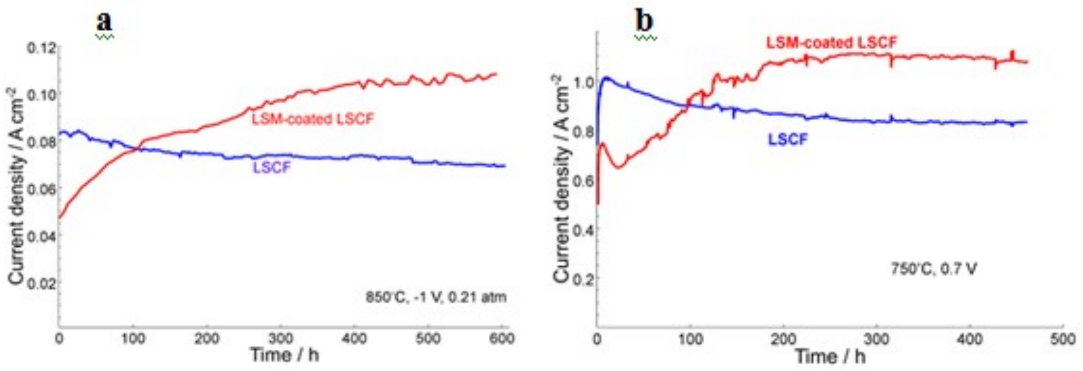


Figure 1. Current density of two test cells with and without LSM infiltration as a function of time under a constant cell voltage of 0.7 V at (a) 850 °C and approximate cathodic overpotential of -0.1 V and (b) 750 °C and approximate cathodic overpotential of -0.12 V [6].

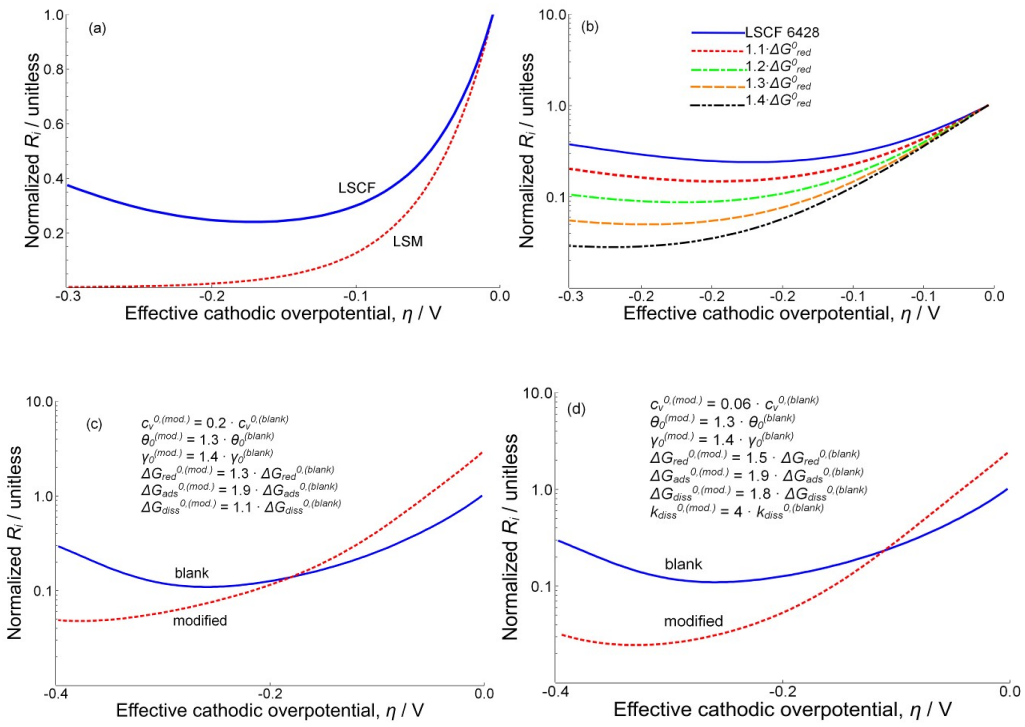


Figure 2. (a) Normalized interfacial resistance of LSCF and LSM films, normalized to their respective values at OCV. (b) Normalized interfacial resistance associated with tighter oxygen binding associated with lower free energy of oxygen reduction assuming current proportional to oxygen vacancy concentration. (c) Simulated normalized interfacial resistance versus effective cathodic overpotential for blank LSCF and LSCF with modified surface properties when $\Delta G_{red}^{0(surface)} < \Delta G_{red}^{0(LSCF)}$, $\Delta G_{diss}^{0(surface)} < \Delta G_{diss}^{0(LSCF)}$, and $\Delta G_{ads}^{0(surface)} < \Delta G_{ads}^{0(LSCF)}$. Ri is normalized to the value of the blank LSCF at OCV. (d) Simulated normalized interfacial resistance versus effective cathodic overpotential for blank and LSCF with modified surface properties when $\Delta G_{red}^{0(surface)} < \Delta G_{red}^{0(LSCF)}$, $\Delta G_{diss}^{0(surface)} < \Delta G_{diss}^{0(LSCF)}$, $\Delta G_{ads}^{0(surface)} < \Delta G_{ads}^{0(LSCF)}$, $k_{diss}^{0(surface)} > k_{diss}^{0(LSCF)}$ [6].

***Particle Deposition of Catalyst Coating on the LSCF Cathode***

When the surface of a porous LSCF cathode was covered with a discontinuous layer of small particles of catalysts, the performance was significantly enhanced as well, including $Sm_{0.2}Ce_{0.8}O_{1.95-\delta}$ (SDC)[9], $La_{0.4875}Ca_{0.0125}Ce_{0.5}O_{2-\delta}$ (LCC)[10], and $Sm_{0.5}Sr_{0.5}CoO_{3-\delta}$ (SSC)[11]. As shown in Figure 3, when the LSCF cathode was infiltrated with 10 μL of 0.25 mol $L^{-1}$ SDC, the interfacial resistances were 0.074, and 0.44 Ωcm² at 750 and 650 °C, respectively, with about half of those for the blank cathode without modification (0.15 and 1.09 Ωcm²). In addition to visible improvement in electro-catalytic activity with a symmetrical cell configuration [10], it is also found that the performance and stability of the full cells with the LSCF cathode can be enhanced by a LCC coating, leading to ~18% improvement in peak power density and stable operation (without observable degradation) for over 550 h (Figure 3b). SSC infiltrated LSCF showed noticeable decrease in $R_p$ at 550 °C to 750 °C.

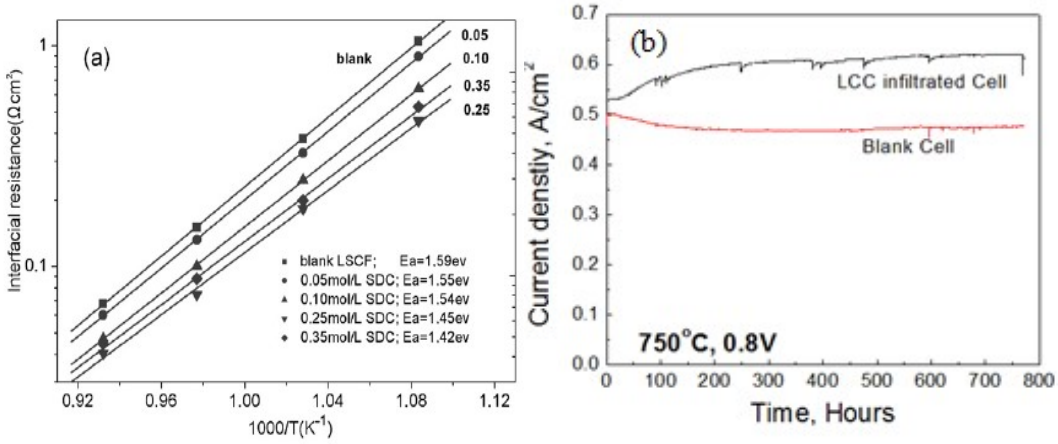


Figure 3. (a) Temperature dependence of interfacial polarization resistance of blank LSCF cathode and LSCF cathode with different concentrations of SDC infiltration measured at OCV. (b) Typical long-term stability of the homemade button cells with an LCC-infiltrated LSCF cathode and a baseline LSCF cathode at a constant voltage of 0.8 V at 750 °C.

Doped ceria have been widely used as catalyst materials due to their high ionic conductivity and excellent surface exchange and oxygen storage capability [12]. Improved performance is also demonstrated in the SDC infiltrated LSM cathodes [13,14]. SDC infiltration may promote the surface exchange and diffusion of oxygen on LSCF surface, leading to improved ORR of the cathode. Among various dopants, the incorporation of La into ceria can significantly enhance the oxygen transfer capability [15]. Although LCC showed pretty low ionic conductivity, the high doping level of ceria by La and Ca created high oxygen vacancy concentration. When the LSCF cathode was modified by a thin LCC coating, the surface layer with high oxygen vacancy concentration may enhance oxygen molecule dissociation into atomic oxygen [16], which may facilitate ORR. Similarly, SSC has shown superior electrocatalytic ability at intermediate temperatures [3]. Enhanced ORR in the SSC infiltrated LSCF cathodes may be related to the increase in 2PB/3PB and the change of the microstructure in the cathode.

## Patterned Electrode Cells for Kinetic Studies of ORR Reaction

### Background

Oxygen reduction in SOFC cathodes is thought to take place through two parallel pathways, the surface transport pathway and the bulk transport pathway. Each of these involves multiple steps including oxygen adsorption, dissociation, electronation, transport through one of two different pathways and incorporation at the triple phase (TPB) and/or two-phase boundaries between the cathode and electrolyte. A schematic is shown in Figure 4.

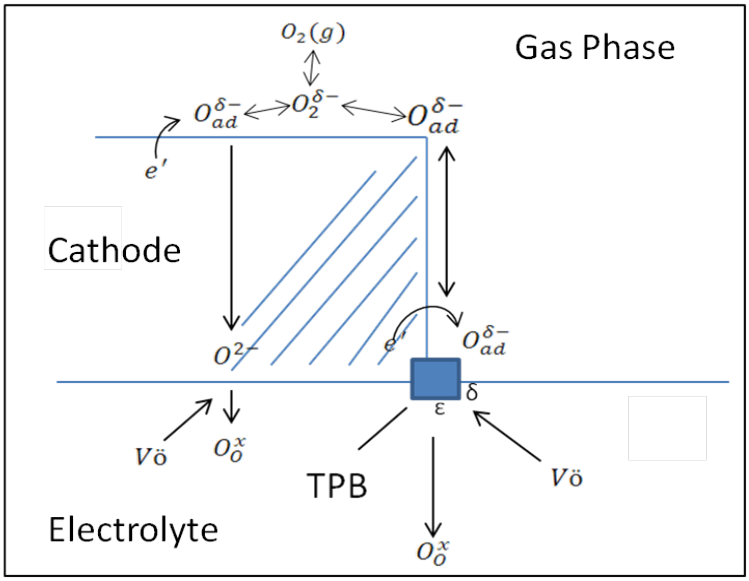


Figure 4. Schematic representation of the oxygen reduction reaction occurring at an SOFC cathode; included are both the bulk transport of oxygen ions as well as surface diffusion.

At Boston University, patterned cathode thin films on YSZ electrolyte have been used to measure the kinetics of the ORR using impedance spectroscopy. Appropriate transport models have been used to deconvolute the various kinetic parameters associated with the ORR.

**Experimental**

Patterned cathodes on YSZ substrates were deposited using photolithography and sputtering. An SEM micrograph of a typical patterned LCM ($(La_{0.87}Ca_{0.13})_{0.95}MnO_{3\pm\delta}$) film on YSZ is shown in Figure 5.

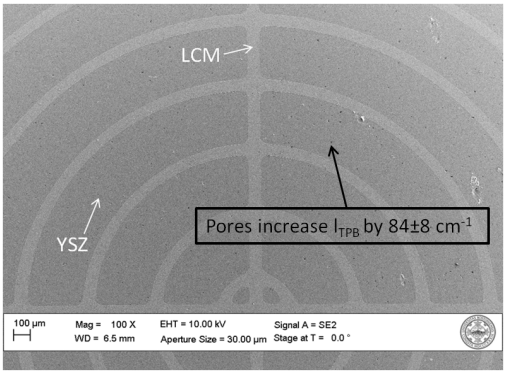


Figure 5. Patterned electrode showing clear pattern of LCM cathode (light) on the YSZ.

Cells of the type Porous LCM-YSZ|YSZ|Patterned LCM and Porous LCM-YSZ|YSZ|GDC barrier|Patterned LSCF ($La_{0.6}Sr_{0.4}Co_{0.2}Fe_{0.8}O_{3-\delta}$) were fabricated using photolithography and sputtering. The cells were fabricates such that the triple phase boundaries were varied over a wide range while the gas exposed cathode area was maintained constant. The cells were characterized in cathodic atmosphere between 600 and 800 °C and in oxygen partial pressures ranging from $10^{-5}$ to 0.21 atm using impedance spectroscopy.

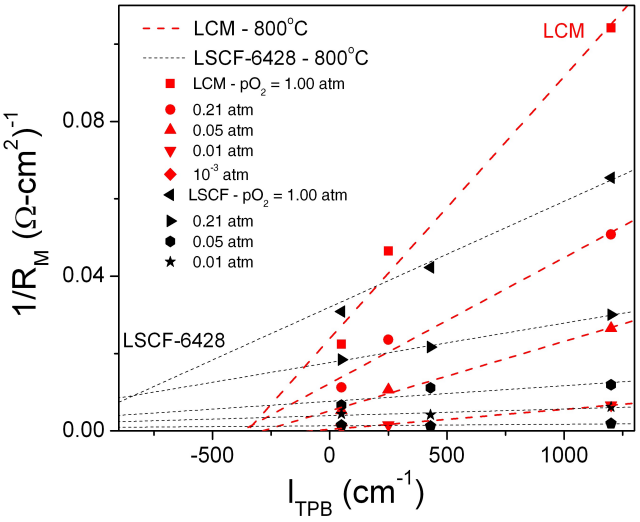


Figure 6. Inverse polarization resistance as a function of TPB. Note the stronger dependence in the case of the LCM films.

**Results and Discussion**

The inverse of polarization resistance measured from impedance spectroscopy is plotted as a function of TPB length in Figure 6 at 800 °C. The far weaker TPB length dependence in the case of LSCF versus LCM shows that, in LSCF, the bulk transport pathway in which the TPB length is relatively unimportant predominates. By contrast, in LCM the there is a strong dependence of the inverse of polarization resistance on TPB length thereby proving that surface diffusion pathways of oxygen to the TPB plays a more important role in the case of LCM.

Further by fitting the impedance results to a suitable model, parameters such as diffusion coefficients, oxygen surface coverage, and ORR rate constants can be obtained. The details of these models are not discussed here, but can be obtained from the reference [16, 17]. A very limited excerpt of the kinds of kinetic parameters that can be estimated from the impedance plots using appropriate transport models are presented below. Figure 7 shows the equilibrium oxygen surface coverage in the patterned LCM thin films, and Figure 8 shows the ratio of the surface diffusion to the bulk diffusion flux (ν) in LSCF thin films.

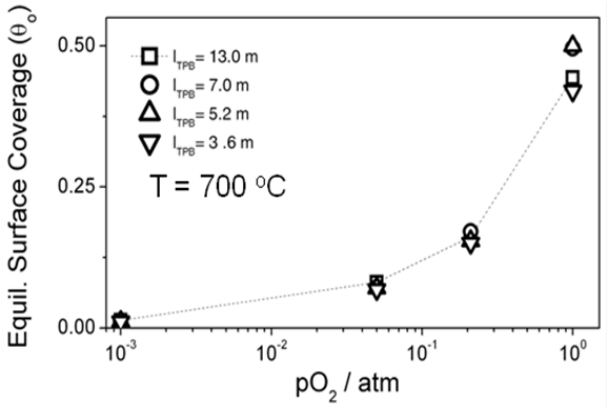


Figure 7. Equilibrium oxygen surface coverage on LCM films [16].

As can be seen from Figure 8, the surface diffusion contribution decreases with decreasing oxygen partial pressure for LSCF thin films. This is consistent with increasing oxygen vacancy concentrations at lower oxygen partial pressure, which directs more of the oxygen transport in LSCF through the bulk diffusion pathways. The ν also decreased with decreasing temperature. The reasons for this are not immediately obvious. However, ancillary X-ray evidence suggests that at lower temperatures, surface segregation of Sr followed by formation of SrO and eventually $SrCO_3$ occurs. It is possible that the presence of these surface phases inhibits surface diffusion of oxygen to the TPBs. This needs to be investigated further.

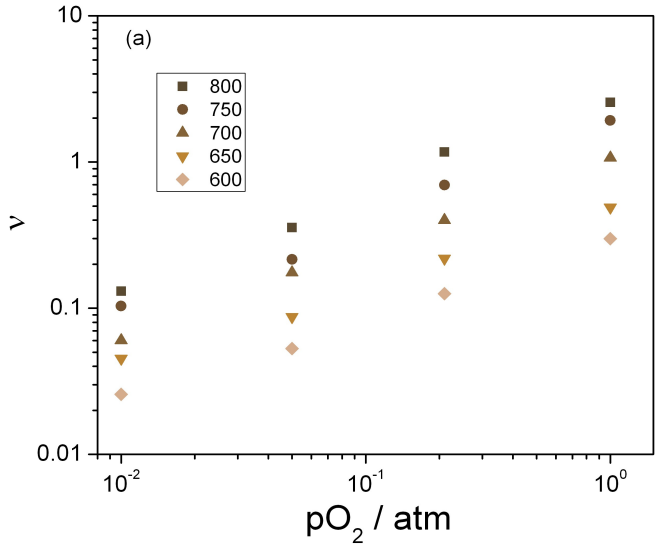


Figure 8. Dimensionless parameter—surface diffusion flux to bulk diffusion flux in LSCF as a function of oxygen partial pressure and temperature [17].

Thus, the patterned electrode approach combined with modeling allows one to obtain detailed kinetics information about the ORR.

Specifically by employing a suitable model it is possible to extract parameters such as the surface oxygen coverage, the surface oxygen diffusivity, and the forward and backward reaction rate constants for electron transfer reactions in the case of a predominantly electronic conductor, and the relative importance of the bulk pathway to the surface pathway in the case of mixed electronic conductors.

In the next phase of the project we will attempt to connect these kinetic parameters directly to cell level experimental parameters such as overpotentials and interfacial polarization resistances. More details about this work can be found in the references [11–12].

**Summary**

An experimental and modeling platform to study the ORR and derive kinetic parameters in a systematic way using patterned electrodes has been developed at Boston University. In the next phase of this program, we plan to study various other cathode materials as potential backbone and infiltrant materials by using the patterned electrode approach. In particular the backbone material will be deposited as the patterned electrode, and the infiltrant material will be deposited as catalyst islands on the patterned electrode. The impedance results combined with a suitable model will be used to choose and optimize the best backbone and infiltrant material. An experimental methodology to use an excellent mixed conductor as a backbone and combine it with electrocatalysts that promote surface exchange reactions through an infiltration technique has been developed at Georgia Tech. These approaches will be extended in phase II. In particular a methodology to correlate kinetic parameters directly with cell performance parameters will be developed.

## References


1) Singhal, S.C., *Advances in solid oxide fuel cell technology.* Solid State Ionics, 2000. **135**(1-4): p. 305-313.
2) Shao, Z.P. and S.M. Haile, *A high-performance cathode for the next generation of solid-oxide fuel cells.* Nature, 2004. **431**(7005): p. 170-173.
3) Xia, C.R., et al., *Sm0.5Sr0.5CoO3 cathodes for low-temperature SOFCs.* Solid State Ionics, 2002. **149**(1-2): p. 11-19.
4) Zhang, Y.L., S.W. Zha, and M.L. Liu, *Dual-scale porous electrodes for solid oxide fuel cells from polymer foams.* Advanced Materials, 2005. **17**(4): p. 487-+.
5) Liu, Y., S.W. Zha, and M.L. Liu, *Nanocomposite electrodes fabricated by a particle-solution spraying process for low-temperature SOFCs.* Chemistry of Materials, 2004. **16**(18): p. 3502-3506.
6) Lynch, M.E., et al., *Enhancement of La(0.6)Sr(0.4)Co(0.2)Fe(0.8)O(3-delta) durability and surface electrocatalytic activity by La(0.85)Sr(0.15)MnO(3 +/-delta) investigated using a new test electrode platform.* Energy & Environmental Science, 2011. **4**(6): p. 2249-2258.
7) Choi, J.-J., et al., *Preparation and Characterization of (La(0.8)Sr(0.2))(0.95)MnO(3-delta) (LSM) Thin Films and LSM/LSCF Interface for Solid Oxide Fuel Cells.* Journal Of The American Ceramic Society, 2011. **94**(10): p. 3340-3345.
8) Ding, H., et al., *Suppression of Sr surface segregation in La1-xSrxCo1-yFeyO3-δ: A First Principles Study.* Physical Chemistry Chemical Physics, 2012(doi:10.1039/C2CP43148C).

9) Nie, L.F., et al., *La0.6Sr0.4Co0.2Fe0.8O3-delta cathodes infiltrated with samarium-doped cerium oxide for solid oxide fuel cells.* Journal Of Power Sources, 2010. **195**(15): p. 4704-4708.
10) Liu, M.F., et al., *Enhanced performance of LSCF cathode through surface modification.* International Journal Of Hydrogen Energy, 2012. **37**(10): p. 8613-8620.
11) Lou, X.Y., et al., *Improving La0.6Sr0.4Co0.2Fe0.8O3-delta cathode performance by infiltration of a Sm0.5Sr0.5CoO3-delta coating.* Solid State Ionics, 2009. **180**(23-25): p. 1285-1289.
12) Steele, B.C.H., P.H. Middleton, and R.A. Rudkin, *Material Science Aspects of Sofc Technology with Special Reference to Anode Development.* Solid State Ionics, 1990. **40-1**: p. 388-393.
13) Xu, X.Y., et al., *LSM-SDC electrodes fabricated with an ion-impregnating process for SOFCs with doped ceria electrolytes.* Solid State Ionics, 2006. **177**(19-25): p. 2113-2117.
14) Ding, D., et al., *Electrochemical characteristics of samaria-doped ceria infiltrated strontium-doped LaMnO(3) cathodes with varied thickness for yttria-stabilized zirconia electrolytes.* Journal Of Power Sources, 2011. **196**(5): p. 2551-2557.
15) Miki, T., et al., *Enhanced Oxygen Storage Capacity of Cerium Oxides in Ceo2/La2o3/Al2o3 Containing Precious Metals.* Journal of Physical Chemistry, 1990. **94**(16): p. 6464-6467.
16) Miara, L.J, Basu,S.N., Pal, U.B. and Gopalan,S. *2D Numerical Model for Identification of Oxygen Reduction Reaction Mechanisms in Patterned Cathodes of $La_{0.6}Sr_{0.4}Co_{0.2}Fe_{0.8}O_{3-\delta}$*, Journal of The Electrochemical Society, 2012. **159** (8): pF419-425
17) Miara, L.J., Davis, J.N., Basu,S.N., Pal, U.B. and Gopalan,S. *Application of a State-Space Model to Patterned Cathodes of $(La_{0.87}Ca_{0.13})_{0.95}MnO_3$*, Journal of The Electrochemical Society, 2011. **158** (12): pB1523-B1531

# Part II: Topical Reports

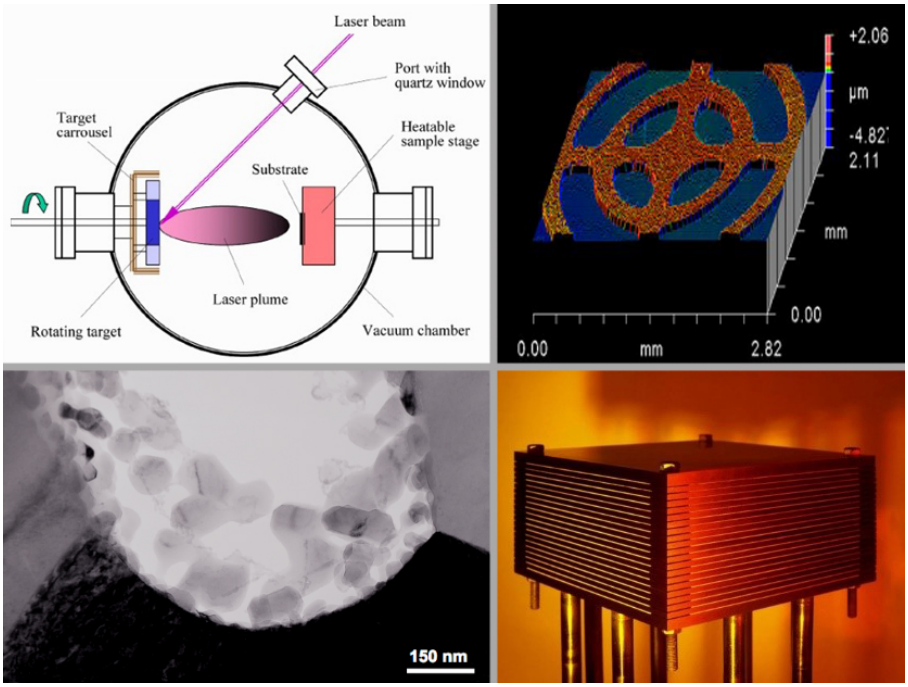

# In Situ X-ray Studies of Solid Oxide Fuel Cell Cathodes *by Paul Fuoss (Argonne National Laboratory) & Hoydoo You (Argonne National Laboratory)*


## Summary

This report is aimed at introducing the capabilities of X-ray analysis of solid oxide fuel cells and, in particular, their cathodes under conditions that closely approximate those of operating fuel cells (i.e., *in operando* measurements). The report provides a high level introduction to X-ray techniques and then highlights several findings derived from the application of X-ray techniques to *in operando* studies of $La_{1-x}Sr_xMnO_3$ (LSM) and $La_{1-x}Sr_xCo_{1-y}Fe_yO_3$ (LSCF) cathode materials to help illustrate their use.

Key findings of the SECA effort to study cathodes with X-ray techniques include:

- Significant structural rearrangements occur in SOFC cathodes at high temperature and with changes in oxygen partial pressures.
- *In operando* measurements are necessary since quenched samples do not always reflect surface configurations under operating conditions. X-ray techniques provide this capability.
- X-ray diffraction techniques can be used probe the local oxygen vacancy concentration and the local activity of cathodes.
- X-ray spectroscopy techniques reveal the oxidation state and local coordination geometry of active species.
- X-ray measurements using laboratory-based sources are effective at providing long-term, *in operando* information about SOFC cathode structural evolution.


## Introduction

A solid oxide fuel cell (SOFC) has only three active components: 1) the anode where fuel is used to produce charged oxygen vacancies ($V_O^{\bullet\bullet}$), 2) the electrolyte that transfers the $V_O^{\bullet\bullet}$ to the cathode while preventing the transfer of electrons, and 3) a cathode that uses oxygen to annihilate the $V_O^{\bullet\bullet}$. However, a detailed examination of these active components reveals surprisingly complex and dynamic processes, at least at the elevated temperature and near atmospheric pressure of SOFC operating conditions. The important processes occur on a variety of length scales from atomic (e.g., catalytic decomposition of oxygen) to many microns (e.g., the porous cathode microstructure), and on time scales that range from the very fast (e.g., surface segregation) to very slow (e.g., grain growth in components). While the overall features of these processes can be deduced from ex situ measurements (e.g., X-ray photoemission spectroscopy or transmission electron microscopy), their potential dynamic response to changes in operating conditions makes the generalization of those results questionable without *in operando* verification.

X-ray techniques are unique in their ability to perform in situ and *in operando* studies of materials properties and processes. When coupled with high energy synchrotron radiation sources, X-rays

can penetrate through high pressure atmospheres and microns-to-millimeters of most oxide materials. This allows atomic-level investigation of structure and properties under elevated temperature environmental conditions relevant to SOFC operation. On the other hand, if desired, X-ray reflectivity from planar samples can be used to limit the penetration of the X-rays to just the surface of the sample. Finally, the high intensity of X-rays enables real-time measurement and spatially resolved imaging of critical materials processes. While X-rays are generally useful for studying all of the components of a SOFC, this report focuses on determining the structure and chemical state of cathode models, the time evolution of those properties, and how those properties relate to performance of a SOFC. We start with a brief introduction to the relevant X-ray techniques. This introduction is aimed at orienting the reader and providing pointers to more complete reference materials. After introducing the X-ray techniques, we will highlight several findings derived from the application of X-ray techniques to in situ studies of $La_{1-x}Sr_xMnO_3$ (LSM) and $La_{1-x}Sr_xCo_{1-y}Fe_yO_3$ (LSCF) cathode materials to help illustrate their use.

## X-ray Techniques

X-ray techniques have a long and rich history, and there are a number of excellent textbooks describing the application of X-ray techniques to materials science problems [1, 2]. Up until the development of broadband synchrotron radiation sources (e.g., Argonne National Laboratory's [ANL] Advanced Photon Source), X-ray techniques were centered around X-ray diffraction. However, the capabilities of X-ray techniques have been greatly extended by the very high brightness and energy tunability of synchrotron X-ray sources based on high-energy electron storage rings, and some of these relatively new capabilities have been described by Als-Nelson and McMorrow [3]. Our goal here is to highlight techniques that are of particular usefulness in the study of the mechanisms and operation of SOFCs.

### X-ray Reflectivity

The use of X-ray reflectivity to convert conventional X-ray techniques into surface sensitive probes has greatly expanded their range of use [4, 5]. X-rays have an index of refraction that is slightly less than unity [6]. Thus, an X-ray beam entering a flat sample, is refracted towards the surface (see inset in Figure 1). As the grazing angle is reduced to the “critical angle,” the refracted wave travels parallel to the surface. Below the critical angle ($\alpha_c$), the X-rays are almost totally reflected from the surface as shown for LSM in Figure 1. Since the X-rays are refracted out of the sample, the X-ray intensity decreases rapidly as a function of depth with an exponential decay. The dependence the penetration length as a function of grazing angle is also shown in Figure 1. It is clear that at shallow grazing angles below the critical angle for total X-ray reflectivity (the inflection point of the X-ray reflectivity curve), X-rays only penetrate a few nanometers into a smooth thin film. By changing the grazing angle by only a few tenths of a degree, X-rays can be used to probe either the surface region or bulk properties of a thin film.

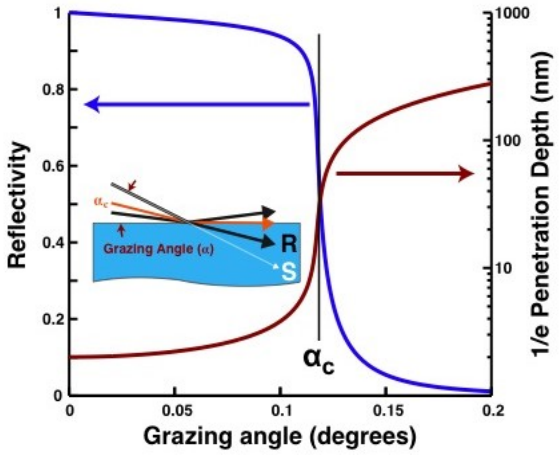


Figure 1. The calculated effect of X-ray refraction on 24 keV X-rays incident at grazing angle on a flat $La_{0.7}Sr_{0.3}MnO_3$ surface.

As the incident angle is increased out of the total reflection regime, X-ray reflectivity measurements become sensitive to both long-range structures in the thin film (e.g., the period of a superlattice or the thickness of a thin film on a substrate), and the sharpness and roughness of both the surface and buried interfaces. For example, Figure 2 shows the X-ray reflectivity from an LSM film grown on $SrTiO_3$ (STO) as a function of temperature. Short period oscillations are clearly present in the data at 30 °C and 400 °C that disappear by 700 °C. These oscillations result from interference between the bottom and top layers of the LSM film and their disappearance indicates that the interfaces are becoming rougher as a function of temperature. A smoother surface (i.e., the oscillations reappear) can be recovered when the temperature is reduced. This result demonstrates that there are significant structural rearrangements taking place during temperature cycling of SOFC cathodes and that measurements on quenched samples may not accurately capture surface configurations under operating conditions.

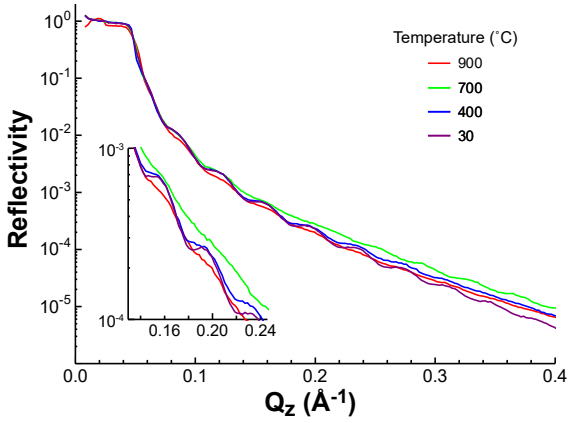


Figure 2. The X-ray reflectivity of a 20 nm thickness film of $La_{0.7}Sr_{0.3}MnO_3$ on a $DyScO_3$ substrate in 150 Torr of $O_2$ (equivalent to atmospheric pressure air) as a function of temperature. Note that the oscillations get weaker as the temperature is raised, indicating that the interfaces are becoming rougher or that interdiffusion is occurring at the LSM-DSO interface.

Quantitative measures of the roughness can be determined by fitting the reflectivity data and the lateral size of the roughness can be determined by looking at the rocking dependence of the reflectivity. Using these types of measurements, X-ray reflectivity has proven to be a powerful in situ probe of film roughening and interdiffusion. van der Lee has written an extensive review of the use of X-ray reflectivity to study the structure of materials [7]. The Center for X-Ray Optics (CXO) at Lawrence Berkeley National Laboratory has an extremely useful website that can be used to model reflectivity from a variety of materials and structures [8].

**Grazing Incidence X-ray Scattering**

The use of grazing incidence X-ray scattering (GIXS) has become a routine surface analysis technique. In the GIXS geometry (shown in Figure 3), the incident X-ray beam strikes the sample at a small grazing angle. As just discussed, by tuning the grazing angle a slight amount, X-ray scattering measurements (e.g., powder diffraction) can be performed as a function of depth. The use of GIXS to study the surface structure of thin films has been employed to study surface structure (e.g., Robinson et al. [9, 10]), crystal growth in reactive environments (e.g., Fuoss and coworkers [11–13]), and the study of surface catalytic reactions (e.g., You and coworkers [13, 14]). There have been a number of good reviews of the technique. Fuoss and Brennan is an early review that discusses application to a variety of materials science problems [15]. Renaud et al. is a review focused on the use of GIXS to study larger surface structures such as nanoparticles [16].

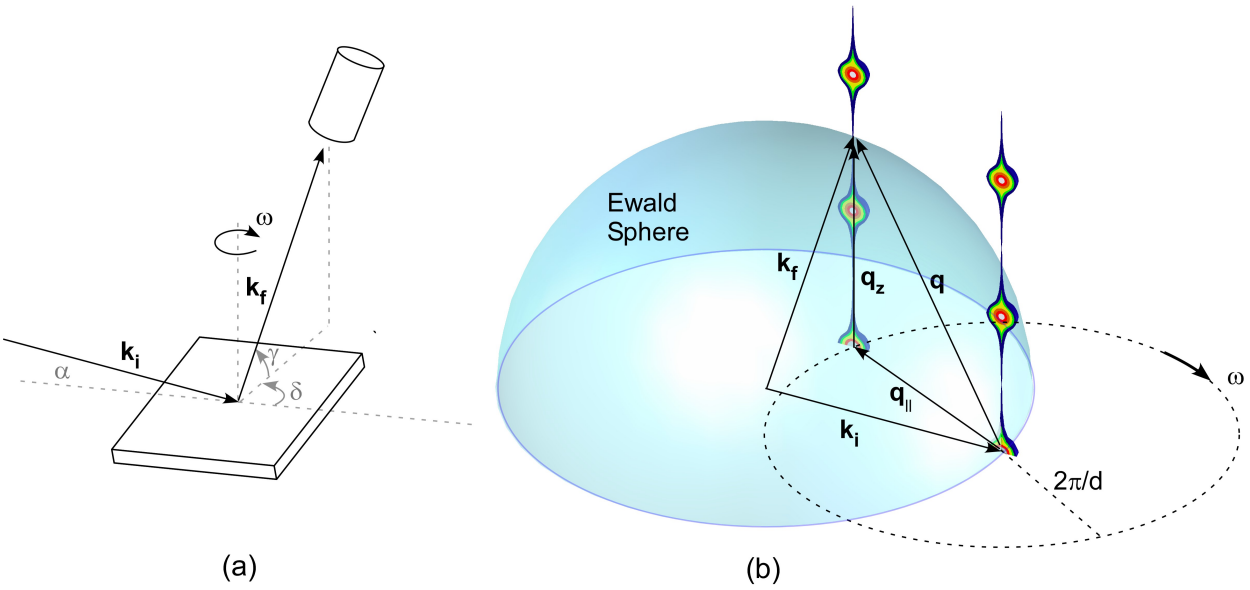


Figure 3. The grazing incidence scattering (GIXS) geometry. The X-rays are incident at a grazing angle α and detected at a different grazing angle γ. (b) The resulting relationships in reciprocal space.

For analysis of surfaces, buried interfaces and very thin films, crystal truncation rod analysis is a powerful technique that allows, for example, the measurement of the roughness of a particular crystalline component of a surface or buried interface (compared with reflectivity that measures the roughness of the atomic density). For an infinite crystal, the Bragg diffraction spots are points in reciprocal space. However, if the crystal is cut, creating a surface, streaks of intensity perpendicular to the surface are added to every Bragg reflection. Since these streaks are due to truncating the crystal, they are typically referred to as crystal truncation rods (CTRs). The dependence of the CTR intensity with distance away from a Bragg point is very similar to that of an X-ray reflectivity measurement except that only the aligned crystalline portions of the sample contribute to the CTR. For a simple surface, Figure 4 shows a schematic representation of the difference between a rough and smooth interface.

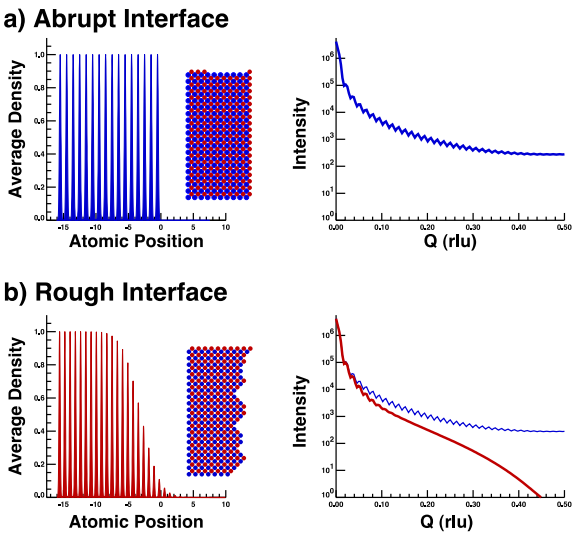


Figure 4. Schematic representation of the crystal truncation rod (CTR) from a smooth and rough interface.

The shape of the CTR perpendicular to the surface normal (e.g., along H or K when L is perpendicular to the surface) also contains a great deal of information about surface structures. Schematic line shapes (e.g., rocking curves) of a few simple surfaces are shown in Figure 5. Since the CTRs are perpendicular to the surface, an undulating surface causes a broadened rocking curve (Figure 5c) and a miscut surface causes satellites (Figure 5d). In the latter case, the higher order satellites can be thought of as coming from Bragg peaks with larger L (e.g., the 113) or as diffraction from a periodic array of steps. The interpretation of more complex structures has been discussed in an excellent review of the use of CTR analysis by Robinson and Tweet [18] and Vlieg has published a CTR data analysis package [19].

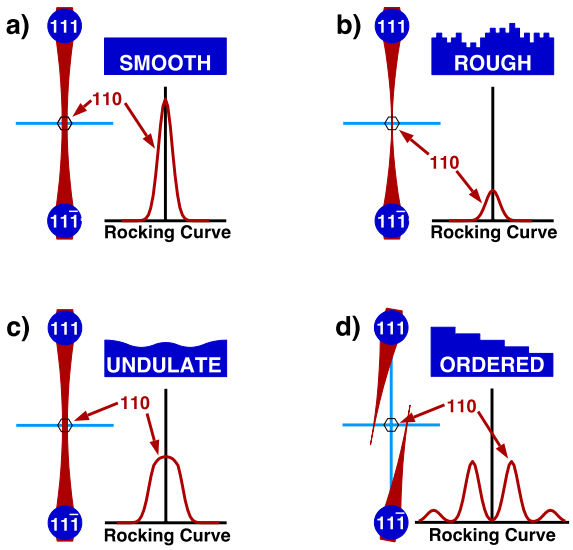


Figure 5. Schematic profiles of the CTR at the anti-Bragg position. In particular, note the splitting in (d) that arises because the CTR's are perpendicular to the surface and not aligned with the reciprocal lattice of the crystal.

As a simple yet practical example, Figure 6 shows the CTR from a thin film of LSM on STO as a function of oxygen partial pressure ($pO_2$). Similar to the X-ray reflectivity data in Figure 2, there are oscillations present that reflect the thickness of the film. As the $pO_2$ is reduced, these oscillations become less intense, indicating that the interfaces are becoming rougher (this behavior is reversible). In addition, the LSM Bragg peak at roughly 2.05 (in room temperature indices) shifts to slightly lower L indicating that the lattice parameter of the film is increasing. In other systems that depend on catalysis, such structural rearrangements have been shown to have important catalytic implications. In particular, the reversible incorporation and segregation of Pd in automobile catalytic converters reduces the amount of Pd required by over an order of magnitude [17]. While there is currently no evidence that the same effect occurs in SOFC cathodes, the presence of temperature dependent surface structures may impact the design of degradation resistant cathodes.

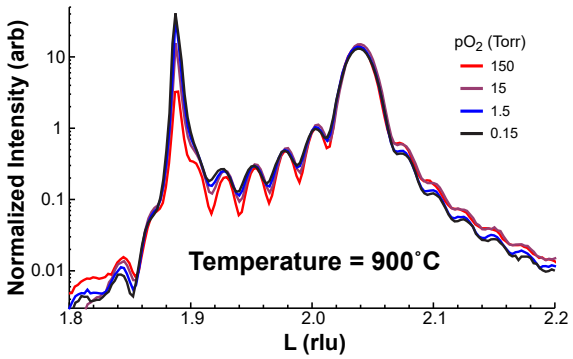


Figure 6. The (02L) crystal truncation rod (CTR) of a 20 nm film of $La_{0.7}Sr_{0.3}MnO_3$ on a $DyScO_3$ substrate at 900 °C as a function of oxygen partial pressure. Note that the oscillations get stronger as the $pO_2$ is raised, indicating that the interfaces are becoming smoother.

**Small Angle X-ray Scattering**

Typically, cathodes for SOFCs are made by sintering small particles into porous films. The resultant size (and size distribution) of both the remaining particles and the pores in the films can be non-destructively measured using small angle X-ray scattering (SAXS) [16, 20, 21]. From SAXS data, quantitative information about the average particle size, particle size distribution and the surface-to-volume ratio can be extracted. Standard SAXS measurements that use a 2-D detector provide structural information at length scales of 1–100 nm. This range of sizes is often too small for the porous cathode materials relevant to SOFCs and ultra small angle X-ray scattering (USAXS) needs to be measured [22]. In order to discriminate the ultra-small angle diffraction from the intense main beam, a multiple-bounce channel cut monochromator is used to precisely shape the incoming beam. Then, another set of channel-cut crystals is used to analyze the beam scattered from the sample. A typical setup for USAXS is schematically shown in Figure 7.

In general, small angle X-ray scattering measures the absolute value of deviations from the average density. Thus, SAXS cannot differentiate between positive and negative fluctuations in density, and the derived characteristic lengths represent those of void spaces as much as of the actual particles within the cathode material. Since a SOFC cathode is typically made from sintered powders that form a rather dense interconnected network, the spatial fluctuation in density is primarily caused by the void space. As a result, the SAXS intensity is dependent on the pore size distribution.

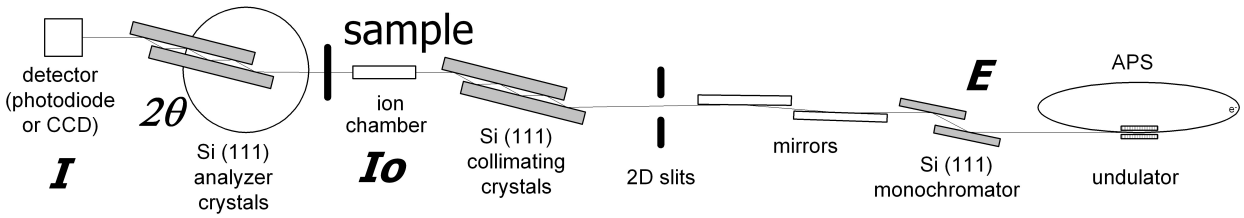


Figure 7. A typical ultra-small angle X-ray scattering instrument layout. The use of Bragg collimators produces a very low divergence X-ray beam with a very sharp angular distribution.

The SAXS intensity, typically presented in a log-log plot, can be divided into two angular ranges in and analyzed with a dilute, two-phase model. In the low Q region, the SAXS intensity typically shows a sharp drop off (or "knee") corresponding to the average size of the scattering object. Analysis of that peak allows the extraction of an average particle size (or pore size in dense materials) using the familiar scattering relationship $I(q) \propto \exp(-q^2R^2/3)$ where $q=4\pi\sin(\theta)/\lambda$, $\theta$ is one half of the total scattering angle, and $\lambda$ is the photon wavelength. In the high Q region, the SAXS intensity follows a power-law with a slope of -4 (-3 when radially integrated), known as Porod's law. This allows the extraction of surface-to-volume ratio. With detailed analysis and modeling, internal surface area and void volume size distributions can be extracted from the data.

In USAXS, the X-ray beam size can be varied in the range between ~1×2 mm to ~15×200 um and scanned over different areas of the sample. Sample homogeneity and thickness are the main concerns for sample preparation. Multiple layer structures complicate the analysis, so the sample should be as homogenous as possible along the beam path. The sample also has to be the correct thickness to produce sufficient scattering intensity while not attenuating the X-rays. The ideal sample thickness depends on the X-ray energy, but is in the order of ~10 μm for X-ray energies of 10–17 keV. Because of these requirements, either microtoming [22, 23] or thin layer printing on low atomic number single crystal substrates is needed for SOFC sintered cathode samples. Despite the special sample preparation and the resultant uncertainties in data analysis, USAXS measurements non-destructively average over a large volume of the sample and can be performed with the sample at elevated temperatures under conditions that simulate fuel cell operation. Thus, USAXS measurements are well suited to determining changes in the internal morphology of a cathode and correlating those changes in performance.

**X-ray Spectroscopy**

***Total-Reflection X-ray Fluorescence Analysis***

Since the chemical reactivity of materials is often controlled by the surface or by nanoparticles on the surface, it is of particular importance to understand the surface and near surface composition of cathodes. For planar structures, this can be accomplished by combining total external reflection of X-rays and X-ray fluorescence analysis. The combined technique, referred to as total-reflection X-ray fluorescence analysis (TXRF), is sensitive to the top ≈5 nm of a film and is commonly used in the semiconductor industry to examine cleanliness of surfaces [24, 25].

The X-ray absorption process is dominated by deep, tightly bound electrons in atoms [26]. Figure 8 shows the two deepest energy levels for Sr and a typical absorption process. As the X-ray photon energy is increased above binding energy of a K-shell electron, there is a sharp jump in the X-ray absorption coefficient. The X-ray removes a K-shell electron and the atom relaxes by dropping a higher shell electron (e.g., an L-shell electron) into the K-shell. To conserve energy, this relaxation either requires the X-ray fluorescence emission of another X-ray (in this case with an energy of 14,165 eV) or an Auger electron. Since the atomic levels in an atom are mainly determined by the atomic number of the atom and are unique to that element, X-ray absorption spectroscopy is routinely used to identify impurities and to determine composition in materials. This technique commonly measures X-ray fluorescence intensities using an energy dispersive X-ray detector and fits the resultant spectra to the known X-ray fluorescence lines. A very useful compilation of X-ray absorption information including the location and relative intensity of the fluorescence lines is available in a free publication from the Center for X-Ray Optics at Lawrence Berkeley Laboratory [27].

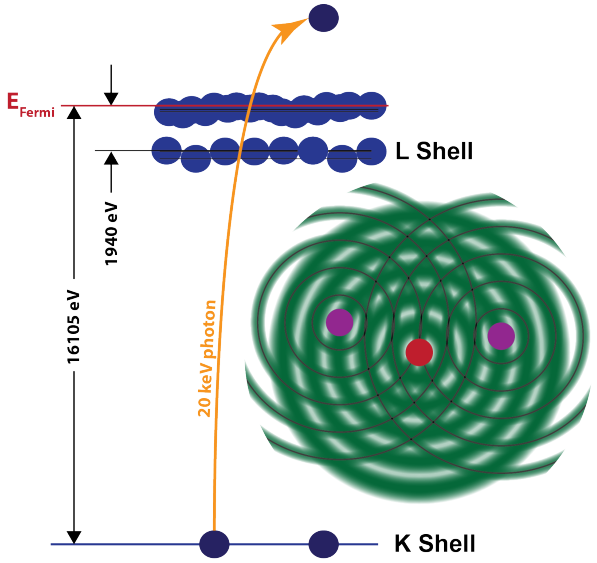


Figure 8. A schematic of the electron binding levels in Sr. A common X-ray absorption and decay process would be for a high-energy photon to excite a K-shell electron to the continuum. An L-shell electron then decays, emitting a characteristic $K_\alpha$ photon. The probability of absorption is modulated by reflected electrons from the neighboring atoms leading to extended X-ray absorption fine structure (EXAFS).

Because of the importance of surface composition to the cathode oxygen reduction reaction, the ANL team has adapted TXRF to the study of the surface composition of LSM under conditions modeling the operation of a SOFC cathode [28]. These results will be discussed in detail in the examples section, but Figure 9 shows a typical result from a $La_{0.7}Sr_{0.3}MnO_3$ film on a $DyScO_3$ substrate chosen to minimize interference between the substrate and film fluorescence lines. The intensity of the Sr line (blue dots) is higher than the La line at small grazing angle and indicates a

surface enhancement of Sr. This difference can be quantitatively analyzed to extract the Sr concentration averaged between the surface and a depth Λ (see top scale).

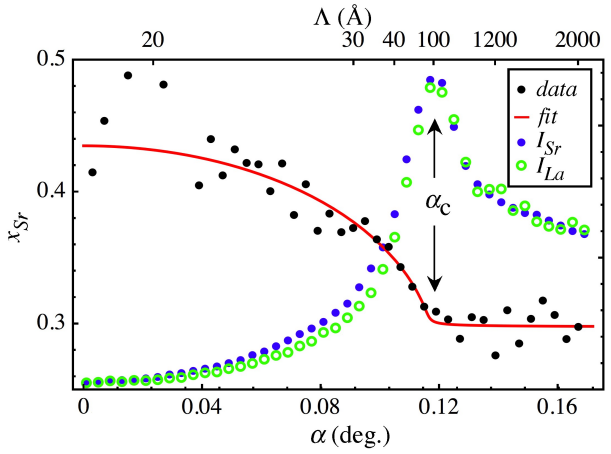


Figure 9. The X-ray fluorescence intensity of Sr and La (both normalized to the same height) from a 16 nm $La_{0.7}Sr_{0.3}MnO_3$ film on $DyScO_3$ measured at 700 °C and in 150 Torr $pO_2$. The Sr composition as a function of depth is determined from the relative intensities of Sr and La.

***X-ray Absorption Near-Edge Structure***

X-ray absorption spectra contain essential information about the oxidation state, local coordination geometry, and electronic structure of the absorbing atom. As shown in Figure 10, at specific energies corresponding to the core energy levels of an absorbing atom, sharp increases in the absorption are observed due the resonance transition of the core electron into empty density of states. This X-ray absorption can be measured using the X-ray transmission coefficient, the X-ray fluorescence intensity or the total electron yield depending on the type of sample and the sample environment. X-ray transmission measurements are most common, but require samples to be a specific thickness (on the order of 10–100μm) for each of the elements of interest to optimize the sensitivity. X-ray fluorescence is used on thin or dilute samples. Electron yield can be used for surface sensitivity in UHV environments.

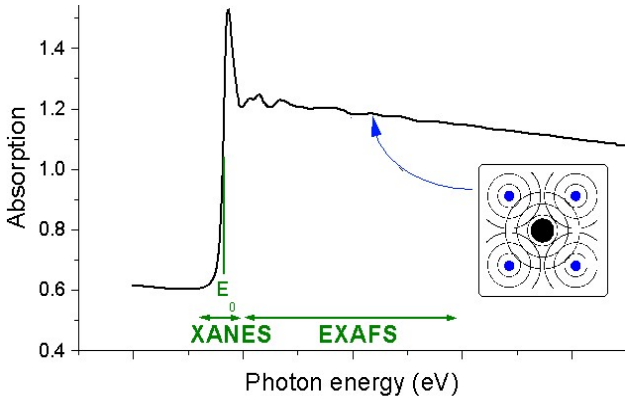


Figure 10. Typical XAF data. $E_0$ indicates the absorption edge energy. Inset: a photoelectron emitted from the X-ray absorbing atom (black) is diffracted from the surrounding atoms (blue) and modulate the absorption spectrum in the EXAFS region.

X-ray absorption spectra can be divided into two regions. A typical example is schematically shown in Figure 10. The spectrum close to the edge energy is called the X-ray absorption near edge structure (XANES) and the energy region extending 500–1000eV above the edge is called the extended X-ray absorption fine structure (EXAFS). XANES contains the sharply increasing absorption edge, while EXAFS has gently modulated absorption that decays at higher energies.

XANES is due to the electric transition from a core state to an unoccupied state and can, in principle, be described by Fermi's Golden Rule. However, due to the presence of the core hole created during the absorption process, the final electronic state of the system is different from the initial state before the transition, which greatly complicates the calculation of XANES from first principles. The electric transition can be approximated by a dipole transition in the first order, and thus follow dipole selection rules. But for K edges, a quadrupole transition also needs to be considered.

XANES spectra contain information about the oxidation state, local coordination geometry and the electronic structure of the absorbing atom. At higher oxidation state, the edge energy increases due to the tighter binding of the core electrons. The amount of edge shift can be compared with standards for a rough measure of oxidation state. The shape of the edge changes with the local coordination geometry around the absorbing atom since that coordination affects the electronic structure. A quantitative interpretation of XANES data is difficult due to the lack of good computational tools, but progress is being made in this field [29, 30]. However, we can still obtain qualitative information about the oxidation state, otherwise difficult to obtain, from the XANES spectra. The application of XANES on ceramics has been reviewed by Tanaka [31] and the interpretation of 3-D metal XANES pre-edge structures has been discussed in a paper by de Groot [32].

### *Extended X-ray Absorption Fine Structure*

The difference between the incident X-ray energy and the edge energy imparts kinetic energy to the excited core electron, which becomes a photoelectron that scatters from neighboring atoms. From a quantum mechanical point of view, the absorbing atom is the origin of a propagating photoelectron wave, while the neighboring atoms are point sources of the backscattered electron waves. EXAFS arises from the modulations in the X-ray absorption resulting from the interference between the propagating and the backscattered waves (see schematic in Figure 10). Because of this interference, X-ray absorption increases or decreases depending on the photoelectron wavelength. Therefore, the modulation in X-ray absorption can be simply modeled by scattering of the photoelectron from muffin-tin type atomic potentials. The main feature of EXAFS can often be obtained in the single-scattering plane-wave approximation [33]. Detailed analysis of EXAFS data are routinely performed by employing full multiple-scattering spherical-wave calculation using FEFF code [34]. In contrast with XANES, therefore, EXAFS has a solid framework for quantitative data analysis.

EXAFS contains information on the distance, coordination number and the type of neighboring atoms around the absorbing atom. EXAFS can be obtained from the normalized XAS data by subtracting a smooth background function and is plotted as a function of the wave number $k$, obtained from the photoelectron kinetic energy using the de Broglie equation. Neighboring atoms at a specific distance away from the absorbing atom contributes a damped sine wave term to the EXAFS signal. The amplitude of this sine term is dependent on the number and type of neighboring atom and its period is simply related to the interatomic distance.

## Application Examples

### Surface Structure and Chemistry

Many of the surfaces of perovskite materials such as LSM and LSCF are polar and, because of long-range electric fields, cannot be abruptly terminated [35]. That is, the material must eliminate the surface charge by a structural reconstruction (e.g., eliminating a portion of the surface atoms), changing the surface composition (e.g., by surface segregation), or by a chemical modification (e.g., changing the valence of surface atoms). There are many studies indicating that the surface composition of LSM and LSCF films can be significantly different than the bulk composition. For example, Kumigashira et al. [36] found significant Sr enrichment at the surface of LSM and van der Heide [37] found significant Sr enrichment in a variety of $La_{1-x}Sr_x$ films with the perovskite structure.

For SOFCs, there is evidence that changes in the surface composition can markedly impact the electrochemical performance of a cathode. For example, Bauman and coworkers [38] demonstrated significant bias-induced changes in the resistance of an LSCF film. A cathodic treatment decreased the resistance while an anodic treatment increased the resistance. From XPS measurements, these resistance changes were correlated with an increase in Sr surface composition with cathodic treatment and a corresponding decrease with anodic treatment. However, it is not clear from XPS studies at very low $pO_2$ what the equilibrium state of the surface is under operating conditions.

Thus, the Argonne team conducted a study of the equilibrium segregation of A- and B-site constituents in LSM and LSCF as a function of $pO_2$ and temperature.

Using TXRF, Fister et al. determined the amount of Sr surface segregation as a function of temperature and pressure for $La_{0.7}Sr_{0.3}MnO_3$ [28]. An example of an individual measurement is shown in Figure 9 and a summary of those results is shown in Figure 11. In Figure 11, we show results from a 16-nm-thick $La_{0.7}Sr_{0.3}MnO_3$ (LSM) film on $DyScO_3$ for $pO_2$ = 0.15 – 150 Torr (the $pO_2$ of atmospheric pressure air is ≈150 Torr) at 300, 500, 600, 700, and 900 ˚C. The Sr surface concentration is observed to exceed the bulk stoichiometry $x_{Sr}$ = 0.3 at all temperatures and $pO_2$ conditions. There are two distinct trends displayed in Figure 11, the amount of Sr surface segregation decreases with higher oxygen partial pressure and higher temperature. To highlight the $pO_2$-dependence, segregation isotherms are given in Figure 11a. The same data is recast in Figure 11b as an Arrhenius plot to emphasize the temperature dependence for each $pO_2$.

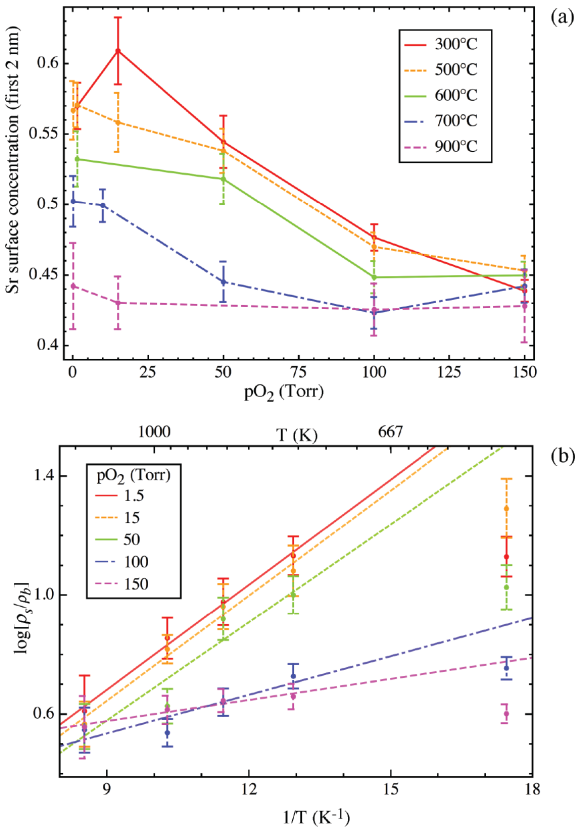


Figure 11. (a) Sr surface region concentration vs. oxygen partial pressure at T = 300–900 °C. (b) Sr surface enrichment as a function inverse temperature for a variety of oxygen partial pressures. The quantity $\rho_s$ denotes the Sr/La ratio integrated over the first 2 nm, while $\rho_b$ is the bulk ratio, i.e., 3/7. The lines are linear fits to equilibrium data taken between 500 and 900 °C.

As seen in Figure 11a, Sr surface segregation is a function of the oxygen partial pressure, but some degree of segregation is present at all experimental conditions. The $pO_2$-dependent enthalpy of segregation $\Delta H_{seg}$ can be extracted from the Arrhenius plot shown in Figure 11b. According to the McLean model, equilibrium surface segregation has an exponential dependence with inverse temperature [39]. In Figure 11b, the deviation from linearity of the outlying 300 °C data indicates that achieving thermodynamic equilibrium requires longer equilibration time than the typical one hour used in our experiments. Equilibrium was established, however, at all higher temperatures. The enthalpy of segregation values for $pO_2$ = 1.5 – 150 Torr were calculated from the linear slopes in Figure 11b and are shown in Figure 12.

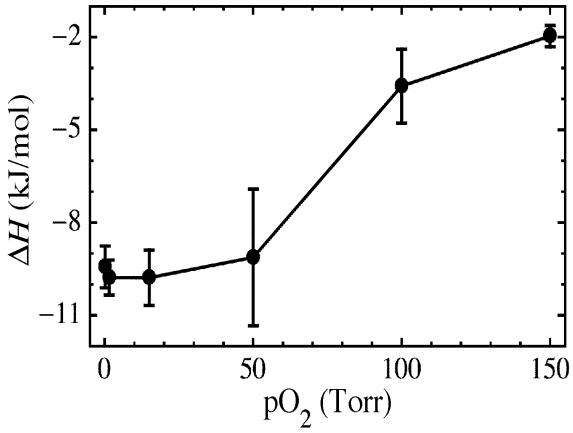


Figure 12. Enthalpy of Sr surface segregation as a function of $pO_2$ for $La_{0.7}Sr_{0.3}MnO_3$.

In agreement with Herger et al. [40] the exothermic heat of segregation is relatively small; however, Fister observed a systematic variation in $\Delta H_{seg}$, with values varying from -9.5 to -2.0 kJ/mol with increasing $pO_2$. This large variation in the enthalpy of segregation, combined with the significant equilibration times at lower temperatures, suggests that the surface composition of LSM measured at room temperature is highly sensitive to thermal history, and in situ measurements are important for understanding segregation behavior in LSM at the high temperature conditions relevant to SOFC operation.

The segregation behavior of LSCF is potentially more complicated for two reasons. First, segregation can occur on both the A site (La,Sr) and B site (Co,Fe). In addition, there can be rapid and significant changes in the bulk cation vacancy concentration that are not allowed in LSM because of its lack of ionic conductivity. ANL researchers have determined using TXRF that Sr segregation occurs in $La_{0.6}Sr_{0.4}Co_{0.2}Fe_{0.8}O_3$ but, unlike the case of LSM, there is essentially no dependence on $pO_2$.

In addition, the ANL team has found that Co segregates to the surface of LSCF at elevated temperature under normal atmospheric conditions (see Figure 13) [41]. This segregation is slightly

enhanced by a cathodic potential and is strongly suppressed by the application of an anodic potential.

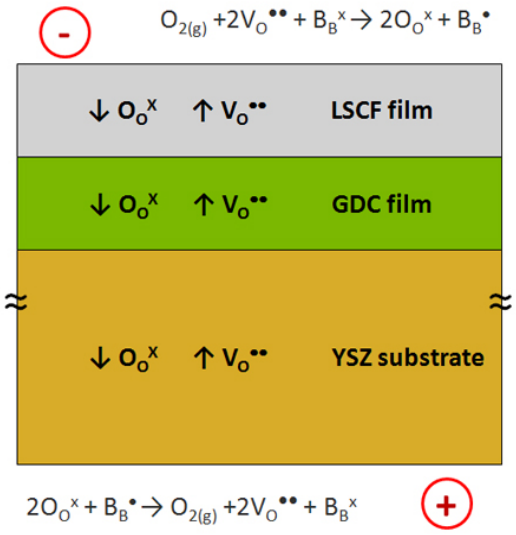


Figure 13. An overview of the sample geometry for examining the dependence of vacancy concentration as a function of electrochemical potential and oxygen partial pressure.

**Oxygen Surface and Interface Exchange**

Studies of the lattice parameter of a cathode material like LSCF can reveal a great deal about the underlying mechanisms and dynamics of charge transport because there is a well-defined correlation between the lattice parameter and vacancy concentration [43]. In particular, the concentration of $V_O^{\bullet\bullet}$ in the LSCF layer (see Figure 14) is determined by concentration gradients across the LSCF surface (controlled primarily by ORR), and by the gradient across the buried interface between LSCF and the electrolyte (or buffer layer). For a given current through the structure, the LSCF vacancy concentration will reach steady state and the LSCF film will have a well-defined lattice parameter. When the current is changed, there will be a period where the vacancy concentration is changing and reveals further information about *the relative kinetics of the surface ORR and transport of $V_O^{\bullet\bullet}$ across the buried interface*. Unlike other surface exchange coefficient measurements, these measurements provide a high spatial resolution determination of film activity.

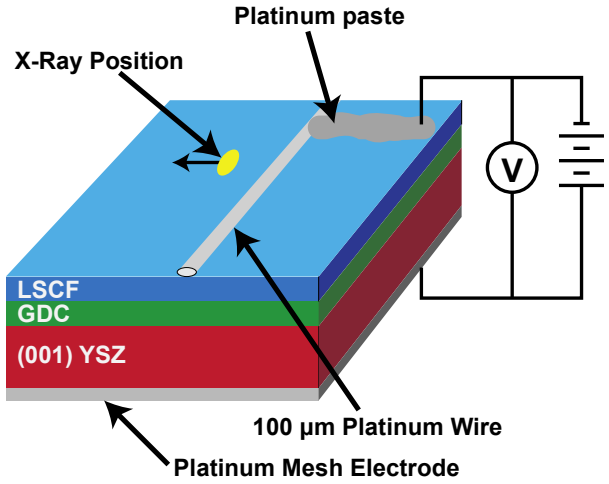


Figure 14. The sample geometry used for dynamic lattice parameter measurements performed by the ANL group.

Ingram and coworkers have made static and dynamic measurements of the lattice parameter of LSCF as functions of temperature, $pO_2$, and electrochemical bias [44]. Using ≈20 nm thick epitaxial films of LSCF deposited on a ≈5 nm gadolinium-doped ceria (GDC) buffer layer grown on (001) YSZ, they attached electrodes to the sample (see Figure 15) and measured the position of the LSCF (004) Bragg peak and, indirectly, the change in oxygen vacancy concentration. In addition, information about the relative conductivities of the LSCF film and the YSZ substrate can be determined from measurements as a function of the lateral distance from the Pt electrode.

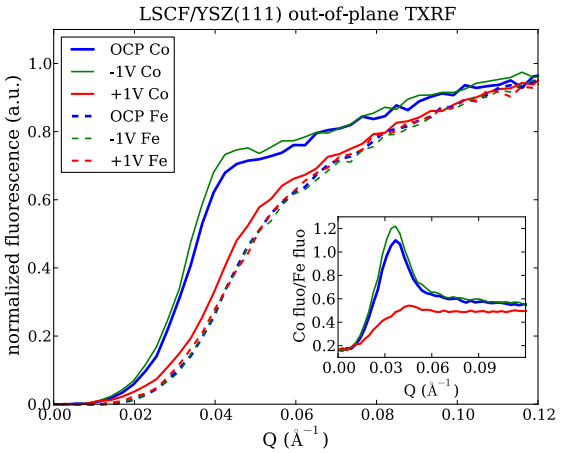


Figure 15. The normalized cobalt and nickel fluorescence signals from a $La_{0.6}Sr_{0.4}Co_{0.2}Fe_{0.8}O_3$ film on yttria-stabilized zirconia for three different electrochemical conditions. The data indicates that cathodic bias favors cobalt segregation.

The device structure shown in Figure 15 can be characterized by measuring i-V curves, an example of which is shown in Figure 16 for two different oxygen partial pressures. The lower cathodic saturation current for lower oxygen partial pressures is consistent with the surface ORR being the rate limiting step, as expected.

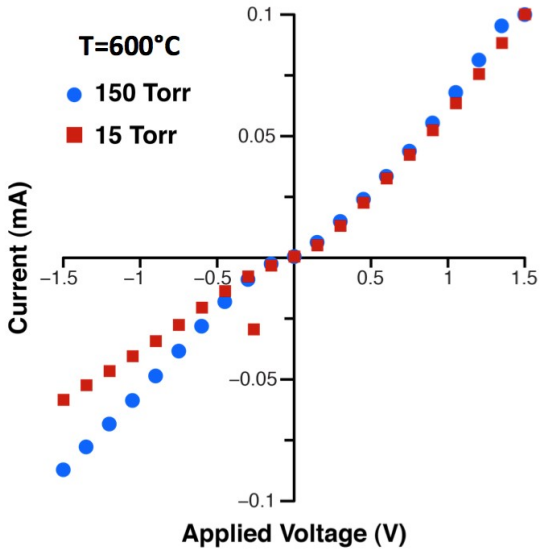


Figure 16. The i-V curve of the LSCF sample grown on GDC/YSZ(001) as described in the text. The data, taken at 600 °C is fit with the Butler-Volmer relation yielding the charge transfer coefficients indicated for the cathodic condition.

Figure 17 shows the Bragg peak shift observed as a function of varying the applied potential at 600 °C at 1.3 mm from the platinum electrode. The increase in lattice parameter under cathodic potential shows that not only is the surface ORR limiting the conduction, it is significantly slower than the vacancy transfer rate at the buried interface. The relative rates of vacancy transport across the interfaces can be further explored by examining the time dependence of the lattice parameter.

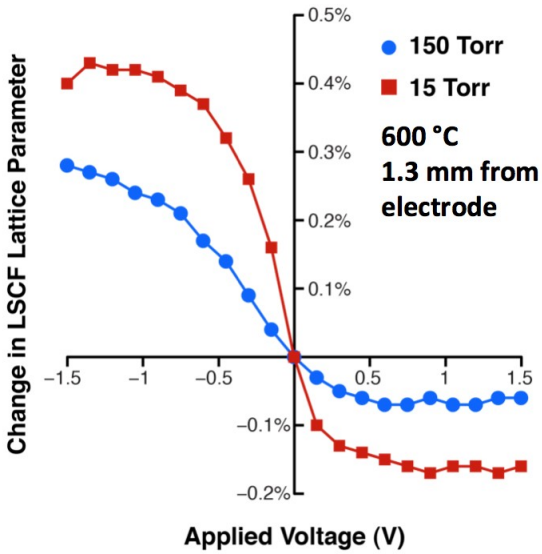


Figure 17. The LSCF Bragg peak shift as a function of applied potential at 600 °C and 1.3 mm from the platinum top electrode.

Figure 18 shows the time dependence of the Bragg peak shift and demonstrates that the lattice parameter of the film responds in less than 1 second to the change in potential. From data not presented, the active area of the charge transfer for the sample geometry in Figure 15 is approximately 0.1 $cm^2$. Using the measured current of 0.05 mA, this results in a current density of 0.5 $mA/cm^2$ or $\approx 1.6\times10^{17}$ $V_O^{\bullet\bullet}$ second/$cm^2$. For a 20 nm thick film, there are $\approx 6\times10^{18}$ oxygen sites/$cm^2$. Thus, for an $La_{0.6}Sr_{0.4}Co_{0.2}Fe_{0.8}O_{3-\delta}$ sample, the maximum $\delta$ can change in 1 second is estimated at ≈0.08. This is comparable, but larger, than the estimated $\delta$ of 0.05 (see the inset of Figure 17) and much of the initial current is dedicated to building up an oxygen vacancy reservoir in the LSCF cathode. From measurements such as this, the ANL group is attempting to determine the impact of processes at the various interfaces and to test models of charge transfer in SOFC structures.

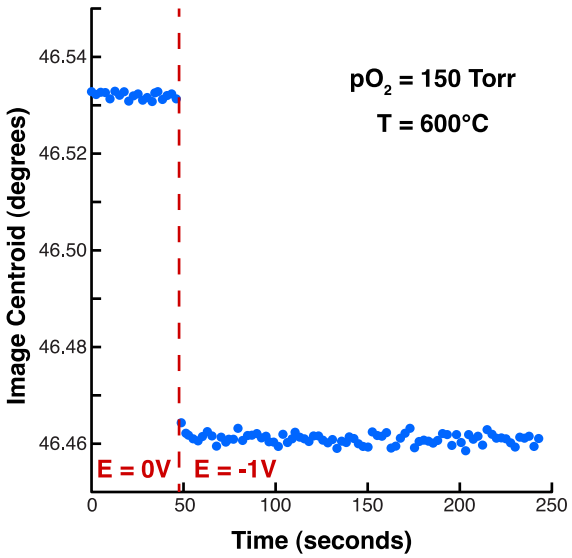


Figure 18. The LSCF (004) Bragg peak position change with an abrupt -1 V applied potential at 50 seconds. The sample was at 600 °C in a partial pressure of 150 Torr and the data was acquired 0.3 mm from the platinum electrode. The inset shows the steady state rocking curve before and after the potential change.

## In Situ Study of Operating Fuel Cells

While the ANL group has concentrated on rapid time resolved measurements, Hardy et al. [45] from Pacific Northwest National Laboratory have demonstrated that a laboratory X-ray source can be used to monitor the evolution of cathodes in an operating fuel cell. Using a conventional X-ray source, they measured six diffraction peaks every hour and 120 diffraction peaks every 20 hours from a LSCF-based SOFC during operation at 750 °C. Figure 19 shows the power density of the SOFC along with a measure of the change in X-ray diffraction peaks called the "Similarity Index". This index indicates that all of the diffraction peaks are evolving in a slow, consistent manner towards lower Bragg angle or increased lattice parameter.

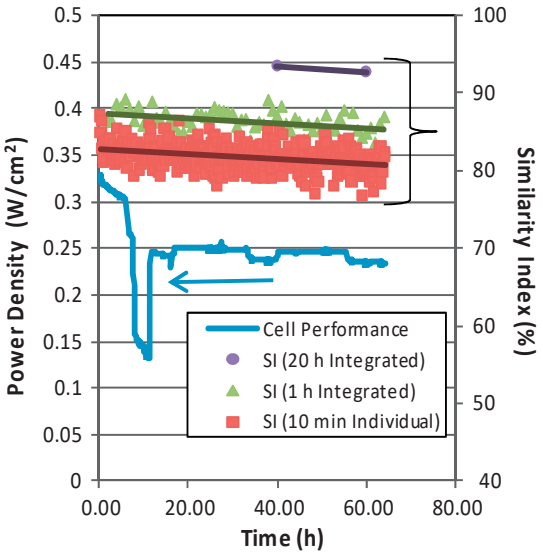


Figure 19. A comparison of the trend of X-ray diffraction patterns (Similarity Index) with the performance of an LSCF based SOFC.

Using Rietveld refinement, Hardy et al. determined the lattice parameter as a function of time from the LSCF cathode. This refinement, shown in Figure 20, demonstrates that the lattice parameter of LSCF slowly changes at operating conditions and is consistent with gradual loss of Sr under typical SOFC operating conditions.

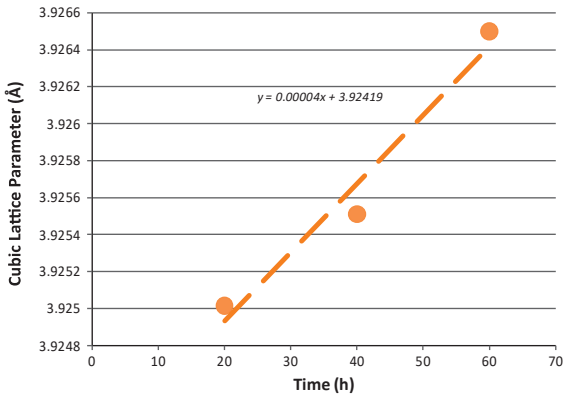


Figure 20. The lattice parameter for a LSCF cathode determined by Hardy et al. from X-ray diffraction data determined in situ from a SOFC operating at 750 °C.

**Valence State**

The catalytic and ionic conductivities properties of SOFC cathodes are expected to depend strongly on the valence state of the B-site atoms. Chang and coworkers have carried out extensive in situ XANES studies of the valence state of B-site atoms in LSM and LSCF [41]. For in situ electrochemical and X-ray measurements, PLD film cathodes were prepared with two contact

electrodes and the sample configuration is illustrated in Figure 21. Two parallel flattened platinum wires were pressure-contacted ~1 mm from the edge of a 10×10 mm2 sample. The samples were then held at 700 °C with a constant electrochemical potential for 80–85 hours. The potential was applied between an "active" platinum wire, i.e., working electrode (WE), and the counter electrode (CE). The second "inactive" wire, 8 mm away from the "active" wire, was used to monitor the surface potential. For the X-ray measurements, that X-ray beam direction was aligned parallel to the Pt wires on the sample. They aimed to find structure/potential correlations by looking for features that only occurred under the active wire.

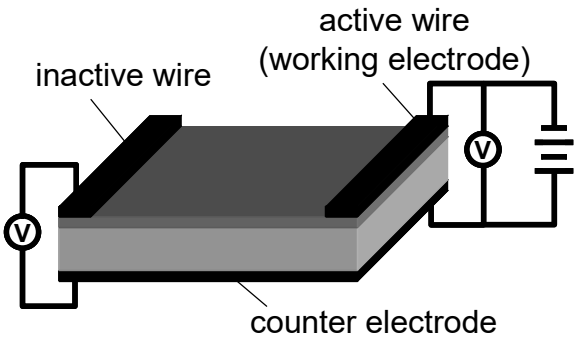


Figure 21. A schematic of the sample configuration for the in situ X-ray spectroscopy measurements.

Chang and coworkers saw reductions of Co and Fe valence in the Co and Fe XANES spectrum under the active wire as illustrated in Figure 22. Only the bulk Co XANES is shown because it is identical to the surface Co XANES. The Co XANES spectrum indicates that the local structure around the Co is spinel-like (seen by 3 split peaks in the derivative of the XANES) rather than perovskite, suggesting that the Co is already reduced. Under the active wire, the Co XANES edge is shifted to lower energy, implying further reduction in the oxidation state. Fe is also slightly reduced under the active wire, which can be seen by the widening of the peak in the Fe XANES. In this way, XANES can be used to characterize the oxidation state of cathode materials.

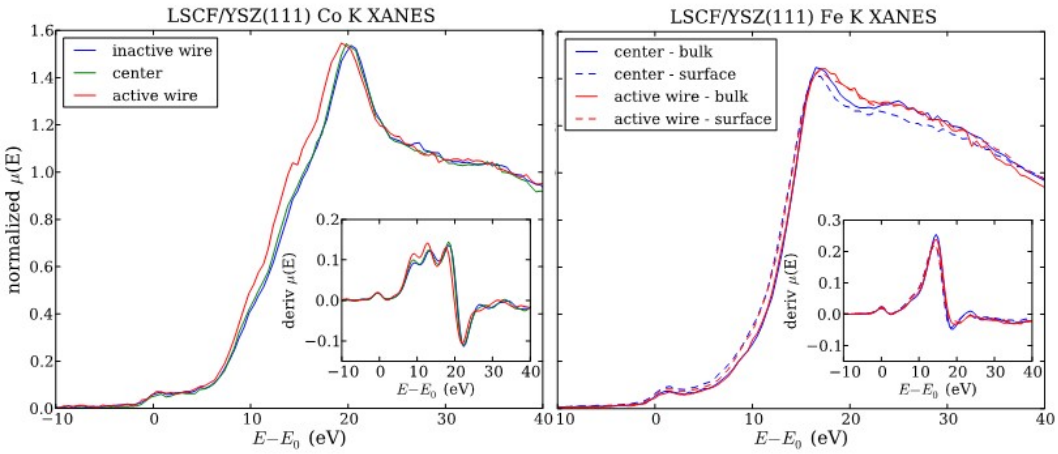


Figure 22. Co and Fe K-edge X-ray absorption near-edge structure (XANES) data for $La_{0.6}Sr_{0.4}Co_{0.2}Fe_{0.8}O_3$ samples held under a constant electrochemical potential of -1V.

There is significant interest in infiltrating a second species into a porous cathode to improve the electrochemical performance of the cathode. For example, LSM is known to be a better oxygen reduction catalyst than LSCF while LSCF is a better ionic conductor. Thus, a thin layer of LSM on LSCF might create a higher performance cathode. To help understand these possibilities, Chang and coworkers deposited a thin layer of LSM on top of LSCF films grown on YSZ(111) substrates to model infiltration. While the LSM layer was too thin to be measured with X-ray reflectivity, the TXRF showed evidence of surface Mn even after annealing which suggests that the LSM layer did not diffuse into the LSCF film. In contrast to LSCF/YSZ(111) without the LSM layer, the surface Co XANES of these samples show an edge shift, indicating that the Co is reduced, but the local structure around the Co remains perovskite instead of transforming into spinel as shown in Figure 23. This Co XANES spectrum is consistently found in the samples under both anodic and cathodic conditions, and, unlike LSCF/YSZ(111) spectra, was constant across the surface, showing that it does not have a strong potential dependence. Thus, measurements indicate that Co chemistry is significantly changed when a thin LSM film is added to the top of an LSCF thin film.

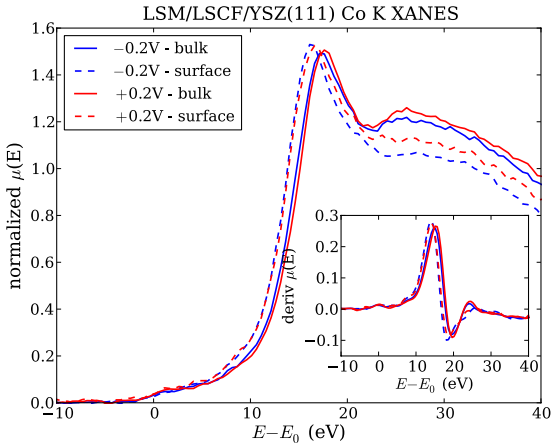


Figure 33. Bulk and surface Co XANES for an LSCF cathode treated with the thin addition of an LSM layer. Measurements under cathodic and anodic potential indicate that the Co chemistry is significantly different than that of an LSCF cathode without an LSM layer.

## Concluding Remarks

Synchrotron radiation sources have revolutionized X-ray science and led to the development of powerful new structural and chemical probes of materials processes and systems. These new X-ray techniques offer a unique ability to probe within the complex structures and reactive environments of solid oxide fuel cells. The SECA program has made significant strides in understanding the cathode interface structures at operating temperatures in typical atmospheres. Using total reflection X-ray fluorescence analysis, the program has demonstrated that Sr and Co segregation are intimately linked to the oxygen vacancy concentration and the electrochemical loading of the cathode. Using the unique ability of X-rays to probe deeply into the material, the composition of Sr at the interface between the cathode and the electrolyte has been studied. Using X-ray spectroscopy techniques, the program has developed a more complete understanding of the chemical state of the cathode as important operating parameters like temperature, oxygen partial pressure, and electrochemical loading are changed. The most recent results have demonstrated that there are large, dynamic lattice parameter changes that occur as the electrochemical loading on the cathode changes. These lattice parameter shifts can be used to identify the rate-limiting oxygen exchange behavior of within model SOFC structures. Long-term evolution of the lattice parameter of cathodes in operating fuel cells has been followed using conventional, laboratory-based X-ray sources and this capability has potential for probing degradation mechanisms.

As the program moves forward, X-ray imaging techniques can be coupled with X-ray diffraction and spectroscopy techniques to examine the chemical state and structure of the cathode (and entire fuel cell) as a function of position, operating conditions, and time.

## References

1. Warren, B.E., *X-Ray Diffraction*. 1969, Reading, Mass.: Addison-Wesley.

2. Cullity, B.D., *Elements of X-Ray Diffraction*. 1978, Reading, Mass.: Addison-Wesley.

3. Kaminski, A., et al., *Crossover from coherent to incoherent electronic excitations in the normal state of Bi2Sr2CaCu2O8+delta.* Physical Review Letters, 2003. **90**(20): p. 207003.

4. Fuoss, P.H. and S. Brennan, *Surface Sensitive X-Ray-Scattering.* Annual Review of Materials Science, 1990. **20**: p. 365-390.

5. Parratt, L., *Surface Studies of Solids by Total Reflection of X-Rays.* Physical Review, 1954. **95**(2): p. 359-369.

6. James, R.W., *The Optical Principles of the Diffraction of X-Rays*. 1982, Woodbridge, Connecticut: Ox Bow Press.

7. van der Lee, A., *Grazing incidence specular reflectivity: theory, experiment, and applications.* Solid State Sciences, 2000. **2**(2): p. 257-278.

8. *X-Ray Interactions With Matter*. 2011; Available from: http://henke.lbl.gov/optical_constants.

9. Robinson, I. and P. Fuoss, *X-ray diffraction evidence of adatoms in the Si (111) 7× 7 reconstructed surface.* Physical Review B, 1986.

10. Robinson, I., P. Fuoss, and L. Norton, *Observation of strain in the Si (111) 7× 7 surface.* Physical Review B, 1988.

11. Fuoss, P., et al., *Time-resolved X-ray scattering studies of layer-by-layer epitaxial growth.* Physical Review Letters, 1992.

12. Fuoss, P., et al., *Atomic nature of organometallic-vapor-phase-epitaxial growth.* Physical Review Letters, 1989.

13. Komanicky, V., A. Menzel, and H. You, *Investigation of oxygen reduction reaction kinetics at (111)-(100) nanofaceted platinum surfaces in acidic media.* Journal of Physical Chemistry B, 2005. **109**(49): p. 23550-23557.

14. You, H., et al., *Resonance X-ray scattering from Pt(111) surfaces under water.* Physica B, 2000. **283**(1-3): p. 212-216.

15. Fuoss, P. and S. Brennan, *Surface sensitive X-ray scattering.* Annual Review of Materials Science, 1990.

16. Renaud, G., R. Lazzari, and F. Leroy, *Probing surface and interface morphology with Grazing Incidence Small Angle X-Ray Scattering.* Surface Science Reports, 2009. **64**(8): p. 255-380.

17. Nishihata, Y., et al., *Self-regeneration of a Pd-perovskite catalyst for automotive emissions control.* 2002. **418**(6894): p. 164-167.

18. Coppens, P., et al., *Synchrotron radiation crystallography*. 1992, London ; San Diego: Academic Press. xii, 316 p.

19. Vlieg, E., *ROD: a program for surface X-ray crystallography.* Journal of Applied Crystallography, 2000. **33**(2): p. 401-405.

20. Roe, R.J., *Methods of X-ray and neutron scattering in polymer science*. Topics in polymer science. 2000, New York: Oxford University Press. xiv, 331 p.

21. Glatter, O. and O. Kratky, *Small angle X-ray scattering*. 1982, London: Academic. x, 515 p.

22. Ilavsky, J., et al., *Ultra-small-angle X-ray scattering at the Advanced Photon Source.* Journal of Applied Crystallography, 2009. **42**: p. 469-479.

23. Allen, A.J., J. Ilavsky, and A. Braun, *Multi-scale Microstructure Characterization of Solid Oxide Fuel Cell Assemblies With Ultra Small-Angle X-Ray Scattering.* Advanced Engineering Materials, 2009. **11**(6): p. 495-501.

24. Group", E.A. *Total Reflection X-Ray Fluorescence*. 2011; Available from: http://www.eaglabs.com/techniques/analytical_techniques/txrf.php.

25. Baur, K., et al., *Recent advances and perspectives in synchrotron radiation TXRF*, in *Nuclear Instruments & Methods in Physics Research Section a-Accelerators Spectrometers Detectors and Associated Equipment*2001. p. 1198-1201.

26. Bearden, J. and A. Burr, *Reevaluation of X-Ray Atomic Energy Levels.* Reviews Of Modern Physics, 1967. **39**(1): p. 125-142.

27. Thompson, A., et al., *X-Ray Data Booklet*. 2009, Berkeley, Ca: Lawrence Berkeley National Laboratory.

28. Fister, T.T., et al., *In situ characterization of strontium surface segregation in epitaxial La0.7Sr0.3MnO3 thin films as a function of oxygen partial pressure.* Applied Physics Letters, 2008. **93**(15): p. 151904.

29. Benfatto, M. and S. Della Longa, *Geometrical fitting of experimental XANES spectra by a full multiple-scattering procedure.* Journal Of Synchrotron Radiation, 2001. **8**: p. 1087-1094.

30. Smolentsev, G. and A.V. Soldatov, *FitIt: New software to extract structural information on the basis of XANES fitting.* Computational Materials Science, 2007. **39**(3): p. 569-574.

31. Tanaka, I., T. Mizoguchi, and T. Yamamoto, *XANES and ELNES in Ceramic Science.* Journal of the American Ceramic Society, 2005. **88**(8): p. 2013-2029.

32. de Groot, F., G. Vanko, and P. Glatzel, *The 1s X-ray absorption pre-edge structures in transition metal oxides*, in *Journal of Physics-Condensed Matter*2009. p. -.

33. Sayers, D., E. Stern, and F. Lytle, *New Technique for Investigating Noncrystalline Structures: Fourier Analysis of the Extended X-Ray—Absorption Fine Structure.* Physical Review Letters, 1971. **27**(18): p. 1204-1207.

34. Rehr, J. and R. Albers, *Theoretical approaches to X-ray absorption fine structure.* Reviews Of Modern Physics, 2000. **72**(3): p. 621-654.

35. Tasker, P., *The stability of ionic crystal surfaces.* Journal of Physics C: Solid State Physics, 1979.

36. Kumigashira, H., et al., *In situ photoemission characterization of terminating-layer-controlled La[sub 0.6]Sr[sub 0.4]MnO[sub 3] thin films.* Applied Physics Letters, 2003. **82**(20): p. 3430-3432.

37. van der Heide, P.A.W., *Systematic X-ray photoelectron spectroscopic study of La1?xSrx-based perovskite-type oxides.* Surface and Interface Analysis, 2002. **33**(5): p. 414-425.

38. Baumann, F., et al., *Strong Performance Improvement of LaSrCoFeO SOFC Cathodes by Electrochemical Activation.* Journal of the Electrochemical Society, 2005. **152**: p. A2074.

39. McLean, D., *Grain Boundaries in Metals*. 1957, London: Oxford University Press.

40. Herger, R., et al., *Structure determination of monolayer-by-monolayer grown La1−xSrxMnO3 thin films and the onset of magnetoresistance.* Physical Review B, 2008. **77**(8).

41. Chang, K.C., et al., *Supporting R&D for Solid Oxide Fuel Cells*, 2010, Argonne National Laboratory: Argonne, IL.

42. Perritt, E., et al., *Resonant X-ray Scattering Studies of Segregation in LSCF*, 2011.

43. Bishop, S.R., K.L. Duncan, and E.D. Wachsman, *Thermo-Chemical Expansion in Strontium-Doped Lanthanum Cobalt Iron Oxide.* Journal of the American Ceramic Society, 2010. **93**(12): p. 4115-4121.

44. Ingram, B.J., et al., *Oxygen Vacancy Concentrations in Thin Film Solid Oxide Fuel Cell Cathodes*, 2012.

45. Hardy, J.S., et al., *Lattice expansion of LSCF-6428 cathodes measured by in situ XRD during SOFC operation.* Journal of Power Sources, 2012. **198**: p. 76-82.

46. Finsterbusch, M., et al., *Mechanisms of Sr Segregation in La0.6Sr0.4Co0.2Fe0.8O3-™.* Solid State Ionics, 2012. **To Be Published**.

47. Finsterbusch, M., et al., *Quarterly Progress Report - DE-08NT0004115*, 2011, Montana State University.

# Enhancement of Solid Oxide Fuel Cell Cathode Performance by Infiltration *by Dong Ding and Meilin Liu (Georgia Institute of Technology) & Kirk Gerdes (National Energy Technology Laboratory)*


## Summary

Polarization at the cathode due to oxygen reduction reactions (ORR) contributes significantly to the overall energy loss in anode-supported planar SOFCs (typically ~50 to ~70% at a constant cell voltage of 0.8 V at 800 °C) and more so at reduced operating temperatures. Further, the long-term stability of the cathodes is also a concern to meet the SECA target for performance degradation rate (~0.2%/kh over a minimum lifetime of 40 kh). Thus, the development of cathode materials and structures with high electro-catalytic activity for ORR and excellent stability is imperative to the development of commercially viable SOFCs for operation at 600–800 °C.

Cathode performance depends not only on the intrinsic properties of its components, but also on the microstructure, morphology, and architecture. For example, a composite cathode consisting of a backbone and a thin electro-catalyst coating is an effective electrode structure for efficient use of the unique properties of two different materials: the fast ionic and electronic transport properties of the backbone (e.g., LSCF) and the high catalytic activity and stability of the surface coating (e.g., LSM).

Solution-based infiltration processes have been developed for deposition of both discontinuous (discrete particle) and continuous (dense film) coatings of catalysts into the state-of-the-art LSCF cathode. For example, dense and continuous LSM films with well-controlled structure, composition, morphology, and thickness have been deposited on an LSCF surface to enhance the performance and stability of LSCF cathodes in SOFCs. Microanalysis revealed that such a film is able to effectively suppress the formation of oxides of La and Sr on the surface LSCF after annealing at 850 °C for 900 hours, which may be related to the degradation of LSCF cathodes. Modeling reveals the mechanism of performance improvement through LSM coating, and theoretical analysis agrees with experimental observations. The observed performance enhancement is attributed largely to the formation of a hybrid LSM(C) phase on the cathode surface, which has stronger adsorption of oxygen, more structural defects, and greater increase in oxygen vacancy concentration than LSCF under cathodic polarization to facilitate ORR. Furthermore, several other Mn-containing perovskite materials are developed for infiltration (such as $Pr_{1-x}Sr_xMnO_{3-\delta}$ and $PrSrCoMnO_{6-\delta}$), leading to more significant performance improvement than LSM infiltration.

Although infiltration of electrode/catalyst materials into a scaffold of electrolyte may allow the use of a wide range of catalyst materials, several critical concerns need to be carefully considered for practical applications. First, sufficiently thick coatings must be introduced to ensure that the sheet resistance is small enough for efficient current collection, more so for larger cells or cell stacks. The need for large amount of catalysts not only adds fabrication cost (repeated infiltration steps), but may also lead to decreased porosity, which could be detrimental to cell performance, especially at

high current densities. Further, the CTE mismatch between the infiltrated catalyst and the electrolyte backbone could lead to delamination, especially during thermal cycling.

Since compatibility between the catalyst and the backbone is critical to a stable cathode system, viable catalyst materials must be immiscible with the backbone so that the key constituents will remain on the surface throughout the operational lifetime of the cell, as demonstrated in the case of LSM-infiltrated LSCF cathode. Any chemical reaction or substantial inter-diffusion between the infiltrated catalysts and the backbone may lead to possible degradation in performance. Thus, it is imperative to develop strategies or approaches for minimizing or eliminating detrimental interactions in exploration of new catalytic materials for infiltrations.

Laboratory button cells with catalyst-infiltrated LSCF cathodes showed enhanced performance and stability (~10 to 30%) than those with conventional LSCF cathodes. Yet, the long-term stability of the catalyst-infiltrated cathodes on large commercial cells is yet to be demonstrated. This is the last step toward the transformation of the scientific knowledge learnt from research to a novel technology that can be adopted by SOFC developers.

Briefly summarized in Table 1 are some characteristics of catalyst-infiltrated cathodes, coating morphologies, and performance improvement under different operating conditions.

Table 1. Characteristics of catalyst-infiltrated cathodes, typical coating morphologies, and performance enhancement observed under different conditions, including power density in W $cm^{-2}$, cathodic overpotential in mV, and polarization resistance in Ω $cm^{-2}$. Note: [(i)] The data are based on symmetrical cell configuration and only the optimal results were reported. [(ii)] Repeating infiltration/thermal treatment processes were applied.

| Infiltrant | Backbone | Coating Type | $R_p$ ($\Omega cm^{-2}$)[(i)] at 750°C | Performance of full cell at 750°C | |
|---|---|---|---|---|---|
| $Sm_{0.2}Ce_{0.8}O_{1.9}$ [1] | LSCF | Discrete particle | Infiltrated: 0.074 | Infiltrated 0.4 $Acm^{-2}$ | Initial: 0.33 W $cm^{-2}$ End(105 h): 0.32 W $cm^{-2}$ |
| | | | Blank: 0.150 | Blank 0.4 $Acm^{-2}$ | Initial: 0.29 W $cm^{-2}$ End(105 h): 0.28 W $cm^{-2}$ |
| $Sm_{0.5}Sr_{0.5}CoO_{3-\delta}$ [2] | LSCF | Discrete particle | Infiltrated: 0.037 | Infiltrated 700°C, 0.8 V | Initial: 0.47 W $cm^{-2}$ End: n/a |
| | | | Blank: 0.104 | Blank 700°C, 0.8 V | Initial: 0.42 W $cm^{-2}$ End: n/a |
| $La_{0.4875}Ca_{0.0125}Ce_{0.5}O_{2-\delta}$ [3] | LSCF | Discrete particle | Infiltrated: 0.075 | Infiltrated 0.8 V | Initial: 0.42 W $cm^{-2}$ End(500 h): 0.48 W $cm^{-2}$ |
| | | | Blank: 0.130 | Blank 0.8 V | Initial: 0.40 W $cm^{-2}$ End(500 h): 0.37 W $cm^{-2}$ |

| | | | | | |
|---|---|---|---|---|---|
| $La_{0.6}Sr_{0.4}CoO_{3-\delta}$[ii] [4] | LSCF+ LSCF/SDC | Discrete particle | n/a | Infiltrated 0.25 $Acm^{-2}$ | Initial: 60 mV End(180 h): 58 mV |
| | | | | Blank 0.25 $Acm^{-2}$ | Initial: 79 mV End(168 h):85 mV |
| $Pr_{0.6}Sr_{0.4}CoO_{3-\delta}$[ii] [5] | LSCF+ LSCF/SDC | Discrete particle | n/a | Infiltrated 0.50 $Acm^{-2}$ | Initial Rp:0.129 $\Omega cm^{-2}$ End(187 h): 0.139 $\Omega cm^{-2}$ |
| | | | | Blank 0.50 $Acm^{-2}$ | Initial:0.216 $\Omega cm^{-2}$ End(187 h): 0.237 $\Omega cm^{-2}$ |
| $La_{0.8}Sr_{0.2}MnO_{3-\delta}$ [6] | LSCF | Continuous film | Infiltrated: 0.197 | Infiltrated 0.7 V | Initial: 0.68 W $cm^{-2}$ End(500 h): 0.80 W $cm^{-2}$ |
| | | | Blank: 0.126 | Blank 0.7 V | Initial: 0.7 W $cm^{-2}$ End(500 h): 0.57 W $cm^{-2}$ |
| $Pr_{0.8}Sr_{0.2}MnO_{3-\delta}$ [6] | LSCF | Continuous film | Infiltrated: 0.107 | Infiltrated 0.7 V | Initial: 0.72 W $cm^{-2}$ End(500 h): 0.86 W $cm^{-2}$ |
| | | | Blank: 0.126 | Blank 0.7 V | Initial: 0.7 W $cm^{-2}$ End(500 h): 0.57 W $cm^{-2}$ |
| $PrSrCoMnO_{6-\delta}$ [6] | LSCF | Continuous film | Infiltrated: 0.093 | Infiltrated 0.7 V | Initial: 0.76 W $cm^{-2}$ End(500 h): 0.92 W $cm^{-2}$ |
| | | | Blank: 0.126 | Blank 0.7 V | Initial: 0.7 W $cm^{-2}$ End(500 h): 0.57 W $cm^{-2}$ |

## Introduction

### Background and Motivation

The demand for clean, secure, and sustainable energy has stimulated great interest in fuel cells. Among all types of fuel cells, solid oxide fuel cells (SOFCs) have the potential to offer high energy efficiency and excellent fuel flexibility [7–10]. To make SOFC technology economically feasible, however, the operating temperature must be further reduced in order to make use of less expensive materials such as the low-cost ferrite stainless steels [9–12]. Unfortunately, fuel cell performance decreases rapidly as the operating temperature is reduced, especially the cathode for oxygen reduction reaction (ORR) [13–16]. The search for cathode materials active toward ORR at lower temperatures has led to many alternative materials [17–19]. To date, however, LSM (>800 °C) and La0.6Sr0.4Co0.2Fe0.8O3−δ (LSCF) (<750 °C) still remain the most widely used cathode for SOFC, due primarily to the limitations of alternative cathode materials: unproven long-term stability and inadequate compatibility with electrolyte/other cell components, especially at high temperatures required for adequate sintering of electrolyte and electrode materials. One reliable and effective approach is to modify the surface of the state-of-the-art cathodes to achieve enhancement in activity and stability of these cathodes and thus successful development of efficient, low-cost SOFCs, which can be operated at 600–800 °C.

**Conceptual Design**

The functioning of a cathode involves several processes: (i) chemical and electrochemical processes on cathode surface associated with oxygen adsorption, dissociation and/or reduction, (ii) transport of ionic and electronic defects along surfaces, across-interface, and through the bulk, and (iii) transport of gaseous species through the pores of the cathode. Since it is difficult to find a cathode material that will have all desired properties, an effective approach is to make use of the best properties of different materials. Conventional composite cathodes, consisting of a mixed ion-electronic conducting (MIEC) material and an electrolyte material, have demonstrated better performance than MIEC alone [20], especially for MIEC with poor ambipolar conductivity such as LSM [21–23]. However, a better approach is to use a good MIEC as the backbone and a good catalyst as the surface coating, as schematically illustrated in Figure 1. Ideally, the porous backbone provides excellent ambipolar conductivity (such as LSCF), while the surface coating has high catalytic activity and stability (such as LSM), which can be introduced by an infiltration/impregnation method.

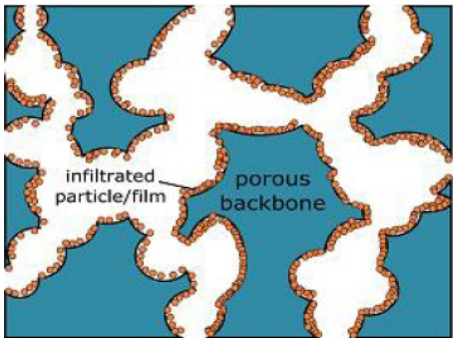


Figure 1. A schematic of composite cathode consisting of a backbone and catalyst particle or film deposition.

**Infiltration/Impregnation Process**

As a traditional process in industry, infiltration has been widely used in fabrication of SOFC components in recent years (especially in lab-scale research) [24–26]. Several groups have done a lot of infiltration studies to improve cell performance and/or stability, including De Jonghe et al. [27], Gorte et al. [28–30], Xia et al. [31–33], Jiang et al. [24, 34], Liu et al. [1–3, 35, 36], and Gerdes et al. [4, 5, 37–40]. In general, an infiltration/impregnation process involves depositing a solution of catalyst precursors into a pre-sintered backbone to form a discontinuous (particles) or continuous (film) coating through a subsequent thermal treatment. The backbone is fired at high temperatures to ensure excellent bonding between the electrode backbone and the electrolyte, excellent connectivity for effective conduction of electron and oxygen ion, and good structural stability of the cathode under operating conditions. The catalyst/electrode coating introduced by infiltration can be fired at temperatures much lower than that needed for the backbone to form the desired phases.

**Preliminary Cost Analysis**

While some uncertainty still remains, a preliminary economic analysis indicates that the infiltration process is economically feasible for application to commercial cells. Our cost estimate is based

mainly on the cost for the amount of precursor materials, additional steps required for the infiltration process, and the subsequent thermal treatment.

The LSM coating is very thin. In fact, an ideal thickness of LSM coating is only about 10 to 50 nm (as observed under TEM), far thinner than other cell components such as the anode support (~0.3 to ~0.7 mm), electrolyte (~10 to ~20 μm), and cathode backbone (~50 μm). Even compared with a typical LSCF cathode, the material cost for LSM coating is less than 0.1%. For the entire cell, the material cost for the LSM coating is less than 0.03% of the total material cost.

In fabrication of commercial cells, the addition of an infiltration and thermal treatment steps contribute to the total cost of cell fabrication. However, the ease of the infiltration process (one-step solution infiltration and drying) and thermal treatment (900 °C or even lower for ~1h) make it possible to be readily implemented in a typical SOFC fabrication process. Thus, the cost incurred in this step, including extra electricity utilization and labor cost, could be likely less than 2%, based on the fabrication processes in our laboratory, although it is yet to be validated in industrial production [41].

If the enhancement in performance of cathode is about 10–30% (depending on operating conditions), it will potentially decrease the capital cost of a power plant and make the plant more efficient, thus reducing the cost-of-electricity, which in turn leads to the ultimate cost reduction for commercial cells by ~10% [42]. Also, certain expensive materials, such as Pr or Pd, which are too expensive to use as cathode material, may be introduced by infiltration.

## Technical Approaches

Infiltration strategies may be classified into two categories: one is to infiltrate an electro-catalyst (e.g., LSM) into an MIEC backbone (e.g., LSCF) whereas the other is to infiltrate a catalyst/electrode material into a scaffold of an electrolyte (e.g., YSZ or a doped ceria). We will focus mostly on the former, but the latter will be briefly discussed.

### Catalysts Infiltrated into MIEC Backbones

In this case, the cathode backbone is a state-of-the-art cathode material that has sufficient electronic conductivity and compatibility with the electrolyte and other cell components. The advantages of this approach include: a) the cathode has already been widely studied and developed with mature manufacturing and processing techniques; b) the required modification to the existing fabrication process is minimal; c) only small amount of catalyst is needed for infiltration; and d) the cost associated with the fabrication could be minimal. However, there is a concern about possible degradation associated with subsequent loss of active coating materials (due to inter-diffusion or chemical reaction) or agglomeration or phase segregation of infiltrated phases.

The morphology of the infiltrated catalyst phase can be a continuous film or a discontinuous coating of discrete particles, depending on the specific infiltration processes and catalysts infiltrated, as schematically shown in Figure 2a and b.

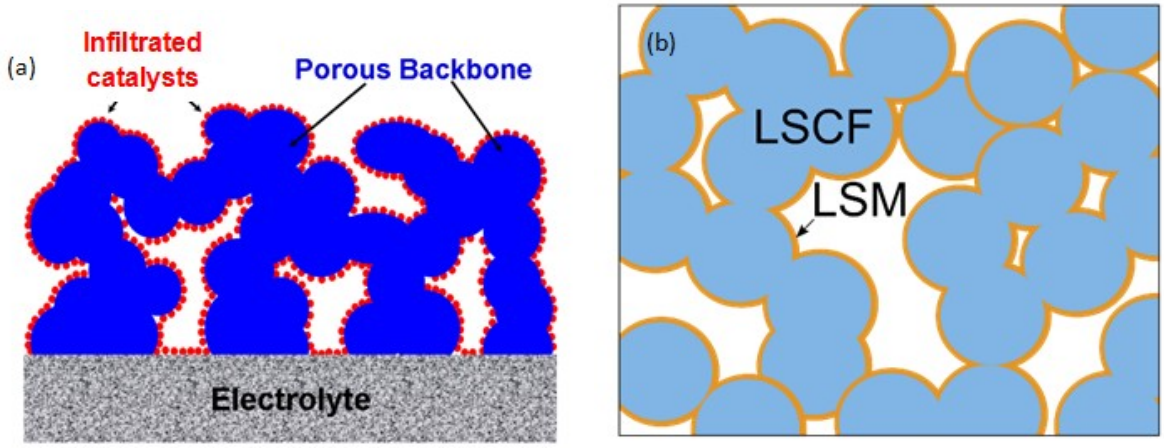


Figure 2. A schematic of composite cathode consists of a backbone (LSCF) with: (a) a discontinuous porous layer of catalyst particles (SDC or LCC), and (b) a continuous dense catalyst coating (LSM).

**Catalyst/Cathode Materials Infiltrated into a Scaffold of Electrolyte**

When the scaffold of an electrolyte material is used as the backbone, a wide range of catalyst/cathode materials may be used because of much lower processing temperatures, especially those that may react with the electrolyte at high temperatures. However, the infiltration process may have to be repeated many times to introduce an adequate amount of material so that the sheet resistance is sufficiently small. Further, current collection could be an issue for commercial cell stacks. Besides, instability in microstructure could be another concern due to mismatch in structure and in coefficient of thermal expansion (CTE) between backbone and the electrode/catalyst materials.

**Infiltration Processes**

There are a few strategies to infiltrate catalysts into a porous backbone. One of most common approaches is a solution infiltration in which a liquid solution, or sol, containing the metal salt precursors required to produce the electrocatalyst is introduced into the porous framework structure, and the desired phase was then derived from the precursors after drying and firing. In this process, inexpensive metal salt precursors are required and the composition or stoichiometry of the infiltrated product can be easily controlled or tailored by adjusting the composition of the precursor solution. With the employment of different solvents, infiltration solutions could be classified as organic-based and non-organic based. In addition, a gas phase deposition has also been successfully developed for catalyst infiltration. Organic precursors were dissolved in a mixture of tetrahydrofuran and ethanol to form a stable solution with a pre-determined concentration. The solution was subsequently pumped to a heated nozzle and the precursor with the solvent was evaporated and transported to the porous cathode backbone.

## Recent Progress in Infiltration

Various infiltration processes have been successfully developed for deposition of nanoparticles or thin-film coating on LSCF backbone or scaffolds of YSZ electrolyte and demonstrated improved

performance (electro-activity and/or long-term stability). The most interesting results are summarized as follows.

**Particle Deposition on MIEC Cathode Backbone**

***Particles of Doped Ceria Infiltrated into MIEC Cathode Backbones***

Fluorite-type doped ceria is chosen as an infiltrate due to its high ionic conductivity, excellent surface exchange rates, and oxygen storage capability. Here we will focus mainly on those results with doped ceria applying for most commonly used MIEC cathode materials, LSCF and LSM.

LSCF-based cathodes show much better performance than those based on LSM because LSCF has much higher ionic and electronic conductivity than LSM, significantly extending the active sites beyond the triple-phase boundaries (TPBs) [43]. However, the catalytic activity of the stand-alone LSCF cathodes is likely to be limited by the surface catalytic properties. Further, the long-term stability of LSCF cathodes is a concern. The infiltration of the doped ceria as well as the detailed microstructures of the porous LSCF and the doped ceria catalyst layer may critically impact the performance of the LSCF cathodes. Shown in Figure 3 (b–e) are typical morphologies of LSCF cathodes infiltrated with different concentrations of Sm-doped ceria (SDC) infiltration at a one-step process. The SDC nanoparticles phase is formed after heat-treated at 900 °C, and uniformly distribute on the surface of LSCF grains. The SDC nanoparticle size is in the range of ~10–100 nm, which is much smaller than 0.2–0.5 μm of the LSCF grains of the pre-sintered LSCF electrode backbone (Figure 3a).

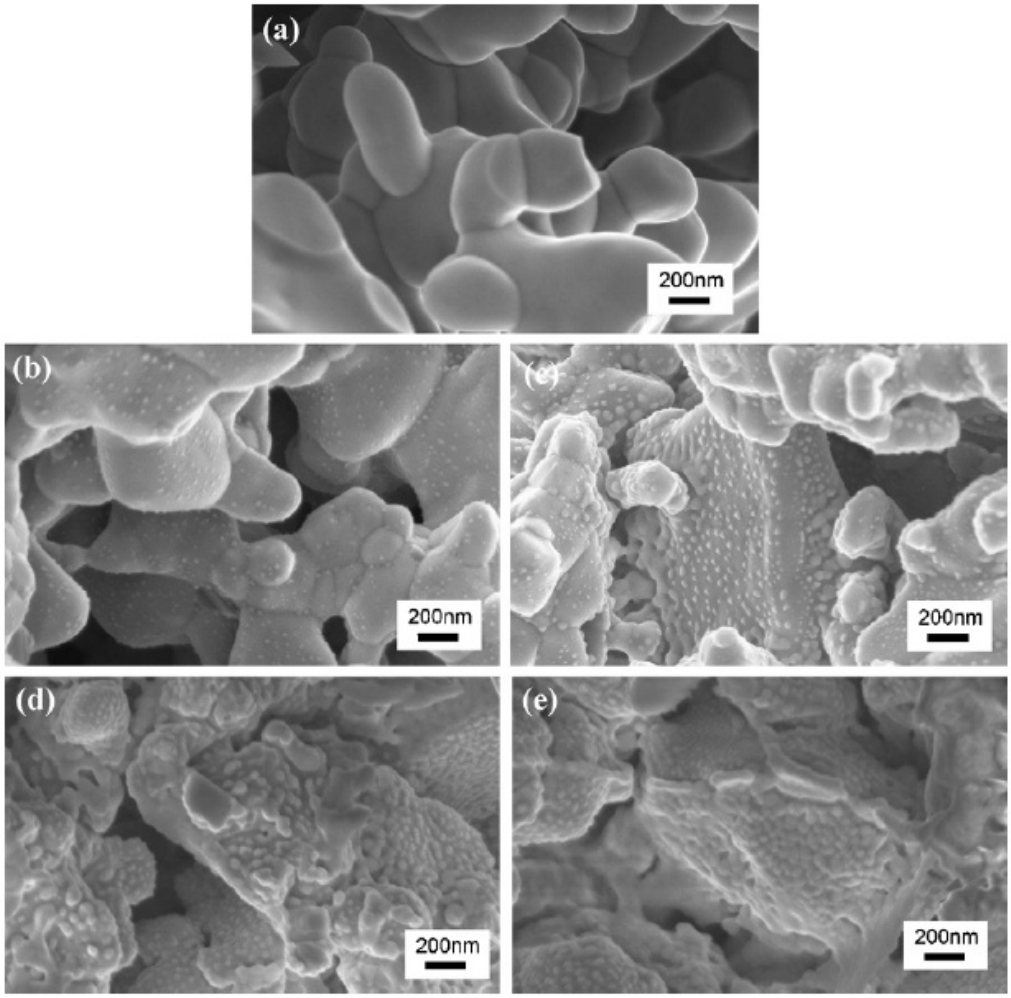


Figure 3. SEM images of the cross-section of LSCF cathodes: (a) blank LSCF, (b) 0.05mol/L SDC infiltration, (c) 0.10 mol/L SDC infiltration, (d) 0.25 mol/L SDC infiltration, (e) 0.35mol/L SDC infiltration [1].

Shown in Figure 4 is temperature dependence of interfacial polarization resistance (Rp) of blank LSCF cathode and LSCF cathode with different concentration SDC infiltration. The SDC infiltrated LSCF cathodes show significantly lower Rp than the blank LSCF cathodes at 650–800 °C. The microstructures and performances of SDC infiltrated cathodes depend sensitively on the amount of SDC introduced and the microstructure of the SDC coatings. For the LSCF cathode infiltrated with 10 μL of 0.25 mol $L^{-1}$ SDC, the interfacial resistances were 0.074, and 0.44 $\Omega cm^2$ at 750 and 650 °C, respectively, about half of those for the blank cathode (0.15 and 1.09 $\Omega cm^2$). Note that further increase in SDC concentration might result in slight increase in Rp possibly because that the gas-phase molecules may difficult to diffuse to the LSCF surface since the microstructure has been changed as shown in Figure 3e.

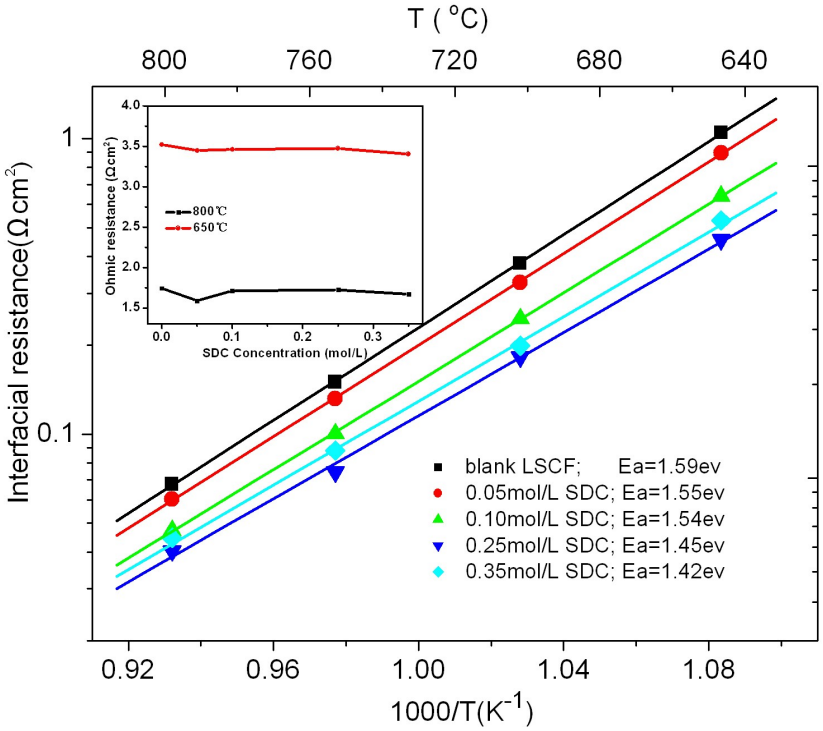


Figure 4. Temperature dependence of interfacial polarization resistance of blank LSCF cathode and LSCF cathode with different concentration SDC infiltration, measured under open circuit condition (OCV).

Sholklapper et al. [44] also observed the improved performance of the LSCF cathode with $Y_{0.2}Ce_{0.8}O_{1.9}$ (YDC) infiltration. A decrease in the phase angle of the low frequency arc of the bode plot (around 1 Hz) suggests that even LSCF, a good electrocatalyst at intermediate operating temperatures, can be catalytically enhanced by infiltrated nanoparticles.

Because of its thermal stability and chemical compatibility, Sr-doped $LaMnO_3$ (LSM) is the most commonly used cathode for the yttria-stabilized zirconia (YSZ) electrolyte in solid oxide fuel cells (SOFCs) operating above 800 °C [7, 15]. Construction of a composite cathode is a potentially effective strategy to improve the LSM cathode performance through infiltration. Jiang et al. studied Gd-doped ceria (GDC) infiltrated LSM cathodes on YSZ electrolytes using asymmetric cells [45–47], and they found that a 5.8 mg $cm^{-2}$ GDC infiltrated LSM electrode had a polarization resistance (Rp) of 0.21 $\Omega cm^2$ at 700 °C, much lower than that of the baseline LSM electrode without infiltration (12 $\Omega cm^2$). The same group had also demonstrated that GDC infiltration may significantly enhance the electro-catalytic kinetics of the LSM electrode. Xia et al. investigated the SDC infiltrated LSM cathodes on SDC electrolytes. Their work was mainly concerned with the oxygen reduction mechanism[48] and some preparation parameters [49, 50]. The peak power density of 0.14 and 0.20 W $cm^{-2}$ was reported at 600 °C when SDC was used as the electrolyte, respectively. These results implied that the infiltrated LSM electrode is more suitable for use at a temperature range of 700 °C and above in which YSZ is more commonly used as the electrolyte. Thus, Ding et al. [51] further investigated the application of SDC-infiltrated LSM cathodes with YSZ electrolytes.

Significant improvements in performance are observed in symmetrical cells, half cells and full cells with SDC infiltration. Maximum peak power density of 1.1 W is obtained for the cells with optimal SDC-infiltrated LSM cathode at 800 °C. In addition, it is shown that the Rp of the infiltrated electrodes decreases with increasing electrode thickness in the range of 5 to 30 μm. When the thickness is greater than 30 μm, Rp is relatively constant [51]. Chen et al. [52] also found that the performance was further improved when SDC was infiltrated into a porous SDC-LSM composite backbone with an optimized microstructure. In addition, SDC and LSM co-infiltrated LSM-YSZ composite cathodes were also reported to have improved performance [53]. The characteristics of the infiltrated LSM electrodes are summarized in Table 2.

Table 2. Summary of characteristics of infiltrated LSM electrodes. Note: [(i)] for the cell with the mechanically mixing LSM+SDC cathode.

| Infiltrant | Cathode backbone | electrolyte | Cell configuration | performance | | Ref |
|---|---|---|---|---|---|---|
| | | | | Infiltrated | Blank | |
| $Gd_{0.2}Ce_{0.8}O_{2-\delta}$ | LSM | YSZ | asymmetrical cell | $R_p$: 0.21 $\Omega cm^{-2}$ at 700°C | 11.8 $\Omega cm^{-2}$ | [46] |
| $Sm_{0.2}Ce_{0.8}O_{2-\delta}$ | LSM | SDC | symmetrical cells | $R_p$: 0.23 $\Omega cm^{-2}$ at 700°C | 5.3 $\Omega cm^{-2}$ | [48] |
| $Sm_{0.2}Ce_{0.8}O_{2-\delta}$ | LSM | SDC | symmetrical cells | $R_p$: 1.13 $\Omega cm^{-2}$ at 600°C | n/a | [49] |
| | | | full cells | $P_{max}$: 0.14 W $cm^{-2}$ at 600°C | n/a | |
| $Sm_{0.2}Ce_{0.8}O_{2-\delta}$ | LSM | SDC | full cells | $P_{max}$: 0.20 W $cm^{-2}$ at 600°C | 0.17 W $cm^{-2}$ [(i)] | [50] |
| $Sm_{0.2}Ce_{0.8}O_{2-\delta}$ | LSM | YSZ | symmetrical cells | $R_p$: 0.048 $\Omega cm^{-2}$ at 800°C | n/a | [51] |
| | | | full cells | $P_{max}$: 1.1 W $cm^{-2}$ at 800°C | n/a | |
| $Sm_{0.2}Ce_{0.8}O_{2-\delta}$ | LSM | YSZ | full cells | $P_{max}$: 1.1 W $cm^{-2}$ at 700°C | $P_{max}$: 0.23 | [52] |
| $Sm_{0.2}Ce_{0.8}O_{2-\delta}$ | LSM+SDC | YSZ | symmetrical cells | $R_p$: 0.039 $\Omega cm^{-2}$ at 750°C | 0.19 $\Omega cm^{-2}$ | [53] |

Similar to SDC infiltration, a new catalyst material, $La_{0.4875}Ca_{0.0125}Ce_{0.5}O_{2-\delta}$ (LCC), with very low ionic conductivity was also studied as an infiltrate intro porous LSCF cathodes [3]. Results suggest that when uniformly deposited on the LSCF grain surface, a small amount of discrete LCC nanoparticles significantly increased the performance, as seen in Figure 5.

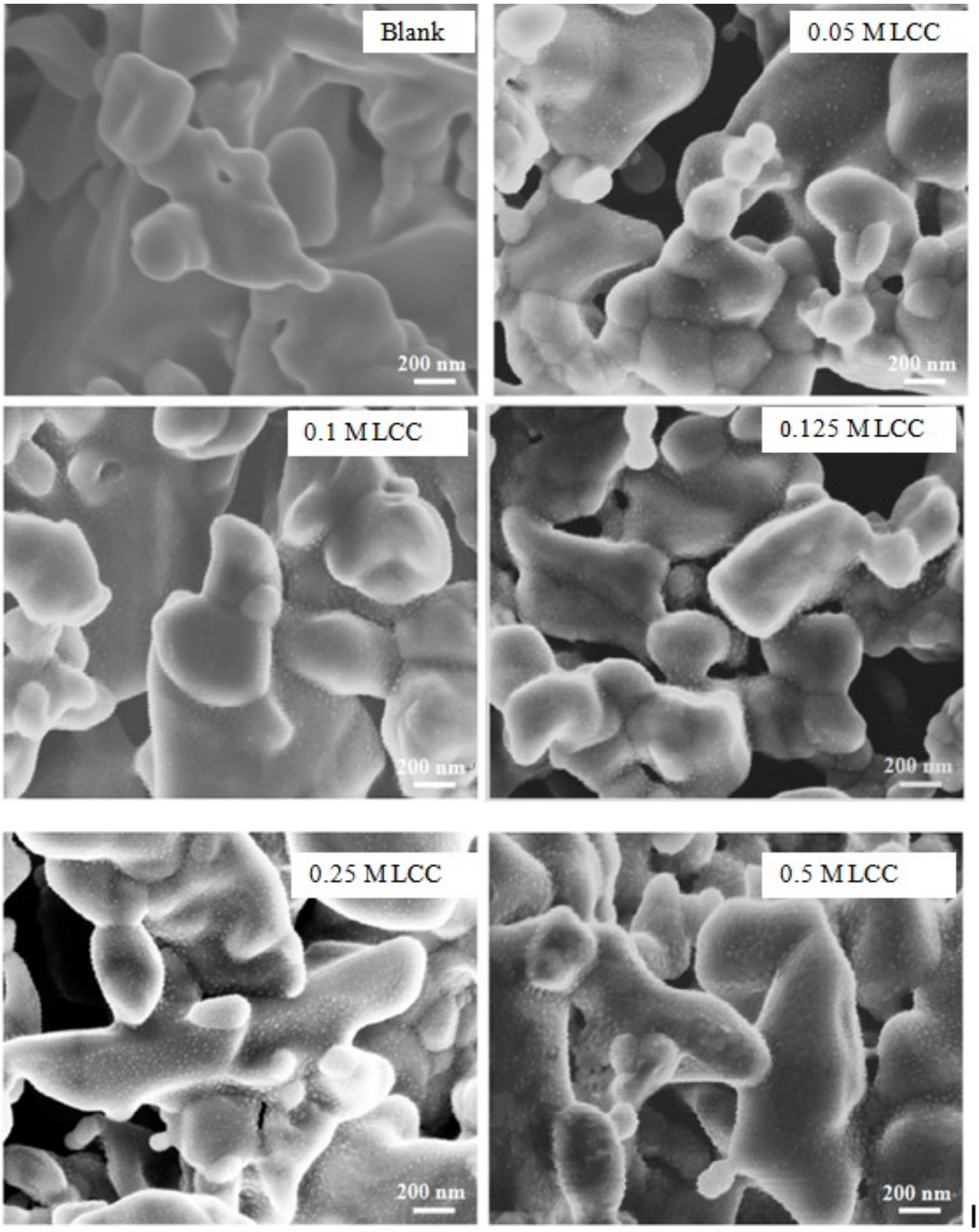


Figure 5. Typical surface morphology (SEM images) of (a) a porous LSCF cathode without LCC infiltration and (b–f) porous LSCF cathodes infiltrated with 5 µL of LCC solution of different concentrations: (b) 0.05 M, (c) 0.1 M, (d) 0.125 M, (e) 0.25 M, and (f) 0.5 M [3].

In addition to visible improvement in electro-catalytic activity with a symmetrical cell configuration, it is also found that the performance and stability of the full cells with the LSCF cathode can be enhanced by a LCC coating [54], leading to ~18% improvement in peak power

density and stable operation (without observable degradation) for over 550 h (Figure 6). This could be associated with the enhanced surface activity for oxygen reduction reaction on the LSCF surface, as well as excellent solubility of SrO through LCC coating. This surface modification requires a simple solution infiltration followed by a heat treatment, which can be incorporated easily into the fabrication of commercial cells to improve the performance and reliability at low cost.

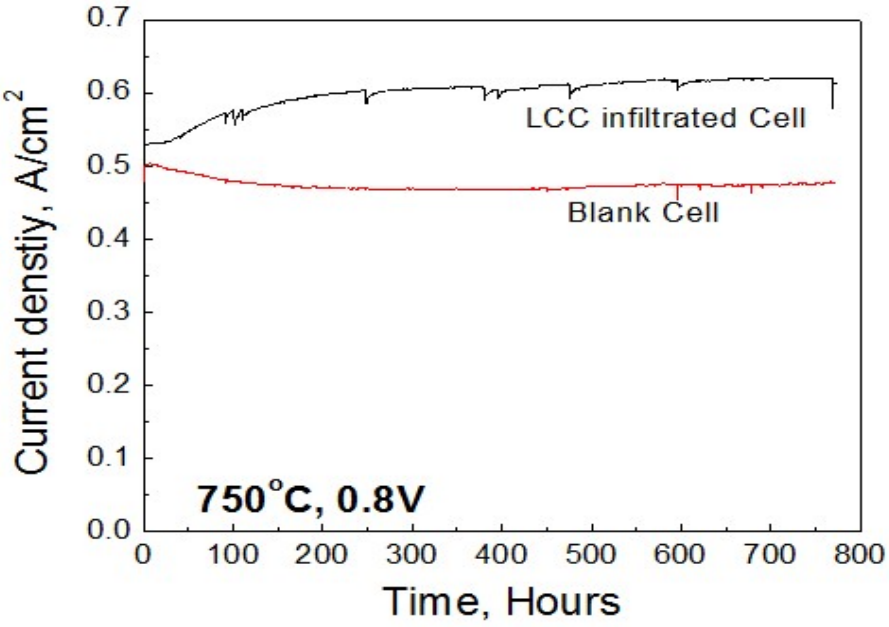


Figure 6. Typical lifetime of the homemade button cells with LCC infiltrated LSCF as well as baseline LSCF cathode with a constant voltage of 0.8 V at 750 °C.

***Particles of MIEC Infiltrated into LSCF Backbones***

As a typical MIEC, strontium-doped samarium cobaltite with composition of $Sm_{0.5}Sr_{0.5}CoO_3$ (SSC) has been studied as a cathode material for SOFCs with YSZ, LSGM, and doped ceria electrolytes [17]. It was found that the overpotential of dense SSC was ~50% lower than that of LSC under similar conditions. And the rate-determining step of dense SSC cathodes was shown to be adsorption–desorption at the surface of the electrode, the same as LSC. But the adsorption and desorption rate constants of SSC were approximately one order of magnitude higher than the corresponding values for LSC and LSCF. Superior performance has been reported in intermediate-temperature SOFCs with SSC cathodes [55, 56]. We thus developed a one-step infiltration process to deposit Sm0.5Sr0.5CoO3−δ (SSC) coating on the surface of a porous LSCF cathode, as shown in Figure 7. Electrochemical impedance spectroscopy reveals that the SSC coating has dramatically reduced the polarization resistance of the cathode, achieving area-specific resistances of 0.036 Ω $cm^2$ and 0.688 Ω $cm^2$ at 750 °C and 550 °C, respectively (Figure 8).

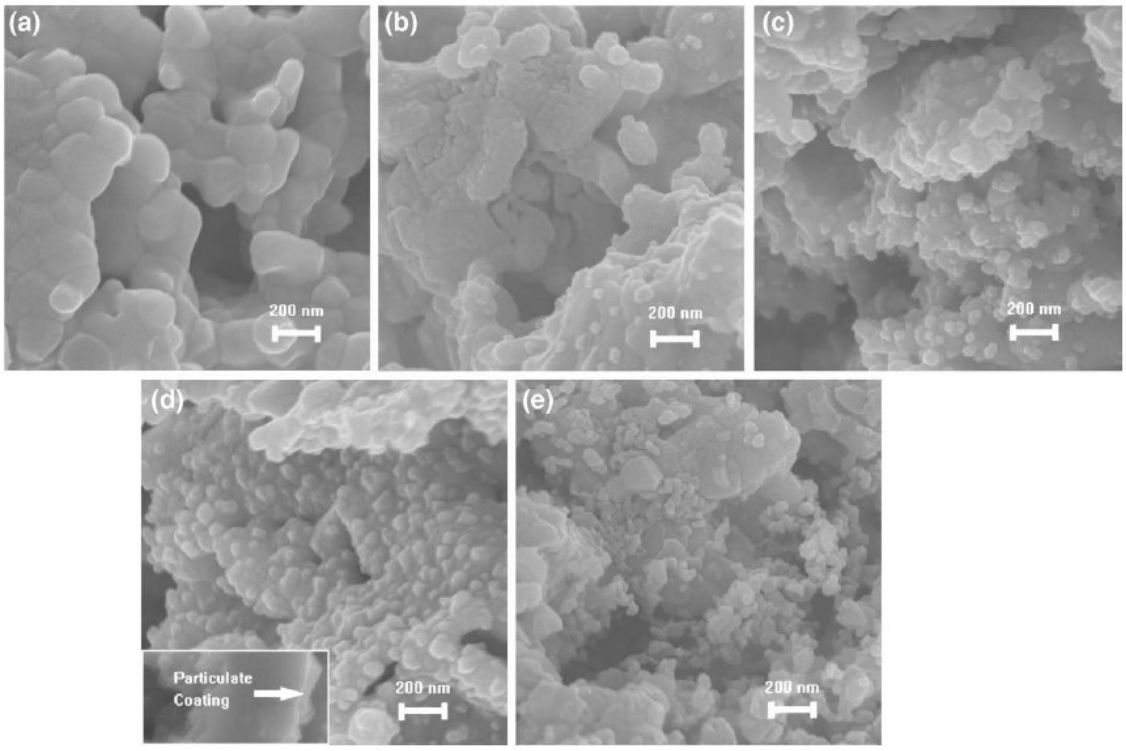


Figure 7. SEM images of the cross-section of LSCF cathodes: (a) blank LSCF, (b) 0.16 mol/L SSC infiltration, (c) 0.48 mol/L SSC infiltration, (d) 1.44 mol/L SSC infiltration, (e) 0.48 mol/L LSCF infiltration.

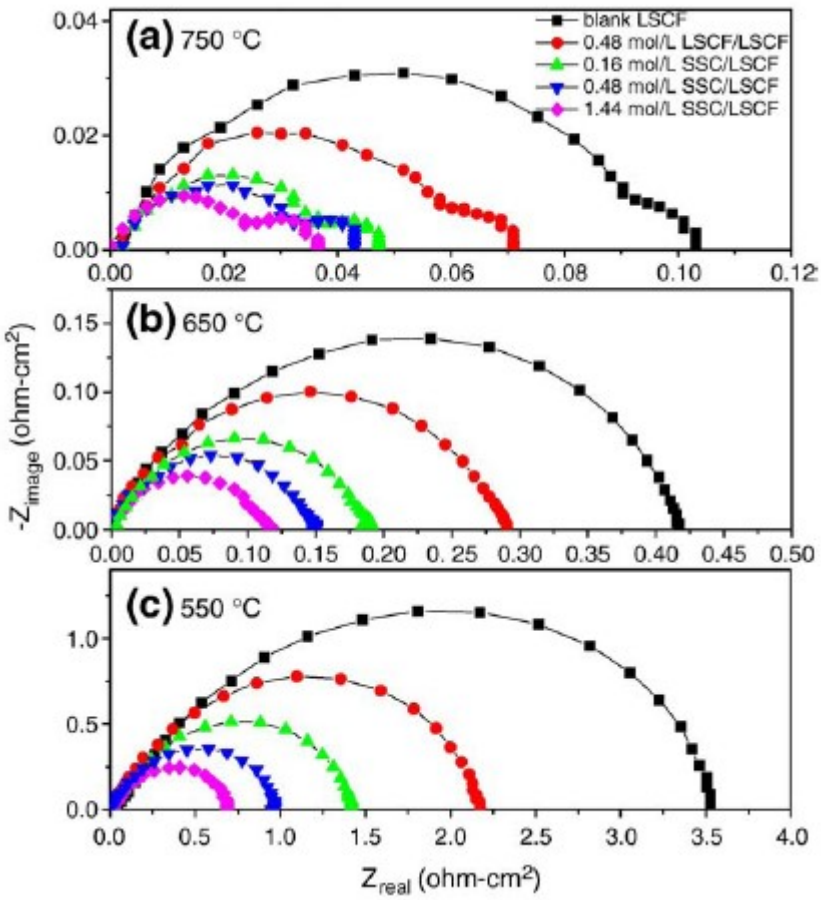


Figure 8. Impedance spectra of LSCF cathodes with different treatments at various temperatures: (a) 750 °C, (b) 650 °C, (c) 550 °C.

In the subsequent study, the effect of various complexing reagents on formation of infiltrated SSC phase was examined, including Triton X-45, Triton X-100, citric acid, and urea. Only citric acid and urea assist the formation of pure phase. To obtain a perfect perovskite phase, the molar ratio of urea to SSC was suggested to be higher than 10:1 based on XRD results. We also presented how the surface tension of the infiltration solution influences the morphology and the performance of the cathode. Ethanol, with lower surface tension than that of water, is added to the aqueous solution to adjust the surface tension of the infiltration precursor solution. Wetting contact angles of precursor solutions with different water-to-ethanol ratio were measured on flat and dense YSZ, GDC, LSM, and LSCF substrates. The aqueous solution without the addition of ethanol wets SOFC electrolyte materials (GDC and YSZ) better than cathode materials (LSM and LSCF). Contact angles decrease with the increase in ethanol content. When the water-to-ethanol ratio reached 1:0.6, the precursor solution displayed similar low contact angles on all substrates. The improved wetting property leads to more uniform morphology of the infiltrated SSC particles as well as enhanced electrode performance [57].

Significant progress in infiltration of stable nanoparticles of $La_{0.6}Sr_{0.4}CoO_3$ and $Pr_{0.6}Sr_{0.4}CoO_3$ has been reported by Lee et al. in a series of reports [4, 5, 37, 38]. In these studies, commercially available anode supported cells possessing SDC/LSCF cathodes (MSRI, Salt Lake City) were infiltrated and operated in hydrogen/air at 750 °C. The numerous tests that have been completed on the LSC infiltrated system identify a statistically significant decrease in polarization resistance and a concomitant increase in achievable power density. Furthermore, infiltrate stability has been examined in a series of detailed comparative tests, some lasting more than 1500 hours. The principal findings include: 1) infiltration of only 6 wt.% of LSC produces a decrease in polarization resistance of more than 25% and a power density increase greater than 30% in full cell tests relative to the baseline cells; 2) electrochemical performance of the infiltrated cell degrades at a rate equal to or less than the baseline cell, even in tests lasting more than 1500 hours; and 3) the infiltrate acts as an electrocatalytic agent, as demonstrated through impedance testing. Some characteristic results of LSC infiltration are depicted in Figure 9.

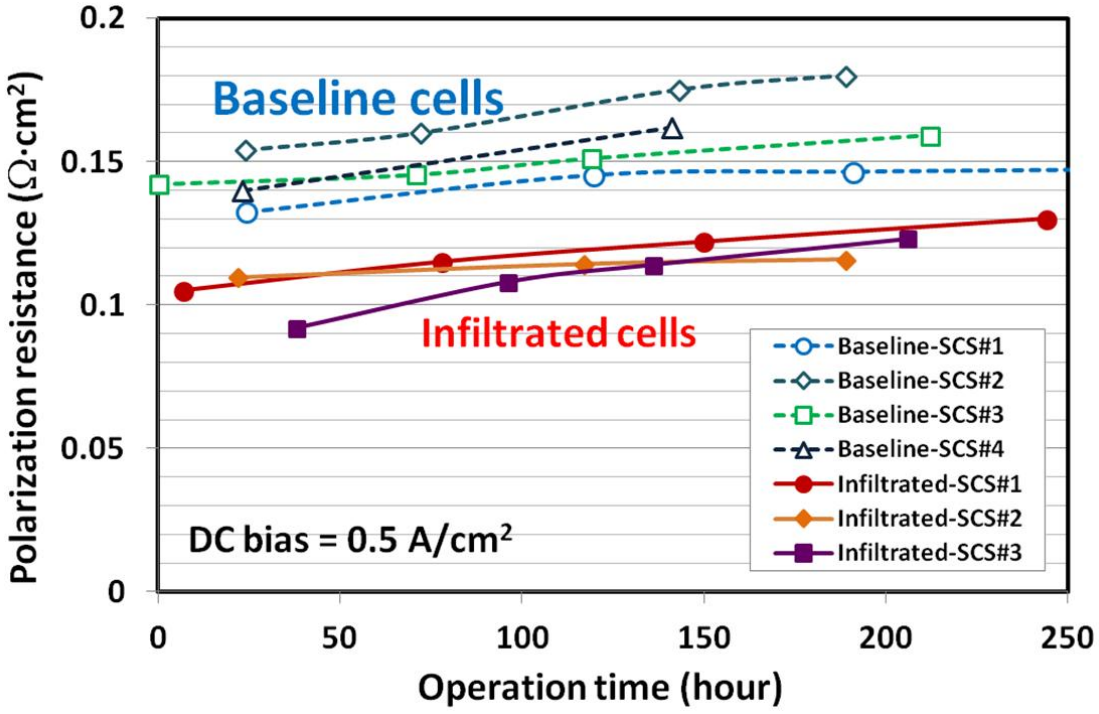


Figure 9. Comparison of polarization resistance observed over time for 4 baseline cells and 3 cells infiltrated with LSC. Cells are MSRI anode supported with SDC/LSCF cathodes.

Infiltration of stable and high surface area infiltrates has also been reported by Chao et al. [39]. A method known as Evaporation Induced Self Assembly (EISA) is used to generate mesoporous LSM and LSC possessing as-fabricated surface areas greater than 50 $m^2/g$, which is more than one order of magnitude greater than achievable through conventional Pechini methods. By adjusting precursors in the starting infiltrate mixture, the mesoporous materials are stabilized at SOFC

operating temperatures, and free-standing powders have been shown to lose only 6% of the starting surface area after 100 hours of exposure to air at 750 °C. Symmetric cell testing results indicated that the infiltration of mesoporous LSM reduces polarization resistance by more than 65% over an identical, but non-infiltrated, cell [40]. Full electrochemical tests on anode supported MSRI cells with SDC/LSCF cathodes demonstrated polarization resistance decreases of more than 30%.

#### *Precious Metal Infiltrated into MIEC Cathode Backbones*

Uchida et al. reported that infiltration of Pt into an LSC cathode has significantly promoted $O_2$ reduction [58, 59]. However, Simner et al. did not find significant enhancement by infiltrating Pt into the LSF–YSZ cathode. Also, infiltration of Pd was reported effective for the LSF-based cathode performance enhancement [60], but the introduction of neither Pd nor Pt enhances the performance of LSM cathodes [61]. However, others report Pd is effective for LSCF cathode [62, 63]. We believe that high catalytic activity for $O_2$ reduction of precious metal and fine noble metal particles that have high surface area would be accounted for the enhanced cathode performance. In addition, Pd has been reported to enter the lattice of LSCF [64], $LaFeO_3$ [65, 66], and $BaCeO_3$ [67] to occupy the B site. Serra and Buchkremer [64] indicate that the incorporation of Pd adjusts the surface composition of the perovskite and thus leads to the enhancement of the catalytic activity. This catalytic promotion is more pronounced for MIEC cathode because the whole surface of MIEC is active for $O_2$ surface exchange, but the effect diminishes for an LSM electrode because the active sites are largely confined to the TPBs [61]. In addition, the infiltration of Ag also enhanced the performance of LSCF [68] and $Nd_{0.6}Sr_{0.4}Co_{0.5}Fe_{0.5}O_3$ [69], although there is a concern on long-term stability of cathode performance associated with low melting point of Ag.

### Film Coating on MIEC Cathode

#### *LSM-Infiltrated LSCF Cathode*

Dense continuous LSM films are successfully fabricated with desired structure, composition, morphology, and thickness on LSCF surface by two kinds of solution infiltration processes: non-aqueous and water-based. In the former approach, 2-methoxyethanol and acetic acid were used to replace water as solvents, and strontium acetate and manganese acetate as metal organic precursors to replace nitrate precursors. The water-free LSM sol showed improved wettability on the LSCF surface. Continuous and dense LSM films on LSCF substrates were fabricated, as shown in Figure 10.

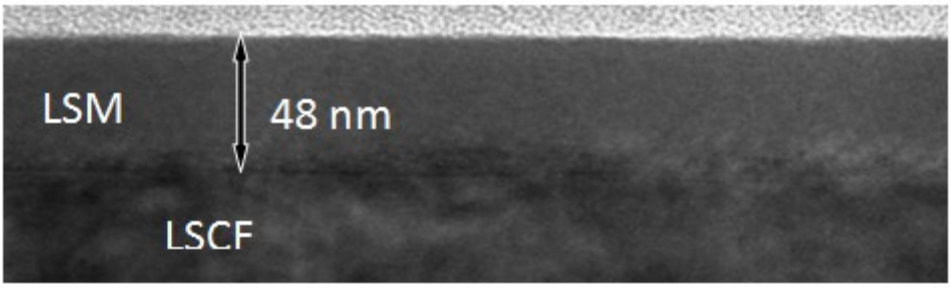


Figure 10. Cross-sectional TEM micrograph of LSM-coated LSCF surface derived from a sol-gel process on LSCF pellets annealed at 850 °C for 900 hours.

The identical infiltration process was applied to porous LSCF cathode. Due to the structural similarity of LSM and LSCF, it is hard to observe formation of the dense film or coating, as seen in Figure 11. Careful analysis of cross-sectional TEM images indicates an epitaxial relationship of LSM with underlying LSCF cathode.

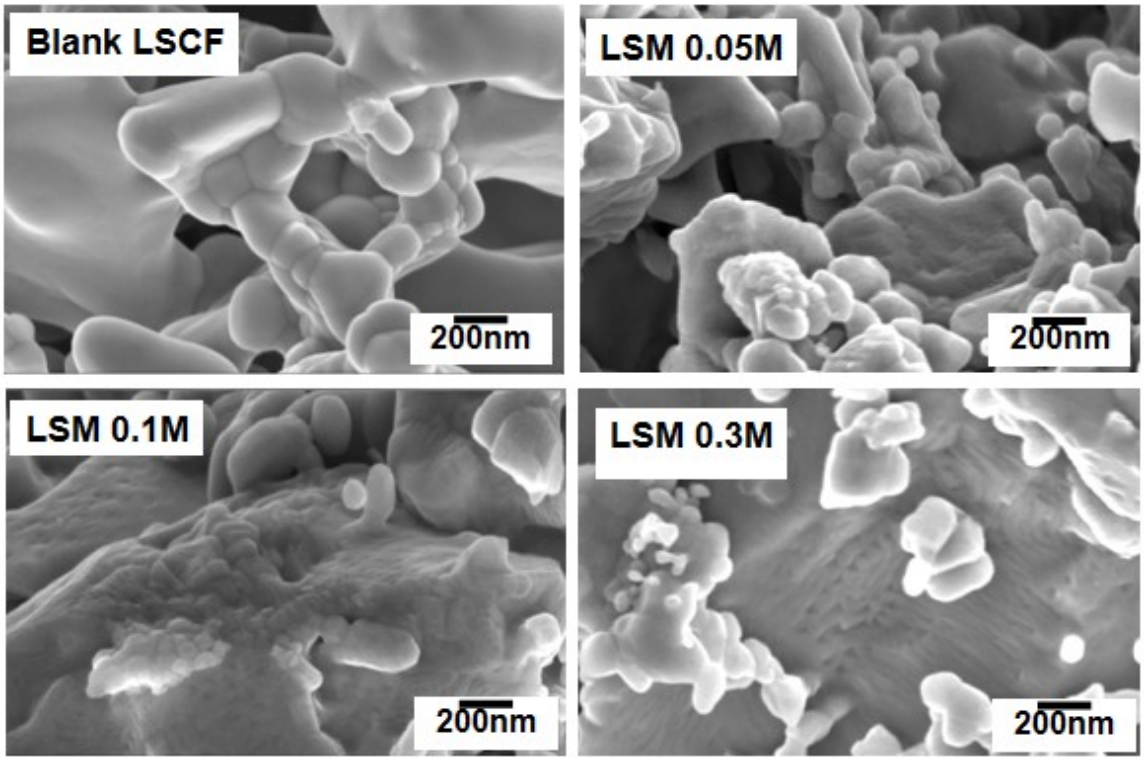


Figure 11. Microstructure of porous LSCF cathode with a sol LSM solution infiltration at different concentrations.

However, such a water-free-based solution infiltration method seems to have some drawbacks, which may be undesirable in SOFC industry. First, all solvents in non-aqueous solution will be more expensive than water-based solution. Second, the freezing temperature of the acetic acid is relatively low (16.5 °C); the viscosity of the solution would change a lot at room temperature, which is less desirable for deposition of the thin film in porous cathode backbone.

A water-based LSM infiltration process is also developed. Several process parameters have been demonstrated to have critical effects on the ultimate quality of LSM films, including solution pH value, surfactant addition, as well as ambient humidity (drying time). The ultimate objective was to maximize the enhancement in the electrocatalytic activity and stability of LSM-coated LSCF cathode through proper control of the infiltration process. Figure 12 shows the current density change of the blank cell and the LSM-infiltrated cell with time under a constant voltage of 0.7V at 750 °C. The cell with LSM-infiltrated LSCF cathode initially had lower performance than the cell with blank LSCF cathode. However, the cell displayed a time-dependent activation that led to a considerable increase in performance in the first 200 h of operation. This increase contrasts with the rapid decrease in performance of the blank LSCF cell in the same time period. Considering the extremely stable anode of the commercial cells, the degradation behavior is associated with cathode phenomena.

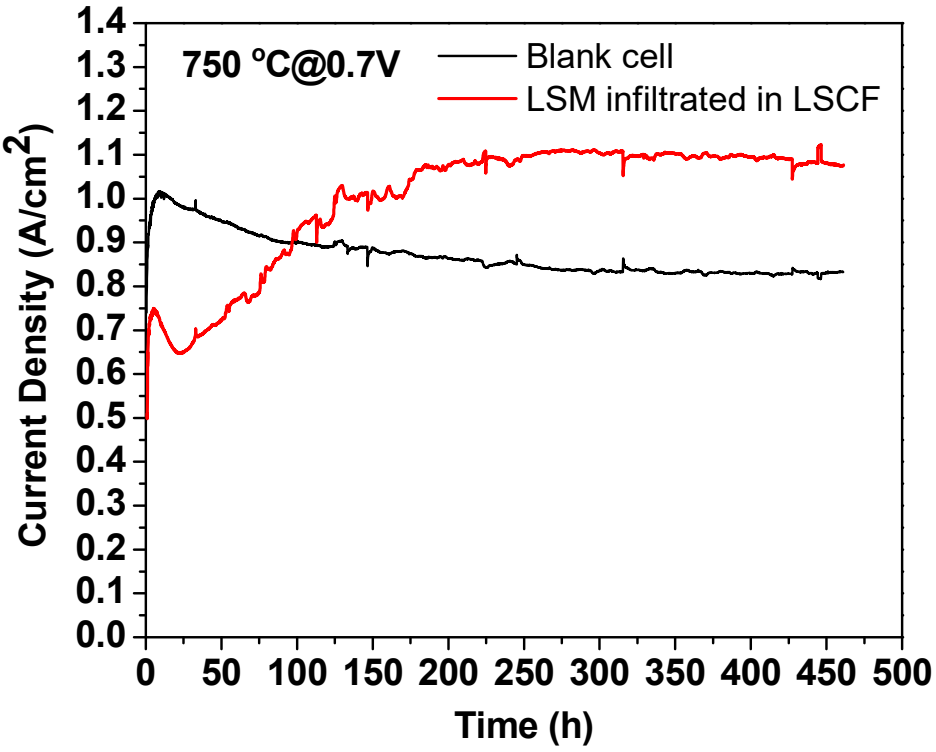


Figure 12. Typical lifetime of the button cells with blank LSCF and LCC infiltrated LSCF cathode at 750 °C with a constant voltage of 0.7 V.

Advanced electron microscopy and spectroscopy were used to examine the morphology, composition, and structure of the LSCF surfaces, as well as the LSM/LSCF interface before and after long-term annealing, to understand the stability enhancement of the LSM-coated LSCF cathode. The Sr-enrichment has been widely accepted as the major cause of instability and performance degradation in LSCF cathodes [70]. We firstly examine the blank LSCF pellet after annealing at 850 °C for 900 hours. Figure 13 presents a bright-field STEM image of the surface of an LSCF pellet after annealing at 850 °C for 900 hours. The sample was coated with a thin layer of Cr to provide delineation of the sample surface, and then prepared using focused ion beam (FIB). EDS profiling was performed from the surface of the annealed pellet to a depth of about 1.7 μm as shown in Figure 13b, with a 1-nm probe along a line marked by the rightmost arrow in Figure 13a. EDS quantification was calibrated with commercial 6428LSCF powder. The profiles show a uniform composition of LSCF over the entire depth within LSCF. The LSCF composition averaged within LSCF (under the surface La-Sr-oxide/LSCF interface or equivalently from ~200 nm to 1.7μm) is 12% La, 8% Sr, 5% Co, and 15% Fe, which is very close to 12% La, 8% Sr, 4% Co, and 16% Fe for 6428LSCF. On the surface only La and Sr were detected.

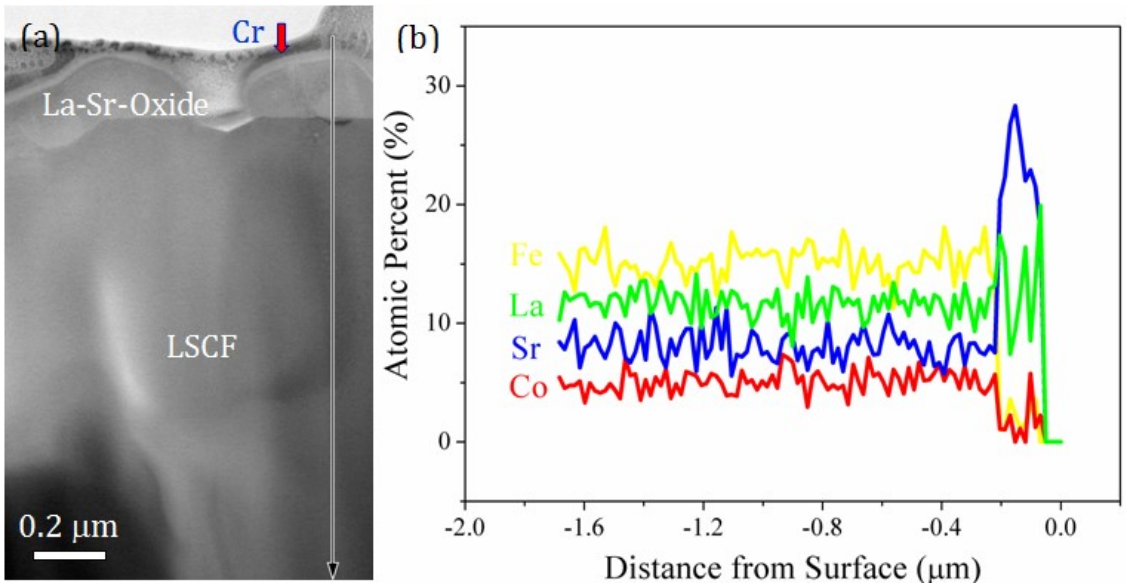


Figure 13. (a) Bright-field STEM image of surface of LSCF pellet annealed at 850 °C for 900 hours. A thin layer of Cr coating was used to delineate the sample surface. The rightmost arrow indicates the EDS profile line. (b) Atomic percent profiles acquired along the profile line marked in (a).

As a sharp contrast, Figure 14a shows the cross-sectional view (TEM image) of a LSM film deposited surface layer in the as-deposited state on a dense LSCF pellet, while Figure 14b shows the cross-sectional view of a similar surface layer after annealing at 850 °C for 900 h (under zero-current conditions). Figure 14c and d show EDS composition profiles of the surface layer and outermost portion of the underlying LSCF in the as-deposited state and in the long-term annealed state, respectively. The surface layer retains Mn during long-term annealing, but also experiences an addition of Co. These TEM observations suggest that the formation of thick oxide of La and Sr after annealing on the blank LSCF pellet (and possibly along the LSCF grain boundaries on the LSM-coated LSCF pellet where Mn is largely absent). As a sharp contrast, there is no such thick oxide on the LSM-coated LSM after annealing. Such thick surface oxide particles that are expected to severely hamper electrochemical activities have not emerged after annealing on LSM-coated surface of LSCF.

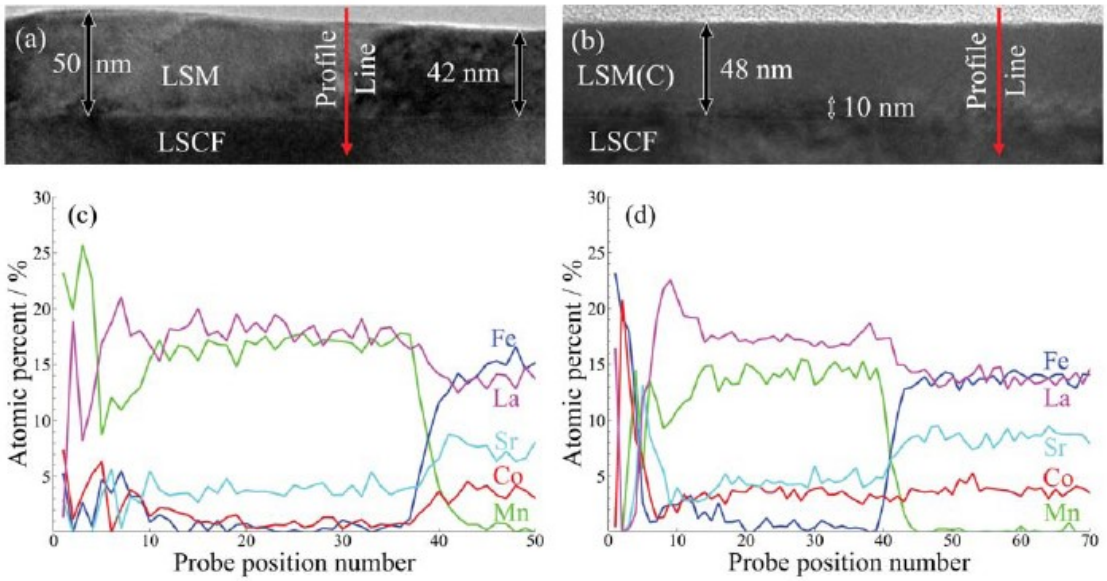


Figure 14. Cross-sectional TEM micrograph of a sol–gel LSM-modified LSCF surface (a) in the as-deposited condition and (b) after long-term annealing at 850 °C for 900 hours. EDS compositional profiles across the sol–gel surface layer and outermost part of LSCF layer (c) in the as-deposited condition and (d) after long-term annealing [36].

A semi-empirical phenomenological model was further developed to explain the mechanism of performance enhancement by the LSM coating. These results indicate that the LSM coating is less active at open circuit voltage because it has fewer oxygen vacancies; however, its activation under large cathodic bias due to larger relative increase in vacancy concentration, as well as its suspected more favorable adsorption properties, makes it more active at mild cathodic bias. The modeling results trend agree with our experiments in both thin-films and porous, operational cathodes.

***Other Mn-Containing Catalysts Infiltrated LSCF***

As presented above, LSM coating can improve the activity and stability of LSCF cathode. Since Mn in B site has been demonstrated to play a key role in the activation process under operation and suppression of SrO segregation from LSCF, Mn element should be retained in the catalytic layer. Mn-containing materials are usually more stable under SOFC operation conditions than Co- and/or Fe-containing materials. More active Mn-containing catalyst coatings are also examined to further enhance performance. Moreover, perovskite-based catalyst may form a continuous and dense film on LSCF cathode due to structural similarity. Thus, a series of Mn-containing active catalyst for infiltration are developed, including:

- Simple perovskite $Pr_{1-x}Sr_xMnO_{3-\delta}$ (i.e., replacing La in LSM by Pr)
- Complex perovskite $PrSrCoMnO_{6-\delta}$ (i.e., substituting half of the Co in $PrBaCo_2O_{6-x}$ by Mn or replacing Ba in the A site by Sr).

Figure 15 shows some typical performances, at 750 °C at a constant voltage of 0.7 V, of homemade button cells infiltrated with different catalytic coatings. The cells with PSCM-infiltrated LSCF cathodes showed the best performance with significant activation behavior. Compared to cells with LSM, PSM, and PBCM infiltration, the PSCM infiltrated cells showed a gradual increase in performance, implying a continuous activation during operation. The "long-term activation" phenomenon could counter some other degradation mechanism to offer constant performance, which has attracted our attention for further study.

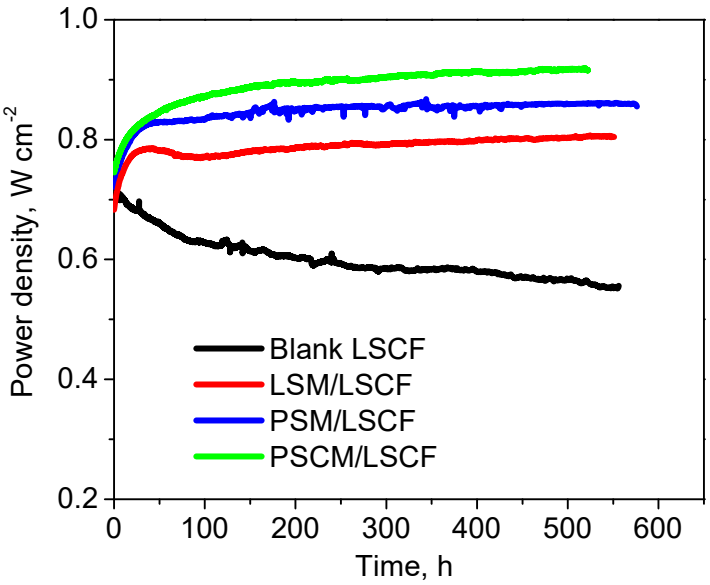


Figure 15. Typical lifetime of the homemade button cells with PSCM, PSM, and LSM infiltrated LSCF as well as baseline LSCF cathode with a constant voltage of 0.7 V at 750 °C.

**Catalyst Infiltrated into Scaffolds of Electrolytes**

When a scaffold of the electrolyte is used as the backbone, the catalyst or electrode materials to be infiltrated should have sufficient electronic conductivity in addition to excellent electrocatalytic activity. Thus, the main types of electrode/catalyst materials are conductive metal oxides, or MIECs. In some cases, precious metals are also added as catalyst to further enhance the catalytic activity.

The conductive metal oxides used for infiltration include (La,Sr)$MnO_3$ (LSM) [28, 33, 44, 71–74], (La,Sr)$CoO_3$ (LSC)[75, 76], (La,Sr)(Co,Fe)$O_3$ (LSCF) [77, 78] (Sm, Sr)$CoO_3$ (SSC)[79, 80] and $PrBaCo_2O_5$ [81]. Since most of the MIECs are complex in composition, the infiltration process has significant effect on the stoichiometry, microstructure, and morphology, which may critically affect the performance. As Jiang et al. indicated [74], direct decomposition of nitrate precursors at 800 °C will not yield a pure perovskite-phase LSM, making it necessary to use proper additives. For example, in the presence of glycine dispersant, perovskite phase LSM can be readily formed. In this case, the glycine acts as a chelating agent to form the metal ion complex in the solution, so that the

individual metal ions do not segregate upon firing of the metal salt precursor. The presence of additives also influences the microstructure of the infiltrated electrode. Figure 16 shows some cross-sectional micrographs of three electrodes prepared from different sources, an LSM solution of $La(NO_3)_3$, $Sr(NO_3)_2$, $Mn(NO_3)_2$ [72], a mixed solution of LSM and Triton X-100 [27], and a mixed solution of LSM and glycine [33]. Without proper additives, the infiltrated LSM particles seem to fill the pores of the backbone, limiting the gas transport within the cathode, as seen in Figure 16a. On the other hand, nanoscale LSM particles cover the backbone surface in the presence of additives, either Triton X-100 or glycine, as shown in Figure 16b and c.

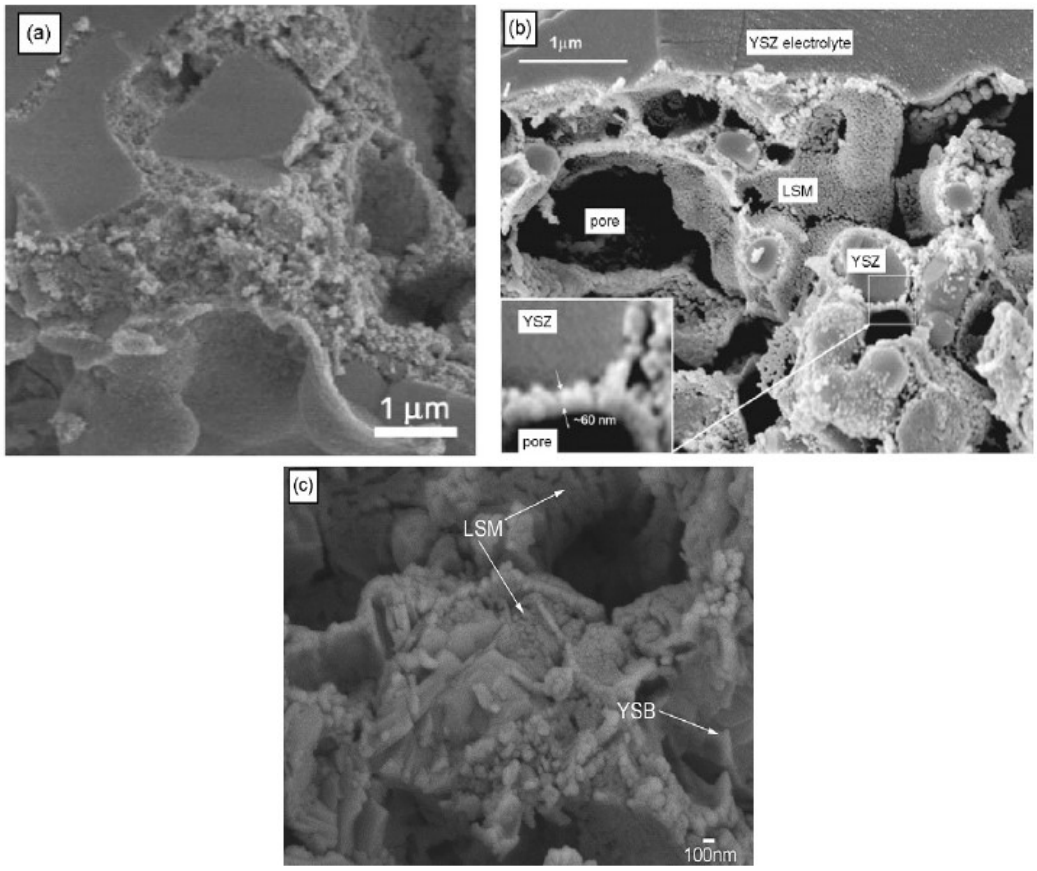


Figure 16. Microstructure of LSM infiltrated cathodes prepared from different LSM sources. (a) Mixed nitrate solution of $La(NO_3)_3$, $Sr(NO_3)_2$, and $Mn(NO_3)_2$, (b) mixed nitrate solution with Triton X-100, and (c) mixed nitrate solution with glycine. ([a], [b], and [c] are reproduced from references [72], [27] and [33].)

MIEC infiltrated electrolyte scaffold cathodes show encouraging performances. Huang et al. [72] have studied the performances of the 40 wt.% LSM infiltrated YSZ cathodes with LSM fired at 850, 1050, and 1250 °C. The single cells with LSM infiltrated cathodes also show good performance. A cell with single-step LSM infiltrated YSZ cathodes produces a maximum power density of 0.27 $Wcm^{-2}$ at 650 °C [27], while the maximum power density of a cell with conventional LSM-YSZ composite cathode is only 0.14 $Wcm^{-2}$ [82]. By substituting YSZ with YSB, the maximum power density increases to 0.33$Wcm^{-2}$ under similar testing conditions [33]. After repeating the

infiltration process, the maximum power density further increases to 0.45 $Wcm^{-2}$ [74]. For LSCF infiltrated GDC cathode, the GDC backbone firing temperature is found to be important, achieving a minimum polarization resistance at a firing temperature of 1100–1200 °C. Polarization resistance decreases with increased LSCF loading. A low firing temperature of 800 °C is also important for achieving a nanoscale (~50 nm) LSCF network structures that shows polarization resistance as low as 0.24 $cm^2$ at 600 °C. These results indicate that the ability to separately control the firing conditions of the GDC backbone and the LSCF infiltrated particles is critical to achieving low polarization resistance. Recently, a nano-network SSC infiltrated SDC cathode is reported by Zhao et al. [79]. By simply increasing the heating rate, nano-network is formed on the surface of SDC backbone. The nano-network consists of nanowires formed from the nanobeads of less than 50nm in diameter, thus exhibiting large surface area and high porosity, forming straight path for ion and electron conduction, and consequently showing remarkably low interfacial polarization resistances. The nano-network cathode has the lowest interfacial polarization resistances (0.21 $\Omega cm^2$ at 500 °C and 0.052 $\Omega cm^2$ at 600 °C) ever reported for the SSC cathode materials. Generally, Rp is found to depend on the firing temperatures and infiltration loading [48, 49, 83], which should be results of varied morphology and microstructure of MIEC coating on the backbone surface

MIEC infiltrated electrolyte scaffold cathodes could have excellent thermal cycle durability, compared with conventional composite electrode. As shown in Figure 17, the high stability of a LSC infiltrate SDC cathode is due most likely to the formation of a continuous and stable LSC nanoparticles anchored on the SDC scaffold. The modeling study suggests that the size of the nanoparticles is probably the most important factor to stabilize the nanostructure during thermal cycle [84].

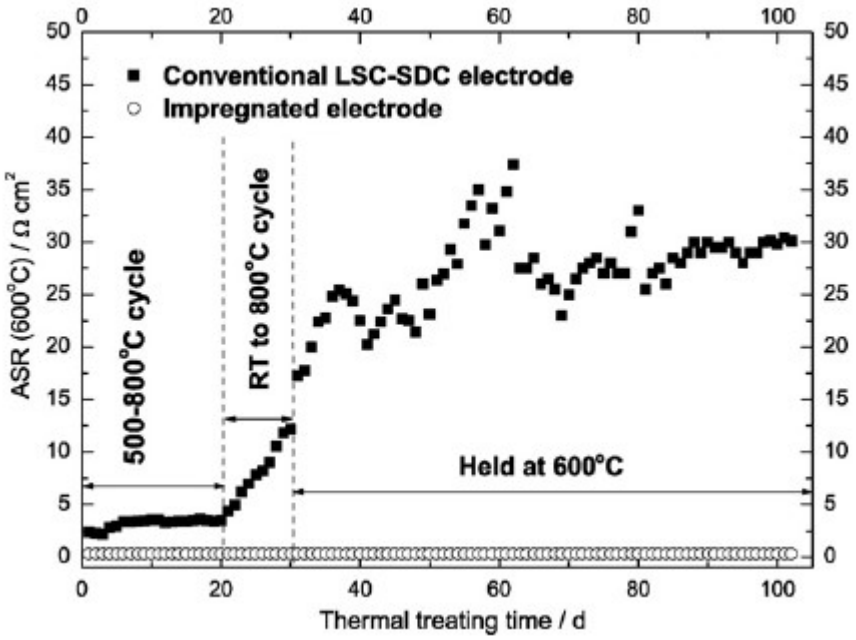


Figure 17. ASR at 600 °C for the LSC infiltrated SDC electrode and the conventional LSC-SDC electrode upon thermal treatment [79].

Recently, Jiang et al. reported a Pd infiltrated YSZ and LSM+YSZ cathode. [85] They first deposited LSM nanoparticles on highly porous YSZ scaffold to achieve the reasonable conductivity even below the normal percolation threshold of 30 vol%. Pd nanoparticles are subsequently deposited to form Pd+LSM-YSZ cathode (Figure 18). Although the microstructure of LSM infiltrated YSZ and Pd infiltrated LSM-YSZ appears similar, they suggest that the reaction paths are different. In the latter case, the deposition of Pd nanoparticles into an LSM-YSZ scaffold not only provides additional reaction sites but also enhance the rate of oxygen dissociation and diffusion, leading to high performance of the cell with Pd+LSM-YSZ composite cathodes.

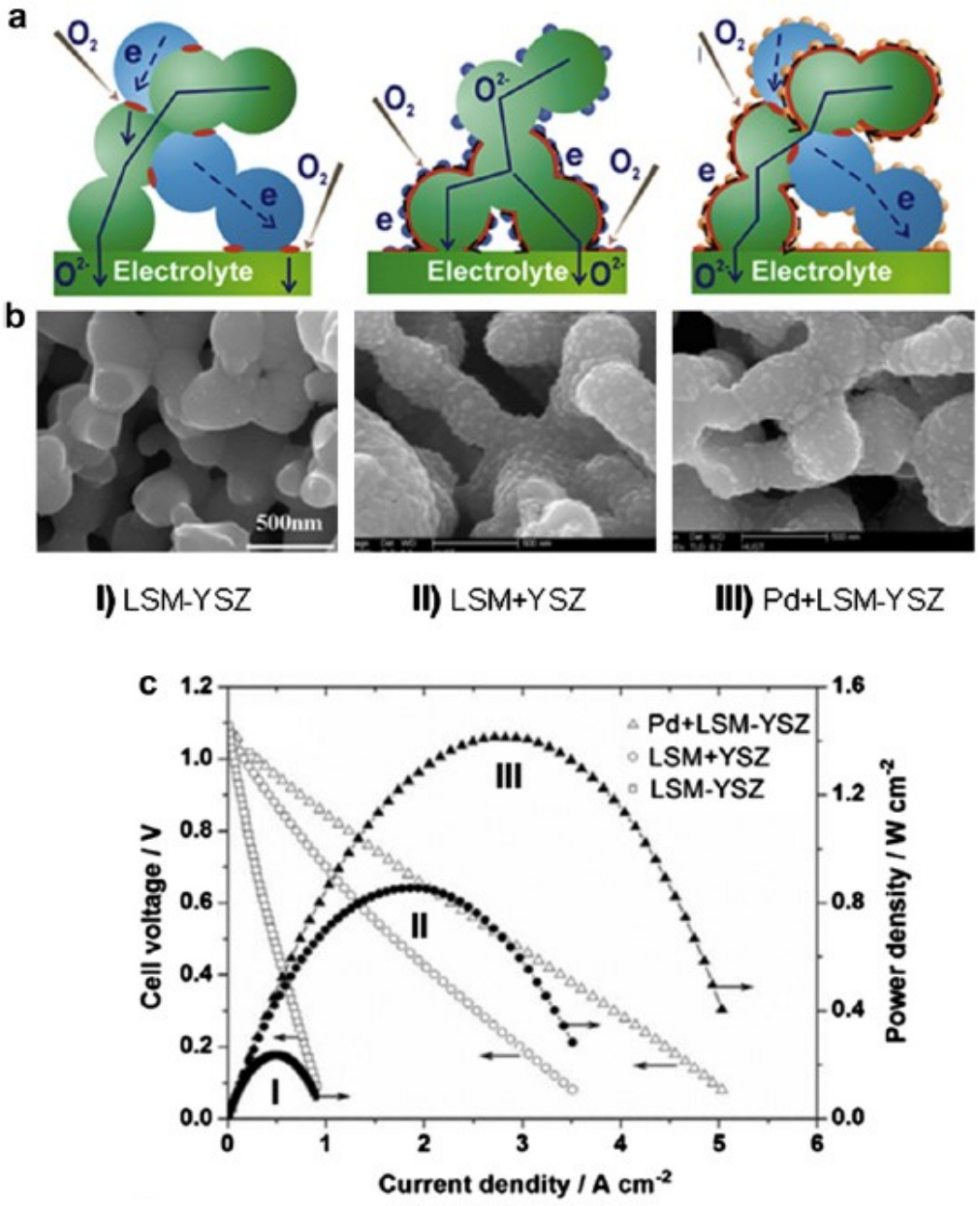


Figure 18. Demonstration of the performance and microstructure of the nanostructure electrodes. (a) Schematic illustrations of electrodes I, II, and III, showing the paths of transport for electrons and oxygen ions and reaction sites for the $O_2$ reduction reaction; (b) SEM micrographs of electrodes I, II, and III; (c) Power output of anode-supported cells with electrode types I, II, and II, measured at 750 $^oC$ in $H_2$/air. Electrodes: (I) standard LSM-YSZ composite cathode by mechanical mixing of LSM and YSZ phases; (II) nanostructured LSM-infiltrated YSZ (LSM+YSZ) composite cathode; and (III) nanostructured Pd-infiltrated LSM-YSZ (Pd+LSM-YSZ) composite cathode [85].

## Conclusions

Since cathode polarization still contributes considerably to energy loss in SOFC operation, one of the critical challenges facing the development of a new-generation of SOFCs is to create a highly active and stable cathode.

Cathode performance depends not only on the intrinsic properties of its components, but also on the microstructures. A composite cathode, consisting of a backbone and a thin electro-catalyst coating, is an effective electrode structure for efficient use of the unique properties of two different materials: the fast ionic and electronic transport properties of the backbone (e.g., LSCF) and the high catalytic activity and stability of the surface coating (e.g., LSM).

Infiltration is an effective approach to modification of electrode surface for better performance and stability. Among the two main infiltration strategies, infiltration of an electro-catalyst (e.g., LSM) into an MIEC backbone (e.g., LSCF) is more effective in performance enhancement and applicable to industrial fabrication processes at low cost, although the infiltration of a catalyst/electrode material into a scaffold of an electrolyte (e.g., YSZ or a doped ceria) may allow the use of other alternative cathode materials.

Solution-based infiltration processes have been developed for deposition of both discontinuous (discrete particle) and continuous (dense film) coatings of catalysts into the state-of-the-art LSCF cathode. For example, dense and continuous LSM films with desired structure, composition, morphology, and thickness have been deposited on LSCF surface to enhance the performance and stability of LSCF cathodes in SOFCs. Microanalysis revealed that such a film is able to effectively suppress the formation of oxides of La and Sr on the surface LSCF pellets after annealing at 850 °C for 900 hours, which may be related to the degradation of LSCF cathodes. Modeling reveals the mechanism of performance improvement through LSM coating, and theoretical analysis agrees with experimental observations. Furthermore, several Mn-containing perovskite materials are developed for infiltration, leading to more significant performance improvement over LSM infiltration.

Although infiltration of electrode/catalyst materials into a scaffold of electrolyte may allow the use of a wide range of catalyst materials, several concerns need to be carefully considered. First, sufficiently thick coatings must be introduced to ensure that the sheet resistance is small for efficient current collection, more so for larger cells or cell stacks. The need for large amounts of catalysts not only adds fabrication cost (repeated infiltration steps), but may also lead to decreased porosity, which could be detrimental to cell performance, especially at high current densities. Further, the CTE mismatch between the infiltrated catalyst and the electrolyte backbone could lead to delamination, especially during thermal cycling.

Compatibility between the catalyst and the backbone is critical for a stable cathode system. Any incompatibility may lead to possible degradation due to formation of secondary phase, derived from reaction or inter-diffusion between the infiltrated catalysts and the backbone.

However, the long-term stability of the catalyst-infiltrated cathodes in large commercial cells or cell stacks is yet to be demonstrated. This is the last step toward the transformation of the scientific knowledge into a novel technology that can be adopted by industry teams.

## References


1. Nie, L.F., M.F. Liu, Y.J. Zhang, and M.L. Liu, *La0.6Sr0.4Co0.2Fe0.8O3-delta cathodes infiltrated with samarium-doped cerium oxide for solid oxide fuel cells.* Journal Of Power Sources, 2010. **195**(15): p. 4704-4708.
2. Lou, X.Y., S.Z. Wang, Z. Liu, L. Yang, and M.L. Liu, *Improving La0.6Sr0.4Co0.2Fe0.8O3-delta cathode performance by infiltration of a Sm0.5Sr0.5CoO3-delta coating.* Solid State Ionics, 2009. **180**(23-25): p. 1285-1289.
3. Liu, M.F., D. Ding, K. Blinn, X.X. Li, L.F. Nie, and M.L. Liu, *Enhanced performance of LSCF cathode through surface modification.* International Journal of Hydrogen Energy, 2012(doi:10.1016/j.ijhydene.2012.02.139).
4. Lee, S., N. Miller, H. Abernathy, K. Gerdes, and A. Manivannan, *Effect of Sr-Doped LaCoO(3) and LaZrO(3) Infiltration on the Performance of SDC-LSCF Cathode.* Journal Of The Electrochemical Society, 2011. **158**(6): p. B735-B742.
5. Lee, S., N. Miller, M. Staruch, K. Gerdes, M. Jain, and A. Manivannan, *Pr(0.6)Sr(0.4)CoO(3-delta) electrocatalyst for solid oxide fuel cell cathode introduced via infiltration.* Electrochimica Acta, 2011. **56**(27): p. 9904-9909.
6. Ding, D., M.F. Liu, Z.B. Liu, X.X. Li, K. Blinn, X.B. Zhu, and M.L. Liu, *Efficient electro-catalysts for enhancing surface activity and stability of SOFC cathodes* Advanced Energy Materials, Submitted.
7. Minh, N.Q., *Ceramic Fuel-Cells.* Journal of the American Ceramic Society, 1993. **76**(3): p. 563-588.
8. Steele, B.C.H. and A. Heinzel, *Materials for fuel-cell technologies.* Nature, 2001. **414**(6861): p. 345-352.
9. Singhal, S.C., *Solid oxide fuel cells for stationary, mobile, and military applications.* Solid State Ionics, 2002. **152**: p. 405-410.
10. Liu, M., M.E. Lynch, K. Blinn, F.M. Alamgir, and Y. Choi, *Rational SOFC material design: new advances and tools.* Materials Today, 2011. **14**(11): p. 534-546.
11. Yang, L., S.Z. Wang, K. Blinn, M.F. Liu, Z. Liu, Z. Cheng, and M.L. Liu, *Enhanced Sulfur and Coking Tolerance of a Mixed Ion Conductor for SOFCs: BaZr0.1Ce0.7Y0.2-xYbxO3-delta.* Science, 2009. **326**(5949): p. 126-129.
12. Yang, L., Y. Choi, W. Qin, H. Chen, K. Blinn, M. Liu, P. Liu, J. Bai, T.A. Tyson, and M. Liu, *Promotion of water-mediated carbon removal by nanostructured barium oxide/nickel interfaces in solid oxide fuel cells.* Nature Communications, 2011. **2**.
13. Yamamoto, O., *Solid oxide fuel cells: fundamental aspects and prospects.* Electrochimica Acta, 2000. **45**(15-16): p. 2423-2435.
14. Steele, B.C.H., *Material science and engineering: The enabling technology for the commercialisation of fuel cell systems.* Journal of Materials Science, 2001. **36**(5): p. 1053-1068.
15. Fleig, J., *Solid oxide fuel cell cathodes: Polarization mechanisms and modeling of the electrochemical performance.* Annual Review of Materials Research, 2003. **33**: p. 361-382.
16. Sun, C.W., R. Hui, and J. Roller, *Cathode materials for solid oxide fuel cells: a review.* Journal of Solid State Electrochemistry, 2010. **14**(7): p. 1125-1144.
17. Xia, C.R., W. Rauch, F.L. Chen, and M.L. Liu, *Sm0.5Sr0.5CoO3 cathodes for low-temperature SOFCs.* Solid State Ionics, 2002. **149**(1-2): p. 11-19.
18. Shao, Z.P. and S.M. Haile, *A high-performance cathode for the next generation of solid-oxide fuel cells.* Nature, 2004. **431**(7005): p. 170-173.

19. Kim, G., S. Wang, A.J. Jacobson, L. Reimus, P. Brodersen, and C.A. Mims, *Rapid oxygen ion diffusion and surface exchange kinetics in PrBaCo2O5+x with a perovskite related structure and ordered A cations.* Journal Of Materials Chemistry, 2007. **17**(24): p. 2500-2505.
20. Steele, B.C.H., K.M. Hori, and S. Uchino, *Kinetic parameters influencing the performance of IT-SOFC composite electrodes.* Solid State Ionics, 2000. **135**(1-4): p. 445-450.
21. Juhl, M., S. Primdahl, C. Manon, and M. Mogensen, *Performance/structure correlation for composite SOFC cathodes.* Journal of Power Sources, 1996. **61**(1-2): p. 173-181.
22. Murray, E.P., T. Tsai, and S.A. Barnett, *Oxygen transfer processes in (La,Sr)MnO3/Y2O3-stabilized ZrO2 cathodes: an impedance spectroscopy study.* Solid State Ionics, 1998. **110**(3-4): p. 235-243.
23. Jorgensen, M.J. and M. Mogensen, *Impedance of solid oxide fuel cell LSM/YSZ composite cathodes.* Journal of the Electrochemical Society, 2001. **148**(5): p. A433-A442.
24. Jiang, S.P., *A review of wet impregnation - An alternative method for the fabrication of high performance and nano-structured electrodes of solid oxide fuel cells.* Materials Science and Engineering a-Structural Materials Properties Microstructure and Processing, 2006. **418**(1-2): p. 199-210.
25. Jiang, Z., C. Xia, and F. Chen, *Nano-structured composite cathodes for intermediate-temperature solid oxide fuel cells via an infiltration/impregnation technique.* Electrochimica Acta, 2010. **55**(11): p. 3595-3605.
26. Vohs, J.M. and R.J. Gorte, *High-Performance SOFC Cathodes Prepared by Infiltration.* Advanced Materials, 2009. **21**(9): p. 943-956.
27. Sholklapper, T.Z., C. Lu, C.P. Jacobson, S.J. Visco, and L.C. De Jonghe, *LSM-infiltrated solid oxide fuel cell cathodes.* Electrochemical and Solid State Letters, 2006. **9**(8): p. A376-A378.
28. Huang, Y., J.M. Vohs, and R.J. Gorte, *SOFC cathodes prepared by infiltration with various LSM precursors.* Electrochemical and Solid State Letters, 2006. **9**(5): p. A237-A240.
29. Park, S.D., J.M. Vohs, and R.J. Gorte, *Direct oxidation of hydrocarbons in a solid-oxide fuel cell.* Nature, 2000. **404**(6775): p. 265-267.
30. Wang, W.S., M.D. Gross, J.M. Vohs, and R.J. Gorte, *The stability of LSF-YSZ electrodes prepared by infiltration.* Journal of the Electrochemical Society, 2007. **154**(5): p. B439-B445.
31. Ding, D., W. Zhu, J.F. Gao, and C.R. Xia, *High performance electrolyte-coated anodes for low-temperature solid oxide fuel cells: Model and experiments.* Journal of Power Sources, 2008. **179**(1): p. 177-185.
32. Zhu, W., D. Ding, and C. Xia, *Enhancement in three-phase boundary of SOFC electrodes by an ion impregnation method: A modeling comparison.* Electrochemical and Solid State Letters, 2008. **11**(6): p. B83-B86.
33. Jiang, Z.Y., C.R. Xia, F. Zhao, and F.L. Chen, *La0.85Sr0.15MnO3-delta Infiltrated Y0.5Bi1.5O3 Cathodes for Intermediate-Temperature Solid Oxide Fuel Cells.* Electrochemical and Solid State Letters, 2009. **12**(6): p. B91-B93.
34. Jiang, S.P., Y.Y. Duan, and J.G. Love, *Fabrication of high-performance NiOY2O3-ZrO2 cermet anodes of solid oxide fuel cells by ion impregnation.* Journal of the Electrochemical Society, 2002. **149**(9): p. A1175-A1183.
35. Choi, J.-J., W. Qin, M. Liu, and M. Liu, *Preparation and Characterization of (La(0.8)Sr(0.2))(0.95)MnO(3-delta) (LSM) Thin Films and LSM/LSCF Interface for Solid Oxide Fuel Cells.* Journal Of The American Ceramic Society, 2011. **94**(10): p. 3340-3345.
36. Lynch, M.E., L. Yang, W. Qin, J.-J. Choi, M. Liu, K. Blinn, and M. Liu, *Enhancement of La(0.6)Sr(0.4)Co(0.2)Fe(0.8)O(3-delta) durability and surface electrocatalytic activity by La(0.85)Sr(0.15)MnO(3 +/-delta) investigated using a new test electrode platform.* Energy & Environmental Science, 2011. **4**(6): p. 2249-2258.
37. Lee, S., N. Miller, and K. Gerdes, *Long-term stability of SOFC composite cathode activated by electrocatalyst infiltration.* Accepted to the Journal of Electrochemical Society, 2012.

38. Lee, S., N. Miller, K. Gerdes, and A. Manivannan, *Time-dependent stability of SOFC activated by nano-sized cathode electrocatalyst.* 12th Annual SECA Workshop, July 26-28, 2011.
39. Chao, R., J.R. Kitchin, K. Gerdes, E.M. Sabolsky, and P.A. Salvador, *Preparation of Mesoporous La0.8Sr0.2MnO3 Infiltrated Coatings in Porous SOFC Cathodes Using Evaporation-Induced Self-Assembly Methods.* ECS Transactions, 2011. **35**(1): p. 2387-2399.
40. Chao, R., *Improving Solid Oxide Fuel Cell Cathode Performance by Infiltrating Mesoporous Perovskite Coatings.* Carnegie Mellon University, PhD dissertation, Materials Science and Engineering,, 2012.
41. This is based on our lab-scale fabrication processes. Since there is no need for any extra equipment for a solution infiltration process, the cost estimate covers only materials, labor, and extra electricity utilization. Typically it takes over 250 hours to make a batch of cells while the infiltration process will take almost 10 hours. Extra electricity use will be ~10% of the total utilization. However, this could be further reduced to less than 2% or even lower when the firing process is combined with the high-temperature start-up for the cell operation since the infiltration process is single step.
42. Since the performance enhancement is 10-30% as we domenstrated, it implies that we could reduce the cell quantity by at least 10% to reach the same power output in a stack configuration. In conjuction with our calculation on extra cost due to the infiltration process, it is reasonable to expect the ultimate cost reduction for commercial cells by ~ 10%.
43. Jiang, S.P., *A comparison of O2 reduction reactions on porous (La,Sr)MnO3 and (La,Sr)(Co,Fe)O3 electrodes.* Solid State Ionics, 2002. **146**(1-2): p. 1-22.
44. Sholklapper, T.Z., H. Kurokawa, C.P. Jacobson, S.J. Visco, and L.C. De Jonghe, *Nanostructured solid oxide fuel cell electrodes.* Nano Letters, 2007. **7**(7): p. 2136-2141.
45. Jiang, S.P., Y.J. Leng, S.H. Chan, and K.A. Khor, *Development of (La, Sr)MnO3-based cathodes for intermediate temperature solid oxide fuel cells.* Electrochemical and Solid State Letters, 2003. **6**(4): p. A67-A70.
46. Jiang, S.P. and W. Wang, *Fabrication and performance of GDC-impregnated (La,Sr)MnO3 cathodes for intermediate temperature solid oxide fuel cells.* Journal of the Electrochemical Society, 2005. **152**(7): p. A1398-A1408.
47. Jiang, S.P. and W. Wang, *Novel structured mixed ionic and electronic conducting cathodes of solid oxide fuel cells.* Solid State Ionics, 2005. **176**(15-16): p. 1351-1357.
48. Xu, X.Y., Z.Y. Jiang, X. Fan, and C.R. Xia, *LSM-SDC electrodes fabricated with an ion-impregnating process for SOFCs with doped ceria electrolytes.* Solid State Ionics, 2006. **177**(19-25): p. 2113-2117.
49. Zhang, L., F. Zhao, R.R. Peng, and C.R. Xia, *Effect of firing temperature on the performance of LSM-SDC cathodes prepared with an ion-impregnation method.* Solid State Ionics, 2008. **179**(27-32): p. 1553-1556.
50. Tian, R.F., J. Fan, Y. Liu, and C.R. Xia, *Low-temperature solid oxide fuel cells with La1-xSrxMnO3 as the cathodes.* Journal of Power Sources, 2008. **185**(2): p. 1247-1251.
51. Ding, D., M.Y. Gong, C.C. Xu, N. Baxter, Y.H. Li, J. Zondlo, K. Gerdes, and X.B. Liu, *Electrochemical characteristics of samaria-doped ceria infiltrated strontium-doped LaMnO(3) cathodes with varied thickness for yttria-stabilized zirconia electrolytes.* Journal Of Power Sources, 2011. **196**(5): p. 2551-2557.
52. Chen, K.F., Z. Lu, N. Ai, X.J. Chen, J.Y. Hu, X.Q. Huang, and W.H. Su, *Effect of SDC-impregnated LSM cathodes on the performance of anode-supported YSZ films for SOFCs.* Journal of Power Sources, 2007. **167**(1): p. 84-89.
53. Hojberg, J. and M. Sogaard, *Impregnation of LSM Based Cathodes for Solid Oxide Fuel Cells.* Electrochemical And Solid State Letters, 2011. **14**(7): p. B77-B79.

54. Liu, M.F., D. Ding, K. Blinn, X.X. Li, L.F. Nie, and M. Liu, *Enhanced performance of LSCF cathode through surface modification.* International Journal Of Hydrogen Energy, 2012. **37**(10): p. 8613-8620.
55. Zhang, X., M. Robertson, S. Yick, C. Dec?es-Petit, E. Styles, W. Qu, Y. Xie, R. Hui, J. Roller, O. Kesler, R. Maric, and D. Ghosh, *Sm0.5Sr0.5CoO3 + Sm0.2Ce0.8O1.9 composite cathode for cermet supported thin Sm0.2Ce0.8O1.9 electrolyte SOFC operating below 600 °C.* Journal of Power Sources, 2006. **160**(2 SPEC. ISS.): p. 1211-1216.
56. Ding, D., L. Li, K. Feng, Z.B. Liu, and C.R. Xia, *High performance Ni-Sm2O3 cermet anodes for intermediate-temperature solid oxide fuel cells.* Journal of Power Sources, 2009. **187**(2): p. 400-402.
57. Lou, X.Y., Z. Liu, S.Z. Wang, Y.H. Xiu, C.P. Wong, and M.L. Liu, *Controlling the morphology and uniformity of a catalyst-infiltrated cathode for solid oxide fuel cells by tuning wetting property.* Journal of Power Sources, 2010. **195**(2): p. 419-424.
58. Uchida, H., S. Arisaka, and M. Watanabe, *High performance electrodes for medium-temperature solid oxide fuel cells: Activation of La(Sr)CoO3 cathode with highly dispersed Pt metal electrocatalysts.* Solid State Ionics, 2000. **135**(1-4): p. 347-351.
59. Uchida, H., S. Arisaka, and M. Watanabe, *High performance electrode for medium-temperature solid oxide fuel cells - Control of microstructure of La(Sr)CoO3 cathodes with highly dispersed Pt electrocatalysts.* Journal of the Electrochemical Society, 2002. **149**(1): p. A13-A18.
60. Simner, S.P., J.R. Bonnett, N.L. Canfield, K.D. Meinhardt, J.P. Shelton, V.L. Sprenkle, and J.W. Stevenson, *Development of lanthanum ferrite SOFC cathodes.* Journal of Power Sources, 2003. **113**(1): p. 1-10.
61. Haanappel, V.A.C., D. Rutenbeck, A. Mai, S. Uhlenbruck, D. Sebold, H. Wesemeyer, B. Rowekamp, C. Tropartz, and F. Tietz, *The influence of noble-metal-containing cathodes on the electrochemical performance of anode-supported SOFCs.* Journal of Power Sources, 2004. **130**(1-2): p. 119-128.
62. Sahibzada, M., S.J. Benson, R.A. Rudkin, and J.A. Kilner, *Pd-promoted La0.6Sr0.4Co0.2Fe0.8O3 cathodes.* Solid State Ionics, 1998. **115**: p. 285-290.
63. Chen, J., F.L. Liang, B. Chi, J. Pu, S.P. Jiang, and L. Jian, *Palladium and ceria infiltrated La0.8Sr0.2Co0.5Fe0.5O3-delta cathodes of solid oxide fuel cells.* Journal of Power Sources, 2009. **194**(1): p. 275-280.
64. Serra, J.M. and H.P. Buchkremer, *On the nanostructuring and catalytic promotion of intermediate temperature solid oxide fuel cell (IT-SOFC) cathodes.* Journal of Power Sources, 2007. **172**(2): p. 768-774.
65. Zhang, R., H. Alamdari, and S. Kallaguine, *Fe-based perovskites substituted by copper and palladium for NO plus CO reaction.* Journal Of Catalysis, 2006. **242**(2): p. 241-253.
66. Zhang, R.D., A. Villanueva, H. Alamdari, and S. Kaliaguine, *Cu- and Pd-substituted nanoscale Fe-based perovskites for selective catalytic reduction of NO by propene.* Journal Of Catalysis, 2006. **237**(2): p. 368-380.
67. Li, J., U.G. Singh, J.W. Bennett, K. Page, J.C. Weaver, J.-P. Zhang, T. Proffen, A.M. Rappe, S. Scott, and R. Seshadri, *BaCe1-xPdxO3-delta (0 <= x <= 0.1): Redox Controlled Ingress and Egress of Palladium in a Perovskite.* Chemistry Of Materials, 2007. **19**(6): p. 1418-1426.
68. Sakito, Y., A. Hirano, N. Imanishi, Y. Takeda, O. Yamamoto, and Y. Liu, *Silver infiltrated La0.6Sr0.4Co0.2Fe0.8O3 cathodes for intermediate temperature solid oxide fuel cells.* Journal of Power Sources, 2008. **182**(2): p. 476-481.
69. Lee, K.T. and A. Manthiram, *Electrochemical performance of Nd0.6Sr0.4Co0.5Fe0.5O3-delta-Ag composite cathodes in intermediate temperature solid oxide fuel cells.* Journal of Power Sources, 2006. **160**(2): p. 903-908.
70. Simner, S.P., M.D. Anderson, M.H. Engelhard, and J.W. Stevenson, *Degradation mechanisms of La-Sr-Co-Fe-O3SOFC cathodes.* Electrochemical And Solid State Letters, 2006. **9**(10): p. A478-A481.

71. He, H.P., Y.Y. Huang, J. Regal, M. Boaro, J.M. Vohs, and R.J. Gorte, *Low-temperature fabrication of oxide composites for solid-oxide fuel cells.* Journal of the American Ceramic Society, 2004. **87**(3): p. 331-336.
72. Huang, Y.Y., J.M. Vohs, and R.J. Gorte, *Characterization of LSM-YSZ composites prepared by impregnation methods.* Journal of the Electrochemical Society, 2005. **152**(7): p. A1347-A1353.
73. Sholklapper, T.Z., V. Radmilovic, C.P. Jacobson, S.J. Visco, and L.C. De Jonghe, *Synthesis and stability of a nanoparticle-infiltrated solid oxide fuel cell electrode.* Electrochemical and Solid State Letters, 2007. **10**(4): p. B74-B76.
74. Jiang, Z., Z. Lei, B. Ding, C. Xia, F. Zhao, and F. Chen, *Electrochemical characteristics of solid oxide fuel cell cathodes prepared by infiltrating (La,Sr)MnO(3) nanoparticles into yttria-stabilized bismuth oxide backbones.* International Journal Of Hydrogen Energy, 2010. **35**(15): p. 8322-8330.
75. Huang, Y.Y., K. Ahn, J.M. Vohs, and R.J. Gorte, *Characterization of Sr-doped LaCoO3-YSZ composites prepared by impregnation methods.* Journal of the Electrochemical Society, 2004. **151**(10): p. A1592-A1597.
76. Zhao, F., R.R. Peng, and C.R. Xia, *A La0.6Sr0.4CoO3-delta-based electrode wit high durability for intermediate temperature solid oxide fuel cells.* Materials Research Bulletin, 2008. **43**(2): p. 370-376.
77. Chen, J., F.L. Liang, L.N. Liu, S.P. Jiang, B. Chi, J. Pu, and J. Li, *Nano-structured (La, Sr)(Co, Fe)O-3+YSZ composite cathodes for intermediate temperature solid oxide fuel cells.* Journal of Power Sources, 2008. **183**(2): p. 586-589.
78. Shah, M. and S.A. Barnett, *Solid oxide fuel cell cathodes by infiltration of La0.6Sr0.4Co0.2Fe0.8O3-(delta) into Gd-Doped Ceria.* Solid State Ionics, 2008. **179**(35-36): p. 2059-2064.
79. Zhao, F., Z.Y. Wang, M.F. Liu, L. Zhang, C.R. Xia, and F.L. Chen, *Novel nano-network cathodes for solid oxide fuel cells.* Journal of Power Sources, 2008. **185**(1): p. 13-18.
80. Zhang, H., F. Zhao, F. Chen, and C. Xia, *Nano-structured Sm(0.5)Sr(0.5)CoO(3-delta) electrodes for intermediate-temperature SOFCs with zirconia electrolytes.* Solid State Ionics, 2011. **192**(1): p. 591-594.
81. Wang, Y., H. Zhang, F. Chen, and C. Xia, *Electrochemical characteristics of nano-structured PrBaCo2O5+x cathodes fabricated with ion impregnation process.* Journal Of Power Sources, 2012. **203**: p. 34-41.
82. Leng, Y.J., S.H. Chan, K.A. Khor, and S.P. Jiang, *Performance evaluation of anode-supported solid oxide fuel cells with thin film YSZ electrolyte.* International Journal of Hydrogen Energy, 2004. **29**(10): p. 1025-1033.
83. Leng, Y.J., S.H. Chan, K.A. Khor, and S.P. Jiang, *(La0.8Sr0.2)(0.9)MnO3-Gd0.2Ce0.8O1.9 composite cathodes prepared from (Gd, Ce)(NO3)(x)-modified (La0.8Sr0.2)(0.9)MnO3 for intermediate-temperature solid oxide fuel cells.* Journal of Solid State Electrochemistry, 2006. **10**(6): p. 339-347.
84. Zhang, Y. and C. Xia, *A durability model for solid oxide fuel cell electrodes in thermal cycle processes.* Journal Of Power Sources, 2010. **195**(19): p. 6611-6618.
85. Liang, F.L., J. Chen, S.P. Jiang, B. Chi, J. Pu, and L. Jian, *High performance solid oxide fuel cells with electrocatalytically enhanced (La, Sr)MnO3 cathodes.* Electrochemistry Communications, 2009. **11**(5): p. 1048-1051.

## **Electrochemical Effects on Solid Oxide Fuel Cell Cathodes including In Situ/Ex Situ Comparisons** *by Kee-Chul Chang, Brian Ingram & Hoydoo You (Argonne National Laboratory)*


### Summary

Solid oxide fuel cell (SOFC) cathodes are examined in situ during growth, annealing, and half-cell operation under electrochemical control by synchrotron X-ray techniques. The samples are also examined ex situ at room temperature before and after the cell operation and compared to the in situ measurements. Two types of samples were used: thin film cathodes grown on YSZ single crystal substrates using pulse laser deposition (PLD) and powder sample on porous YSZ backbone using liquid-phase infiltration followed by sintering. The thin-film cathodes are mainly used for surface-sensitive measurements of structural and chemical states, using the total reflection X-ray fluorescence (TXRF) technique. The elemental and depth sensitivity of the TXRF technique was mainly used to study cation segregations. The porous samples were mainly used for in situ coarsening experiments and ex situ characterization of the structure modifications, using the ultra-small angle X-ray scattering (USAXS) technique.

The Sr segregates during annealing. One of the most prominent results of TXRF measurements is the fact that Sr is mobile and segregates (or desegregates) to the surface as the film sample is annealed in air. The samples are grown by PLD in low $pO_2$ and at temperatures lower than the fuel cell operating temperature. Therefore, when the sample is subjected to the real operating condition or simply annealed in air, a new equilibrium is obtained. In addition, thin film geometry has one interface and one surface, which can also affect the equilibrium. In the example discussed below, Sr segregates to the surface when the film is cooled to room temperature. However, the Sr segregation can disappear or desegregate at high temperature and return at room temperature as the sample cools down. In essence, Sr is highly mobile and dynamic at the fuel-cell operating temperature range, although it segregates to the surface at low temperature.

Another consequence of Sr segregation is its effect on the composition. Since the samples are only a few tens of nanometers and the Sr-rich phase can be as large as several nanometers thick, the remainder of the sample is therefore the Sr composition less than the original composition. Our observations suggest that the Sr-segregation may depend sensitively on the overall initial Sr composition of the thin film. Within the limited experiments with a few compositions, we estimate that ~20% Sr composition is thermodynamically favored under the film or microscale LSM geometry. If the overall composition is more or less than the optimum composition, the thermodynamic selection of the optimum composition will lead to Sr segregation or desegregation in a film or microscale particle. The optimum composition can be influenced because of the presence of the surface and interfaces that are not present in bulk.

Probably one of the most interesting results of this report is the observation that B-site cation, Co, segregates in response to external polarization, not by simple annealing, unlike Sr segregation. In fact, Co appears as mobile as Sr *and* responds to polarization, i.e., a cathodic polarization makes Co segregate to the surface and an anodic polarization makes it desegregate. While Fe maintains the perovskite structure, it appears that Co can migrate in response to the applied potential. The response of Co to the potential suggests that Co will also respond to oxygen reduction reaction or that Co enhancement occurs during oxygen reduction reaction. In fact, Co enhancement appears to be the reason for the enhanced oxygen reduction activity, compared to LSM.

In a series of our experiments using the film cathodes, we confirm that LSM has a low activity and a high stability and LSC has a high activity and a low stability. The case of LSCF is particularly interesting because it maintains the activity of LSC, probably due to the Co mobility, yet remains as stable as LSM, probably because of the immobility of Fe that keeps the average perovskite structure intact.

The USAXS technique can be used for porous cathode materials. It is an average technique much like a powder diffraction technique. However, its high angular resolution makes it sensitive to the sizes of particles and pores typical for industrial porous cathodes. We show its sensitivity to the possible infiltrated porous cathode materials and in situ sintering measurements. In the near future, we plan to set up for realistic fuel cell cathodes in operation and monitor structural evolutions over long-term operations to follow up on the cause of long-term instability of industrial fuel cell cathodes.

## Introduction

Direct in situ examination of SOFC cathodes in operating or near operating conditions is important in elucidating the molecular-level reaction mechanism. However, in situ conditions are difficult to access with a variety of popular electron-based methods, such as X-ray photoelectron spectroscopy (XPS), scanning electron microscopy (SEM), transmission electron microscopy (TEM), and scanning tunneling microscopy (STM). The studies with these techniques were thus mainly limited to ex situ investigations. Nevertheless, the techniques have been extensively used in the past and provided valuable electron structure and microscopic information.

X-ray and STM based methods enable in situ characterization, but the advantage of direct in situ characterization of the sample under different conditions must be considered against the time and effort needed to achieve true in situ equilibrium or steady state and the experimental complexity associated with the measurements. In many cases, quick surveys of different conditions ex situ can result in valuable information on how to plan further in situ experiments. More importantly, by comparing in situ and ex situ studies, we can delineate the information directly relevant for operating conditions of SOFC cathodes, which is difficult sometimes with ex situ studies alone. Establishing the correlation between in situ and ex situ characterizations is also important for comparing measurements using different methods.

Since SOFC systems usually operate at temperatures greater than 600 °C, the basic assumption in ex situ measurements is that in situ conditions can be “frozen in” when it is quenched at a sufficiently

fast rate from high temperature. The frozen-in ex situ state of the sample is determined not only by the state of the sample at quenching but also by the quenching rate. The quench rate is limited by the cooling rate of the furnace and how much thermal shock the sample can withstand. Although ex situ measurements permit initial/final state comparisons, we need to determine the validity of quenching by in situ measurements of kinetic time scales. In situ measurements are also needed to verify that the sample is at equilibrium or steady state at the time of the quenching.

## In Situ and Ex Situ Sample Preparations for X-ray Characterizations

Planar thin-film model cathodes are chosen for in situ and ex situ comparison studies. While porous cathodes are used in industrial applications, thin-film geometry of the model cathodes has several advantages over the porous ones. First of all, the thin-film geometry enables use of advanced X-ray techniques. The advanced X-ray techniques can be used for in situ studies of atomic to nanoscale structures and chemical states during operation (*in operando*). The well-defined surface of the cathodes allows, for example, depth-sensitive advanced X-ray measurements. The use of advanced techniques is more difficult for porous cathode samples, and obtainable information is much more limited. It also enables STM measurements. Use of scanning tips makes it impossible to apply probe microscopy techniques for porous cathodes that have no well-defined surfaces. X-ray techniques and scanning probe are the two most important in situ techniques. In addition, the same planar geometry is used for electrical conductivity relaxation (ECR) measurements that can be directly compared to in situ measurements. Since the thin-film cathodes can be operated under ambient air as a full fuel cell or a half cell, much like industrial cathodes, the results obtained are still directly relevant to the porous cathodes. The information obtained from the thin-film cathodes can be directly applicable to the microscopic structures and chemistry of the porous cathodes made of the same materials.

Typically a pair of identical PLD-grown samples was used in our comparison measurements. One is prepared for use in in-situ APS measurements, and the other is prepared for use in a conventional electrochemical testing setup for ex situ characterization. The main difference in preparation is the installation of additional electrodes (wire) for the in situ sample. Then, the samples were subjected to similar thermal and electrochemical conditions for comparison. The electrochemical conditions applied were identical. However, the thermal cycles are approximately the same because the ex situ samples were treated in an enclosed furnace while the in situ experiments were performed in air with a sample heater. The temperature uncertainty is estimated to be $\pm 50$ °C. The typical set temperature was 700 °C and the set potentials were between 0.3 to 1 V either cathodic or anodic. Ex situ characterization was performed after the sample cooled to room temperature after thermal and electrochemical cycles, and the in situ characterization was performed during the course of the thermal and electrochemical cycles. The samples to be discussed in this section are LSM, LSC, and LSCF thin film samples grown by PLD directly or with GDC buffer layer on YSZ substrates.

## Sr Segregation During Annealing without Electrochemical Bias

The first in situ and ex situ comparison was made without applying potential, focusing only on the long-term thermal annealing effect. Impedance vs. time during thermal annealing of LSCF samples grown directly on YSZ(111) and on GdC(100)-layered YSZ(100) are shown in Figure 1. The gradual increase of impedances (several hours or days) is the typical long-time behavior of the film samples although low-frequency components can improve over a short period of time initially.

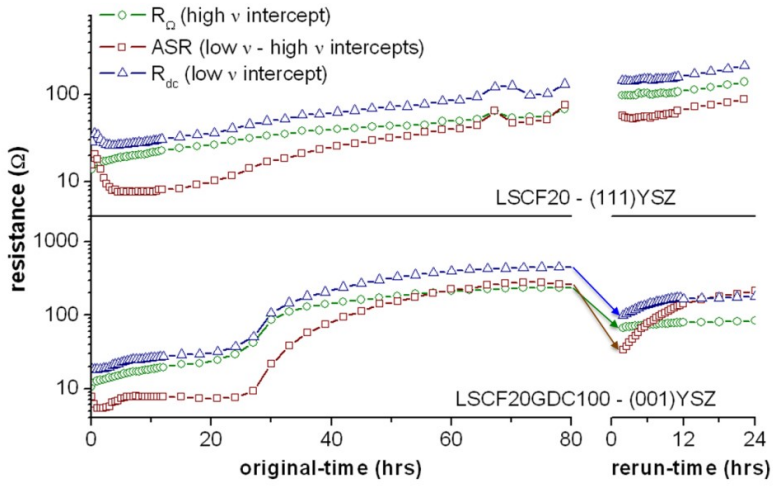


Figure 1. Impedance measurements at three different frequencies (ν) during thermal annealing to 700 °C in air. The samples were essentially unbiased during the impedance measurements.

The LSCF 20 nm film grown directly on the YSZ (111) substrate exhibits a monotonic increase of impedances even during the rerun after cooling down the sample days later. On the contrary, the LSCF 20 nm film grown on the GdC (100) pre-deposited substrate maintains low impedance with a slow increase over a day, but the increase accelerates over the course of several days. Furthermore, impedance improves during the cool down period, but eventually impedance increases again back to the values similar to the LSCF/YSZ(111) sample. This example illustrates that the impedance behavior depends not only on the sample compositions but also on the substrates that the samples are grown on. However, most samples studied exhibit generally similar behavior, namely, that the impedance increases gradually over a long time period without electrochemical biasing. We believe this behavior is related to the Sr segregation behavior discussed below. The Sr segregation has been seen in both in situ and ex situ X-ray measurements of all samples that we studied. As we will further discuss below, the segregation is strictly the result of thermal annealing and almost independent of electrochemical control. The qualitative behaviors of the samples are the same while there are some quantitative differences.

At least for the starting composition of 30–40% Sr, all samples, LSM, LSC, and LSCF, which we studied, show Sr segregation behavior. The Sr segregation is evident as a shoulder at low angle (~0.02 $Å^{-1}$) in our depth-sensitive chemical/elemental profiling technique, TXRF measurements. The TXRF data are shown in Figure 2. Based on the development of the shoulder (marked by grey

arrows in (a) and (b), we can identify that the Sr-rich phase exists as nanoscale particles on the surface. In fact, the nanoscale particles are also seen in our post annealing ex situ AFM images (not shown). The size and number of the Sr-rich particles are significantly larger for LSC than for LSM, which are consistent with the size and width of the shoulders seen in (a) and (b). In both cases, LSM and LSC, the shoulder nearly disappears at the operating temperature, but the shoulder reappears and grows larger as the sample is cooled. The disappearance of the shoulder does not mean Sr segregation completely disappeared. As seen in the X-ray technique section, the TXRF yield below the critical angle should have a concave shape (shown as dashed lines in Figure 2). The TXRF at 700 °C does not have a concave shape, indicating that a significant Sr fluorescence exists below the critical angle. However, it does indicate that the Sr-rich particles no longer remain as particles. The Sr segregation remains on the surface but is rather uniformly distributed. In the case of LSC, the distinction between the particles and uniform distribution become blurry since particles or islands are so dense and nearly overlap each other. The different morphologies of the Sr-rich phases between low and high temperatures are illustrated as the insets for (b).

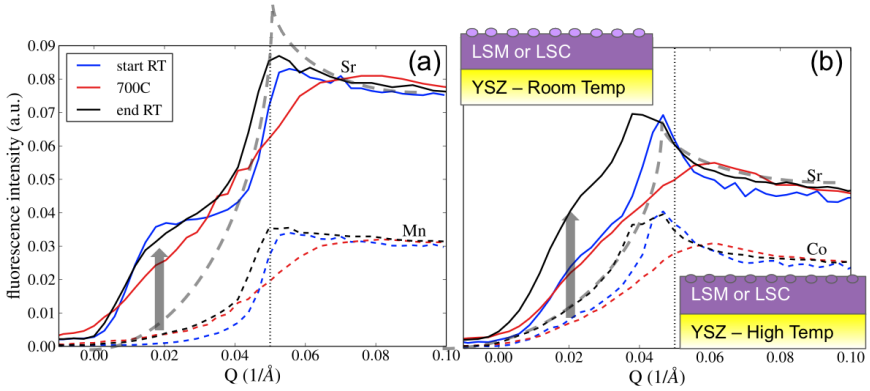


Figure 2. Sr fluorescence measurements at glancing angle: (a) LSM and (b) LSC films grown on YSZ. The critical angle of total external reflection is shown as a dashed vertical line, and the expected signal is shown as dashed curves.

The Sr segregation affects a significant fraction of the sample thickness. Since the samples are only a few tens of nanometers and the Sr-rich phase can be as large as several nanometers thick, the remainder of the sample is therefore Sr composition less than the original composition. On the other hand, in our previous study with LSM samples of 20% Sr composition,[28] the Sr segregation was considerably less evident. Furthermore, a recent measurement with LSM samples of 15% Sr composition exhibits Sr depletion on the surface. [29] These observations suggest that the Sr-segregation may depend sensitively to the overall initial Sr composition of the thin film. This can

[28] K.C. Chang and H. You, unpublished.

[29] S. Gopalan and K. Ludwig, private communication.

occur if there is an optimum Sr composition that the film maintains during annealing. Within the limited experiments with a few compositions, we may speculate that ~20% Sr composition is thermodynamically favored under the film or microscale LSM geometry. If the overall composition is more or less than the optimum composition, the thermodynamic selection of the optimum composition will lead to Sr segregation or desegregation in a film or microscale particle. The optimum composition can be influenced because of the presence of the surface and interfaces that are not present in bulk. The surface and interface energy contribution to the total free energy can lead to a phase separation even when it was not possible in bulk.

It is interesting to examine the composition near 30% Sr from the standpoint of the known phase diagrams of LSM. The bulk phase diagram of LSM is well established in condensed matter physics.[30] In fact, the phase diagram is rather complex due to the spin and orbital degrees of freedom, in particular, of the B-site Mn and surrounding oxygen octahedron. The known bulk phase diagram of LSM is shown in Figure 3a. The important aspect of the phase diagram in the view of cathode materials is the phase boundary between metal (higher Sr composition) and insulator (lower Sr composition). The boundary is at 30% Sr composition at the cathode operating temperature. Noting that the initial PLD-prepared composition of our cathode film samples is at the metal composition, the Sr segregation makes the LSM film move to an insulator or, at least, closer to the metal-insulator phase boundary. This is certainly not desirable in terms of electronic conductivity and is probably responsible for the low activity of LSM.

The situation is very similar with LSC. Its bulk phase diagram[31] is shown in Figure 3b. However, LSC maintains a semiconducting state at low Sr composition, rather than an insulating state. Therefore, even with the Sr segregation, LSC remains semi-metallic and highly active, although not very stable. We found that LSCF behaves similarly, showing the property intermediate between LSM and LSC. The degree of Sr segregation measured with TXRF (to be discussed in more detail below) is also consistent with behavior intermediate between LSC and LSM. The TXRF shoulders are more pronounced than those of LSM but not as much as those of LSC. In this regard, we can speculate that the slow increase of the impedance shown in Figure 1 may be an indication that the film composition drifts slowly at the operating temperature to a lower average Sr composition.

[30] A. Urushibara, Y. Moritomo, T. Arima, A. Asamitsu, G. Kido, Y. Tokura, Phys. Rev. B 51, 14103 (1995).

[31] J. Wu and C. Leighton, Phys. Rev. B 67 174408 (2003).

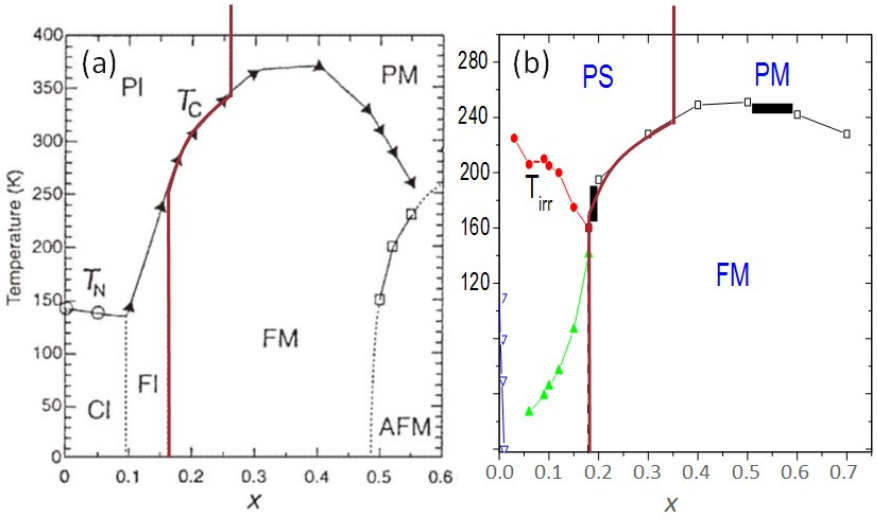


Figure 3. Bulk phase diagrams of (a) LSM and (b) LSC. PI: Paramagnetic insulator, PM: Paramagnetic metal, PS: Paramagnetic semiconductor, FM: Ferromagnetic metal, FI: Ferromagnetic insulator, CI: Spin-Canted insulator, AFM: Anti-ferromagnetic metal, $T_N$: Néel's temperature, $T_{irr}$: irreversible glass transition. The brown solid lines are metal to insulator (semiconductor) transition lines.

There is an important observation to be mentioned here in light of in situ and ex situ comparison. Even though the LSM, LSC, and LSCF film cathodes are at the insulating or semiconducting state in the operating in situ condition, they are metallic when the cathodes are cooled to a room-temperature ex situ condition for various characterization purposes. Therefore, caution should be exercised in interpolating the properties measured at room temperature to the operating temperature. Also, it is important to note that the metal-insulator or metal-semiconductor boundaries are more important at lower temperature. That is, the conductivity jump is larger and sharper at lower temperature than at high temperature. At 800 K or below, the conductivity jump can be larger than an order of magnitude and the small composition changes can make a large difference in conductivity measurements. Although commercial cathodes run at much higher temperature, it is important to keep in mind that any ex situ or in situ investigations at 800 K or lower must take into consideration that the measurements can be sharply dependent on a small change in Sr composition.

## XANES Characterization of LSCF: Surface vs. Bulk

We studied changes in physical properties of ~20 nm thick LSCF films during half-cell operation with the applied potential. LSCF films were grown in two different substrates: directly on YSZ(111) and on a 40 nm thick GdC(001) epitaxially grown on YSZ(001). Just heating the sample to 800 °C induces several reversible changes that are common to both samples. The widths of specular reflectivity peaks broaden at high temperature indicating increased roughness. Also in the XANES, we have K edge shifts in Sr, Fe, and Co to lower energy. This is consistent with increased oxygen vacancies in the LSCF film, which results in lower oxidation states for the cations. Co K-edge is

shown in Figure 4 as an example. In (a), the edge spectra are shown for the film in three conditions: as received and measured at room temperature, measured at 800 °C, and measured again at room temperature after cool down. Note that the edge position shifts to lower energy indicating a partial reduction. In (b), the surface-sensitive (TXRF) measurement is compared to that of the film. This comparison clearly indicates the film surface (~ a few nm thick) is more reduced (and more oxygen deficient) than the film bulk.

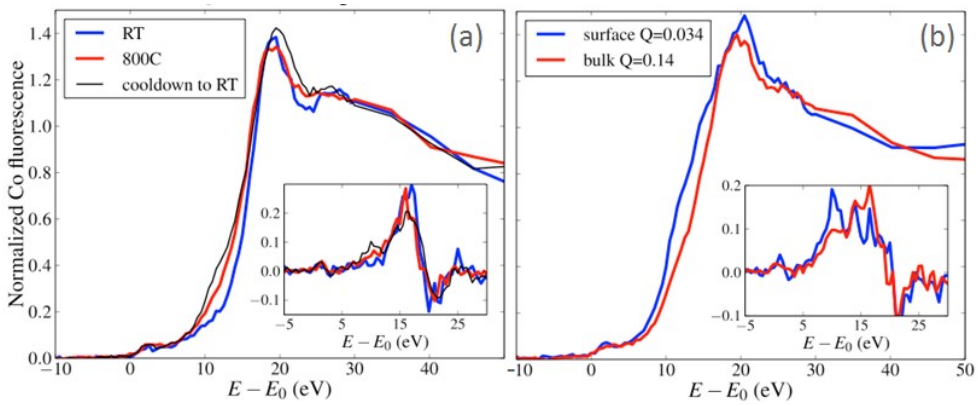


Figure 4. Co K-edge XANES of LSCF on YSZ(111) for (a) film at three conditions and (b) film and surface comparison.

## In Situ TXRF Characterization of Cation Segregation During Half-Cell Operation (*in operando*): LSCF

The ex situ measurements prompted further in situ measurements. It is clear from the above ex situ measurements that LSCF film grown directly on the YSZ(111) substrate does not form islands and maintains the integrity of the film structure. Sr and Fe segregate to the surface and distribute narrowly uniform on the surface. Furthermore, it appears to be responding to electrochemical polarizations. In order to further understand the cation migration behavior, we investigated the LSCF film on YSZ(111) during potential control to see if B-site cations may respond to the applied potentials. (We used Au wires as the contact electrodes, instead of Pt, to avoid possible catalytic activity of Pt affecting the film's activity.[32]) The experiments were repeated with two different electrode configurations to understand better the effect of geometric configurations. One sample was used for both configurations, simply by switching from in-plane to out-of-plane configuration during experiments, and the results were reproducible. The order of applied potential was OCP, +1V, -1V for in-plane measurements, shown in Figure 5a and OCP, -1V, +1V for out-of-plane measurements, shown in Figure 5b. The in-plane and out-of-plane configurations are schematically shown as the insets. Higher potentials of ±1 V were used to amplify the effects for a clear demonstration.

[32] J. Nielsen, T. Jacobsen, Solid State Ionics. 178, 1001 (2007).

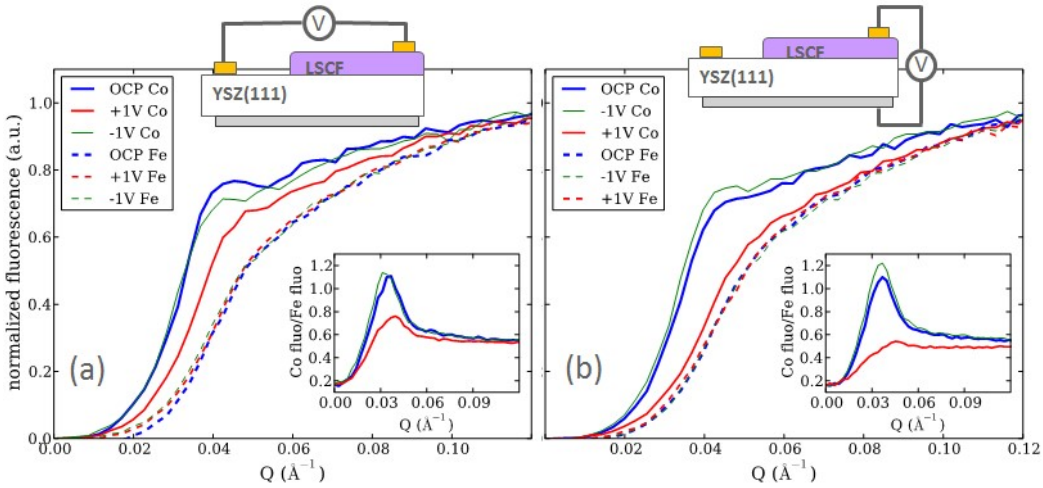


Figure 5. B-site cation fluorescence signals during under (a) in-plane and (b) out-of-plane potential controls.

The fluorescence signal of Co responds well to electrochemical potential. Both geometries show the same trend of Co segregation. The Co signal rises at lower angles than the Fe signal at OCP or at -1V. Then, the Co signal moves towards the Fe signal in (a) and almost overlaps in (b) with the Fe signal at +1V. The Fe signal does not respond to the potentials. Therefore, we can plot the ratio of Co intensity to Fe intensity (the insets) to show the potential dependences.

The surface enhancement of elements is evidenced by a shift of the rising edge of the fluorescence signal. The shift to a lower angle indicates an enhancement of the corresponding element at the surface. The shape of the fluorescence intensity increases near the critical angle and indicates that the enhancement is rather uniform over the entire surface with a thickness of a few nanometers. The insets show the ratio of the Co enhancement on the surface. Since the signal enhancement is quadratic to the elemental enhancement, the Co enhancement factor is ~1.25 (a) and ~1.55 (b).

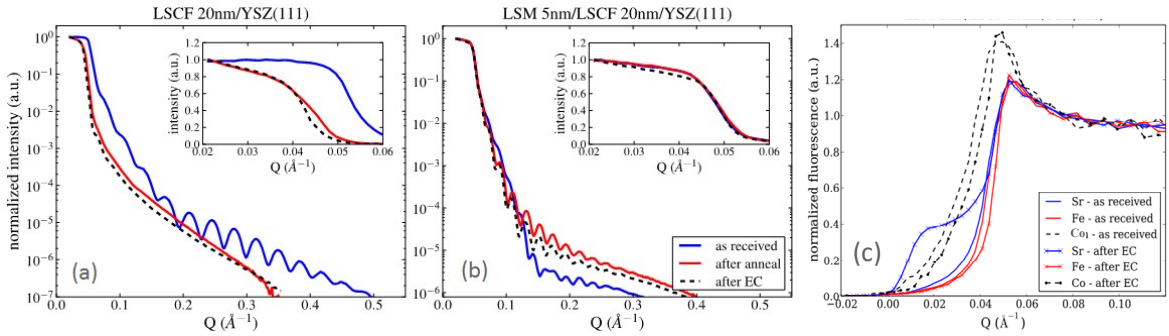


Figure 6. X-ray reflectivity of 5 nm LSM on 20 nm LSCF/YSZ(111) without (a) and with (b) a capping layer. The reflectivity data show a significant reduction of the critical angle and disappearance of the fringes in (a) while there is no critical angle change and the thickness fringes in (b), after annealing and cell operations. TXRF data (c) shows Sr segregation.

## Effect of LSM Capping Layer

We also studied the LSM on LSCF/YSZ(111) to model LSM infiltration. The samples with and without the LSM capping layer are studied with X-ray reflectivity and TXRF, and the data are shown in Figure 6. The reflectivity data are shown in (a) and (b) for the samples without and with, respectively. The TXRF data are shown in (c) for the capped sample. Comparing the critical angles shown in the insets, we can see that the critical angle does not change after annealing when there is a LSM capping overlayer. This suggests that the LSM stabilizes the surface of the thin film under annealing and operating conditions.

In the presence of a LSM capping layer, surface Co is reduced but does not go into a spinel state. Instead, it shows an edge shift with no white line peak change (data not shown), implying no structural change around the Co. We also see no evidence of Mn intermixing with the other B-site cations.

## Ex Situ Characterization of MnO Model Infiltration by Atomic Layer Deposition

Liquid-phase infiltration of LSM to LSCF cathodes has been successful[33] in improving the stability and catalytic activity. While liquid-phase infiltration is successful, we expect that gas-phase infiltration has a certain advantage in terms of penetration of the infiltrant deep into the porous cathode materials. We chose therefore the atomic layer deposition (ALD) technique to test the infiltration to the porous cathode materials, in particular LSCF. As the initial step, we deposited two types of MnO model infiltrates by ALD. One type is the ALD-film of MnO formed on a layered cathode. The film type was grown on LSCF thin film, which is epitaxially grown on $NdGaO_3$ (011) substrate by PLD. It was studied with the X-ray reflectivity technique. The second type of model

[33] X. Lou, Z. Liu, S. Wang, Y. Xiu, C.P. Wong, M. Liu, J. Power Sources, 195 419 (2010).

infiltrate was made by ALD deposition of MnO directly on sintered porous YSZ powder samples. The powder-type samples were examined by the USAXS technique.

Ultra-small angle X-ray scattering is a powerful tool to investigate more realistic cathode materials non-destructively. It can be used to examine the overall average particle and pore distribution of the size in the range from 10 nm to 10 μm. In analyzing and understanding the X-ray reflectivity or small-angle scattering, it is convenient to write the equation for the scattering intensity from interfaces since X-rays scatter only from interfaces in both cases. We call 'X-ray reflectivity' when the interfaces are overall relatively well-defined flat surface and 'small-angle scattering' when the interfaces are complex, and often convoluted. In both cases, however, the scattering angles are small (mostly forward scattering) and X-rays scatter only from the interfaces across which appreciable density changes occur (not sensitive to individual atoms).

Approximately 5 nm thick MnO ALD film was grown on a 10 nm thick LSCF PLD film on $NdGaO_3$ (011) substrate. Figure 7 shows the evolution of the X-ray reflectivity on this sample during annealing up to 700 °C. The reflectivity of the as-grown film measured shows a fringe of ~0.05 $Å^{-1}$, which corresponds to the overall thickness (~15 nm). Preliminary analysis indicates that, while there is no change in the overall thickness of the film, the major cause of the reflectivity change is due to air/MnO interface roughness, which was initially at 10 Å at room temperature but decreases to 5 Å at 500 °C. There is also a slight increase in the MnO/LSCF interface roughness from 2 to 4 Å above 500 °C, which accounts for the decreased intensity at high Q values. This result suggests that the initial grown ALD layer undergoes significant smoothening at 500 °C.

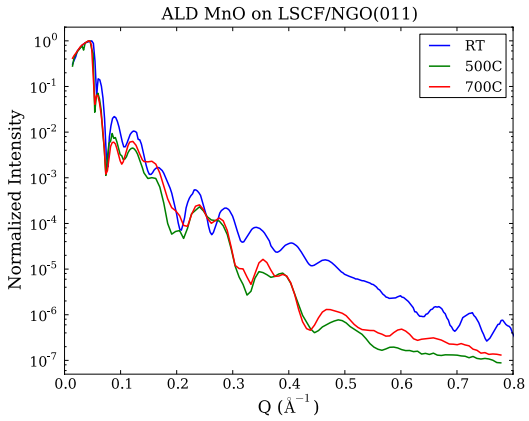


Figure 7. X-ray reflectivity of ALD MnO grown on 10 nm LSCF on NGO(011).

We used USAXS to characterize the infiltrate grown on sintered porous YSZ powder samples. We prepared 10 nm thick and 50 nm thick MnO layer samples. However, an initial USAXS pattern from the 10 nm thick sample was indistinguishable from that obtained from pure porous YSZ powder samples without the MnO layer. Therefore, we focus on in situ measurements of the 50 nm thick infiltrate. In situ USAXS data were taken on the 50nm thick MnO film from room temperature up to 600 °C and are shown in Figure 8. The ALD layer results in the fringes at high Q values ($Q \geq 100 Å^{-1}$)

of USAXS data in Figure 8. The fringes are shown more clearly by dividing the data for the infiltrated sample by the data obtained from a pure porous YSZ sample. The normalized data are shown in the inset of Figure 8.

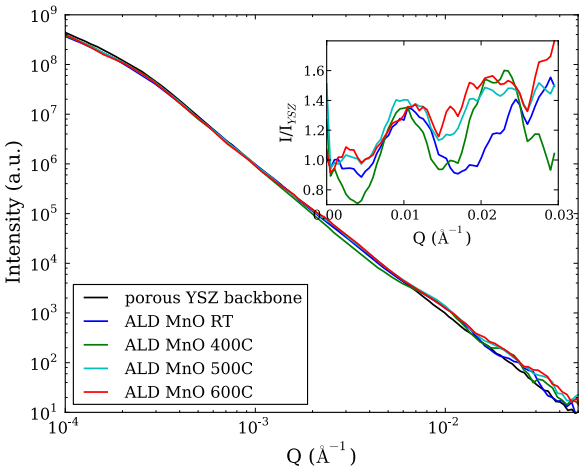


Figure 8. Ex situ USAXS of 50 nm ALD MnO films grown on porous YSZ at different temperatures. The inset shows the ratio of the ALD to the porous YSZ intensity.

Although our data is fairly noisy, we estimate that the ALD film thickness is ~60 nm in good agreement with the deposited film thicknesses. The fringes grow less distinct at 600 °C suggesting that the ALD film may start to lose uniformity at this temperature. At higher temperature, it is expected that the ALD film may not remain as a uniform coating of the particles as it did at lower temperature. However, we expect that the ALD film can still remain on the surface of the particles.

## In Situ USAX Measurements of the LSCF Sample Growth on Porous YSZ Backbone

We used USAXS to track in situ the temperature- and time-dependent microstructural evolution of an infiltrated LSCF second phase (Figure 9). The experimental geometry is also schematically shown. A screen-printed porous YSZ backbone was prepared and infiltrated with LSCF in tartaric acid. The increase in overall intensity at 400 °C is due to the organics from tartaric acid leaving the system. The presence of the organics reduces the density difference and, therefore, the scattering power. Up to 400 °C, there is no qualitative change in the intensity, which is essentially featureless in Q. However, infiltrates begin to nucleate to ~1 nm size particles at 600 °C. The particles continue to coarsen to ~5 nm from 600 °C to 800 °C, and we observe an accelerated coarsening of the infiltrates at 900 °C to ~100 nm.

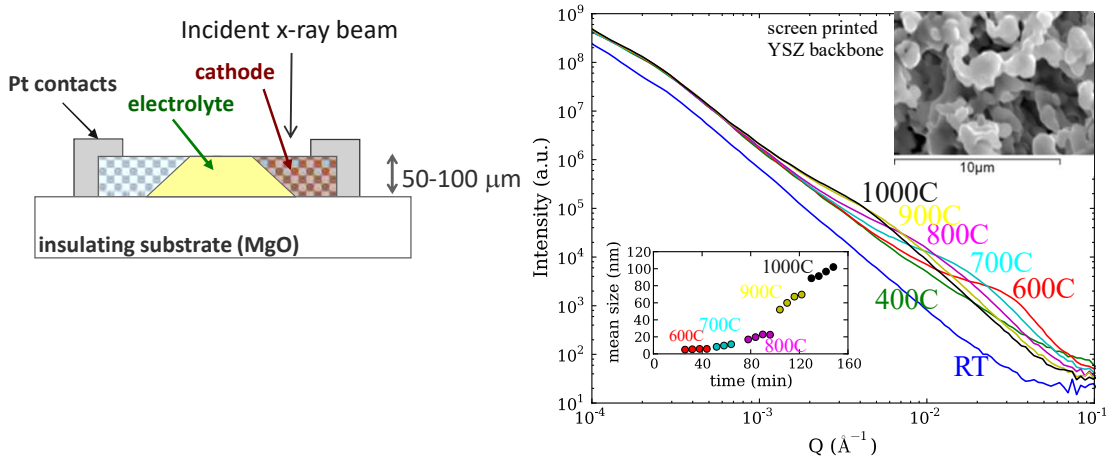


Figure 9. In situ USAXS of tartaric acid based LSCF grown on porous YSZ during annealing to 1,000 °C and a schematic diagram for the experimental geometry.

## Conclusion

While in situ investigation of SOFC working cells is most desirable for realistic evaluation of the cathode properties, well-designed ex situ investigations can reduce cost and effort. In this section, we presented X-ray techniques performed in situ and ex situ, both of which provide valuable information. The in situ studies were performed with a half cell cathode where the potential was artificially controlled. Even in in-situ studies, we find a need to delineate the effect of high temperature and the effect due to polarization. We conclude that the major structural and chemical changes, such as cation segregations, are due to the extended annealing of the initially PLD prepared film cathodes. However, significant segregations were also observed under the electrochemical polarizations as well as other subtle effects such as lattice expansion. Extensive in situ studies are now underway.

## Degradation in State-of-the-Art Solid Oxide Fuel Cell Cathodes *by Kirk Gerdes (National Energy Technology Laboratory) & Hoydoo You (Argonne National Laboratory)*


### Summary

Fuel cell degradation is considered to be any evolution of cell microstructure or chemistry that deviates from the initially constructed or ideal state, and which usually manifests as a time-dependent reduction in performance. Fuel cell degradation processes are influenced by both the contemporaneous operating condition and by the cumulative history of multi-modal degradation. Cathode materials in particular are subjected to *intrinsic* and *extrinsic* degradation processes, and both *primary* (direct) and *secondary* (multi-step or indirect) modes exist. A framework to categorize degradation processes is presented in Table 1, which distinguishes between modes on the basis of mechanistic complexity and the origin of the degradation-inducing thermodynamic potentials.

Broad modes of degradation are shared among all SOFC cathodes. Such modes include:

- Cation diffusion creating depressed activity phases and unwanted secondary phases;
- Agglomeration of grains resulting in diminished porosity and decreased triple phase boundary length;
- Accumulation of impurities at critical reaction interfaces, which depress or halt reaction kinetics; and
- Reaction between cathode and electrolyte to produce inactive phases.

Specific processes can be organized into these broad modes, and the mathematical descriptions of specific modes within the broad divisions will be similar.

The specifically manifested degradation processes experienced by a particular cell construction in a certain industrial stack design are expected to be unique, and consequently detailed analysis of degradation modes must be completed for each cell construction to categorize and quantify the expressed degradation. For example, Sr and Mn are broadly known to respond to the applied conditions of operation (temperature, overpotential), but the specific degradation behavior appears to be strongly dependent upon the exact composition of the cathode. Some evidence even suggests that LSM 80/20 and LSM 70/30 will degrade in very different manners. Examples of other modes that should be specifically examined in LSM and LSCF cathodes in all applications include:

- Segregation of Sr and Mn towards the surface of cathode grains, and the impact on surface exchange;
- Agglomeration of cathode particle clusters and grain growth, principally at specialized interfaces;

- Separation of YSZ into *t*-YSZ and *c*-YSZ domains as a function of applied overpotential; and
- Attack of cathode surfaces by $H_2O$, $CO_2$, and Cr.

Fortunately, a broad matrix of tests and analytical techniques have been leveraged to examine the common modes of degradation, and simple extrapolations may extend knowledge of a generalized mode to the specific degradation experienced by a certain cell/stack. Appropriate tests render definable and quantifiable degradation processes, and rational mitigation approaches can be advanced.

Table 1. Categories of principal cathode degradation modes.

| | **Intrinsic** |
|---|---|
| **Primary (direct or single step)** | *Degradation arises from relaxation of thermodynamic potentials within the cathode under intended, designed, or standard conditions of operation*<br>_____<br>Cathode cation diffusion forms an enriched phase<br>Crystallographic distortion results in phase breakdown<br>Sintering or grain coarsening results in microstructural evolution<br>Delamination arising from incompatible thermal expansion |
| **Secondary (indirect or multi-step)** | *Degradation arises from relaxation of thermodynamic potentials within the cathode in response to:*<br>*i) Operation of the cell beyond intended, designed, or standard conditions*<br>*ii) Multi-step degradation processes (cascading failure)*<br>_____<br>Activation or acceleration of primary modes at new conditions<br>Cathode delamination due to substantial secondary phase formation |
| | **Extrinsic** |
| **Primary (direct or single step)** | *Degradation arises from relaxation of cathode thermodynamic potentials influenced by external sources in response to:*<br>*i) Non-standard conditions of elemental exposure (gas phase)*<br>*ii) Cell fabrication outside of the design specifications*<br>_____<br>Diffusion of cations present as contaminants in cathode pre-cursor materials<br>Adsorption/reaction of contaminant molecules in gas feed (Cr, Si)<br>Operating point disruptions (load, fuel, etc.) |
| **Secondary (indirect or multi-step)** | *Degradation arises from relaxation of cathode thermodynamic potentials influenced by external sources. Degradation is characterized by a multi-step process (sequential or simultaneous), and at least one step includes a solid state degradation reaction of a cell component proximal to the cathode*<br>_____<br>Reaction of cathode with electrolyte/interconnect/seal<br>Overpotential variations arising from failure of current collecting mesh |

## Introduction

Research and development progress on the topic of SOFC systems has been rapid for more than ten 10 years owing to the large investment of private capital coupled with the application of federal research support through the SECA program [ML-1, EW-1]. Indeed, the industry reported performance demonstrations and cost projections have continuously met or exceeded federal program milestones [SECA-0, FCB-1, FCB-2], the rate of cost reduction and device innovation is projected to continue apace [RRT-1], and the advent of first-generation commercial SOFC systems exceeding 50 kW approaches [FCB-3, SECA-1, SECA-2, and SECA-3]. As the fundamental and applied technical challenges encumbering prototype generation have been overcome, research is pivoting towards optimization of material performance, particularly with respect to long-duration material service. At the cell level, optimization of performance is a function of electrochemical activity, intrinsic material stability, extrinsic material compatibility, and the costs of raw materials and fabrication processes. Performance optimization requires collection of data pertaining to subtle and evasive phenomena, and such data are critical to ensure developmental superiority of the next-generation of SOFC systems.

A conventional fuel cell stack consists of individual components acting in concert to facilitate global electrochemical reaction and transport processes influenced by gradients in the thermodynamic state [11]. Cell components are distinguishable by spatial occupancy (location and dimension), primary function (e.g., anode, electrolyte, cathode, interconnect, seal), and in terms of the primary modes of degradation exhibited. When considering the myriad processes and coupled modes that may occur in just the principal functional cell components, the task of assessing degradation becomes rapidly overwhelming. Therefore, degradation considerations in this report are restricted to primary (single, or discrete) and secondary (coupled, or synergistic) intrinsic and extrinsic processes affecting the cathode. The processes considered are local processes fundamentally occurring on a sub-micron scale and influenced by thermal, chemical, and electrical gradients. Bulk mechanical degradation arising from cell-scale mechanical forces are not addressed here. Specific modes of degradation can be identified as sub-parts of more generalized processes, and must be considered in a framework such as that depicted in Table 1 due to the complexity of the processes.

## Cathode Intrinsic, Primary Modes of Degradation

The most commonly occurring and widely studied degradation processes are categorized as primary intrinsic modes. These processes include cation diffusion producing altered physical properties, phase breakdown, and grain coarsening or sintering. Primary intrinsic modes arise during normal cell operation and are manifested through dissipation of potential gradients. Some potential gradients (such as cation distribution) exist in the fresh cell as a function of the fabrication process. Other potential gradients are applied via operating conditions (current density, temperature, chemical exposure) considered as “normal” for the particular cell, that is conditions for which a particular cathode has been designed. Degradation exhibited under such conditions is considered “primary” since the degradation arises in direct response to the thermodynamic state of operation and the cell is assumed to be engineered for performance in that operating state. Given that most primary intrinsic degradation processes involve solid state diffusion caused by exposure

to modest gradients in thermodynamic potentials, the degradation time scale is on the order of hundreds to thousands of hours.

Thermochemical cathode degradation resulting from intrinsic chemical potential gradients at the atomic scale is manifested as cation diffusion, defect generation/consumption, crystallographic relaxation, and phase separation. Although cation diffusion processes fundamentally proceed at the atomic scale, diffusion can occur *en masse* over a spatial region spanning nm to μm. Readily observable alterations to electrical transport and crystallography result from such diffusion. A recent and particularly innovative examination was reported [1] describing the continuous lattice expansion of a LSCF cathode operating electrochemically and examined in situ by XRD. The time-dependent lattice expansion was shown to correlate reasonably well over 60 hours to the observed degradation in cell performance. Strontium segregation in LS(C)F cathodes has also been well documented, with a characteristic study given in [10]. In the reported system, no microstructural evolution was observed within the cathode, yet impedance measurements revealed substantial degradation in the non-ohmic processes. A widely reported cation diffusion phenomenon inherent to LSM cathodes involves the transport of Mn ions [Mogensen 1]. Manganese is reported to partially diffuse from the LSM crystal and enrich the surface of the electrolyte near the triple phase boundaries. Initially this process enhances the performance of LSM cells, but eventually the Mn diffusion facilitates cascading degradation.

Thermochemical degradation at the particle scale is exhibited as evolution of the as-fabricated microstructure including densification of constituent phases, alteration of surface areas, and constriction of cathode pores. Microstructural evolution arises from relaxation of gradients in the particle surface free energy, which can require hours to days. Isothermal expansion of the crystal lattice of $LaMnO_3$ systems was investigated in response to oxygen partial pressure [Miyoshi 1], with the result that lengths could change more than 0.1% through the tested oxygen partial pressure range. The phenomenon of particle coarsening was clearly noted in research of GDC/LSCF systems, with contrasts made to LSM/YSZ systems [Barnett 1]. Although tested at elevated temperature, particle coarsening and surface morphological evolution were plainly evident. Another study demonstrated the role of electrical polarization on the sinterability of LSM materials [Jiang 1], and concluded that polarization impedes grain growth possibly due to the absence of cation vacancies at the perovskite's A-sites. Another study also reported the influence of the substrate over the cation diffusion process, whether leading to phase breakdown or particle agglomeration [Kim 1].

Electrochemically or electrically driven degradation processes may also occur in the cathode, whereby an electrical gradient is diminished through non-chemical diffusion processes such as ionic transport or charge transfer. One prominent example was generated for Mn contained within LSM cathodes [Backhaus 1, Backhaus 2]. In the course of both in situ and ex situ studies, Mn departed from the LSM crystal under cathodic polarization and begin populating the adjacent YSZ surface. In the case that cathodic polarization is removed or that anodic polarization is applied, the Mn returns to the LSM grain. Although degradation of the LSM lattice helps to activate the SOFC cathode in this case, the cathode so degraded may possess an enhanced susceptibility to failure. Ad hoc observations of cathode delamination at high overpotential also tend to indicate that some

modes of degradation may be activated or accelerated in the presence of an electrical gradient. Observed electrical degradation processes typically occur on the scale of seconds to minutes.

The thermodynamic state of the system is also influenced by the chemical composition of both the bulk gas and the local gas within the cathode structure. For some cathode materials, the magnitude of water present serves to activate or accelerate degradation processes. Both LSCF and LSM cathodes were reported to degrade under elevated water partial pressures, with degradation accelerated at operating temperatures below 800 °C [Sasaki 1]. A detailed study of the impact of water on the degradation of LSM cathodes has been reported [Mogensen 1], but a multi-step mechanism is postulated, so this mode is further described in a subsequent section treating cascading cell failure.

## Cathode Extrinsic, Primary Modes of Degradation

Degradation induced by primary processes involving cathode extrinsic materials arises from fabrication and gas exposure conditions that are outside of the ideal fabrication tolerances or the intended operational envelope. For example, cells fabricated from source materials containing excessive impurities will tend to degrade at a much faster rate than cells that are fabricated from high purity stocks. Likewise, cells that are overheated during cell fabrication may also possess undesirable secondary phases. In any case, the associated degradation modes are considered extrinsic because they arise from elements that are not intended for inclusion in the cathode and can be diminished through external controls (quality control practices, for example). Undesirable elements and molecules may also be introduced into the cathode via the feed gas, and act as degradation inducing agents. Agents introduced in such a way include everything from environmental molecules such as water to constituents of the upstream process hardware such as Cr and Si.

The impact of contaminant elements derived from impurities in the pre-cursor materials or deposited through gas phase transport from adjacent cell components has been widely investigated. Principal examples of the accumulation of contaminant materials have been demonstrated [Horita 1], and the primary elements identified include Na, Cr, Al, and Si. Commercial cells produced by Kyocera (flattened tube with $CeO_2$/LFO cathode) were operated for more than 8,000 hours and subsequently examined by SIMS at both the free cathode surface and at the cathode interlayer adjacent to the electrolyte. Si and Cr were found at the free surface, and Si was found to penetrate to the interlayer. Conductivity tests of YSZ completed at 500 °C [de Ridder 1] were also impacted by accumulation of Ca at the cell surface. Published results also reveal the impact of processing that deviates from standard conditions. The impacts of overheating the cell are discussed as well as potential impacts from off-specification Y content [Ji 1, Mori 1], and relationships to conventional cells can be readily extrapolated.

Volatile Cr species are widely known to evolve from the Cr-containing metals [Fergus 1] that often compose the balance of plant equipment. Thermodynamic consideration regarding reaction of several common cathodes with pre-cursor impurities was described, and Cr-containing phases were determined stable but formation was kinetically slow [Yokokawa 1]. Cathodes containing

tetravalent elements such as Fe and Co were more susceptible to secondary phase formation, and Cr phases typically formed at the TPB. Separate reports also indicated that the mechanism of Cr-poisoning (and therefore the magnitude) was sensitive to the cathode operating conditions, specifically polarization [Paulson 1, Komatsu 1].

## Cathode Intrinsic, Secondary Modes of Degradation

Secondary modes of cell degradation include all modes in which the electrochemical performance decrease is precipitated by a separate cathode-intrinsic primary failure or by inability to maintain the operating conditions within the range for which the cell was designed. The precursor failure may or may not manifest a detectable impact to electrochemical performance, but the secondary degradation mode will be evident and stronger than the precursor mode. Secondary modes will not strongly occur in the absence of the precursory failure. Cathode-intrinsic degradation may also occur in response to an unwanted or uncontrolled cell operating condition or thermodynamic state that is beyond the designed operating envelope. Examples of such upset states include load spikes or rejections, serious thermal fluctuations, or unwanted changes in the fuel composition. Although such changes may be considered to arise external to the cell, the degradation source ultimately depressing electrochemical performance is cathode-intrinsic.

One prominent example of cascading failure is evident in accelerated LSM cathode degradation due to over-humidification of cathodes. Water exposure is initially expected to mobilize the Mn cations within the LSM lattice, and permanent degradation was observed to increase in magnitude for higher water concentrations and for greater applied overpotentials [Mogensen 1]. Continued exposure to humidified conditions results in diffusion of Mn cations that may volatilize from the cell surface. A comparison between LSCF and LSM performance in high humidity conditions was also reported [Sasaki 1], with greater long-term susceptibility of LSCF observed. Exposure of the LSCF cathode to high water concentrations created substantial phase transformations that ultimately delaminated the LSCF cathode from the GDC interlayer.

Published reports documenting the degradative impact of unwanted thermodynamic conditions through a series of systematic and controlled tests are not available. However, satisfactorily approximate results are obtainable from studies performed under harsh operating conditions, especially at elevated temperatures and current densities (overpotentials). Examples of extraordinary cathode/electrolyte reactions at high temperature and current density have been shown [Nielsen 1, Hsaio 1], and typically include the formation of undesirable secondary phases (LZO), the acceleration of phase formation rates, and the appearance of unusual phases.

## Cathode Extrinsic, Secondary Modes of Degradation

Cathode extrinsic degradation occurring through secondary modes includes all processes by which initial degradation of a non-cell component induces degradation at the cathode/component interface. Typically, such processes feature a solid state reaction. Examples include formation of interfacial phases between components and phase breakdowns near interfaces arising from cation diffusion. All principal interfaces with the cathode must be considered including the

cathode/electrolyte, the cathode/contact material, and the cathode/interconnect. Cross-contamination of elements during cell fabrication must also be considered.

Cathode/electrolyte reactions have been widely reported for both the traditional LSM/YSZ systems and the LSCF/YSZ systems possessing no interlayer. In such systems, the cation exchange generates a non-conducting phase (e.g., lanthanum zirconate) that effectively destroys cathode activity. Other cation diffusion from the cathode to the electrolyte have been reported for standard and novel cathode/electrolyte compositions [5, Malzenbender 1, Mitterdorfer 1, Barnett 2, Shimazu 1]. Degradation processes involving cathode contact material can include mechanical degradation (e.g., cracking) due to thermal expansion mismatch between the contact material and the cathode or coarsening/sintering of the contact material over time. A representative investigation of several contact materials was conducted and critical performance metrics have been outlined including morphological and microstructural stability [Yang 1]. Undesirable interactions between the cathode and interconnect commonly arise from introduction of elements arising from the base interconnect [Schuler 1]. Cathode exposure intensifies when protective coatings applied to the interconnect crack or spall. Rapid degradation of the interconnect conductivity may also intensify local thermal conditions, which could impart sufficient energy to otherwise inactive degradation processes.

Cross contamination of the cathode with elements that constitute other cell components can also induce degradation. Such cross contamination may occur prior to complete sintering of the cell, whereby elements within the anode diffuse through the electrolyte to the cathode. The diffused element then either reacts with the cathode elements or alters the physical properties of the cathode. In one example, cathode grain coarsening was observed due to Ni crossing the electrolyte to the cathode [2].

## Time Dependent Degradation

The degradation processes occurring at a given operating time are influenced by the cumulative history of degradation. That is, while the cathode's instantaneous response to extrinsic chemical and electrical forces will be dictated by its contemporaneous operating state, degradation is a function of the total time of operation and the unique degradation path that the system has already traversed. This thermodynamic concept can be pictured as a multi-dimensional energy surface over which unique portions are accessible at a given time depending on the equilibrated operating conditions and the current thermodynamic operating state (which is dictated by operating history). To add additional complexity, the degradation rate of a given mode is unlikely to be linear over the course of the cell lifetime, and the identity of the dominant degradation mode expressed at a given time is likely to change.

The degradation rates that can be expected from cascading processes over long time scales are therefore imprecisely predictable. This fact complicates interpretation of any cathode-related cell failures observed following a step change in operating condition or a process upset, as the resulting degradation may not be directly correlated to the imposed condition. Even for two cells operated under identical initial conditions, the same cell performance (current density) will not necessarily

be observed after the same elapsed time unless the exact temporal operating conditions were imposed identically on the cells. Therefore, cell failures must be subjected to root cause analysis, with an increase in analytical intensity that is proportional to the service time of the stack being analyzed.

## Conclusions and Postulated Mitigations of Cathode Degradation

Cathode degradation has been shown in this brief summary to arise from diverse primary and secondary modes, and a framework has been proposed to categorize the modes according to the complexity of the degradation mode and its origin (cathode intrinsic or cathode extrinsic). Many modes documented in the peer-reviewed literature have been used to illustrate the degradation associated with each category, and prominent degradation processes have been highlighted. Although not exhaustive, the literature cited here and within the cited literature's references is expected to provide a comprehensive outline of the principal processes by which cathodes degrade. Voluminous detailed reports could be written on each of the modes identified, but such a task should only be undertaken for particularly vexing modes that are identified by industry teams.

Although the global problem of cathode degradation is complex, consideration of the topic provides some insight into general strategies to address the issue in a relatively simple fashion, and the principal strategies to mitigate cathode degradation align well with the categorization of degradation modes as shown in Table 2. Broadly considered, mitigation of cathode degradation can occur through a combination of best engineering practices and operating protocol. Best engineering practices can be used effectively to mitigate degradation through careful material selection, accurate specification of operating conditions, and verification of component compatibility. Operating protocols can be implemented to ensure limits and controls are in place for operating stacks to prevent activation of degradation modes that occur principally through deviation from standard operating conditions. Judicious use of cathode interlayers and infiltration of electro-catalytically active materials (see section on infiltration) may also help to stabilize cathode performance.

Table 2. General approaches to mitigation of cathode degradation.

| | **Intrinsic** | **Extrinsic** |
|---|---|---|
| **Primary (direct or single step)** | *Best Engineering Practices* | *i) Best Engineering Practices*<br>*ii) Operating Protocols* |
| **Secondary (indirect or multi-step)** | *i) Operating Protocols*<br>*ii) Best Engineering Practices* | *Best Engineering Practices* |

## References

[ML-1]: Materials Today 14, 11 (Nov 2011) 534-46

[W-1]: Energy & Environmental Science 5 (2012) 5498-509

[SECA-0]: 12th Annual SECA Workshop, DOE/NETL presentation, July 26-28, 2011

[FCB-1]: Fuel Cells Bulletin (Sept 2007) 13-16

[FCB-2]: Fuel Cells Bulletin (March 2005) 4

[RRT-1]: Energy Conversion and Management 57 (2012) 86-96

[FCB-3]: Fuel Cells Bulletin (June 2011) 6

[SECA-1]: 12th Annual SECA Workshop, Versa-Fuel Cell Energy presentation, July 26-28, 2011

[SECA-2]: 12th Annual SECA Workshop, UTC-Delphi presentation, July 26-28, 2011

[SECA-3]: 12th Annual SECA Workshop, Rolls-Royce presentation, July 26-28, 2011

[1] SECA: Journal of Power Sources 198 (2012) 76– 82

[2] SECA: Journal of the Electrochemical Society, 157 (5) B643-B649 (2010)

[3] SECA: J. Phys. Chem. C 2008, 112, 13299–13303

[4] SECA: Journal of The Electrochemical Society, 157 (7) B1019-B1023 (2010)

[5] SECA: Journal of The Electrochemical Society, 157 (6) B964-B969 (2010)

[6] SECA: Journal of The Electrochemical Society, 152 (4) A740-A745 (2005)

[7] SECA: Journal of The Electrochemical Society, 152 (9) A1851-A1859 (2005)

[8] SECA: Journal of Power Sources 129 (2004) 188–192

[9] SECA: Solid State Ionics 161 (2003) 11–18

[LQ Chen 1]: This work is in progress, and a citable reference is expected to be forthcoming

[Salvador 1]: Journal of the American Ceramic Society, submitted 2012

[SL 1]: Electrochemica Acta 56 (2011) 9904-09

[SL 2]: Journal of the Electrochemical Society 158 (6) B735-B742 (2011)

[Ohodnicki 1]: This work is in progress, and a citable reference is expected to be forthcoming

[10] SECA: Electrochemical and Solid State Letters 9 (10) A478-81 (2006)

[11] SECA: Journal of The Electrochemical Society, 157 (5) B643-B649 (2010)

[Mogensen 1]: Solid State Ionics 189 (2011) 74–81

[Miyoshi 1]: Solid State Ionics 161 (2003) 209–217

[Barnett 1]: Solid State Ionics 187 (2011) 64–67

[Jiang 1]: Solid State Ionics 176 (2005) 1185–1191

[Backhaus 1]: Solid State Ionics 179 (2008) 891–895

[Backhaus 2]: Solid State Ionics 177 (2006) 2195–2200

[Park 1]: International Journal of Hydrogen Energy 35 (2010) 8670- 77

[Horita 1]: Journal of Power Sources 193 (2009) 194–198

[Sasaki 1]: Journal of Power Sources 196 (2011) 7090– 7096

[Malzenbender 1]: Journal of Power Sources 201 (2012) 196– 203

[Mitterdorfer 1]: Solid State Ionics 111 (1998) 185-218

[Barnett 2]: Solid State Ionics 93 (1997) 207-217

[Komatsu 1]: Journal of Power Sources 195 (2010) 5601–5605

[Schuler 1]: Electrochemistry Communications 12 (2010) 1682–1685

[de Ridder 1]: Solid State Ionics 156 (2003) 255

[Yokokawa 1]: Solid State Ionics 177 (2006) 3193–3198

[Nielsen 1]: Solid State Ionics 179 (2008) 1314–1319

[Hsaio]: Solid State Ionics 98 (1997) 33 –38

[Shimazu 1]: Solid State Ionics 204-205 (2011) 120–128

[Kim 1]: Journal of The Electrochemical Society, 158 (2) B79-B83 (2011)

[Ji 1]: Solid State Ionics 176 (2005) 937–943

[Mori 1]: Solid State Ionics 123 (1999) 113 –119

[Fergus 1]: International Journal of Hydrogen Energy 32 (2007) 3664 – 3671

[Paulson 1]: Journal of The Electrochemical Society, 151 (11) A1961-A1968 (2004)

[Yang 1]: Journal of Power Sources 155 (2006) 246–252

# Oxygen Reduction at Solid Oxide Fuel Cell Cathodes: A Comprehensive Study on Electronic and Mixed Ionic and Electronic Conductors Using Thin Film Studies on Patterned Electrodes, Heteroepitaxial Layers, and Infiltration Experiments *by Srikanth Gopalan (Boston University)*

## Background

The oxygen reduction reaction (ORR) in the cathode is to date a significant source of polarization and efficiency loss in a solid oxide fuel cell (SOFC), especially at lower operating temperatures in the 600–800 °C. Depending on the materials set employed, particularly the electrolyte, several cathode materials have been used. However, $La_{1-x}Sr_xMnO_3$ (LSM), a predominantly electronic conductor, and $La_{1-x}Sr_xCo_{1-y}Fe_yO_3$ (LSCF), an excellent mixed conductor, have been the principal candidates used as SOFC cathodes. Many new materials continue to be investigated. It has been long recognized that the structural and compositional changes that occur at the surface of the cathode, i.e., gas-cathode interface, plays a key role in the ORR. However, the specific details of the role that these factors play has not been clearly elucidated. Further, a detailed understanding of the relationship between the various kinetic parameters related to the ORR, namely, oxygen surface adsorption, bulk and surface diffusivities of oxygen to the sites of the electrochemical reduction reaction, and the relative importance of triple phase boundaries and gas exposed surfaces of the cathode is still emerging. Ultimately, research on cathode materials will need to provide the mechanistic link between the compositional and structural changes at the cathode surface to the measured kinetic parameters. Such a linkage is essential to design new cathode materials and cathode architectures.

## Patterned Electrodes: Thermodynamics and Kinetics of Oxygen Reduction

### Introduction

The first step to improving cathode performance is for researchers to develop an understanding of the oxygen reduction process itself. Simply stated, oxygen is fed to the cathode side of the SOFC and is reduced to oxygen ions by the half reaction:

$$2e^- + \frac{1}{2}O_2 \rightarrow O^{2-} \quad (1)$$

Oxygen ions migrate selectively through the electrolyte to the anode, where a similar half reaction with gaseous fuel occurs to form either $H_2O$ or $CO_2$ depending on the fuel stream. The overall half-reaction given by Equation (1) is misleading in its simplicity, for in practically all conditions this reaction is composed of several intermediate elementary steps each of which occur with a finite

rate. Over the last 20–25 years, numerous studies have made substantial progress investigating the ORR [1–3]. Researchers have tended to focus on electrode materials and microstructure, and how and why the performance changes with experimental conditions such as temperature, oxygen partial pressure, and time, as well as other factors such as impurities and thermal cycling.

This is a complicated process, but in the simplest terms, there are some necessary material and geometric considerations that must be met in order for this reaction to proceed with a reasonable rate. The cathode must be exposed to the gas phase, it must be a good electronic conductor, and it must be in electrical contact with the external circuit. The cathode must also be in intimate contact with the ionically conducting electrolyte phase for transport of the ions towards the anode. The gas is reduced at some point in the vicinity of the gas/cathode/electrolyte region; the necessary reactions are shown schematically in Figure 1 [4, 5].

Cathode materials are chosen to fulfill these requirements, because, among other characteristics, they are efficient electronic conductors at high temperature and stable under oxidizing conditions. Noble metal catalysts such as Au, Ag, and Pt fit these requirements, yet are too costly to be considered practical for commercial deployment. As an alternative, ceramic oxides with a perovskite ($ABO_3$) structure have proven to be a suitable and less expensive replacement. Since the current density is limited by the availability of oxygen at the electrolyte interface, adequate porosity is generally required to allow adequate gas supply. Performance improvements have also been made by switching to materials with good ionic conductivity as well as electronic conductivity (called MIECs) such as Sr-doped $LaCoO_3$ [6]. This increased active area available for $O_2$ reduction was thought responsible for improved kinetics seen at temperatures below 800 °C. Alternatively (or in combination), composite structures such as LSM-YSZ mixtures allow for larger contact area between electronic and ionic conductors. Unfortunately, improvements of this sort were largely empirical and not systematically optimized, suffering from stability problems related to many unknown variables. Another approach, becoming more widely adopted, is infiltration. In this technique a porous network of electrolyte material is first fabricated on top of the dense electrolyte, and then a cathode catalyst is impregnated into this network to form a very thin, sometimes dense, layer for oxygen reduction [7, 8].

Early studies of oxygen reduction focused on noble metal cathodes and perovskites such as Ca-doped $LaMnO_3$ (LCM) which are good electronic conductors, but have little ionic conductivity. Work showed that oxygen incorporation into the electrolyte is confined to the triple phase boundary (TPB) region with little involvement of the bulk of the material [9] (schematically this is represented by the path along the surface of the cathode to the TPB region seen in Figure 1).

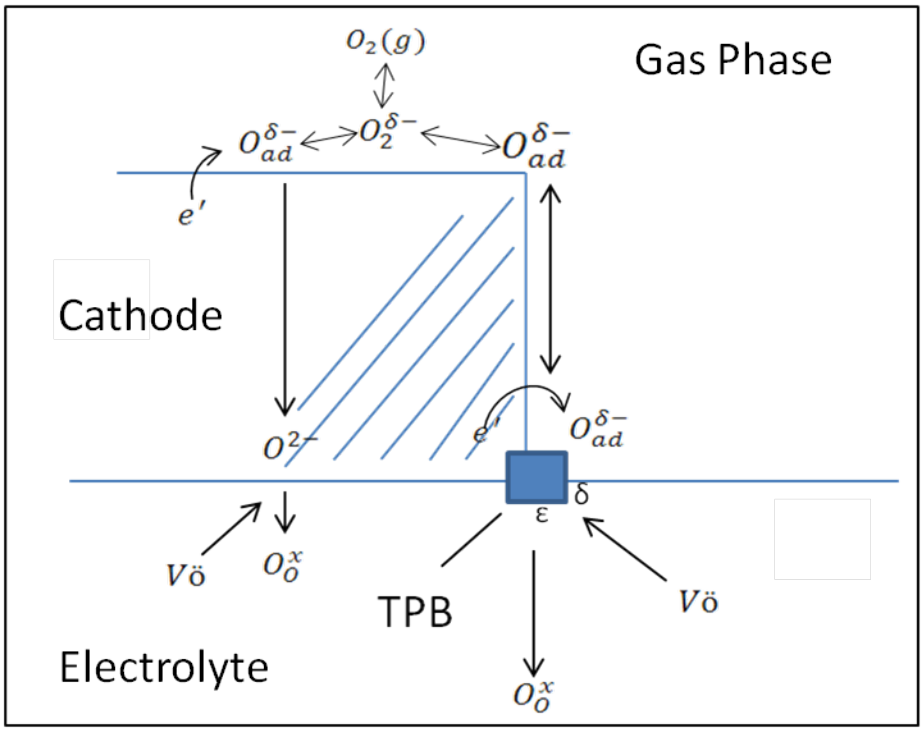


Figure 1. Schematic representation of the oxygen reduction reaction occurring at a SOFC cathode, included are both the bulk transport of oxygen ions as well as surface diffusion. Adapted from ref. [25].

The importance of a TPB region was first demonstrated in the 1920s [10], when researchers studying the oxidation of $H_2$ on Pt (in gas diffusion electrodes or GDEs) noticed that the Pt must be simultaneously exposed to both a gaseous phase and immersed in solution to achieve high reaction rates. This concept has been applied to SOFC cathodes where overall performance has been shown to scale with TPB length, thus guiding microstructure design. By the 1960s however, the limitations of the TPB concept became apparent when researchers working on GDEs tried to understand the nature of the reaction steps occurring in the vicinity of the TPB [11]. To delve deeper, these researchers broke up the half-cell reaction into a combination of multiple individual steps thought to be important to the kinetic rate of reaction such as diffusion, and oxidation of the $H_2$ at the Pt/solution interface. These studies were important since they introduced the concept of co-limitation by diffusion, which can mimic Butler-Volmer type kinetics yet is not activation limited. This insight has proved important for SOFC oxygen reduction where, in practically all cases, some co-limitation exists between diffusion and surface chemical reactions that take place away from the electrochemical two or three phase interface.

Recent work has shown that oxygen reduction generally involves not only the cathode surface but also the bulk of the material. Oxygen adsorption takes place on a surface and undergoes partial reduction via catalytic or electro-catalytic steps. At some point these ad(b)sorbed species must transport to the TPB or two phase cathode/electrolyte interface where they are fully reduced and incorporated into the electrolyte. Unfortunately, the nature and location of these steps for different

materials at different operating conditions as well as an understanding of which processes dominate the rate is generally only partially understood [4]. Further, even less is known about the kinetic constants involved in the elementary reactions. This ambiguity arises from two main areas: first, sample to sample variation is generally high and thus interpretation of experimental results is difficult; and second, the reaction mechanisms tend to be complicated and thus are rarely, if ever, dominated by a single elementary reaction [5]. Much work, both modeling and experimental, has been performed to understand this complex reaction. The next section attempts to provide the reader with a cross-section of the history of these investigations.

**Methods and Models for Understanding the ORR**

A thorough review of the oxygen reduction process was performed by Adler in 2004 [12]. Early experiments were typically conducted on Pt-YSZ systems and generally were steady-state measurements. From these measurements it was found that the i-V behavior is highly non-linear. To explain this behavior, researchers used the ideas developed for metal catalysts immersed in a liquid electrolyte, and analyzed the steady-state results by Tafel analysis, or fitting the ln (i) vs. V measurements to specific rate determining steps occurring at the interface [13]. However, as was described for the gas diffusion electrodes, often this analysis fails to account for the true rate limiting steps such as diffusion and adsorption away from the interface.

To probe deeper, the last 40 years has seen the widespread use of electrochemical impedance spectroscopy (EIS) or a.c. impedance. In this technique a sinusoidal perturbation of either voltage or current is applied across the system and the resulting sinusoidal i-V response is measured. The frequency of the response is the same as the applied frequency, but it is shifted in magnitude and phase. By applying perturbations across a range of frequencies spanning several decades (i.e., 1 MHz–1 mHz), reaction steps can be separated by timescale [14]. Much of our understanding of the ORR process comes from this technique.

Measurements by Kleitz et al. [15] demonstrated that by modeling EIS response, of noble metal catalysts in contact with YSZ electrolytes, as an RC circuit the capacitance was too high and the frequency response was seen at too low a frequency to be caused by a classical double layer. Accordingly, they hypothesized that a diffusive limitation must be present. This analysis was further refined by Van Herle and McEvoy who concluded that for silver droplets, used as electrodes, the reaction was partially limited by both surface adsorption/dissociation processes and diffusion limitations [2]. In 1987, Mizusaki et al. showed that fitting their data collected for Pt-YSZ system to Butler-Volmer kinetics leads to the wrong $pO_2$ dependence [16, 17]. They instead showed how either surface adsorption or surface diffusion could individually limit, or together limit the ORR. Yet, in either case a non-linear i-V response is seen without the necessity of charge transfer occurring at the interface. This observation was formally modeled by Robertson and Michaels who proposed that the surface is not at equilibrium with the surrounding gas phase, and there is a finite rate of diffusion to the interface. They concluded that the system is always at least partially co-limited by both of these processes [18]. A simple, yet illuminating, demonstration of this is given by Adler in ref. [4].

Subsequently, much evidence of co-limited behavior has been demonstrated and modeled in the literature since these early works. Two works of great interest in this regard are: a numerical modeling scheme developed by Mitterdorfer and Gauckler, which accounts for contributions from the electrolyte, interfacial charge transfer, surface adsorption, and diffusion processes [5]. To model these phenomena they used a state-space modeling (SSM) framework which allows linearization of time dependent equations and subsequent conversion to frequency response. The SSM technique is applicable to any electrochemical situation and will be used to examine EIS results from LCM-YSZ patterned cathodes. The second model is the Adler-Lane-Steele model (ALS), which is a 1-D model for porous mixed conducting cathodes that accounts for surface adsorption followed by bulk diffusion to the electrolyte [19]. This model predicts that the impedance response can be broken into contributions from the electrolyte resistance, electrochemical interfacial impedance, and chemical impedance caused by adsorption and diffusion limitations.

Since 2004, work has focused on models that account for the full time-dependent nature of the oxygen reduction reaction. A sophisticated numerical model was developed by Mebane et al. [20] and later extended by Lynch et al. to include surface transport [21]. This model considers that the adsorbed oxygen is charged, and therefore the rate of adsorption follows a Butler-Volmer type relationship whereby the charge at the surface dictates the rate of reaction. Also transport through the bulk of the MIEC was treated using the drift-diffusion methodology. Fleig, also using a Butler-Volmer type surface reaction, modeled simple geometric structures such as a cathode mesh, and stacked particles in three dimensions using a finite element approach to account for surface reactions followed by bulk diffusion [22]. Another time dependent model was developed to account for all the possible reaction steps occurring on the cathode side by Bidrawn et al. [7], who model the potential drops across the various components of an infiltrated electrode. Recently, the ALS model was extended to three dimensions and modified to include contributions from surface diffusion in addition to bulk diffusion [23]. This latter model has been modified later in this report to numerically simulate the EIS response of patterned cathodes of $La_{0.6}Sr_{0.4}Co_{0.2}Fe_{0.8}O_{3-\delta}$ (LSCF-6428) under a variety of operating conditions.

Any model, however, is only useful if it predicts or explains processes that actually occur in an operating device. Therefore, experimental data is necessary to measure parameters, or to compare modeling results with experimental results. For example, the ALS model requires researchers to know macrohomogeneous properties of a porous cathode such as porosity ($\varepsilon$), tortuosity ($\tau$), surface area ($a$ given as surface area/volume), while the Mitterdorfer model requires knowledge of the triple phase boundary contact length. For a porous single phase or composite cathode, these numbers are either extremely difficult to measure accurately or taken as a broad range in the model. In reaction to these geometric difficulties, over the last 10 years there has been a rise in the use of patterned cathodes. Numerous studies have been conducted in which cathodes with a well-defined geometry were fabricated [24–28]. With patterned cathodes, researchers can systematically control geometric features such as TPB length, diffusion path length (i.e., film thickness), or area. In addition, by fabricating samples with well controlled geometries, researchers gain a measure of reproducibility that has typically been difficult in the past. Thus, with better

inputs, and more reliable data, researchers are able to test their model hypotheses against measurable changes in sample geometry.

Patterned cathodes have opened another avenue of research. This involves examining the influence that surface structure and composition have on oxygen reduction kinetics. The surface is involved in many, or all, of the oxygen reduction steps such as adsorption, dissociation, surface diffusion, and incorporation into the electrolyte. Yet it is becoming apparent that the surface structure in some cases may be vastly different from the cathode bulk [29–31]. Thus, understanding the evolving nature of the surface under operating temperatures and oxygen partial pressures may prove critical to improving the overall performance of the device. Samples with a clean well-oriented surface have been grown by pulsed laser deposition (PLD) and are used for soft X-ray analysis.

There are numerous advantages to using SOFCs for electrochemical power generation, such as high theoretical efficiency, very low water use, and the production of an easy to sequester $CO_2$ stream when hydrocarbons are used as fuel. Unfortunately high stack costs, and materials processing have prevented rapid commercialization. One promising materials system—$La_{0.85}Ca_{0.15}MnO_3$ (LCM) cathode, a dense 8 mol% yttria-stabilized zirconia (YSZ) electrolyte, and a Ni/YSZ anode—has reduced costs through single step co-firing, while achieving a high power density of 1.5 W $cm^{-2}$ at 800 °C [32]. Unfortunately, this system rapidly loses power with decreasing temperature [33], which is due to cathode activation polarization [1, 34, 35]. This finding is not uncommon for SOFCs where large cathode polarization loss at low operating temperatures is seen in virtually every materials system used for SOFCs [36–40], thus it is important to understand the mechanism for the torpid cathode kinetics by developing a model to identify the rate determining steps occurring at the cathode.

The overall oxygen reduction reaction (ORR) occurring at the cathode is given by Equation (1), repeated below:

$$2e^- + \frac{1}{2}O_2 \rightarrow O^{2-} \qquad (1)$$

Polarization curves generally show Tafel behavior (i.e., linear dependence of ln[i] vs. V) [41], yet it has been fairly well established that the reaction is not simply charge transfer limited, rather a combination of elementary steps all contribute to the rate of the overall reaction [4, 16, 17]. A general scheme for the ORR is shown in Figure 1, where the cathode acts as a typical heterogeneous catalyst. Two limiting cases for the incorporation of oxygen into the electrolyte are described as the "surface path" and the "bulk path" [42]. Cathodes with high electrical conductivity but negligible oxygen permeability (e.g., Pt) are thought to exclusively follow the "surface path," while cathodes with very high bulk oxygen vacancy content (and thus high oxygen ion mobility) called mixed electronic and ionic conductors (MIECs) such as $La_{1-x}Sr_xCo_{1-y}Fe_yO_{3\pm\delta}$ (LSCF), are dominated exclusively by the "bulk path." For both limiting cases, the following steps occur in series: gas phase

diffusion of oxygen to the cathode, adsorption of the molecular oxygen onto the cathode surface. Then, the "surface path" likely involves dissociation into partially reduced atomic oxygen and surface diffusion to the triple phase boundary (TPB) where it is fully reduced and incorporated into the electrolyte [21, 43]. The "bulk path" involves dissociation into fully reduced atomic oxygen followed by incorporation of the adsorbed oxygen into the bulk of the cathode, bulk diffusion of the ionic species to the cathode/electrolyte interface, and finally incorporation of the ionic species into the bulk of the electrolyte.

The aim of this work is to establish an experimental system capable of identifying the dominant path, and, once established, extract information about the rate determining steps present in LCM and LSCF cathodes as a function of temperature and $pO_2$. We first generate patterned cathodes, through a combination of photolithography and rf-magnetron sputtering, with a constant gas exposed surface area, but a TPB that varies in length over several orders of magnitude. Since these samples have a well-defined geometry, we neglect contributions from gas phase diffusion, and eliminate uncertainties created by compositional inhomogeneities found in composite cathodes. The performance of the cathodes is probed by electrochemical impedance spectroscopy (EIS). Data were collected from half-cells by EIS with no applied DC bias over a temperature and $pO_2$ range of 600–800 °C and $10^{-3}$- 1.00 atm respectively. As mentioned previously we consider two model materials calcium-doped lanthanum manganite (LCM) and strontium-doped lanthanum iron cobalt oxide (LSCF).

## Study of Surface Pathway Using LCM

### Intrinsic Resistivity

The important parameter for oxygen reduction occurring for predominately electronic conducting cathodes is the length of the TPB line ($l_{TPB}$), which is typically reported as the length of the line per unit area of electrode/electrolyte contact and is given in units of $cm^{-1}$. Following the method developed by Radhakrishnan et al. we relate the area specific polarization resistance occurring at the TPB as [26, 44]:

$$R_p^{TPB} = \frac{\rho_p}{l_{TPB}} \tag{2}$$

Where $\rho_p$ is the intrinsic polarization resistivity (Ω-cm) taking into account that the TPB is not a point but has a thickness, δ, and width, ε, see Figure 1, through which incorporation occurs. However, δ, and ε are not amenable to measurement, and thus are lumped into the intrinsic resistivity. The fabrication processes is likely to create extra triple phase boundary due to the presence of imperfections such as pores and defects. These imperfections lead to an increase in the available TPB length beyond the value measured from the pattern. Additionally, while the

fabrication produces high quality samples, microscopically there may be a certain amount of line waviness formed during the annealing of the samples. Thus, the $l_{TPB}$ in Equation (2) is defined as:

$$l_{TPB} = l_{TPB_p}(1+\alpha) + l_{TPB_o} \quad (3)$$

Where $l_{TPB_p}$ is the measured TPB length from the pattern, α is line waviness (as a fraction of actual to nominal $l_{TPBp}$), and $l_{TPB_o}$ is the additional TPB length introduced from defects and pores (depicted schematically in Figure 2). Microscopically the edges appeared to be straight, so α was considered to be ≈0. The number of defects such as pitting and cracking is expected to be roughly constant from one sample to the next, so it is assumed that $l_{TPB_o}$ is roughly constant between samples and can be estimated using quantitative stereology techniques.

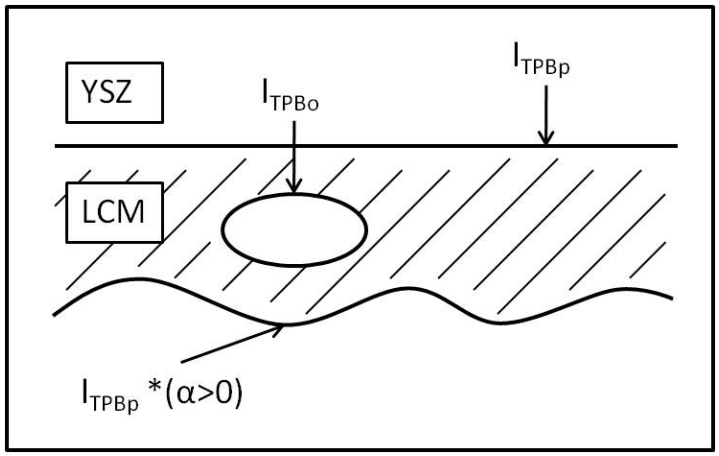


Figure 2. Schematic of Equation (3) showing the increase in the native TPB length ($l_{TPBp}$) due to pores in the film ($l_{TPBo}$) and line waviness (α>0) created during deposition. However, even microscopically, the lines in our films appeared straight and thus α ≈ 0.

Oxygen reduction occurring near the two possible TPB locations ($l_{TPB_p}$ and $l_{TPB_o}$), are expected to occur in parallel. We also leave open the possibility for some parallel transport of oxygen through the bulk, despite the low ionic conductivity of LCM. Taking all of the preceding transport paths into account, Equation (4) relates these parallel processes:

$$\frac{1}{R_p} = \frac{1}{R_p^{TPB}} + \frac{A_A}{R_p^{MIEC}} = \frac{l_{TPB_p}}{\rho_p} + \frac{l_{TPB_o}}{\rho_p} + \frac{A_A}{R_p^{MIEC}} \quad (4)$$

Where $R_p$ is the total area-specific polarization resistance (Ω-cm$^2$), $A_A$ is the area fraction of the LCM electrode (LCM gas exposed area/counter electrode area), and, $R_p^{MIEC}$ (Ω-cm$^2$), is the area-specific polarization resistance associated with oxygen transport and incorporation through the bulk of the cathode. The bulk path resistance scales with the inverse of the contact area between cathode/electrolyte [45], and since the contact area and material is the same for all samples, $R_p^{MIEC}$, is expected to be constant for all samples.

With patterned cathodes we can determine several important characteristics about the ORR in LCM. By plotting $1/R_p$ vs. $l_{TPB_p}$ at various temperatures and $pO_2$ we can determine the microstructure independent resistivity, $\rho_p$, which allows us to compare various cathode materials. Also, from Equation (4), we see that the intercept is expected to be non-zero if a) there is a contribution from the oxygen reduction occurring at $l_{TPB_o}$, b) there is reduction occurring through the bulk, or c) some combination of both. In principle, because $l_{TPB_o}$ can be measured from quantitative stereology techniques, the bulk contribution, $R_p^{MIEC}$, can also be estimated.

In the limiting case where adsorption is fast such that surface coverage is equilibrated, then the partial pressure dependence of the intrinsic polarization resistivity, $\rho_p$, may be given as:

$$\rho_p = \frac{\rho_p^{''}}{\theta} \quad (5)$$

Where $\rho_p^{''}$ is the intrinsic resistivity corresponding to θ=1, and is assumed to be constant within the measured $pO_2$ range. θ is the surface coverage of oxygen as a function of $pO_2$. According to refs. [26, 44], we can determine the partial pressure dependence of the surface coverage from the Langmuir isotherm model. Depending on whether adsorption is associative or dissociative, the Langmuir equation is given as:

Associative Adsorption: $$\theta_{O_2} = \frac{b' p_{O_2}}{1 + b' p_{O_2} + b'' p_{N_2}} \quad (6)$$

Dissociative Adsorption: $$\theta_{O} = \frac{b^* \sqrt{p_{O_2}}}{1 + b^* \sqrt{p_{O_2}} + b^{**} \sqrt{p}_{N_2}} \quad (7)$$

However, nitrogen adsorption is not expected to play a role in the oxygen reduction reaction, so we neglect its contribution. By substituting Equations (6) and (7) into Equation (5) and simplifying, we arrive at expressions for $\rho_p$ in terms of the partial pressure dependence of oxygen:

Associative Adsorption: $$\rho_p = \frac{\rho_p''}{b' p_{O_2}} + \rho_p'' \quad (8)$$

Dissociative Adsorption: $$\rho_p = \frac{\rho_p''}{b' \sqrt{p}_{O_2}} + \rho_p'' \quad (9)$$

Therefore if the polarization resistivity is determined by the surface coverage (i.e., other electrode properties remain constant over the $p_{O_2}$ range), then a plot of $\rho_p$ vs. $(p_{O_2})^{-1}$ should be linear for the associative adsorption model, whereas $\rho_p$ vs. $(p_{O_2})^{-1/2}$ should be linear for the dissociative adsorption model. A more rigorous analysis would consider the change in conductivity and the resulting change in electro-catalytic activity of the LCM as a function of $pO_2$. Thus, the present analysis is simply a first order approximation.

**EIS Measurements on Patterned LCM on YSZ**

To fabricate the patterned cathodes of LCM on YSZ, a combination of photolithography and rf-magnetron sputtering techniques were used as described elsewhere. Samples were fabricated with different TPB lengths, but with the same cathode/electrolyte contact area and electrode thickness. An SEM image of the patterned cathode is shown in Figure 3.

Table I shows the polarization resistivity data for the different temperatures and $pO_2$ examined.

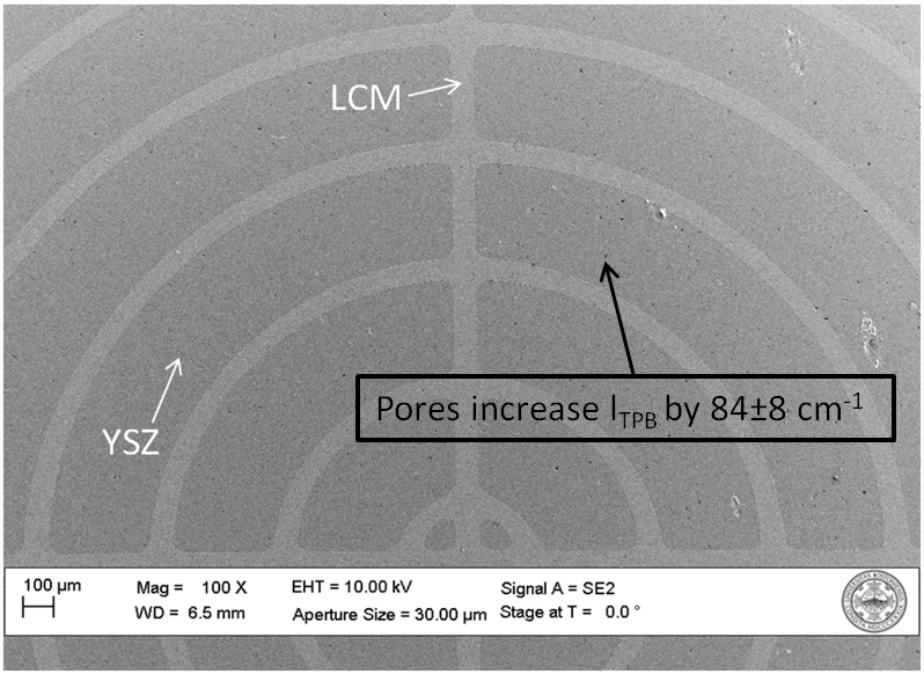


Figure 3. SEM showing clear pattern of LCM cathode (light) on the YSZ substrate (dark). Porosity was measured as $l_{TPB_0} = 84 \pm 8\ \mathrm{cm}^{-1}$.

Polarization resistances are plotted as inverse polarization resistances as a function of TPB length in Figure 4.

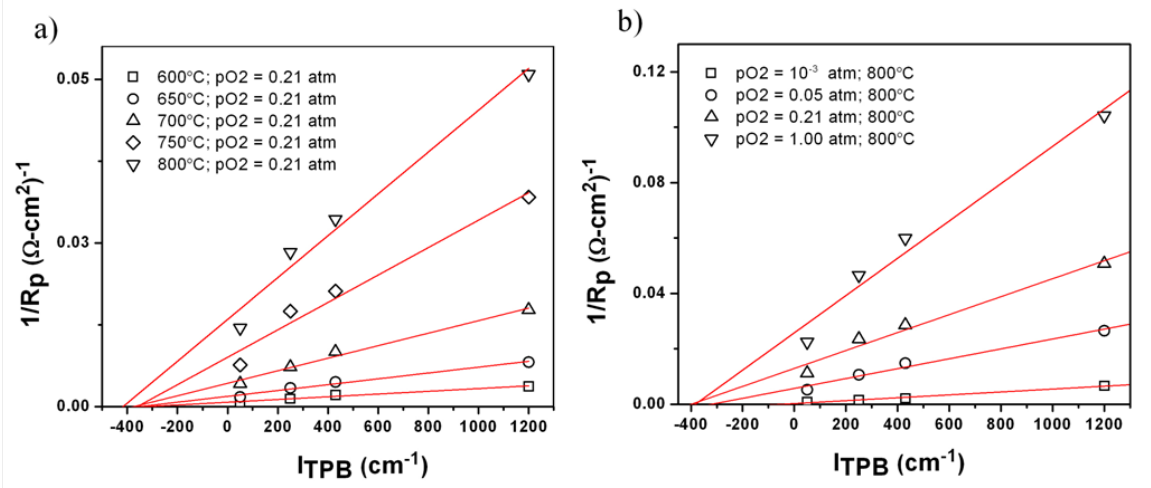


Figure 4. Plots of $1/R_p$ vs. $l_{TPB}$. (a) is plotted at various temperatures in air. (b) is plotted at various $pO_2$ at 800 °C.

Plots of $1/R_p$ vs. $l_{TPBp}$ are given at different temperatures in Figure 4a, and at different $pO_2$ in Figure 4b. The slope of the linear interpolations gives the value of the area specific intrinsic resistivity, $\rho_p$, as seen in Equation (4).

It is seen in Figure 4 that the lines do not pass through the origin, from Equation (4), this implies that there is oxygen reduction occurring not only through the patterned TPB length, $l_{TPB_p}$, but also through either, or both, the increased TPB length from porosity, $l_{TPB_o}$, and from bulk path contributions. With Equation (4) and the estimate of $l_{TPBo}$, from quantitative stereology, the area specific resistance through the bulk path, $R_p^{MIEC}$, is estimated. From these results, and Equation (2), the area specific resistance occurring at the TPB or, $R_p^{TPB}$, can be estimated. The results for the 1200 $cm^{-1}$ in air at different temperatures are presented in Table 1. The significant result from the findings in Table 1 is that the bulk transport path has about a fourfold greater resistance than the TPB path and thus most reduction is expected to occur at the TPB.

To determine whether the adsorption of oxygen occurs via dissociative or associative adsorption, we generated plots of $\rho_p$ vs. $p_{O_2}^{-1}$ and $p_{O_2}^{-1/2}$ as seen in Figures 5a and 5b respectively. The linear interpolation of the dissociative adsorption model (Figure 5b) is in much better agreement with the data, suggesting that the dissociative model is more appropriate. This result agrees with the findings for the similar LSM/YSZ system [26]. It bears repeating, however, that EIS does not directly measure the rates of the adsorption process, instead it is an experimental manifestation of all the processes occurring at the cathode, and thus it is difficult to determine exact mechanisms from the impedance spectra alone.

Table 1. The $\rho_p$ (Ω-cm) calculated from the slopes in Figure 4 at different T, and $pO_2$.

| T °C | 1.00 atm | 0.21 atm | 0.05 atm | 0.001 atm |
|---|---|---|---|---|
| 800 | 14,900 | 31,300 | 56,100 | 191,000 |
| 750 | 27,300 | 47,700 | 97,500 | 413,000 |
| 700 | 52,100 | 105,000 | 169,000 | 846,000 |
| 650 | 103,000 | 224,000 | 373,000 | 1,590,000 |
| 600 | 207,000 | 480,000 | 809,000 | 3,180,000 |

Table 2. The contributions of the various polarizations found in Equation (4), at 800 °C in air for the 1200 $cm^{-1}$.

| T °C | $R_p$ | $R_p^{(TPB)}$ | $R_p^{(miec)}$ |
|---|---|---|---|
| 800 | 15 | 19 | 74 |
| 750 | 25 | 30 | 121 |
| 700 | 53 | 62 | 285 |
| 650 | 116 | 134 | 662 |
| 600 | 253 | 290 | 1,597 |

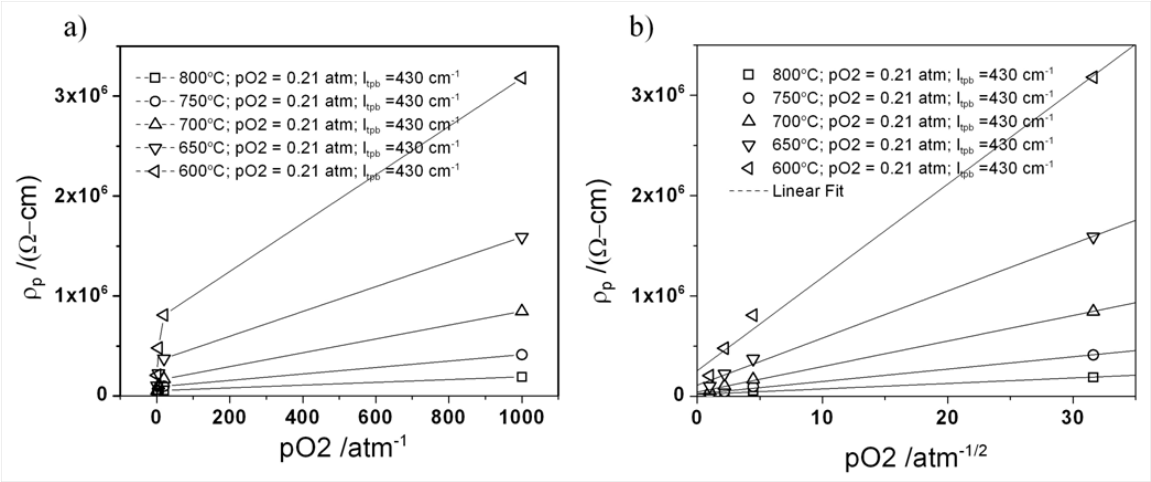


Figure 5. Equations (8) and (9) predict a linear relationship with the correct isotherm. (a) $\rho_p$ plotted vs. $pO_2^{-1}$ does not show a linear fit; the connected lines just connect the data points for reference. (b) on the other hand, the plot of $\rho_p$ vs. $pO_2^{-1/2}$ is linear, which suggests that oxygen adsorbs dissociatively on the cathode surface; the lines are a linear fit to the data.

From the impedance measurements and their fit to a straightforward model it is clear that:

1) Surface diffusion and incorporation at the TPBs are the dominant pathways for oxygen reduction in LCM.

2) Dissociative adsorption is dominant.

In the next section we provide a methodology to determine the thermodynamic and kinetic parameters associated with oxygen reduction in LCM by the application of a state space model.

**State Space Model**

To interpret the results, researchers tend to fit the resulting data by combining circuit elements as proxies for elementary reaction steps until the resulting spectra show excellent registry with the experimental measurements. Unfortunately, close fits do not mean that the chosen elements are unique, and different choices of circuits lead to different mechanistic interpretations. In response to this ambiguity, researchers have developed kinetic models built from elementary reactions to interpret the current-voltage response of the system [1, 16, 17, 20, 21, 49–52]. The analytical models require assumptions about which steps are rate-limiting, and thus restrict the model usefulness to certain experimental regions. On the other hand more sophisticated models require substantial computational effort, and often do not directly lend themselves to parameter estimation. The state-space modeling (SSM) technique is intermediate between these two extremes where a relatively simple mechanistic interpretation of the oxygen reduction reaction allows for estimation of fundamental parameters of interest. Additionally, since the SSM technique arrives at a numerical solution by approximating the solution to a system of linear differential equations, it is not necessary to constrain the mechanism to different rate-limiting steps [53]. The SSM then allows researchers to determine both the steady-state and frequency response in a straightforward manner with relatively minimal computational requirements. The SSM technique was first applied for cathode/electrolyte systems by Mitterdorfer et al. [5, 51, 52] and then later extended to anode/electrolyte systems by Bieberle et al. [54].

The advantage of the SSM technique arises from the ability of the researcher to build an impedance spectrum from proposed fundamental kinetic equations and their dependence on experimental conditions such as temperature and partial pressure of oxygen, not from ambiguous combinations of circuit elements. Then, if the model is appropriate, the researcher can tune the fundamental kinetic parameters in order to match the simulated spectra with the experimental spectra. This procedure was demonstrated by Mitterdorfer et al. who estimated fundamental kinetic parameters for oxygen reduction occurring at the Pt/YSZ interface using their M2 model, which accounts for dissociative adsorption of oxygen onto the surface of the electrode, and surface diffusion of the oxygen to the TPB region where reduction and incorporation into the electrolyte occurs [51,52].

For cathodes with poor ionic conductivity, the ORR is thought to occur via the “surface path” in which all charge transfer and incorporation occurs at the TPB, and not the electrode/electrolyte two phase interface [43]. This assumption appears appropriate for the alkaline earth doped $LaMnO_3$ perovskites, since previous work on patterned samples of Sr and Ca doped $LaMnO_3$ has shown that with no applied DC bias, the total polarization resistance is inversely proportional to the TPB length [26,55]. This suggests that similar to Pt, the TPB is the main site for oxygen reduction. The elementary reactions, the adsorption sites, and the nature of the adsorbed species are likely different for perovskites and Pt cathodes, but as a first approximation the M2 model is sufficiently general enough to encapsulate these differences. Thus, this work uses a modified M2 model to

estimate relevant kinetic parameters by analysis of our EIS results from patterned cathodes with composition $(La_{0.87}Ca_{0.13})_{0.95}MnO_3$ (LCM). Data were collected from samples having well-defined geometry spanning a total TPB length range of 3.6 to 12 m, and temperature and $pO_2$ ranges from 600–800 °C and $10^{-3}$–1 atm, respectively. The practicality of using this model, and trends in the resultant data are explored. In our model we use a constant phase element (CPE) instead of a pure capacitor to describe the electrical double layer, as was done by Ricciardi et al. on porous Pt electrodes [47]. A second difference is our modification of the surface potential to account for the charge present on the adsorbed oxygen layer. This work constitutes the first known application of a state-space model to describe the ORR occurring at perovskite cathodes and checks the validity of the model across a wide range of temperatures and TPB lengths. The experimental methods were described earlier, so we will jump right into the state space model here.

**State Space Modeling Methodology**

The state-space modeling technique is ideally suited to the purpose of modeling the ORR since the fundamental kinetic relationships can be used to build a simulated impedance spectrum. The SSM technique involves defining state equations as a linear system of differential equations and their dependence on a set of inputs, and also defining the resulting outputs as a function of the inputs and state equations. This is a common technique in control systems and can be written compactly as (more details can be found in numerous control theory textbooks, i.e., ref. [53]):

$$\dot{\boldsymbol{x}} = \boldsymbol{A}\boldsymbol{x}(t) + \boldsymbol{B}\boldsymbol{u}(t) \tag{10}$$

$$\boldsymbol{y}(t) = \boldsymbol{C}\boldsymbol{x}(t) + \boldsymbol{D}\boldsymbol{u}(t) \tag{11}$$

Where $\mathbf{x}(t)$ is the set of state equations, $\mathbf{u}(t)$ is the set of inputs, $\mathbf{y}(t)$ is the set of outputs, and the matrices **A**, **B**, **C**, and **D** are the system matrices. Although SSM can be applied to systems with multiple inputs and multiple outputs (MIMO), classical EIS is a single input single output (SISO) system with applied potential as the input ($u(t) = \eta(t)$) and the output is the Faradaic current ($y(t) = I_F(t)$). A Laplace transform converts the system into the frequency domain (i.e., $I_F(s) = I_F(j\omega)$) and for SISO systems, a simple analytical solution converts the state-space matrices to a transfer function (G(s)):

$$G(s) = C(sI - A)^{-1} \cdot B + D \equiv \frac{I_F(s)}{\eta(s)} = Y_F(s) \tag{12}$$

Where **I** is the identity matrix and $Y_F$ is the Faradaic admittance in the frequency domain. With the application of a sinusoidal input overpotential ($\eta(t) = \tilde{n} \sin(\omega t)$ ) and the governing state equations, an impedance spectrum results by recognizing that $Z_F = 1/Y_F$.

Our goal is to compare simulation results with the measured experimental results. In order to do this we must account for all the processes which contribute to the total measured impedance, Z. The time dependent equations and the overpotential in Equation (12), gives rise to the resulting Faradaic current, or Faradaic impedance. The total impedance, Z, contains other factors such as the electrolyte resistance, Re, and the lead wire inductance, L. The former is measured from experimental EIS by measuring the value of the high frequency intercept on the real axis of a Nyquist plot. The lead wire inductance is known to emerge at high frequencies, so we restrict our attention to frequencies below 25 kHz. A third feature is the double layer capacitance. In principle for ionic solids this double layer usually arises as an inner layer capacitance at the interface between the electrically conductive cathode and the electron blocking electrolyte. The applied AC signal causes charge/discharge cycles and thus the electrical double layer is present as a capacitive effect on the total impedance. If the electrical double layer is a pure capacitance, the total impedance is a slightly depressed semi-circle, but experimental results usually have a great deal of suppression. Thus, researchers tend to use a constant phase element instead which is described by the equation [56]:

$$Z_{CPE} = \frac{1}{Q^{\circ}(j\omega)^n} \tag{13}$$

Where $Q^{\circ}$ is the value of the admittance at $\omega = 1$ rad $s^{-1}$ and n is a value between 0 and 1, which shifts the phase angle from ideality as $-(90*n)^{\circ}$. The relationship between the electrolyte resistance, lead wire inductance, double layer constant phase element, and the Faradaic impedance is shown as a general equivalent circuit in Figure 6. We will now establish the SSM representation which describes the Faradaic Impedance.

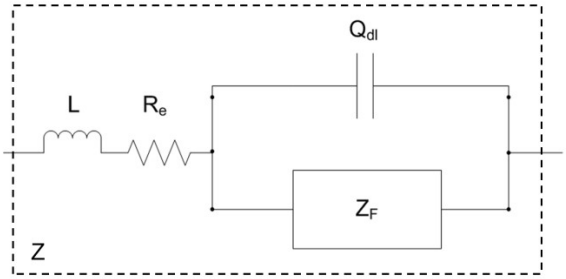


Figure 6. The "generalized equivalent circuit" considered in this work. The SSM model simulates $Z_F$, the Faradaic Impedance, while the measured impedance, Z, includes an electrical double layer constant phase element, $Q_{dl}$, an uncompensated electrolyte resistance, $R_e$, and lead wire inductance, L.

The kinetics of the ORR are described by the following three equations:

Dissociative Adsorption: $$O_2 + 2s \underset{k_{des}}{\overset{k_{ad}}{\rightleftharpoons}} 2O_{ad} \quad (14)$$

Surface Diffusion (Fick's Second Law): $$\frac{d[O_{ad}]}{dt} = D_s \frac{d^2[O_{ad}]}{dz^2} \quad (15)$$

Reduction/Incorporation into Electrolyte (at the TPB): $$O_{ad} + V_{\ddot{o}}(YSZ) \underset{k_{-1}}{\overset{k_1}{\rightarrow}} O_O^x(YSZ) + s + 2h(LCM) \quad (16)$$

Where $O_{ad}$ is an adsorbed oxygen specie, s is a surface site available for adsorption, $D_s$ is the surface diffusivity, $V_{\ddot{o}}$(YSZ) and $O_O^x$(YSZ) are oxygen vacancies and bulk lattice oxygen in the YSZ electrolyte respectively, and h(LCM) are holes in the LCM cathode. Finally, $k_{ad}$, $k_{des}$, $k_1$, and $k_{-1}$ are reaction rate constants associated with the adsorption and incorporation reactions respectively.

Using the 1-D finite difference scheme, described by Mitterdorfer et al., the mass and charge balances of the SSM model are given by [52] (a schematic of the simulation region is shown in Figure 7):

Final Block (ω):

$$\frac{d\theta_{\omega}}{dt} = 2k_{ad}p_{O_2}\Gamma(1-\theta_{\omega})^2 - 2k_{des}\Gamma\theta_{\omega}^{\ 2} + \frac{1}{T_{\omega}}\left(\frac{q\theta_{\omega-1}}{1+q} - \frac{(2q+1)}{1+q}\right) \quad (17)$$

Block i:

$$\frac{d\theta_{i}}{dt} = 2k_{ad}p_{O_2}\Gamma(1-\theta_{i})^2 - 2k_{des}\Gamma\theta_{i}^{\ 2} + \frac{1}{T_{i}}\left(\frac{\theta_{i-1}}{1+q} - \theta_{i} + \frac{\theta_{i+1}}{1+q}\right) \quad (18)$$

TPB Block (1):

$$\frac{d\theta_{1}}{dt} = 2k_{ad}p_{O_2}\Gamma(1-\theta_{1})^2 - 2k_{des}\Gamma\theta_{1}^{\ 2} - k_f\theta_1 + k_b(1-\theta_1) + \frac{1}{T_1} \quad (19)$$

Charge Balance:

$$I_F = 2Fl_{TPB}\cdot w_{TPB}[k_b(1-\theta) - k_f\theta] \quad (20)$$

Where, the time dependent equations have been normalized to surface coverage by $[O_{ad}] = \theta\Gamma$, and $s = (1-\theta)\Gamma$ where Γ is the total sites available for adsorption. The rest of the symbols are: $T_i = \Delta z_i^2/2D_s$ with $\Delta zi^2$ the width of compartment i, F is Faraday's constant, $l_{TPB}$ is the TPB length (m), $w_{TPB}$ is the width of the TPB compartment (m), $k_f = k_1\cdot[V_{ö}(YSZ)]$, and $k_b = k_{-1}\cdot[O_O^x(YSZ)]$. The q in the denominator is a geometric factor that increases the compartment width away from the TPB compartment up to the length 6δ (δ is the penetration depth described in the next paragraph).

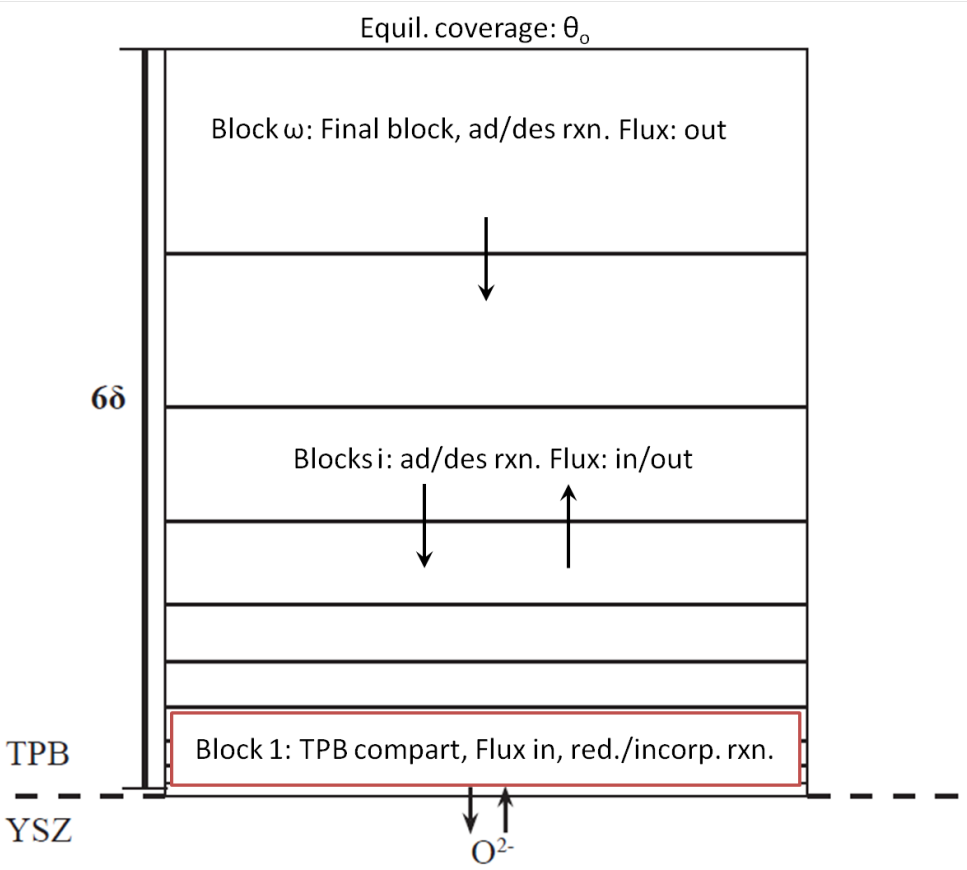


Figure 7. The complete 1-D discretized surface. 10 blocks are formed that expand in size away from the TPB. Adsorption/desorption of oxygen occur in parallel to surface diffusion. Incorporation occurs only in the TPB compartment. Beyond 6δ the adsorbate concentration is uniform set by the adsorption/desorption reaction. See text for explanation of δ.

The boundary and initial conditions are constant surface coverage sufficiently far from the interface determined by the adsorption/desorption reaction. The distance to which the surface is discretized is given by the Nernst diffusion layer thickness, or penetration depth, δ. This implies that beyond a certain distance the concentration is unaffected by the perturbations at the interface. To ensure that we discretize sufficiently far from the interface, our simulation region extends 6δ (see Figure 7) where delta is determined from the summit frequency, $\omega_{max}$, of the experimental impedance by $2\pi^{-1/2} = \delta(\omega_{max}/2D)^{-1/2}$ where D is the diffusivity [5]; this treatment allows the use of a Dirichlet boundary condition. The surface concentration at the TPB is determined by the flux into the compartment from the compartment above it, and by the rate of reduction/incorporation.

Before the application of a current, the surface coverage is considered uniform, governed by adsorption/desorption kinetics considered to occur via the Langmuir Isotherm. The $pO_2$ dependence is explicitly given in the adsorption reaction, whereas the temperature and overpotential dependencies are built into the rate constants. $D_s$, $k_{ad}$, and $k_{des}$, are considered to be

independent of overpotential and have no *a priori* known surface coverage dependence but have an exponential dependence with temperature of the form:

$$\xi = \xi^{o} \exp\left(\frac{-E_a}{RT}\right) \tag{21}$$

Where R is the gas constant, $\xi^0$ is a temperature independent pre-exponential term and $E_a$ is the temperature independent activation energy given in kJ mol$^{-1}$. The other rate constants: $k_1$ and $k_{-1}$ have an exponential temperature dependence of the form above, but also depend on overpotential:

$$k_1 = k_1^{o} \exp\left(\frac{-E_1}{RT}\right) \exp\left(-\frac{\beta F}{RT}(\Delta\chi)\right) \tag{22}$$

$$k_{-1} = k_{-1}^{o} \exp\left(\frac{-E_{-1}}{RT}\right) \exp\left(\frac{(1-\beta)F}{RT}(\Delta\chi)\right) \tag{23}$$

Where $\Delta\chi = \chi - \chi^{eq}$ is the change in surface potential away from its equilibrium value [49], $E_1$ and $E_{-1}$ are the activation energy of the forward and backward rate constants respectively, and β is the transfer coefficient. Finally, it is possible to express $k_{-1}^{o}$ in terms of $k_1^{o}$ since $I_F(\chi^{eq}) = 0$, and with the assumed dissociative Langmuir adsorption model:

$$k_{-1} = k_1^{o}\left(\frac{[V_o(YSZ)]}{[O_O^{x}(YSZ)]}\right)\sqrt{k_{ad}/k_{des}} \tag{24}$$

In applying this model to LCM, several assumptions are called into question. First is the use of a 1-D surface model to describe the ORR. It is known that in good mixed ionic and electronic conducting cathodes, or in very thin films of electronically conducting perovskites below a critical thickness, oxygen ion diffusion through the bulk of the cathode dominates the reaction rate [4, 25, 48]. Yet, previous work on patterned cathodes of LSM and LCM of 0.5 μm thickness has demonstrated that the total polarization resistance is inversely proportional to the TPB length. This serves as our primary justification for use of a "surface path" only model [26,55]. The second assumption is the use of a dissociative Langmuir adsorption model, rather than a more complex multi-step formulation. In work on patterned cathodes of LSM/YSZ, Radhakrishnan et al. showed that this model adequately described the $pO_2$ dependence of the total polarization resistance [26]. Furthermore, since the SSM model does not explicitly assume the dependence of the rate constants on surface coverage, a more complex model does not appear necessary. Finally, we have used the approach of Fleig [49] in our treatment of the potential driving force for the reduction and incorporation reaction occurring at the TPB. Since adsorbed oxygen localizes an electron to the surface, which is screened by electron holes, a surface dipole is formed. This will, by Poisson's equation, cause the surface to change potential relative to the bulk in a concentration dependent manner. The result is that the potential applied to the working electrode (during a.c. impedance spectroscopy) is not the same as that experienced by the surface. To account for this effect, we use the model derived by Fleig, which assumes that charge transfer to an adsorbed $O_{ad}$ atom at the gas/solid interface is rate limiting. If the subsequent elementary steps are near equilibrium, and ion conduction in the electrolyte is fast, the surface potential step is related to surface coverage and the applied potential by Equation (25) [49]:

$$\Delta\chi = 2\eta - \frac{RT}{F}\ln\left(\frac{\theta}{1-\theta}\frac{1-\theta_o}{\theta_o}\right) \tag{25}$$

Where η is the overpotential applied to the cathode/electrolyte interface, θ is the surface coverage, and $\theta_o$ is the equilibrium surface coverage.

**State Space Modeling: Results and Discussion**

Some of the technical aspects of the state space model will not be described in detail here. Only the results of the calculations are presented here. For the technical details, the reader is referred to our JECS publication.

The $pO_2$ dependence of p = [$k_{ad}(\theta)$, $k_{des}(\theta)$, and $D_s(\theta)$] at 700 °C, for various TPB lengths, is seen in Figure 8. The equilibrium surface coverage ranges from 1–50% over the measured $pO_2$ range (Figure 8a plots equilibrium surface coverage). While adsorption enthalpies determined from simulations based on DFT calculations [57, 58] show the surface coverage limited to a few percent, accurate experimental measurements of surface coverage at elevated temperatures and pressures were not found after a literature search. For LCM, surface $Mn^{4+}$ sites are considered to be the

likeliest adsorption sites since the net positive charge acts to compensate any negative charge associated with the adsorbed oxygen.

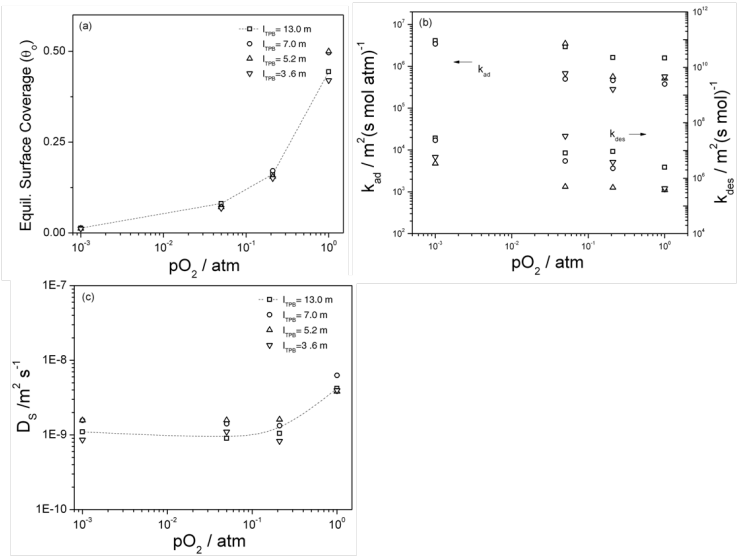


Figure 8. T = 700 °C, TPB length listed in the legend. (a) The surface coverage plotted vs. $pO_2$. (b) The surface coverage dependence of the model parameters $k_{ad}$ (upper cluster—left axis) and $k_{des}$ (lower cluster—right axis) and are shown vs. the surface coverage. (c) $D_S$ vs. surface coverage.

Supporting evidence for this plausible mechanism comes from ex situ XAS and XES measurements performed in our group that point towards an increase in the surface concentration of $Mn^{4+}$ [31] on films annealed in air and quenched. This would provide additional sites for adsorption and would tend to increase surface coverage above what would be predicted from a continuation of the bulk material to the surface. The $pO_2$ dependence of $k_{ad}$ and $k_{des}$ are shown in Figure 8b. The rate constants of adsorption and desorption decrease slightly with increasing $pO_2$ (i.e., surface coverage). This may be evidence of a more complex mechanism such as a precursor mediated dissociation step, but the decrease is slight. Employing a more complicated reaction scheme in our model would introduce more unknown variables without uniquely identifying the complex nature of the reaction.

The surface diffusivity, $D_S$, dependence on $pO_2$ is seen in Figure 8c. The dependence is slight at low coverage, and then appears to increase at the highest coverage. This is possibly due to repulsive interactions between adatoms related to the thermodynamic factor given by [59]:

$$\Gamma = \left[\frac{1}{2k_B T}\frac{\partial(\mu_{O2})}{\partial \ln \theta}\right]_T = \left(\frac{1}{2}\frac{\partial \ln P_{O2}}{\partial \ln \theta}\right)_T \qquad (26)$$

The characteristic utilization length, $l_\delta \propto \sqrt{D_s/k}$, defined as the length of the active electrode away from the TPB was determined through use of equation (2) (ref. [4]) for the various temperatures and $pO_2$ measured. The values ranged from 0.4–13 μm depending on T and $pO_2$ (the lowest T and $pO_2$ have the shortest length since $D_s$ has a stronger T dependence), and had a value of 2.5 μm at 700 °C in air. This is about an order of magnitude greater than was estimated for Pt [4], and represents a significant extension of the utilization region away from the TPB, yet not substantial enough to activate the whole surface, thus the Dirichlet boundary condition assumption remains valid.

Figure 9 shows the surface diffusivity and adsorption and desorption coefficients as a function of temperature. From Figure 9, $D_s$ shows an exponential temperature dependence, consistent with theory, with an apparent activation energy of 248 kJ mol$^{-1}$. As seen in Figure 9, $D_S$ shows a high sensitivity, and since there is very little scatter between samples and a clear Arrhenius activation energy, the model appears to estimate the surface diffusivity with a high degree of accuracy. From Figure 9a the activation energy of $k_{des}$ is $E_{des}$ = 121 kJ mol$^{-1}$. The apparent activation energy for $k_{ad}$ is 24 kJ mol$^{-1}$. The value of $E_{adsorption} = E_{ad} - E_{des}$ is roughly constant with $pO_2$ with an average value of -83 kJ mol$^{-1}$.

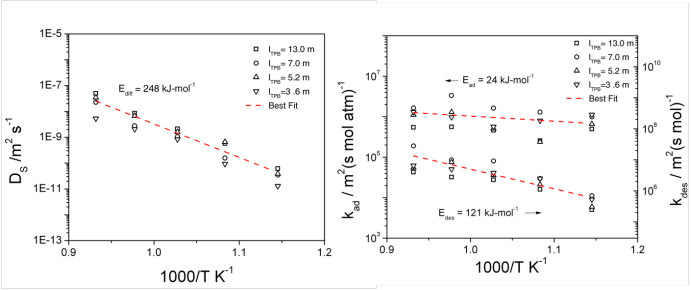


Figure 9. Parameter estimation results from the fits seen in Figure 7. The activation energies were calculated as (a) kad = 24 KJ mol-1 and kdes = 121 KJ mol-1; (b) DS = 248 KJ mol-1.

**Towards a Reaction Mechanism for LCM**

It is possible using the SSM model described above to separate the measured total polarization resistance ($R_p$), into one associated with charge transfer ($R_t$) and one associated with adsorption/desorption and diffusion ($R_c$) processes. Figure 10 shows the $R_p$ deconvoluted in this manner. In fact, the $R_c$ can once again be deconvoluted into adsorption/desorption and diffusion processes, but we shall not discuss the details here. Additional technical details about these issues can be found in our JECS paper and we present only the important results here.

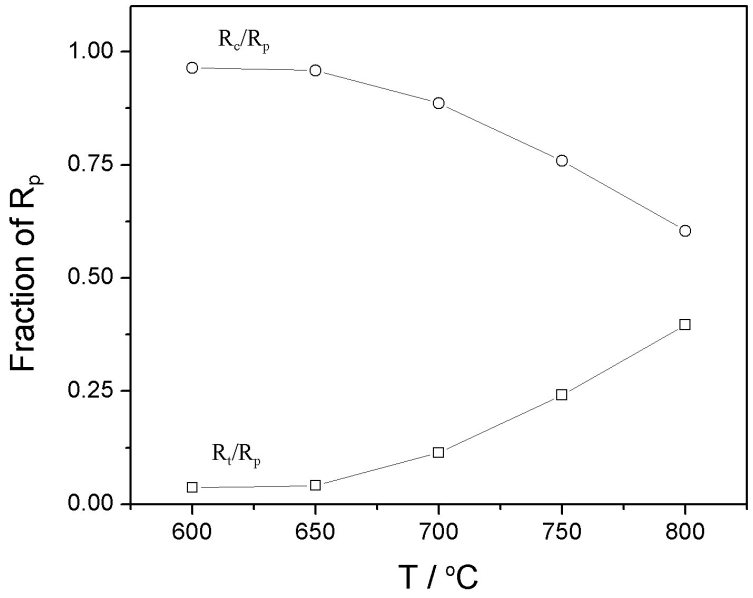


Figure 10. The fraction of the total Faradaic polarization resistance, $R_p$, accounted for by either the charge transfer resistance, $R_t$, or the concentration resistance, $R_c$.

It is seen that at lower temperatures, more of the total polarization is associated with adsorption/desorption and diffusion processes and that as the temperature increases the contributions are comparable.

## Study of Bulk Pathway Using LSCF

### Theoretical Results

The experimental details of fabricating patterned LSCF electrodes will be described shortly. A schematic of the patterned electrode is shown in Figure 11. In these experiments, the TPB length has been maintained constant, and the gas exposed area of the cathode has been varied systematically. To accomplish this, more concentric circles are added, but the annular line width is decreased (i.e., 2W in the 2-D cutout of Figure 11). The films have a constant height (H~500 nm) and a total surface area of 0.8 cm. The model geometry is a cross-section taken through a given circle, as seen in the lower portion of Figure 11, whose total width is given by the patterned line width, 2W, and height, H, is the film thickness. Further, the reaction is expected to be symmetric about the center of the film (the dashed line in Figure 11).

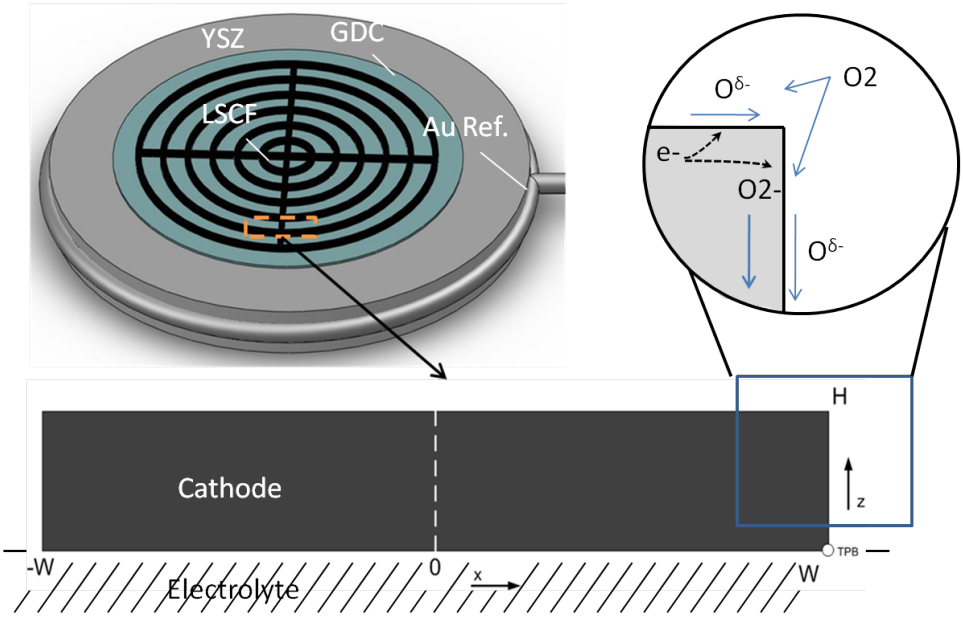


Figure 11. The full patterned cathode is seen in the top left image where the YSZ electrolyte has a sputtered GDC barrier layer (blue) and is then coated with an LSCF-6428 pattern. The 2-D cross-section is shown where the characteristic length W is half the line width. The ORR takes place along the entire surface with incorporation into the electrolyte through the bulk or at the TPB.

The model assumptions are the same as those proposed by Lu et al. [23]. They are summarized as follows: LSCF-6428 is considered to have a uniform electrochemical potential of electrons since LSCF-6428 has high electron mobility, and we maintain adequate current collection from the entire pattern. There is sufficient open space surrounding the entire pattern so no gas phase $pO_2$ gradient develops. Oxygen exchange with the surface is treated with a generalized rate expression driven by changes in oxygen chemical potential of the cathode away from equilibrium with the gas phase, yet this remains close to equilibrium and can be described by the exchange rate, $R_0$. Bulk diffusion is treated by vacancy diffusion, and surface diffusion is treated by assuming equilibrium with the local bulk phase, such that ion exchange between the surface of the cathode and cathode bulk is considered equilibrated. Finally, electrolyte resistance and lead wire inductance are subtracted directly from the experimental EIS results.

Our model deviates from the original model by Lu et al. since: 1) our geometry is rectangular, as opposed to cylindrical, and thus we recast the equations into two Cartesian coordinates, and 2) we have thin films, so our utilization region (active electrode region) likely extends all the way to the top surface of our films [19, 60]. This means we cannot treat our film using an infinite thickness approximation, so the entire surface of the film is allowed to be affected by the perturbation at the electrolyte/cathode interface. The consequence is that oxygen exchange and surface transport are treated along both the surface perpendicular to the electrolyte interface and the surface parallel to the interface at a distance, H, away from the interface. Unfortunately, this requirement adds considerable complexity to the analytical solution. Accordingly, conclusions in this work are based on numerical simulations.

Our model has the same governing equations as in ref. [23], Appendix A; however, as discussed above, it is modified to include oxygen exchange and surface diffusion along the entire surface, and the model domain is in two Cartesian coordinates (x, z). The diffusion equation and its boundary conditions are linearized, non-dimensionalized, and then the time component is removed through separation of variables according to ref. [23]. This leads to the following stationary partial differential equation (PDE) and boundary conditions:

$$j\sigma\bar{\psi} = \frac{\partial^2\bar{\psi}}{\partial\varepsilon^2} + \frac{\partial^2\bar{\psi}}{\partial\xi^2} \tag{27}$$

$\bar{\psi}|_{\xi=0} = 1$ (unit voltage perturbation at electrolyte interface) (28)

$$-\frac{\partial\psi}{\partial z}|_{\xi=H} = (\kappa + j\sigma\phi)\bar{\psi}|_{\xi=H} - \nu\frac{\partial^2\psi}{\partial x^2}|_{\xi=H}$$ (reaction, diffusion on top surface) (29)

$\frac{\partial\psi}{\partial x}|_{\varepsilon=0} = 0$ (symmetric boundary condition) (30)

$$-\frac{\partial\psi}{\partial x}|_{\varepsilon=1} = (\kappa + j\sigma\phi)\bar{\psi}|_{\varepsilon=1} - \nu\frac{\partial^2\psi}{\partial z^2}|_{\varepsilon=1}$$ (reaction, diffusion on vertical wall) (31)

Which have been non-dimensionalized according to:

$$\psi = \frac{x_v - x_v^o}{x_v^o}, \qquad \varepsilon = \frac{x}{W}, \qquad \xi = \frac{z}{W}, \qquad \tau = \frac{tA^oD_v}{W^2} \tag{32}$$

Where $\bar{\psi}(\varepsilon, \xi)$ is a stationary spatial function representing the disturbance of the vacancy concentration, and its phase relationship to an applied voltage perturbation. W is half the film width, $x_v = \delta/3$, is the vacancy concentration, and $A^o$ is the equilibrium bulk diffusion thermodynamic factor. The non-dimensional parameters appearing in Equations (29) and (30) are given by:

$$\kappa = \frac{4R_oW}{c_o x_v^o D_v} = \frac{Surface\ Exchange}{Bulk\ Diffusion} \tag{33}$$

$$\nu = \frac{\Gamma_o\theta_{O_s}^o D_{O_s}}{Wc_o x_v^o D_v} = \frac{Surface\ Diffusion}{Bulk\ Diffusion} \tag{34}$$

$$\phi = \frac{A^{\circ}}{A^{\circ}_{O_s}} \frac{\Gamma_o \theta^{\circ}_{O_s}}{W c_o x^{\circ}_v} = \frac{Surface\ Oxygen\ Storage}{Bulk\ Oxygen\ Storage} \tag{35}$$

Which are equivalent to Equations (6–8) in [23], except that the characteristic length is W. $R_O$ is the exchange rate given in (mols of $O_2$ per area per time). In accordance with the work by Lu et al., it is assumed that, $\phi = 0$, since the bulk is expected to store significantly more oxygen than the surface.

The average current density is found by normalizing to the total gas exposed surface area, $a_{gas}$, and finding the flux through both the TPB path and bulk path by:

$$\frac{i \cdot a_{gas}}{2F} = -l_{TPB} N_{O_s}|_{z=0} + 2 l_{TPB} \int_0^W \boldsymbol{e}_z \cdot N_v|_{z=0} dx \tag{36}$$

Where $l_{TPB}$ is the TPB length in ($cm^{-1}$) and $a_{gas} = l_{TPB}(W + H)$. $N_{O_s}$ is the surface oxygen flux given by Equation (A-4) in [23], and $N_v$ is the vacancy flux occurring through the bulk given by Equation (A-2) in [23].

Upon numerical solution for $\bar{\psi}(\varepsilon, \xi)$ (Equations (27)(31)) it is possible to calculate impedance. The non-dimensional voltage perturbation is given by $\alpha = 2F\bar{V}/ART$, and is set to 1 for convenience. Since the equations have been linearized, Z is independent of $\bar{V}$, thus, through inversion and non-dimensionalization of Equation (36), impedance is given by:

$$\frac{Z(\hat{\omega})}{R_D} = H(\sigma; \kappa, \nu, \phi) = \left(\frac{-i \cdot (W + H)}{4F c_o x^{\circ}_v A D_v}\right)^{-1} = \left[\frac{\nu}{2}\frac{\partial \bar{\psi}}{\partial \xi}|_{\substack{\varepsilon=1 \\ \xi=0}} + \int_0^1 \frac{\partial \bar{\psi}}{\partial \xi}|_{\xi=0} d\varepsilon\right]^{-1} \tag{37}$$

Where $c_o$ is the bulk oxygen content, F is the Faraday constant, $\sigma = \hat{\omega} t_D$ is the dimensionless radial frequency, and $H(\sigma)$ is a dimensionless impedance function, the characteristic resistance, $R_D$, and time constant, $t_D$ are given by:

$$R_D = \frac{R_{gas} T (W + H)}{8F^2} \frac{}{c_o x^{\circ}_v D_v}, \qquad t_D = \frac{W^2}{A^{\circ} D_v} \tag{38}$$

Where $R_{gas}$ is the gas constant.

The computational and numerical details of solving the PDEs are omitted here in the interest of clarity. The details can be found in our JECS paper.

Simulation results are shown for W = 15 μm, in Figure 12 and 13. In Figure 13a–b, contour plots of the solution to $\bar{\psi}(\varepsilon, \xi)$ are shown without surface diffusion ($\nu = 0$), and low surface exchange ($\kappa = 0.1$), for high and low σ values. At low frequencies (Figure 13a) the entire bulk of the film is engaged with significant deviation of vacancy concentration away from equilibrium, whereas at high frequencies (Figure 13b) engagement only occurs close to the electrolyte/cathode interface. In

Figure 13c significant surface diffusion is introduced (ν = 10). Here the right wall and the top surface are engaged faster than the bulk, which is limited to the region close to the cathode/electrolyte interface. Impedance results, from Equation (37) for W = 15 μm, are shown in Figure 13. They are normalized to the maximum of the imaginary part (i.e., $R_M = -R_D \cdot Im(H(\sigma))$, and it is seen that the plots are generally Gerischer shaped, but show some low frequency dispersion at large κ values. Also, a high frequency kink appears at low κ and high ν as seen in Figure 13. These results are similar to those derived by Lu et al. [23].; however, the summit frequency and the characteristic resistances are different.

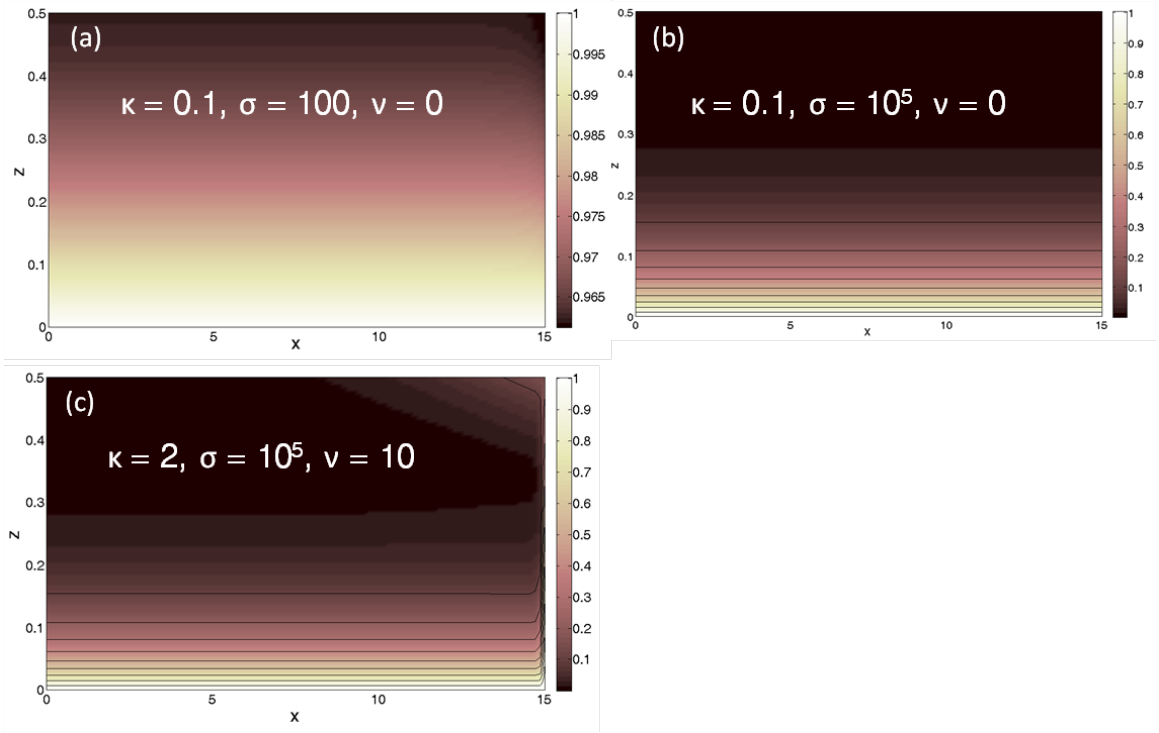


Figure 12. Contour plots for the solution to Equation (27) for various parameter values. (a) κ = 0.1, σ = 100, ν = 0, very high engagement of the entire film. (b) κ = 0.1, σ = $10^5$, ν = 0, engagement is limited to the electrolyte/cathode interface, and (c) κ = 2, σ = $10^5$ ν = 10, the right side and the surface are engaged fastest, with the bulk engagement generally limited close to the interface.

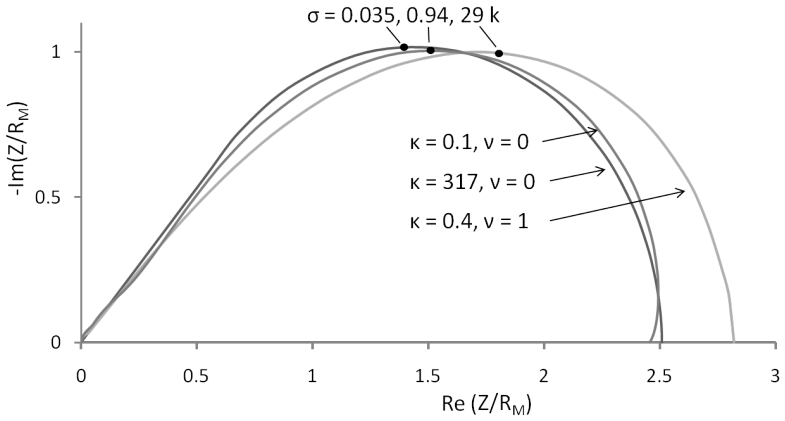


Figure 13. Model impedance results normalized to $R_M$, and $\omega_M$ as described in the text. High κ values cause low frequency dispersion, while the introduction of surface diffusion through ν causes a "kink" at the high frequency end.

**EIS Measurements on Patterned LSCF**

The experimental methodology to deposit patterned thin films of LSCF are described in detail in our JECS paper and will not be described here. A test stand was built out of alumina tubes such that the working and counter electrodes were pressed between gold mesh. Gas was injected near the sample to ensure adequate flow of gas to the electrodes, while gas was removed near the top of the setup. Gold lead wires were wrapped into the mesh and a reference gold wire was wrapped into the cylindrical groove in the YSZ. A thermocouple was suspended within a few millimeters of the sample. The whole setup was then placed within a large one-end closed tube and sealed, gas-tight, with a rubber gasket. The partial pressure of oxygen was regulated by introducing different pre-mixtures of $O_2$ and $N_2$. Initially the test setup temperature was raised at 2 °C/min to 820 °C with flowing gas and allowed to equilibrate for 24 hrs before testing began. Measurements were made at $pO_2$= 1.0, 0.21, 0.05, 0.01, and 0.001 atm, and over a temperature range from 600–800 °C in 50 °C increments.

Electrochemical impedance measurements were collected using a Princeton Applied Research Parstat 2273 potentiostat/FRA. The perturbation amplitude was 10 mV and the frequency ranged from 100 kHz to 10 mHz with 10 frequency points per decade. Measurements were collected for each $pO_2$ at a given temperature, and then the temperature was lowered to the next temperature. Measurements were collected over several hours until no change in spectra was observed.

Scans from the pattern with $l_{TPB}$ = 430 $cm^{-1}$ at 800 °C for various $pO_2$ are shown in Figure 14. The spectra collected were approximately Gerischer shaped with dispersion at low frequency that increased with increasing $pO_2$; they also show a high frequency feature. The Gerischer shape is characteristic of co-limited diffusion as expected for this material [19, 60], whereas the high frequency feature may be explained by the low firing temperature (820 °C) of these samples [61]. The temperature was sufficient to turn the as-deposited amorphous film crystalline, yet it may be poorly adhered to the GDC barrier layer, leading to an interfacial resistance. The model predicts a Gerischer shaped impedance for the entire frequency range, and thus does not account for the high

frequency feature observed in the experimental results. In order to compare the results a reliable method of removing this feature without changing the low frequency Gerischer shape must be established. Berthier et al. [46] demonstrated the ability to remove the double layer capacitance and firmly establish the interfacial (charge transfer) resistance. However, with noisy experimental data at the high frequency, it is difficult to converge on either a consistent value for the high frequency intercept or the exact width of the low frequency feature. Therefore, it is a somewhat tedious and unreliable technique for extracting the low frequency spectra. A more promising approach was demonstrated by Lu et al. who noted that after applying the Berthier correction, the summit frequency on the Nyquist plot and the negative imaginary component of the impedance at that frequency did not change from the corresponding values measured from the total impedance. This characteristic frequency and resistance can then be used to compare with model results.

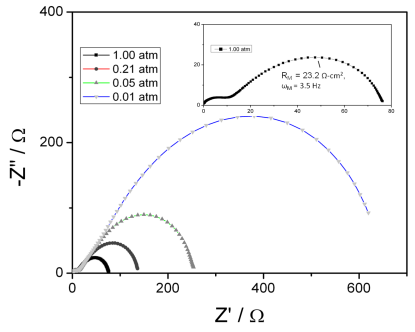


Figure 14. EIS results from the sample with $l_{TPB}$ = 430 $cm^{-1}$, at 800 °C, for various $pO_2$, with the electrolyte resistance subtracted.

The characteristic frequency and resistance, $R_M$ and $\omega_M$, results obtained for the sample with lTPB = 430 $cm^{-1}$, are given as functions of $pO_2$ and T in Figure 15. The activation energy of $R_M$ was 182 kJ-$mol^{-1}$ for all $pO_2$, while both metrics showed a power law dependence on $pO_2$. This dependence is stronger for $\omega_M$, such that the relationship between $1/\omega_M \sim R_M^n$ has n between 1.5 and 1.7. This is consistent with co-limitation between surface exchange and transport processes, independent of interfacial charge transfer.

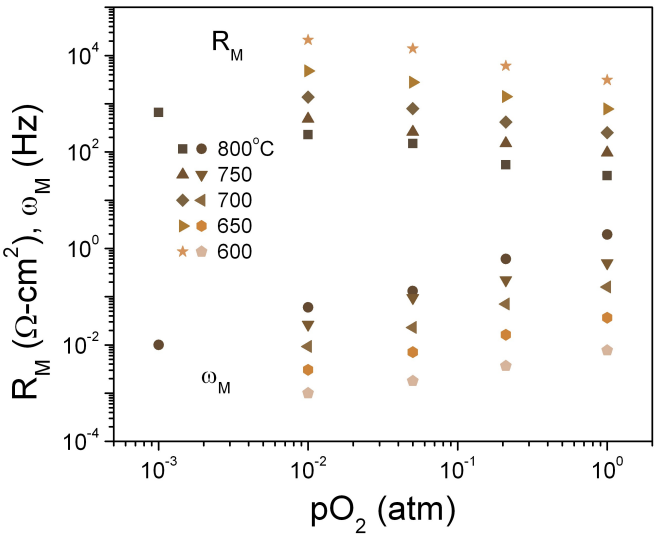


Figure 15. $R_c$ and $\omega_c$ are plotted versus $pO_2$, for the sample with $l_{TPB}$ = 430 $cm^{-1}$. Below 800 °C, the sample showed significant gas phase limitation at $10^{-3}$ atm where a third semicircle become present. Thus, this data was omitted.

The dependence of TPB length is given in Figure 16 by plotting 1/RM vs. TPB length for different $pO_2$ at 800 °C. It is seen that the conductance (i.e., 1/RM) increases with TPB length, consistent with surface transport to the TPB contributing to the overall rate. However, extrapolation of the slope to zero TPB length does not pass through the origin. This can be attributed the activation of both the bulk and surface paths, based on our prior discussion. Using this methodology the contributions to the rate from the bulk path, RMMIEC, and the surface path, RMTPB, were separated. The results for different $pO_2$ at 800 °C for lTPBp = 1200 cm-1 are shown in Table 3. At 1.00 atm the bulk is more resistive suggesting that the surface path is the main path; however, below this $pO_2$ the surface is more resistive and thus the bulk path is the main current carrying pathway. That both paths appear to contribute to the total rate justifies the use of a 2-D model for explaining the observed oxygen reduction kinetics in LSCF-6428.

**Extraction of Kinetic Parameters from Fitting Model to Impedance Results**

We once again eschew presenting technical details of fitting the model to the impedance results as before and simply refer the reader to our JECS paper. However, we remind the reader of the three dimensionless parameters in our fit specified in Equations (33) to (35). To begin with, we set $\phi = 0$ since we expect the bulk oxygen storage to be much larger than surface oxygen storage. This is in accord with Lu's et al. [23] prior model.

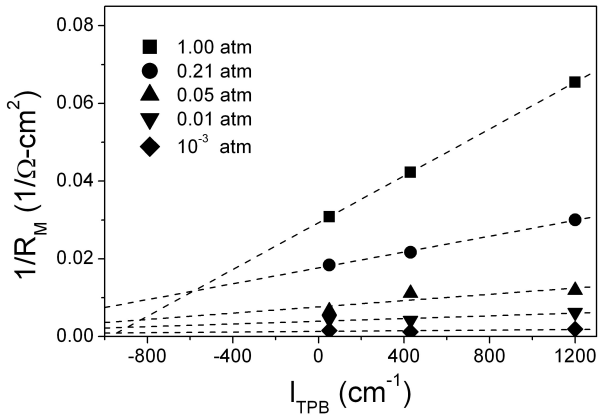


Figure 16. TPB dependence of $1/R_M$ for the samples at 800 °C for different $pO_2$ measured. The lines are linear best fit lines showing that extrapolation to zero TPB length does not meet at the origin, suggesting that the TPB path is involved but so is the bulk path.

Table 3. Bulk and surface path dependence of $R_M$ – 800 °C, $l_{TPBp}$ = 1200 $cm^{-1}$.

| | All resistances in ($\Omega$-$cm^2$) | | | |
|---|---|---|---|---|
| $pO_2$ atm | $R_M$ | $R_M^{TPB}$ | $R_M^{MIEC}$ | $R_M^{MIEC} : R_M^{TPB}$ |
| 1.00 | 15 | 26 | 30 | 1.2 |
| 0.21 | 33 | 76 | 47 | 0.6 |
| 0.05 | 84 | 193 | 119 | 0.6 |
| 0.01 | 161 | 419 | 210 | 0.5 |
| 0.001 | 527 | 1344 | 693 | 0.5 |

The dimensionless κ depends on the bulk diffusivity, $D_V$, and also the surface exchange rate, $R_0$. Very little is known about surface diffusion, i.e., about the diffusivity, the concentration of surface sites, or the thermodynamic factor. Therefore, the surface transport is simply left in terms of ν: the ratio of surface to bulk transport. The bulk diffusivity has been shown to be roughly constant with $pO_2$, in the measured range, for LSCF-6428 and was estimated to be $1.5 \cdot 10^{-7}$ cm-$s^{-1}$ at 800 °C, with an activation energy of 70 kJ-$mol^{-1}$ [62]. Therefore, in our fitting routine, we fixed $D_V$, and estimated $R_0$ and ν.

Figure 16 shows the estimated $R_0$ and ν. The value of 2·10-8 cm-s-1 at 700 °C in air is in a reasonable range for this material, and slightly lower than measured for LSC-82 [43]. $R_0$ is approximately $pO_2$ independent but has an activation energy of about 115 kJ-mol-1 in air, which is higher than LSC-82 (55 kJ/mol) [23].

**Towards a Mechanistic Interpretation of Oxygen Reduction on LSCF**

From Figure 17 it is seen that ν increases with increasing $pO_2$. This $pO_2$ dependence correlates inversely with bulk vacancy concentration. At 800 °C and $10^{-2}$ atm the surface diffusion is the least

significant (ν ~0.13). At the other extreme, 800 °C and 1.0 atm, there is very little bulk vacancy concentration and the surface diffusion increases (ν ~ 2.6). Evidence for this increasing TPB transport is seen in Figure 16 by extending the best-fit lines to the x-intercept. At 1.00 atm the intercept was approximately -1000 $cm^{-1}$ whereas the intercept decreased to approximately -2200 $cm^{-1}$ at $10^{-3}$ atm. However, the correlation between increasing surface contribution with decreasing bulk vacancy concentration does not hold with the observed temperature dependence, since ν is higher at elevated temperatures (the opposite of the bulk vacancy concentration). A potential explanation is the recent discovery in our group of the formation of a Sr-rich phase (not presented in this report), possibly SrO which forms on the surface at lower temperatures, and turns to $SrCO_3$ even at the ppm levels of $CO_2$ present in air. It is possible this phase inhibits surface diffusion, thus forcing more of the oxygen transport through the bulk pathway at lower temperatures. The total range over which ν varies (~0.025–2.5) signifies a shift from bulk diffusion domination to either co-limiting or surface diffusion dominated pathway. This range is similar, yet slightly smaller than that observed for LSC-82 [44] (i.e., ~0.01–15).

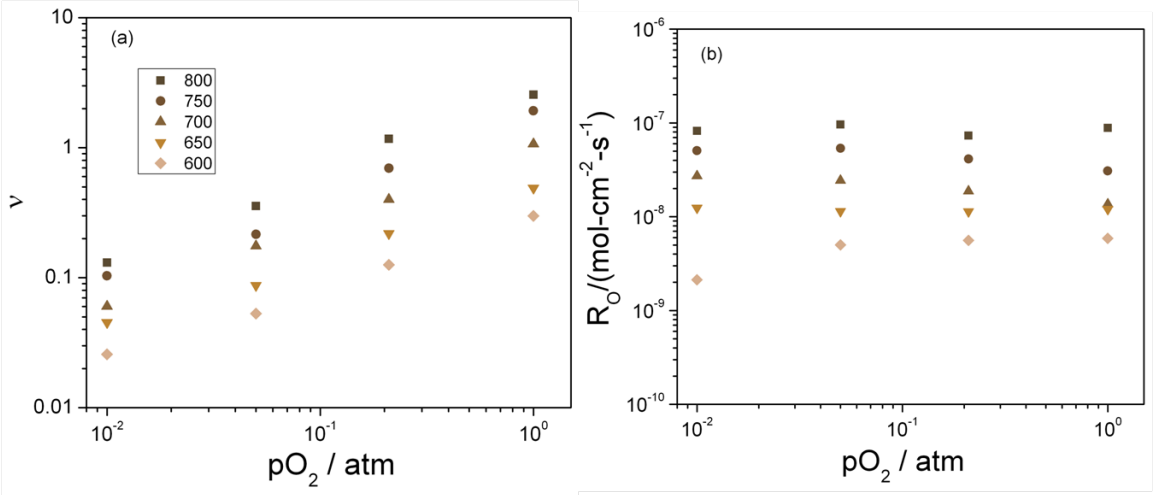


Figure 17. Fitting results from the data in Figure 14 fit to the model predictions, with thermodynamic data taken from [105] and $D_v = 1.5 \cdot 10^{-7}$ at 800 °C and an activation energy of 70 kJ-$mol^{-1}$.

## Concluding Remarks

This report details our efforts over the last 4 years under the SECA program to obtain insights into the oxygen reduction process in predominantly electronic conductors and in MIECs. We have employed EIS on patterned thin film electrodes, and employed suitable transport models to extract kinetic parameters for oxygen reduction from such electrodes. Further by examining the behavior of these parameters as a function of T and $pO_2$, we have attempted to elucidate the oxygen reduction mechanism in these electrodes. In a companion report we expect to present results of X-ray studies that provide additional supporting details to understand some of these results.

## References


1. A. M. Svensson, S. Sunde and K. Nisancioglu. Mathematical Modeling of Oxygen Exchange and Transport in Air-Perovskite-YSZ Interface Regions. *Journal of The Electrochemical Society*, **144**, 2719 (1997).

2. J. Van herle, A. J. McEvoy and K. R. Thampi. Oxygen reduction at porous and dense cathodes for solid oxide fuel cells. *Electrochimica Acta*, **39**, 1675 (1994).

3. Y. Li, R. Gemmen and X. Liu. Oxygen reduction and transportation mechanisms in solid oxide fuel cell cathodes. *Journal of Power Sources*, **195**, 3345 (2009).

4. S. B. Adler. Factors Governing Oxygen Reduction in Solid Oxide Fuel Cell Cathodesâ€ *Chemical Reviews*, **104**, 4791 (2004).

5. A. Mitterdorfer. Identification of the Oxygen Reduction at Cathodes of Solid Oxide Fuel Cells. *PhD thesis ETH Zürich, Department of Materials, Switzerland*, **No. 12380** (1997).
6. M. Gödickemeier, K. Sasaki, L. J. Gauckler and I. Riess. Perovskite cathodes for solid oxide fuel cells based on ceria electrolytes. *Solid State Ionics*, **86-88**, 691 (1996).

7. F. Bidrawn, R. Kungas, J. M. Vohs and R. J. Gorte. Modeling Impedance Response of SOFC Cathodes Prepared by Infiltration. *Journal of The Electrochemical Society*, **158**, B514 (2011).

8. J. M. Vohs and R. J. Gorte. High-Performance SOFC Cathodes Prepared by Infiltration. *Advanced Materials*, **21**, 943 (2009).

9. J. Mizusaki, H. Tagawa, K. Tsuneyoshi and A. Sawata. Reaction Kinetics and Microstructure of the Solid Oxide Fuel Cells Air Electrode La[sub 0.6]Ca[sub 0.4]MnO[sub 3]/YSZ. *Journal of The Electrochemical Society*, **138**, 1867 (1991).

10. F. Foerster. Die Diffusionsgaselektrode. Von Dr. Alfred Schmid (Basel). Mit 19 Abbildungen. Verlag von Ferd. Enke in Stuttgart, 1923. 57 S. *Zeitschrift für Elektrochemie und Angewandte Physikalische Chemie*, **30**, 92 (1924).

11. S. Srinivasan, H. D. Hurwitz and J. O. M. Bockris. Fundamental Equations of Electrochemical Kinetics at Porous Gas-Diffusion Electrodes. *Journal of Chemical Physics*, **46**, 3108 (1967).

12. S. B. Adler. Factors Governing Oxygen Reduction in Solid Oxide Fuel Cell Cathodes. *Chemical Reviews*, **104**, 4791 (2004).

13. T. N. Andersen. Electrochemical Kinetics. Theoretical and Experimental Aspects. Klaus J. Vetter. Translated, with revisions by the author, from the German edition (Berlin, 1961) by Scripta Technica. Stanley Bruckenstein and Brian Howard, Translation Eds. Academic Press, New York, 1967. *Science*, **159**, 970 (1968).

14. J. E. Bauerle. Study of solid electrolyte polarization by a complex admittance method. *Journal of Physics and Chemistry of Solids*, **30**, 2657 (1969).

15. M. Kleitz, L. Dessemond and M. C. Steil. Model for ion-blocking at internal interfaces in zirconias. *Solid State Ionics*, **75**, 107 (1995).

16. J. Mizusaki, K. Amano, S. Yamauchi and K. Fueki. Electrode reaction at Pt, O2(g)/stabilized zirconia interfaces. Part II: Electrochemical measurements and analysis. *Solid State Ionics*, **22**, 323 (1987).

17. J. Mizusaki, K. Amano, S. Yamauchi and K. Fueki. Electrode reaction at Pt, $O_2$(g)/stabilized zirconia interfaces. Part I: Theoretical consideration of reaction model. *Solid State Ionics*, **22**, 313 (1987).

18. N. L. Robertson and J. N. Michaels. Oxygen Exchange on Platinum Electrodes in Zirconia Cells: Location of Electrochemical Reaction Sites. *Journal of The Electrochemical Society*, **137**, 129 (1990).

19. S. B. Adler, J. A. Lane and B. C. H. Steele. Electrode Kinetics of Porous Mixed-Conducting Oxygen Electrodes. *Journal of The Electrochemical Society*, **143**, 3554 (1996).

20. D. S. Mebane, Y. Liu and M. Liu. A Two-Dimensional Model and Numerical Treatment for Mixed Conducting Thin Films. *Journal of The Electrochemical Society*, **154**, A421 (2007).

21. M. E. Lynch, D. S. Mebane, Y. Liu and M. Liu. Triple-Phase Boundary and Surface Transport in Mixed Conducting Patterned Electrodes. *Journal of The Electrochemical Society*, **155**, B635 (2008).

22. J. Fleig and J. Maier. The polarization of mixed conducting SOFC cathodes: Effects of surface reaction coefficient, ionic conductivity and geometry. *Journal of the European Ceramic Society*, **24**, 1343 (2004).

23. Y. Lu, C. Kreller and S. B. Adler. Measurement and Modeling of the Impedance Characteristics of Porous La[sub 1 - x]Sr[sub x]CoO[sub 3 - delta] Electrodes. *Journal of The Electrochemical Society*, **156**, B513 (2009).

24. F. S. Baumann, J. Fleig, H.-U. Habermeier and J. Maier. Impedance spectroscopic study on well-defined (La,Sr)(Co,Fe)O3-[delta] model electrodes. *Solid State Ionics*, **177**, 1071 (2006).

25. J. Fleig, H. R. Kim, J. Jamnik and J. Maier. Oxygen Reduction Kinetics of Lanthanum Manganite (LSM) Model Cathodes: Partial Pressure Dependence and Rate-Limiting Steps. *Fuel Cells*, **8**, 330 (2008).

26. R. Radhakrishnan, A. V. Virkar and S. C. Singhal. Estimation of Charge-Transfer Resistivity of La[sub 0.8]Sr[sub 0.2]MnO[sub 3] Cathode on Y[sub 0.16]Zr[sub 0.84]O[sub 2] Electrolyte Using Patterned Electrodes. *Journal of The Electrochemical Society*, **152**, A210 (2005).

27. A. Bieberle and L. J. Gauckler. Reaction mechanism of Ni pattern anodes for solid oxide fuel cells. *Solid State Ionics*, **135**, 337 (2000).

28. G. J. La O and Y. Shao-Horn. Impedance Studies of Thin-film and Patterned Sr-doped LaMnO3 on Yttria- Stabilized Zirconia to Probe Oxygen Reduction Kinetics. *ECS Transactions*, **7**, 1041 (2007).

29. S. P. Jiang and J. G. Love. Observation of structural change induced by cathodic polarization on (La,Sr)MnO3 electrodes of solid oxide fuel cells. *Solid State Ionics*, **158**, 45 (2003).

30. G. J. la O, R. F. Savinell and Y. Shao-Horn. Activity Enhancement of Dense Strontium-Doped Lanthanum Manganite Thin Films under Cathodic Polarization: A Combined AES and XPS Study. *Journal of The Electrochemical Society*, **156**, B771 (2009).

31. L. F. J. Piper, A. R. H. Preston, S. W. Cho, A. DeMasi, B. Chen, J. Laverock, K. E. Smith, L. J. Miara, J. N. Davis, S. N. Basu, U. Pal, S. Gopalan, L. Saraf, T. Kaspar, A. Y. Matsuura, P. A. Glans and J. H. Guo. Soft X-Ray Spectroscopic Study of Dense Strontium-Doped Lanthanum Manganite Cathodes for Solid Oxide Fuel Cell Applications. *Journal of The Electrochemical Society*, **158**, B99 (2011).

32. K. J. Yoon, S. Gopalan and U. B. Pal. Analysis of Electrochemical Performance of SOFCs Using Polarization Modeling and Impedance Measurements. *Journal of the Electrochemical Society*, **156**, B311 (2009).

33. K. J. Yoon, P. Zink, S. Gopalan and U. B. Pal. Polarization measurements on single-step co-fired solid oxide fuel cells (SOFCs). *Journal of Power Sources*, **172**, 39 (2007).

34. J.-W. Kim, A. V. Virkar, K.-Z. Fung, K. Mehta and S. C. Singhal. Polarization effects in intermediate temperature, anode-supported solid oxide fuel cells. *Journal of The Electrochemical Society*, **146**, 69 (1999).

35. T. Kenjo and M. Nishiya. $LaMnO_3$ air cathodes containing $ZrO_2$ electrolyte for high temperature solid oxide fuel cells. *Solid State Ionics*, **57**, 295 (1992).

36. S. P. Jiang. Issues on development of (La,Sr)MnO3 cathode for solid oxide fuel cells. *Journal of Power Sources*, **124**, 390 (2003).

37. K. J. Yoon, W. Huang, G. Ye, S. Gopalan, U. B. Pal and J. D. A. Seccombe. Electrochemical Performance of Solid Oxide Fuel Cells Manufactured by Single Step Co-firing Process. *Journal of The Electrochemical Society*, **154**, B389 (2007).

38. F. Zhao and A. V. Virkar. Dependence of polarization in anode-supported solid oxide fuel cells on various cell parameters. *Journal of Power Sources*, **141**, 79 (2005).

39. *Fuel Cell Handbook Seventh Edition*, EG&G Technical Services, Inc., National Energy Technology Laboratory, U.S. Department of Energy Morgantown, West Virginia (2004).

40. F. Bidrawn, S. Lee, J. M. Vohs and R. J. Gorte. The Effect of Ca, Sr, and Ba Doping on the Ionic Conductivity and Cathode Performance of $LaFeO_3$. *Journal of The Electrochemical Society*, **155**, B660 (2008).

41. J. S. Newman, *Electrochemical Systems*, Prentice Hall, New York (1991).

42. Nowotny, J, Bak, T, K. M, Sorrell and C. C, *Charge transfer at oxygen/zirconia interface at elevated temperatures Part 2: Oxidation of zirconia*, p. 11, Maney, London, ROYAUME-UNI (2005).

43. A. Mitterdorfer and L. J. Gauckler. La2Zr2O7 formation and oxygen reduction kinetics of the La0.85Sr0.15MnyO3, O2(g)YSZ system. *Solid State Ionics*, **111**, 185 (1998).

44. R. Radhakrishnan, A. V. Virkar and S. C. Singhal. Estimation of Charge-Transfer Resistivity of Pt Cathode on YSZ Electrolyte Using Patterned Electrodes. *Journal of The Electrochemical Society*, **152**, A927 (2005).

45. V. Brichzin, J. Fleig, H. U. Habermeier, G. Cristiani and J. Maier. The geometry dependence of the polarization resistance of Sr-doped LaMnO3 microelectrodes on yttria-stabilized zirconia. *Solid State Ionics*, **152-153**, 499 (2002).

46. Berthier, F, Diard, P. J, G. Le, B, Montella and C, *Method for determining the faradaic impedance of an electrode reaction : application to metal corrosion rate measurements*, NACE International, Houston, TX, (1995).

47. S. Ricciardi, J. C. Ruiz-Morales and P. Nuñez. Origin and quantitative analysis of the constant phase element of a platinum SOFC cathode using the state-space model. *Solid State Ionics*, **180**, 1083 (2009).

48. F. S. Baumann, J. Maier and J. Fleig. The polarization resistance of mixed conducting SOFC cathodes: A comparative study using thin film model electrodes. *Solid State Ionics*, **179**, 1198 (2008).

49. J. Fleig, *On the current-voltage characteristics of charge transfer reactions at mixed conducting electrodes on solid electrolytes*, p. 11, Royal Society of Chemistry, Cambridge, ROYAUME-UNI (2005).

50. B. A. van Hassel, B. A. Boukamp and A. J. Burggraaf. Electrode polarization at the Au, O2(g)/yttria stabilized zirconia interface. Part I: Theoretical considerations of reaction model. *Solid State Ionics*, **48**, 139 (1991).

51. A. Mitterdorfer and L. J. Gauckler. Identification of the reaction mechanism of the Pt, O2(g)yttria-stabilized zirconia system: Part I: General framework, modelling, and structural investigation. *Solid State Ionics*, **117**, 187 (1999).

52. A. Mitterdorfer and L. J. Gauckler. Identification of the reaction mechanism of the Pt, O2(g)yttria-stabilized zirconia system: Part II: Model implementation, parameter estimation, and validation. *Solid State Ionics*, **117**, 203 (1999).

53. N. S. Nise, *Control Systems Engineering*, John Wiley & Sons, Inc., USA (2004).

54. A. Bieberle and L. J. Gauckler. State-space modeling of the anodic SOFC system Ni, $H_2$-$H_2O$|YSZ. *Solid State Ionics*, **146**, 23 (2002).

55. L. Miara, K. J. Yoon, S. G. Topping, L. Saraf, U. Pal and S. Gopalan. Polarization Resistance of La[sub 0.85]Ca[sub 0.15]MnO[sub 3] Cathodes for Solid Oxide Fuel Cells (SOFCs) Measured Using Patterned Electrodes. *ECS Transactions*, **28**, 137.

56. R. Macdonald, *Impedance spectroscopy: Emphasizing solid materials and systems*, Wiley, New York (1987).

57. R. Merkle, Y. A. Mastrikov, E. Heifets, E. A. Kotomin, M. Kukla and J. Maier. Oxygen Incorporation Reaction into Mixed Conducting Perovskites: a Mechanistic Analysis for (La,Sr)MnO[sub 3] Based on DFT Calculations. *ECS Transactions*, **25**, 2753 (2009).

58. Y. A. Mastrikov, R. Merkle, E. Heifets, E. A. Kotomin and J. Maier. Pathways for Oxygen Incorporation in Mixed Conducting Perovskites: A DFT-Based Mechanistic Analysis for (La, Sr)MnO3−δ. *Journal of Physical Chemistry C*, **114**, 3017 (2010).

59. D. A. Reed and G. Ehrlich. Surface diffusion, atomic jump rates and thermodynamics. *Surface Science*, **102**, 588 (1981).

60. J. A. Lane, S. J. Benson, D. Waller and J. A. Kilner. Oxygen transport in La0.6Sr0.4Co0.2Fe0.8O3-[delta]. *Solid State Ionics*, **121**, 201 (1999).

61. L. A. Dunyushkina and S. B. Adler. Influence of Electrolyte Surface Planarization on the Performance of the Porous SOFC Cathodes. *Journal of The Electrochemical Society*, **152**, A2040 (2005).

62. M. Katsuki, S. Wang, M. Dokiya and T. Hashimoto. High temperature properties of La0.6Sr0.4Co0.8Fe0.2O3-[delta] oxygen nonstoichiometry and chemical diffusion constant. *Solid State Ionics*, **156**, 453 (2003).

## **Microstructural Characterization of Solid Oxide Fuel Cells** *by Paul A. Salvador (Carnegie Mellon University)*


### Summary

It is well known that the performance of electrodes in SOFCs is correlated to the nature and distribution of microstructural features in three dimensions and throughout the cell, but making stronger direct connections between specific features and long-term performance is met with significant experimental and computational challenges. In this report, we present important developments in microstructural science, discuss their importance to SOFCs, describe their use in answering questions relevant to SOFCs, and discuss challenges facing the description of commercial SOFCs.

Important developments over the last few decades in microstructural science now allow for precise characterization of the local chemistry and structure at site-specific locations using analytical transmission electron microscopy (TEM), and for 3-D microstructures to be reconstructed from several types of experiments, including scanning electron microscopy (SEM) and X-ray computed tomography (XCT). Each has benefits and drawbacks, which are briefly discussed. Specimen preparation methods have also improved greatly, with focused-ion-beam (FIB) milling allowing for site-selective TEM specimen preparation and for removal of thin layers for slice-by-slice reconstruction of microstructures in the 1–10 μm range. Laser-machining allows the fabrication of samples in the 10–100 micron range, which is suitable to XCT and plasma FIB 3-D reconstructions.

We use examples of site selective TEM to demonstrate our ability to characterize specific degradation modes in lanthanum strontium manganese oxide (LSM)-based cells. In aggressive poisoning environments, the degradation in LSM-based cathodes is highly non-uniform, indicating that electrochemical activity is clearly heterogeneous.

A host of groups have used many of these new techniques to analyze 3-D phase distributions in SOFCs, primarily focused on in-house prepared cells that have high uniformity. Important results will be reviewed, with the take-away message that the average microstructure and average performance seem to be well correlated. 3-D reconstruction of grain-level microstructure is also possible using automated electron back-scatter diffraction (EBSD), and some recent results are reviewed. Here, one can address crystallographic preferences of specific interfaces and phases, as well as the energetic driving forces for microstructural evolution, essential components in computational models that are rapidly improving. Several recent computational models of microstructure are also discussed.

It also seems clear that non-uniformity affects performance, and describing features far from the mean may be important to describe durability. 3-D XCT over a range of length scales are discussed to address homogeneity issues and their impact on SOFC models using reconstructed microstructures. We also address crystallographic heterogeneities in SOFCs using 2-D and 3-D EBSD information to address grain-size heterogeneities and microstructural energetics.

## Introduction

The basic functionality of SOFCs, or the controlled electrochemical combustion of fuels to generate electrical power, relies on the efficient transport of reactive species to, and their reacted products away from, sites at which reactions proceed with minimal losses [1]–[5]. Since reactive/product species generally involve gases, ions, and electrons separated into distinct phases that must transport over macroscopic distances, the fabrication of efficient SOFCs involves the selection of specific functional phases that are compatible with one another, as well as controlling their distributions over a range of length scales, all aimed at generating reproducible performance criteria over the lifetime of a cell. One of these important length scales involves the cell microstructure, reasonably ball-parked as dealing with the sub-micron to sub-millimeter scale (see Figure 1 and Figure 2). Microstructure deals with (among other things) the inherent distribution of the component phases (materials), a distribution that dictates both the transport paths and the locations of internal reactivity (see Figure 2). Because the importance of both phase selection and microstructural distributions has long been recognized, modern SOFCs already involve complex, highly engineered microstructures that have been largely optimized with respect to initial performance criteria and acceptable degradation rates through Edisonian empiricism.

As SOFCs move toward market deployment, cell optimization now also includes hitting these microstructural targets uniformly over larger active cell areas, at a lower cost to manufacture, and often with relatively new materials. Furthermore, as acceptable cell degradation rates decrease, identifying, modeling, or predicting degradation modes often involves preventing phase/microstructural changes that may be inherent to the cell (in the operational conditions) or arising from unintended interactions (possibly from contaminants or operational excursions). The goal of the fundamental science program in microstructural science is to support SOFC development by both applying modern microstructural science methodologies to solving specific issues confronting developers, and pushing forward the boundaries concerning what questions can be asked, both experimentally and computationally. In the latter regard, the ultimate aim is to develop computationally guided development of reproducible and durable SOFCs. Specifically, the goal is to develop methods that can embrace the complexity of SOFCs and implement methods to support developers and scientists in the design and understanding of continually improving SOFCs for power generation. In this report, we discuss a range of important modern approaches that are moving us toward this latter goal.

Traditional approaches to optimizing microstructure are Edisonian in nature, meaning one would vary relevant parameters (phase volumes, lateral distributions, grain sizes, etc.) and assess their impact on performance metrics (power, stability, etc.)[1]. The resultant microstructure of select specimens are then characterized most commonly using optical microscopy (OM) or SEM methods. An example of an SEM of a commercial SOFC button cell is shown in Figure 1. This SEM image was captured using secondary electrons, which are sensitive to topography of solids and to electronic structure. This image demonstrates already that the cell structure at this length scale is fairly complex, as the thickness of each functional

layer is less than 20 μm. Also, while the distribution of porosity varies in each layer, it also varies laterally within a layer.

A higher resolution SEM image of the active cathode of a commercial SOFC button cell is shown in Figure 2. This SEM image was captured using back scattered electrons, which are sensitive to phase (atomic number or Z). In the active cathode of LSM-based cells, a three-phase composite of LSM (electron conducting and catalytically active to oxygen), YSZ (yttria stabilized zirconia, ion conducting), and pores (gaseous oxygen conducting) is often used (as shown). The electrochemically active sites are the triple phase boundaries (TPBs). Traditional microstructural science studies focused on the 2-D grain size, phase size/phase distribution, and number of TPBs per area, from such images. These have been essential to the development of a basic understanding of microstructural impacts on SOFC performance and for initial screening/optimization of SOFCs.

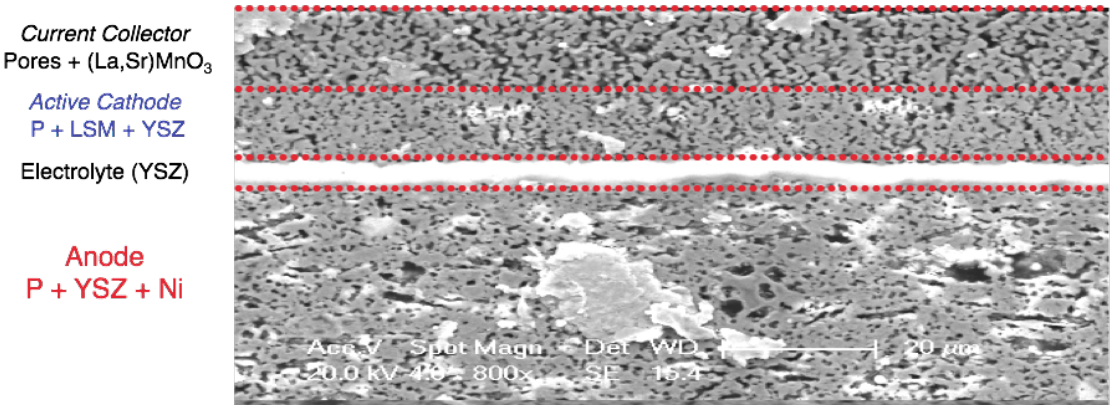


Figure 1. A typical low resolution SEM image, taken using secondary electrons, from an anode supported button cell, highlighting the anode (bulk near anode bottom and active layer near anode top), dense electrolyte (YSZ), cathode active layer (LSM), and cathode current collector.

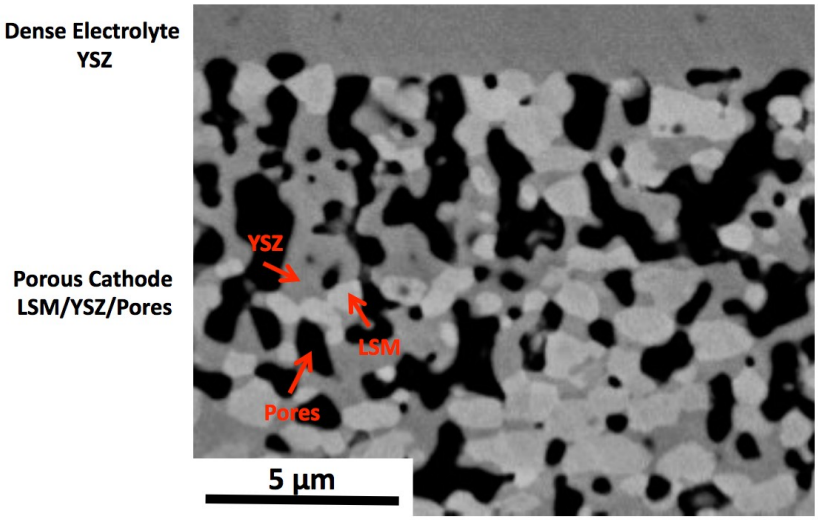


Figure 2. A higher resolution SEM image, taken using back-scattered electrons, from the cathode active layer/electrolyte interface region of a commercially prepared SOFC. Note the fine-scale distribution of phases not observable in Figure 1.

## Methodological Improvements

Over the past decade or so, equipment and methodologies have been improved and developed that afford more and more advanced questions to be addressed relative to the behavior of complex microstructures. Advances in general microstructural sciences over the past decade, not usually focused on SOFCs, are driving the community toward better understanding microstructure and its evolution, especially focused on capturing 3-D descriptions, tackling complexity, and generating computational models that capture this complexity. Largely speaking, the SOFC community is adopting methods developed elsewhere to tackle important problems in the SOFC community. These methods are just beginning to be adapted and are meant here to highlight important methods that will underpin future advances.

The advent of combined FIB and SEM instruments, or dual beam FIBs, ushered in a great increase in the information accessible across science and technology platforms, largely based on increasing the success of sample preparation for characterization by other techniques. Advances in analytical TEMs have also afforded improved characterization of local chemistry and crystallography in SOFCs, from site-specific locations in operated cells. We will discuss this method later related to microstructural degradation analysis, helping unravel the nature of chromium-poisoning in cathodes and address the inherent stability questions in LSCF cathodes.

Using automated analysis of either BSE (phase ID) or EBSD (orientation and phase) signals on an SEM, combined with FIB for sample preparation and material removal, has allowed the direct reconstruction of the 3-D microstructure. This method is generally called the FIB-SEM method of 3-D reconstructions. In the SOFC community, the FIB-SEM using BSE signals is the most commonly adopted method, as one can see in Figure 2 the sensitivity is appropriate for phase analysis.

Automated phase and orientation mapping using backscatter diffraction has been developed over the last 20 years, but has only recently been applied to SOFC systems. EBSD yields both phase and grain structures, as shown in Figure 3, and reconstructing internal boundaries affords one the possibility of characterizing the energetic driving forces for microstructural evolution, information that can be used in computational models to more accurately predict microstructural evolution. 3-D FIB-SEM and 3-D/2D EBSD analysis of SOFC microstructures have already been generated, and the potential of these methods to support durability modeling of SOFCs will be highlighted here.

In most FIB-SEM experiments, one uses the FIB both to remove slices of defined thickness and to define the overall volume to be characterized. Often reconstructed volumes are limited to below 10 $\mu m^3$ based on the time and cost of sample preparation using Ga-ion FIBs. However, it is of interest to interrogate larger volumes using other laboratory methods, such as XCT. Fabricating columns with diameters in the 10–100 μm range is challenging for many materials, especially for brittle, porous ceramic SOFCs with layers on the dimension of the target columns.

Recent advances in laser micro-cutting tools allows for straightforward specimen preparation over these length scales. In Figure 4, an optical microscopy image is shown where one ≈1000 μm wide pedestal and three ≈90 μm high pillars were laser milled from an anode-supported button cell.

Milling was done using a QuikLaze 50ST2 laser micro-mill from ESI (Portland, OR) where the input power was modified to prepare the pedestal and different pillars, approximately 50, 110, and 180 μm in diameter. These pillars can be mounted into XCT or FIB-SEM instruments for further analysis (XCT is described later).

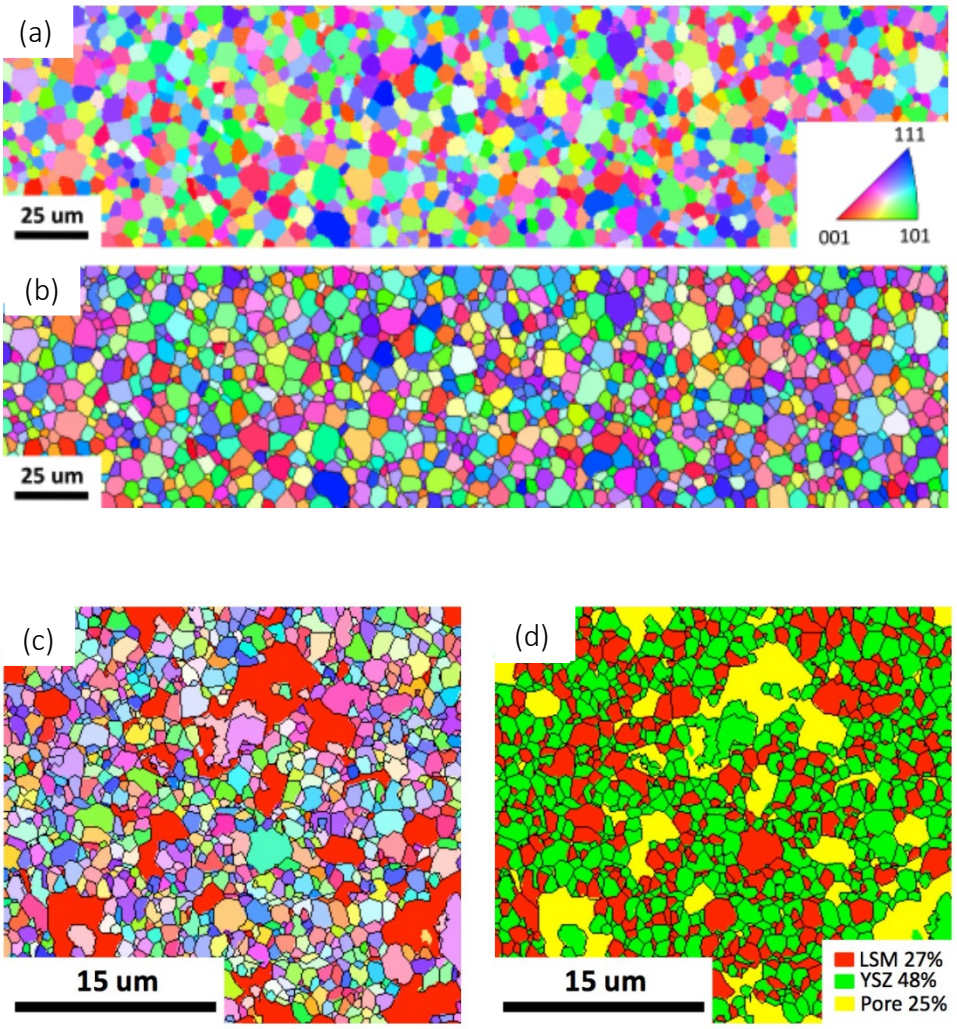


Figure 3. Inverse pole figure map (a,b) [6] of a representative region of a YSZ ceramic, where (a) are the as-collected data and (b) are the cleaned data with reconstructed boundaries, and (c) [7] is cleaned data with reconstructed boundaries from a porous (pores are red) YSZ/LSM ceramic, and (d) is a phase map from the same grains (area ratios are given in phase legend).

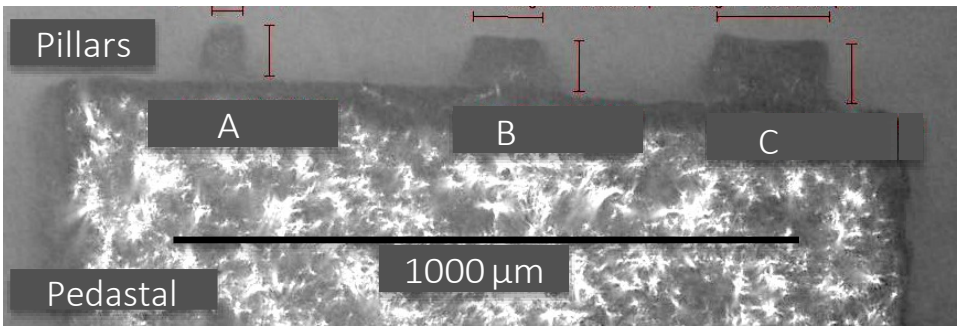

Figure 4. Optical microscopy image of pillars (top A, B, C) on a pedestal (bottom), all of which were fabricated from an SOFC button cell using a laser micro-mill (QuikLaze 50ST2, ESI, Portland, OR). All pillars on the order of 90 µm high and have diameters of ≈50 (A), 110 (B), and 180 (C) µm. FIB and TEM Investigations of Microstructure

One of most important challenges to the durability of SOFCs is related to microstructural changes that result in performance degradation. Traditionally, this work has been carried out as described above, using SEM to explore large regions of space on a 2-D section. Analytical TEM offers improved abilities to isolate compositional and phase variations from the baseline, including subtle chemical interactions. The improved resolution in TEM is in part a manifestation of the sample geometry, which has a thickness on the order of 100 nm (or less) in the beam direction, so the volume of the sample interrogated is small. One of the challenging issues with using TEM for SOFC degradation, as with all microstructural investigations, is ensuring that the local observations are representative of the overall cells. Making several observations in different specimens is often required. Modern analytical TEMs allow for these investigations to be made in reasonable time frames, assuming samples are available. Traditional methods of TEM specimen preparation from specific regions of a cell, with large enough volumes to ensure relevance of the data, are time-consuming and often have low-yield issues. In supporting the Solid State Energy Conversion Alliance (SECA) program using traditional methods, sample preparation was often the bottleneck to data generation. However, using a dual beam FIB to isolate an area with the SEM, and cut TEM samples out with the ion beam, and then attach the specimen to a TEM grid, leads to much greater success in generating usable samples with large volumes of electron transparent material. Two examples are given below that highlight the utility of the approach.

In a series of investigations, the nature of Cr poisoning in LSM cathodes was investigated by Argonne and Carnegie Mellon University [8]–[10]. The goal was to determine to what extent exposure electrochemical parameters played a role in performance and microstructural degradation by Cr. Commercial samples (InDEC, Selb, Germany, H.C. Stark, anode-supported, 600 nm thick Ni/8YSZ, 8% $Y_2O_3$–$ZrO_2$), shown schematically in Figure 5 (left), were treated under a variety of conditions that led to varying degrees of performance degradation (see papers [8]–[10]). Note that owing to the flow channels in the interconnect, which was either a ferritic stainless steel E-Brite (Allegheny Ludlum Corp., Brackenridge, PA) or Au, the contact points and local electrochemical parameters varied laterally in the cathode. The results indicated that both chemical and electrochemical degradation modes existed, where the latter electrochemical mode was associated with the most severe performance degradation.

To determine the local nature of Cr-related microstructural changes, a FIB-based technique was used to locate, isolate, and prepare cross-sectional TEM specimens from specific positions in the SOFC. An in situ lift-out technique was used to prepare the final TEM specimen. A Pt layer was deposited to cover the region of interest and two trenches were made around this area. A membrane was milled down to 1 µm using a 30 keV $Ga^+$ ion beam. The specimen was picked

out using the ominprobe and was welded onto a copper grid. Finally, this 1 μm membrane was polished down to electron transparency using a 5 keV $Ga^+$ ion beam. TEM specimens were examined at 200 keV in a Technai F20 electron microscope fitted with a Gatan imaging filter (Pleasanton, CA) and an option for scanning transmission electron microscopy (STEM). STEM was performed with a high angular annular dark-field detector (HAADF). The energy-dispersive X-ray microanalysis system from EDAX Instruments (EDAX, Mahwah, NJ) was used to perform EDS analysis. Both specimen preparation by FIB and analytical TEM capability is widely available at major centers of electron microscopy. A micrograph of a sample that experienced no performance or microstructural degradation is shown in Figure 5 (right). Sharp pore–solid surfaces are observed free of solid particles or decomposition products that are seen in degraded microstructures, indicating the inherent stability of the cathode in these operational conditions (in the absence of Cr species). This sample was taken specifically from under the landing of the Au contact and close to the electrolyte interface. Sample preparation using FIB is of interest because the yield of comparable specimens in heterogeneous complex systems improves greatly and becomes less of an art, more of a procedure.

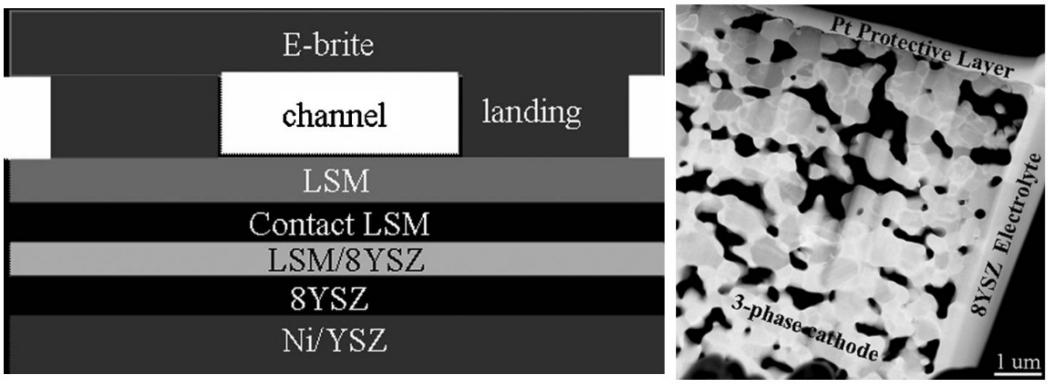


Figure 5. (Left) Schematic cross section of the InDEC cell used in experiments. The channel and landing represent the airflow paths through the interconnect and contact points between the interconnect and the cathode, respectively. The upper LSM is a paste applied to the contact LSM of the commercial cell. The active cathode is the LSM/8YSZ region, and the lower layers are the electrolyte and anode (bottom). Note that this is not drawn to scale. (Right) HAADF-STEM micrograph of the active cathode area near the electrolyte interface (Au interconnect, $T$ = 700°C, $I$ = 1.15 A, $t$ = 500 h). Pt is applied as a protective layer during FIB specimen preparation [10].

A TEM micrograph taken from a similar location in a cell that experienced intermediate degradation (E-brite, $T$ = 800°C, $I$ = 2.3 A) is shown in Figure 6(a). An enlarged view of a region microstructure where LSM is only partially decomposed (dashed circle regions in [a]) and that contains YSZ grains as well is given in Figure 6(b). Two types of contrast are observed that are indicative of degradation. One is light degradation corresponding to Cr–Mn nanoparticles on YSZ surfaces. The nanoparticles on the YSZ surfaces had compositions in

the $(Cr,Mn)_3O_4$ family. These nanoparticles occurred on YSZ in all Cr exposure conditions but did not correlate with degradation extent. The Mn in these nanoparticles appeared to pre-exist on the surfaces (as MnO) and facilitate Cr chemical deposition, but Mn does not poison the cathode.

The other degradation feature is the denser variation in contrast (from white to black) that has a spatial extent similar to the initial grain/pore sizes. Clearly, the extent of degradation is not uniform throughout the whole cathode; it varies while moving away from the electrolyte cathode interface. Within 4 μm of the electrolyte/cathode interface, all 600 nm LSM particles decomposed completely. These areas are shown in solid circles and can be identified by the existence of La-containing species (using location specific EDS). In the area beyond 4 μm from the electrolyte, some (three out of seven in this image) LSM particles did not decompose completely, and these are shown in dashed circles. No LSM degradation was observed in the porous LSM contact layers. Under the interconnect channel, even near the interface, no LSM particles were observed to decompose completely and small particles containing Cr and Mn were attached to the LSM particles. The surface of LSM now seems porous, with many surface grains, some of which extend deep into the pores. The biggest particle in this image had a 2:1 ratio of Cr to Mn, and a selected area electron diffraction pattern could be indexed as a face-centered cubic structure, similar to that expected from $Cr_2MnO_4$. In heavy degradation modes, the Cr continues to fill pores until they are completely blocked.

More of these combined site-selective FIB preparation and analytical TEM observations allowed a universal model of Cr-poisoning in the LSM–YSZ electrodes to be proposed, a model that included two basic mechanisms. First, surfaces of the YSZ in the regions of high electrochemical activity contain Mn species, likely to be MnO, that are very reactive with Cr-vapor species forming solid nanoparticles on the YSZ. Further deposition of Cr occurs on these nanoparticles, including growth of Mn-poor Cr oxides. This degradation mechanism causes a slow overall degradation. At higher operational voltages, LSM decomposes partially yielding MnO, owing to an equilibrium with the oxygen gas [23,41,42]. This equilibrium is upset because of the secondary reaction of MnO with Cr-vapor species, which drives further LSM decomposition, which severely degrades the cell. The latter step can progress in regions of high electrochemical activity to the point that LSM is decomposed completely and pores fill by a similar mechanism to that which occurs on YSZ surfaces. This secondary degradation mechanism is much more severe and should be avoidable both by limiting the Cr activity and by avoiding the LSM decomposition owing to the large local over-potentials.

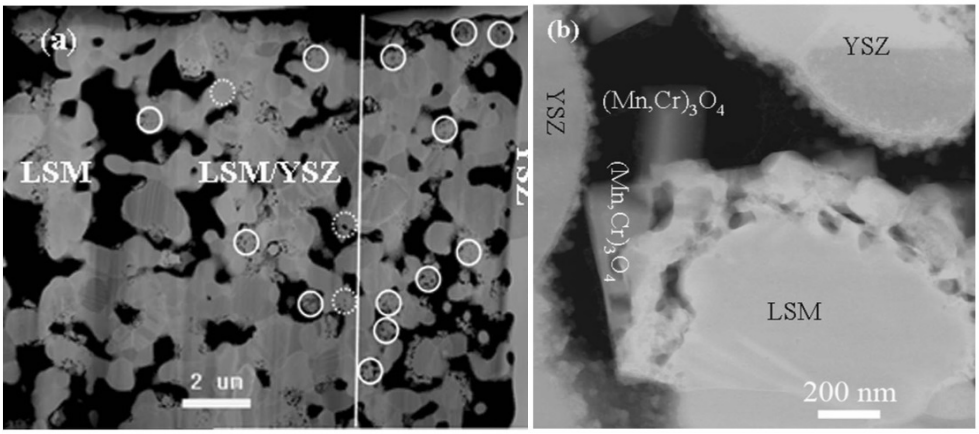


Figure 6. (a) HAADF-STEM micrograph of the overall cathode: the contact LSM, the active LSM/YSZ, and the YSZ electrolyte (E-brite, $T$ = 700°C, $I$ = 1.15 A, $t$ = 500 h). Solid circles indicate regions where the LSM has completely decomposed and dashed circles indicate regions where partial decomposition has occurred. (b) An HAADF-STEM micrograph of nanoparticles attached on the YSZ in close proximity to partially decomposed LSM—a large crystallite of $(Mn,Cr)_3O_4$ is found extending into the pore volume [10].

## 3-D Phase Distributions

The intrinsic reliability and durability of SOFCs is tied closely to the distribution of microstructural features generated during manufacture and to their evolution in operational conditions.

Quantifying the distribution of microstructural features over a 3-D volume that captures all relevant physical properties and at different stages of operation is, therefore, essential to the development of predictive models of SOFC performance. Most prior investigations of 3-D SOFC microstructures have generally focused on cells made in-house, using research-grade (low-throughput) methods that yield relatively uniform microstructures. The 3-D studies briefly discussed herein focus on some commercially prepared cells, but first we will review the prior work.

Two basic approaches are taken to reconstruct cells, FIB-SEM or nano-XCT (nano-CT). In the study by Nelson et al., it was shown that both techniques produce similar results [11]. When FIB-SEM is used, the volumes are generally limited to ≈$10^3$ μm$^3$. FIB-SEM is destructive, but relatively straightforward and available in many research centers. When material removal is carried out by digging trenches [12–15], one is limited in the volume of collection and a significant amount of data processing is required [16–18] to generate the stack of 2-D slices.

When material is removed from pre-processed pillars [19–20], sample preparation is time consuming and has generally low yields. Successful approaches to preparing pillars use FIB [11], [21], standard polishing methods [6], [22], [23], or laser micro-milling (as described above). For XCT, a pillar sample is generally used, but it is a non-destructive technique, meaning the sample investigated is available for further analysis. Also, XCT

analysis with resolutions appropriate to SOFC microstructures is usually done on synchrotron lines [11],[24], but new laboratory-scale nano-CTs have the appropriate resolution to reconstruct SOFC microstructures [21].

Studies on research-grade cells have yielded significant advances in our basic understanding of how the average SOFC microstructure and average initial performance (activity) are connected. A typical volume of SOFC that has been reconstructed is on the order of 5–10 μm on a side, i.e. $(5–10)^3$ $\mu m^3$, with a few investigations having volumes on the order of $(15–25)^3$ $\mu m^3$. Joos et al. found that roughly $6^3$ $\mu m^3$ was sufficient to represent the average features of their research-grade cathode (the active layer) [22]. Laurencin et al. [24] determined the representative volume element (RVE) of the anode support and active layers to be respectively $35^3$ and $13^3$ $\mu m^3$, both larger than the typical reconstruction carried out in the literature. Reasonable correlations between modeling and performance have been shown, and variations in electrochemical activity in 3-D have also been demonstrated [22], [25], [26]. Correlations between multiple features of the microstructure, beyond phase fraction, grain size, and TPBs have been made, such as a combination between electrochemically active TPBs and tortuosity of ion paths [27]. Basically these results (and others [12], [27]) indicate that reconstructed volumes below $10^3$ $\mu m^3$ are likely to be appropriate to the average values in carefully prepared research-grade cells, and that methodologies exist to model the 3-D electrochemical state of real microstructures.

### Heterogeneities in Phase, Boundary, and Grain Size Distributions

If we are to move into investigations of commercial cells, which use high-throughput, low-cost methods, where homogeneity is likely to be sacrificed to a degree, we must develop methods that cover larger volumes in a repeatable fashion. Furthermore, if degradation occurs at features away from the mean, as shown earlier in the Cr degradation study, even larger volumes must be reconstructed for research-grade cells, and electrochemical models must be carried out on the entirety of an active cell. From the perspective of SOFC producers, the prior work in microstructure demonstrates the potential of developing microstructural models of performance over lifetimes, even in systems where the homogeneity is low. In fact, assessing the consequence of heterogeneities may be possible on 3-D microstructures that are built from real cells.

A virtual 2-D slice of a 3-D reconstruction of a commercial-grade cell (a standard anode-supported LSM cathode cell purchased from MSRI, Salt Lake City, UT) from a synchrotron micro-XCT is shown in Figure 7. The overall dimensions of the scan are on the order of hundreds of microns (almost a millimeter). The 2-D pixels (3-D voxels) have an edge length of 1 μm, but many features of the cell can be fully resolved. The different layers are clearly delineated (see caption). Large, irregular pores in the anode support layer (ASL) and spherical pores in the cathode current collector (CCC) are clearly seen, both of which are deliberately introduced by the manufacturer. At the interface of the anode active layer (AAL) and the electrolyte layer (EL), one can also observe resolvable pores, likely an artifact remaining from when the layers were cast together. These indicate that low-frequency heterogeneities exist in commercial samples that ultimately must be assessed. There are similar issues in the cathode active layer

(CAL), where one can see large (>5 μm), bright, roughly circular (spherical in 3-D) features distributed laterally throughout, and there are a few large (>2 μm) pores, which appear as slightly darker grey circles relative to the more uniform background. It should be noted that such heterogeneities often dominate entire regions of CAL specimens prepared for FIB-SEM experiments. Characterizing the low-frequency features requires different volumes to statistically describe microstructures compared to the more uniform backgrounds from these massive heterogeneities.

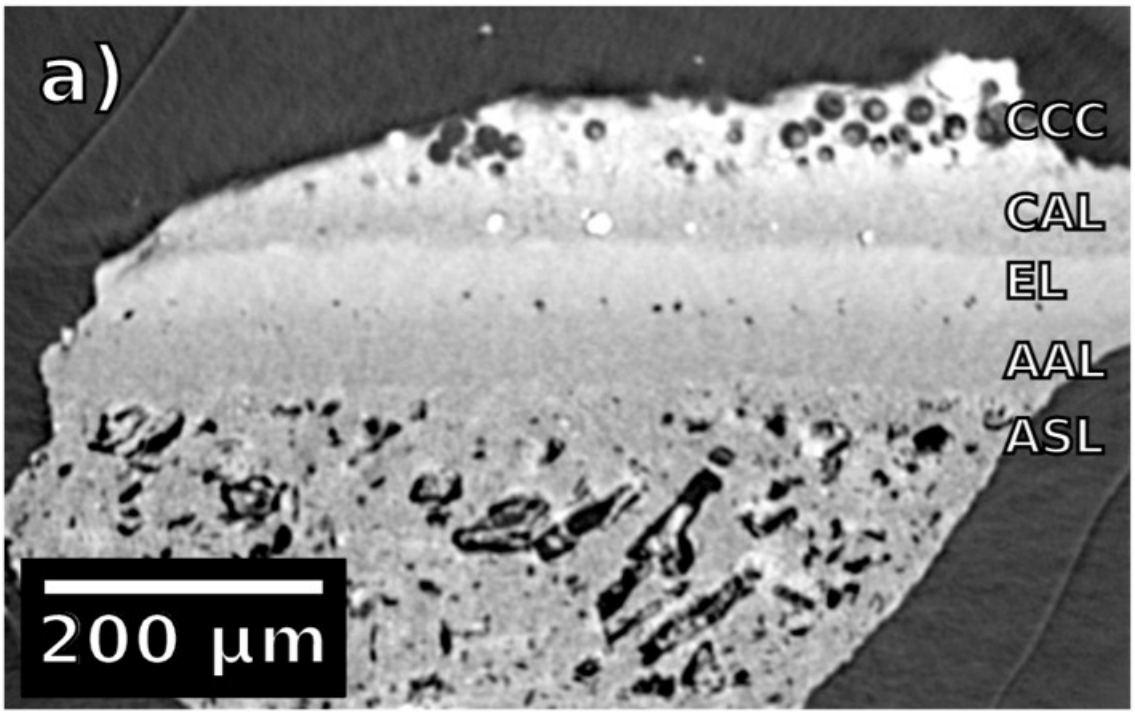


Figure 7. Synchrotron micro-XCT of an MSRI SOFC: a virtual 2-D slice of 3-D synchrotron reconstruction, with CCC, CAL, EL, AAL, and ASL labelled.

While the micro-CT data yields clear information on the low-frequency heterogeneities, one cannot resolve the individual phases in the three-phase CAL (LSM, YSZ, and pores) because the voxel size is larger than the expected characteristic length scale (on the order of several hundreds of nanometers to a few microns). However, variations in the greyscale exist in the CAL, and the greyscale value of voxels provides information on the overall distribution of phases in these layers. A 150 x 150 x 9 $\mu m^3$ region of the CAL was found to be free of the large LSM particles. To determine the relative homogeneity of phases in any given column in the through-thickness direction (normal to the EL), the greyscale values were integrated and normalized, and sub-volumes (sub-images) of the 150 x 150 $\mu m^2$ were compared. The resulting quantification of the 2-D variation of greyscale intensity is shown in Figure 8. The plot illustrates a rapid drop from 13% to 4% variability as the square sub-area size grows from 2 to

20 µm. This is followed by a more gradual decline in variability in the 30-50 µm range, down to 2–3 %. The largest sub-area size of 75 µm is close to 1% of the mean. At sizes above roughly 20 µm, the variability is reasonably low, below 5%; pushing to larger image sizes provides diminishing returns in terms of decreased variability with respect to the average features integrated through the thickness. It should be noted that the heterogeneity calculated in this approach will be slightly under-estimated because the greyscale intensities were integrated through the thickness of the CAL (over 9 voxels).

These results quantify the volume required to determine the average phase fraction within some error range. To be below 4%, a volume of $20^2$ µm$^2$ is required in the CAL of the commercial cell (not including the lower frequency heterogeneities described previously). To drop below 1% error in the phase fractions requires an area (and volume) 16 times bigger at $80^2$ µm$^2$. Both volumes generally fall outside the volumes reconstructed with Ga-ion based FIB–SEM experiments. New laboratory-scale XCT instruments can provide nanoscale resolution over a reasonable volume. For example, the UltraXRM-L200 nanoscale X-ray CT system from Carl Zeiss Microscopy (Pleasanton, CA) is a lab-scale system with 8 keV X-rays and, in the imaging mode used below, has a 150 nm resolution (65 nm voxels) and a 65 x 65 µm field of view. In the CAL of the MSRI cell, the beam attenuation is such that one can reconstruct a maximum of 45 µm in diameter.

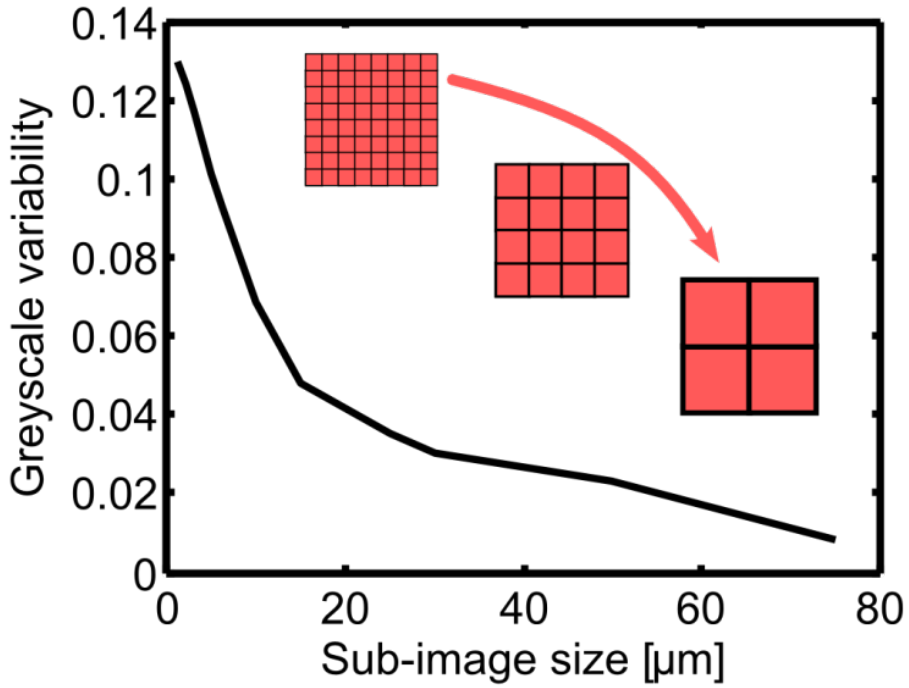

Figure 8. 2-D variability of greyscale intensity (x-ray attenuation) in the 150 x 150 µm2 (x 9 µm) selected region of the synchrotron XCT from the MSRI cell, expressed as 90% confidence intervals based on two-tailed Student-T distribution. The sub-image size is given in square edge length.

An example radiograph from the nano-CT scan can be seen for the commercial MSRI cell in Figure 9(a). A large particle (LP) or boulder of LSM, similar to those evident in the synchrotron micro-XCT, is observed (and are especially problematic in FIB-SEM experiments where volumes are significantly smaller). The overall shape of this reconstruction arises from the sample preparation, further improvements will allow precise geometries to be prepared. A final segmented volume of x 19.8 x 19.4 µm$^3$ is shown in Figure 9(b). Phase fractions, volume-specific interface/surface areas, and volume specific TPB densities were calculated and are similar to those expected: a region of Figure 9(b) is cut out and the TPBs are plotted.

In a similar manner to that shown in Figure 8, the variability in smaller subvolumes was compared for microstructural metrics. The general trend of all features was similar to that shown: a sharp drop-off and then a gentler decrease later. At the maximum independent sub-volume accessible in the nano-XCT data (cubes of 83 µm3), there was still a 20% phase fraction variability: extrapolation indicated that the volume collected in an individual nano-XCT scan is on the order of the necessary volume to capture the mean within 10% of phase fractions. The TPBs behaved similar to the phase fractions, the TPB density variability maintained a value above 20% variability to the highest sub-image size studied, and projections to the full volume indicate a 10 % variability. These larger variations in the sub-volumes, compared to the micro-XCT data, indicate that the lower resolution and column averaging of data put a lower bound on the true variability. Again, this indicates that much larger volumes are required to understand the variability of commercial cells.

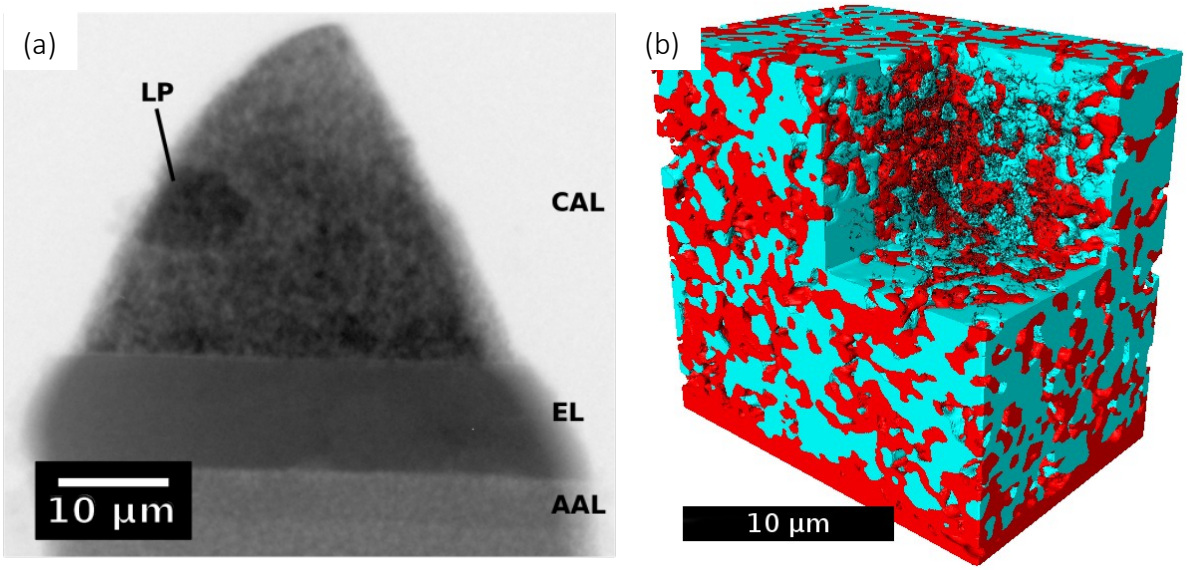

Figure 9. Nano-CT image of CAL from MSRI cell. a) Radiograph of MSRI sample pillar, with CAL, EL, and AAL labelled, as well as a considerably large particle of LSM. Below, equivalent greyscale (b) and segmented (c) virtual 2-D slices of 3-D nano-CT reconstruction of MSRI cell's LSM-YSZ CAL, with the electrolyte situated at the bottom. In the segmented version, LSM is white, YSZ is grey, and pore is black.

3-D FIB-SEM methods are not limited to reconstructing phase distributions, they can also reconstruct grain structure and crystallographic orientations using EBSD instead of backscatter electron (BSE) yield. The process can be fully automated, and was carried out at Carnegie Mellon University using two different commercial cells (anode [Ni/YSZ] supported single cells from InDEC [H. C. Stark, Selb, Germany])[23]. A representative uncleaned EBSD map from a single serial section of an as-reduced cell is shown in Figure 10(a). The cells were indexed in cubic reference frames, and the colors represent differently oriented grains. The large grains at the top of the image are from the dense YSZ electrolyte, and the grains on the bottom are from the active cathode/porous LSM current collector interface. A representative EBSD map from the cleaned data of the same serial section is shown in Figure 1(b). A phase map of the cleaned data is shown in Figure 1(c). Green regions represent YSZ grains (the electrolyte is almost uniformly green), while yellow regions represent LSM grains (the current collector is almost uniformly yellow). These observations indicated that the phase assignment is 90–95% accurate. Oblique projections of the 3-D dataset (80 slices, 20.5 x 19.6 x 5.9 μm = 2371 $\mu m^3$) for the AR cell are shown in Figure 11.

Similar results were obtained for an electrochemically loaded cell, where the volume of the characterized region was 25.8 x 14.9 x 4.725 μm = 1816 $\mu m^3$. The total volume of active cathode considered (after cropping the data) was 607 (1077) $\mu m^3$ in the AR (electrochemically loaded). The YSZ, LSM, and pore volumes were 63%, 28%, 9%, (71%, 11%, and 18%) in the AR (electrochemically loaded) cell. The variation in the volumes of each phase is believed to be related to the small sampling volumes and the natural variation in the phase distributions in local regions of the cells, which was observed in larger 2-D areas as well, and above in the XCT data for another manufacturer.

Not only can phase distributions, surface areas, TPBs, etc. be analyzed in such a dataset, but the crystallographic orientation of features can be identified, as can features associated with boundary evolution, such as the dihedral angle at a TPB. This was done in the paper by Dillon et al.[23] What those analyses demonstrate primarily is that the crystallographic distributions are nearly isotropic (i.e., only weakly anisotropic). In other words, every surface and grain boundary is observed in the overall microstructure. As such, any crystallographic variation in surface properties will locally affect the nature of the surface/TPB; to what extent is not known currently. However, it seems reasonable that future computational models could parameterize the importance of specific variations, to help ascertain their importance in SOFC performance.

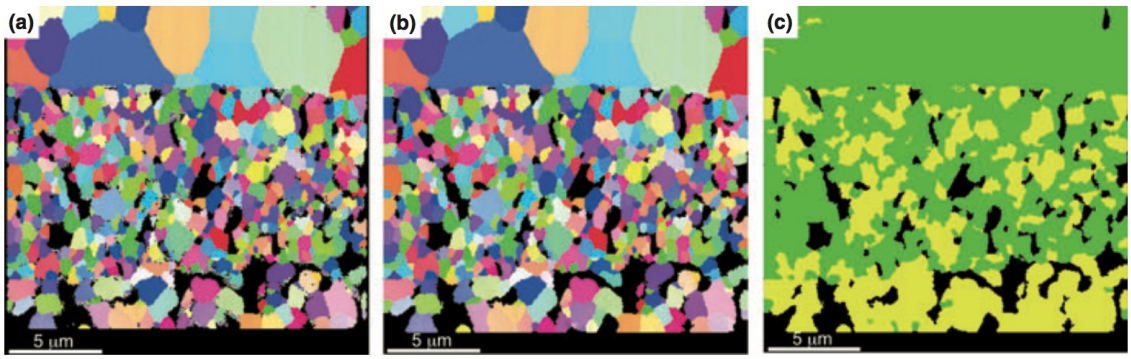


Figure 10. Representative orientation, as inverse pole figures in (a) and (b), and phase (c) maps of the active cathode region in cross-section of the AR cell. The overall dimensions are 20.5 (19.6) μm in the horizontal (vertical) direction. The raw orientation data are given in (a) and the cleaned data in (b). Colors represent different absolute orientations. In the phase map, green indicates YSZ, yellow indicates LSM, and black indicates pores [23].

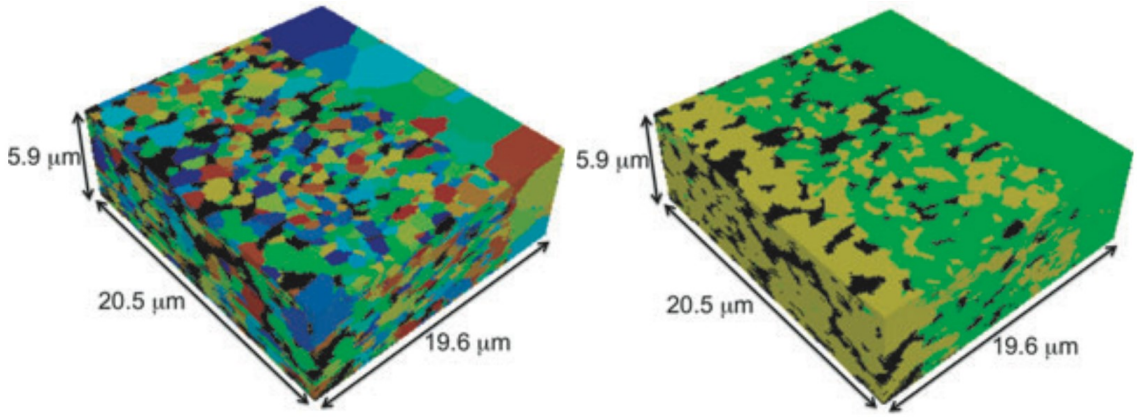


Figure 11. Oblique projections of the reconstructed 3-D volume from the AR cell. In the orientation map in (a), different colors are used to indicate different grains. In the phase map (b), green indicates YSZ, yellow indicates LSM, and black indicates pores [23].

One example of such a distribution is shown in Figure 12, showing the surface dihedral angles around the TPBs. The average dihedral angles in the AR (a and b) and electrochemically loaded (c and d) cells are 114° and 120°, respectively. Overall, the dihedral angles are more isotropic in the electrochemically loaded cell, but both distributions show only weak texture. The small anisotropies in all the populations are interpreted as indications that the interfacial and TPB energies are also weakly anisotropic. The differences in the AR and electrochemically loaded cells could not be directly correlated to cell history, because the volume fraction of phases varied in the local areas, too. In a separate work using EBSD, it was

shown that the different phases perturbed the distributions of other phases [7]. Generating larger volumes of data, as described above for nano-XCT, that also include grain-level information will improve the understanding of microstructural details that can be compared with models. However, determining the nature of energies in typical electrochemical operating conditions will allow for accurate degradation models to be developed.

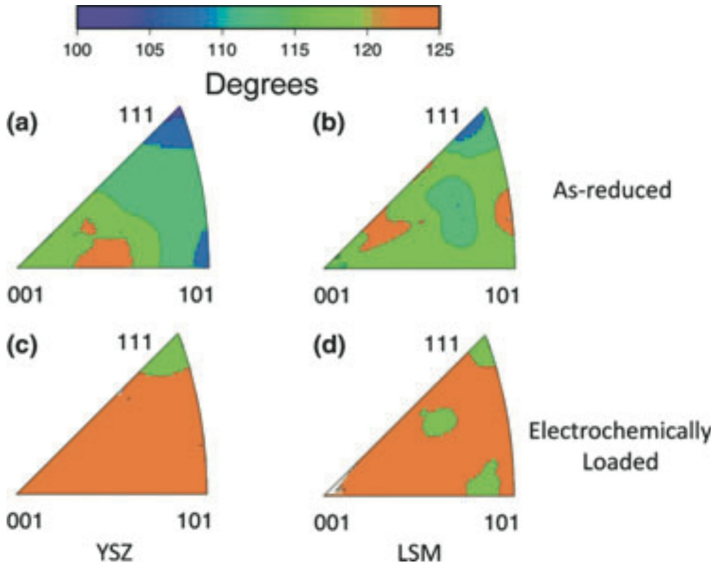


Figure 12. Distribution of dihedral angles between pore surfaces adjacent to TPBs indexed in the YSZ reference frame (a and c) and in the LSM reference frame (b and d) in the AR cell (a and b) and the electrochemically loaded cell (c and d) [23].

In addition to using 3-D FIB-SEM with EBSD on commercial cells, representative component materials have also been investigated [6], [7]. A 3-D reconstruction from a dense YSZ pellet fabricated from fuel cell grade materials is shown in Figure 13(left), which is consistent with an equiaxed structure with a random grain orientation. The misorientation averaged grain boundary plane distribution (GBPD) is shown in Figure 13(right, a) in stereographic projection along the (001) pole of a cubic system. Qualitatively, this distribution (from 170,000 triple lines) is similar to the stereological distributions derived from 2-D EBSD data sets. A weak anisotropy exists in the 3-D GBPD, with (111) planes occurring the least frequently and the (001) planes occurring the most frequently. The width of the distribution is very narrow—the range being from 0.94 to 1.12 multiples of random distribution (MRD). In general, grain boundary character distributions (GBCDs) generated from 3-D data underestimate the anisotropy in comparison with GBCDs generated from stereological 2-D approaches, although the agreements are reasonable. The misorientation averaged grain boundary energy distribution (GBED) is shown in in Figure 13 (right, b) in stereographic projection along the (001) pole of a cubic system. Here, the color scale indicates the normalized grain-boundary

energy, in arbitrary units, such that large values indicate a relatively high-energy grain boundary and small values indicate a relatively low-energy boundary. The range in anisotropy in the averaged grain-boundary energy values is from 0.985 to 1.025, which is similar to very isotropic systems in the literature. An inverse correlation exists between the GBPD and the GBED, where high-energy grain boundaries occur less frequently in the overall population than do low-energy planes. While the GBPD can be readily found using large-area 2-D data sets, the GBED requires 3-D data sets to obtain accurate distributions. The GBED, reflected in the dihedral angles described above, govern the overall evolution of microstructures. Determining the underlying values for the component systems, appropriate mixed systems, and commercial cells, as well as how electrochemistry and phase fractions influence them, will provide the fundamental underpinning to computational models to be developed.

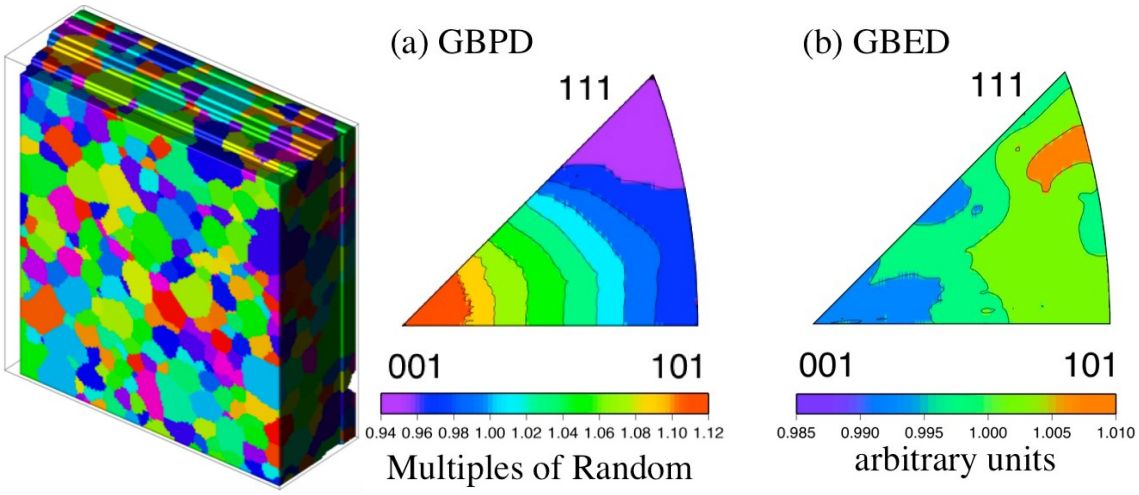


Figure 13. (left) a 3-D orientation map of sintered YSZ. (right) The misorientation averaged (a) GBPD and (b) GBED, given as stereographic projections [6].

As an example of the distributions collected from other representative systems, the misorientation averaged GBPD is given in Figure 14 for (a) dense LSM and (b) porous LSM [28]. Again the distribution as plotted as MRD, with values of 1 indicating the frequency of observation equal to a completely random population. The narrow range of MRD indicates the system is weakly anisotropic, and the introduction of pores further decreases anisotropy, essentially resulting in nearly an isotropic GBPD. The pore boundary plane distribution is essentially isotropic, indicating that every orientation of pore surface (for 164,342 segments) exists in the porous sintered compact. There is a subtle interplay in the three-phase (LSM/YSZ/pore) system that leads to small variations in the GBCD and GBPD, which implies the energetics vary with phase fraction, but overall the system stays relatively isotropic.

Looking at all the component systems [7], it seems that models with nearly isotropic energies are reasonable for microstructural evolution in the absence of electrochemical stresses, and it is an open question as to how electrochemical loads modify the energetics.

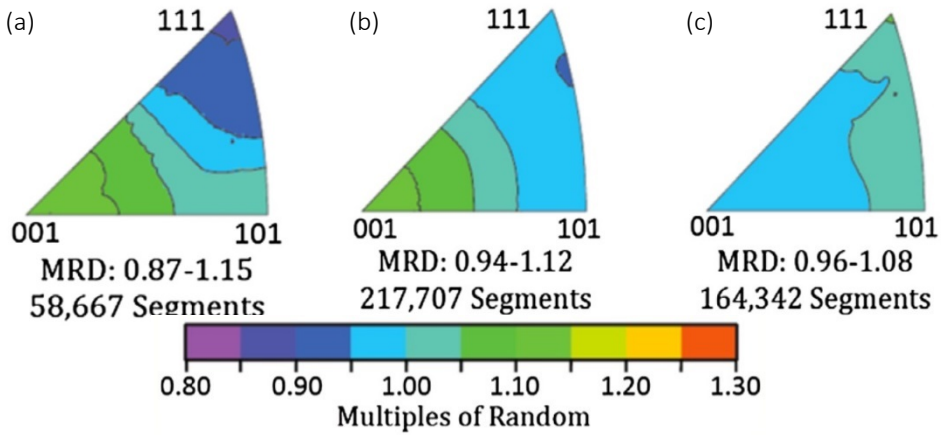


Figure 14. 2-D GBPD for dense (a) and porous (b) LSM, and 2-D pore boundary plane distribution for porous LSM (c) [28].

Most models of microstructural evolution predict that isoptropic systems should have a uniform distribution of microstructural features, such as having a log-normal grain size distribution. Using the 2-D data sets from dense and porous LSM, we investigated the grain size distributions, especially focusing on the upper tails of distributions [28]. Log-normal probability plots of LSM grain sizes are given in Figure 15 for the dense and porous systems. The dense LSM samples (as sintered and sintered then annealed at 1250 °C) both exhibit negative upper tail departures (fewer large grains than expected) from log-normality (the dashed line). These plots are quite similar to the behavior of Mullin's distribution, which indicates nearly normal grain growth [28].

In the as-sintered porous LSM system, however, there is a positive departure of the upper tail (more large grains than expected) from log-normality. In other words, the largest 1% of grains are larger than expected from normal grain growth theory, and are indicative of abnormal grain growth. Very little has been investigated for grain growth in such massively porous systems, but the positive deviation is consistent with models that consider pore boundary migration being important during microstructure evolution. In SOFCs, this implies that the existence of second phases clearly perturbs the overall evolution of the microstructure, but there are too few studies yet to know if normal grain growth theory captures this evolution or if other parameters are required to understand this.

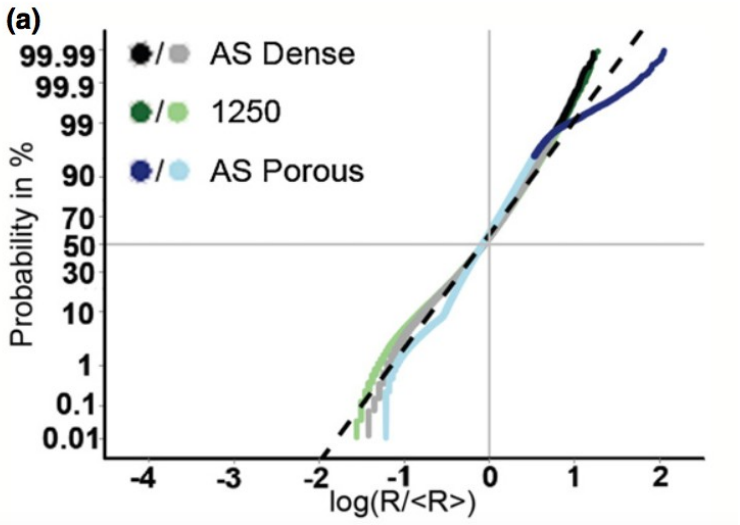


Figure 15. Probability plots of normalized grain sizes from experimental LSM samples. (a) Full distributions for the dense AS, 1250, and porous AS, with the points above the threshold for POT analysis differentiated [28].

## Computational Models of SOFC Microstructural Evolution

The above-described physical experiments serve to establish the relative questions of importance to commercial SOFCs and to contextualize the connection of basic science investigations with technological issues. However, the inherent complexity of the basic SOFC electrodes, the aggressive operational environments, the multiple parallel degradation mechanism, and the expected lifetimes for economic viability limit the practicality of using physical experimentation alone to model and to design dependable and durable SOFC systems. Using properly informed and validated computational experiments, however, promises to accelerate the deployment of more functional and complex materials in SOFCs. As described briefly above, computational models of electrochemistry have been carried out using reconstructions or digitized approximations of SOFC electrodes, and their electrochemical performance compares well to physical experiments. This suggests that computational models soon will capture the basic electrochemical properties of SOFCs, once large enough volumes are collected experimentally for heterogeneous electrodes.

While average electrochemistry has been focused on in the past, more recent models of microstructural evolutions have emerged [29–32]. This will help us understand how architectural degradation proceeds from long-term exposure for a given microstructure in a specific operational condition.

At Penn State, a phase-field model is being developed to describe three-phase electrode microstructures (i.e., electrode-phase, electrolyte-phase, and pore-phase) in SOFCs, using the diffuse-interface theory (composition variables continuously change with finite thickness of the diffuse interphase interfaces) [31]. The driving force for microstructure evolution is the decrease in total interfacial boundary energy. The most important physical parameters in the

model are the gradient energy coefficients ($\kappa^i$ for the $i^{th}$ phase) and the kinetic mobilities (of atoms and grain boundaries). Examples of how the equilibrium TPB contact angles (using 2-D simulations) vary for three sets of gradient energy coefficients of the solid phases are shown in Figure 16. These images show that the model results in well-defined microstructures wherein the microstructural features are affected by the model parameters.

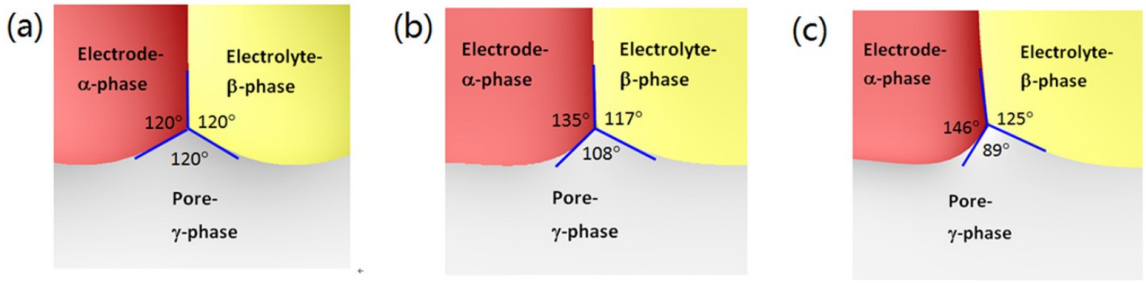


Figure 16. Equilibrium contact angles at triple junctions for three sets of gradient energy coefficients $\kappa^i$ ($\kappa^i$) = (a) 2.5 (2.5), (b) 1.5 (3.5), and (c) 0.5 (5.5) [31].

Thus far, the actual gradient coefficients (and the kinetic mobilities) for SOFC electrode materials have not been physically measured. In, Figure 12 we demonstrated that the dihedral angle (contact angle) could be measured using 3-D FIB-EBSD. In commercial LSM/YSZ cells, the average value in the pore phase was 114° or 120°, for the two different cells (between Figure 16[a] and [b]). The experimental grain boundary energy landscape can also be measured, as shown in Figure 14 for YSZ. Future integrated physical and computational experiments will allow for models to be informed using accurate data and properly validated to specific systems of interest. The result will be predictive models of electrochemical performance over time.

The temporal 3-D microstructural evolution is shown in Figure 17 (left) for phase volumes of 30% electrode (electron channel), 30% electrolyte (ion channel), 40% pore (gas channel) [31]. These began as a randomly disordered microstructure, but phase coalescence occurs and is controlled by the interparticle diffusion through microstructure. Over time, the experimental microstructural changes seem to be slowing down. The simulated microstructures are similar to those observed experimentally.

Figure 17 (right) shows the temporal evolution of TPB fraction for different three-phase volume fractions in SOFC electrode. In the early stages, a rapid decrease of the TPB is observed for all phase fractions. Over time, the TPB fractions seem to stabilize. These values are given for a specific set of energetic and kinetic parameters, which can be validated for specific systems using experimental comparisons. Interestingly, the magnitude of TPB fraction shows a significant dependence on the three-phase volume fraction. The significance of this should be emphasized with respect to the heterogeneities discussed above relative to the phase distributions and TPBs in commercial SOFCs. Since the phase volumes clearly affect the

evolution of microstructural features and electrochemical properties, coupling these together will require a concerted effort, especially when coupled. The important point to emphasize is that the missing piece of the puzzle is the integration of experiments and computations to address the coupled evolution problem, capturing the relevant information for specific heterogeneous systems. This report serves to highlight that the physical and computational models now exist to tackle the complex issues governing intrinsic degradation, which could also address extrinsic degradation.

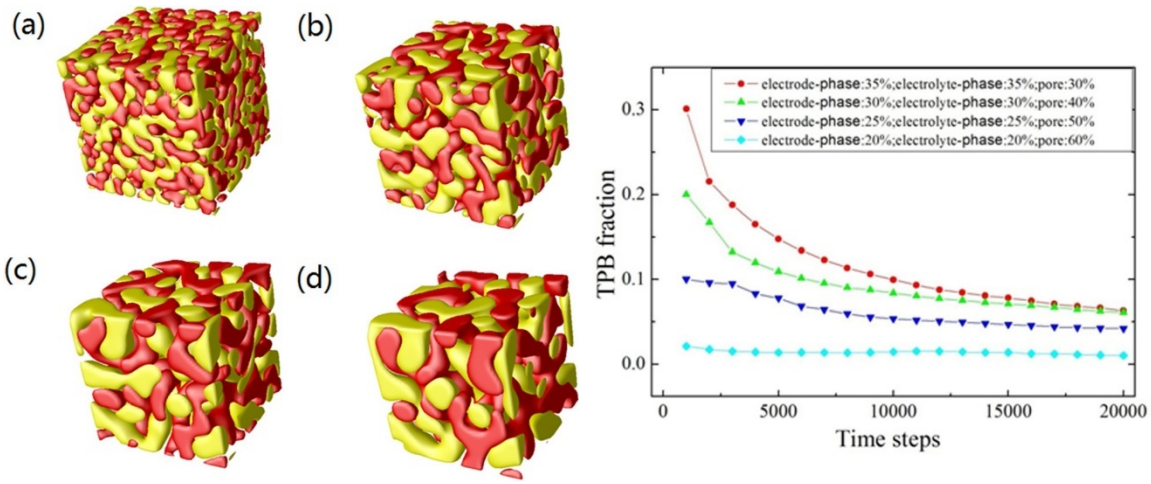


Figure 17. (Left) Temporal microstructural evolution in a three-phase SOFC electrode system at time step: (a) 1,000, (b) 5,000, (c) 10,000, and (d) 20,000. The electrode phase, electrolyte phase, and pore phase are represented in red, yellow, and transparent (volume fractions are 30%, 30%, and 40%, respectively). (Right) Temporal evolution of TPB fraction for different three-phase volume fractions with the fixed gradient coefficient $\kappa$! ($\kappa$! ) = (a) 1.5 (3.5) (Figure 16[b]) [31].

Recently, the phase-field model developed for three-phase cathode microstructures was extended to include an infiltrate phase of nanoparticles [32]. First, a three-phase LSM/YSZ cathode backbone microstructure was generated (for phase volumes of 33% electrode [electron channel], 33% electrolyte [ion channel], 34% pore [gas channel]), where the particle size was ≈1 μm. Then, small nuclei of infiltrate phase with particle size around 5 nm (small) or 10 nm (large) were randomly placed on the LSM and YSZ surfaces (with twice as much on YSZ as on LSM, and volume fractions the same for small and large particles). The temporal evolution of the small infiltrate system is shown in Figure 18 (left), where the nanoparticles have coarsened to ≈50–100 nm after 1.3 x $10^5$ time steps. Figure 18 (right), shows a comparison of 3PB density for non-infiltrated and infiltrated cathodes with different initial infiltrate particle sizes (infiltrates were considered to be the same as the electrode phase [LSM]. The initial TPBs are in accordance with intuition. The model shows that the 3PB density drops significantly owing to infiltrate coarsening at the initial stage, but stabilize over time. In all cases tested, the infiltrated cathode retained high 3PB length throughout the "operational lifetime," and always exhibited higher 3PB

densities than the as-fabricated cathode backbone. The smaller infiltrate particles give better cathode performance for a certain amount of infiltrate.

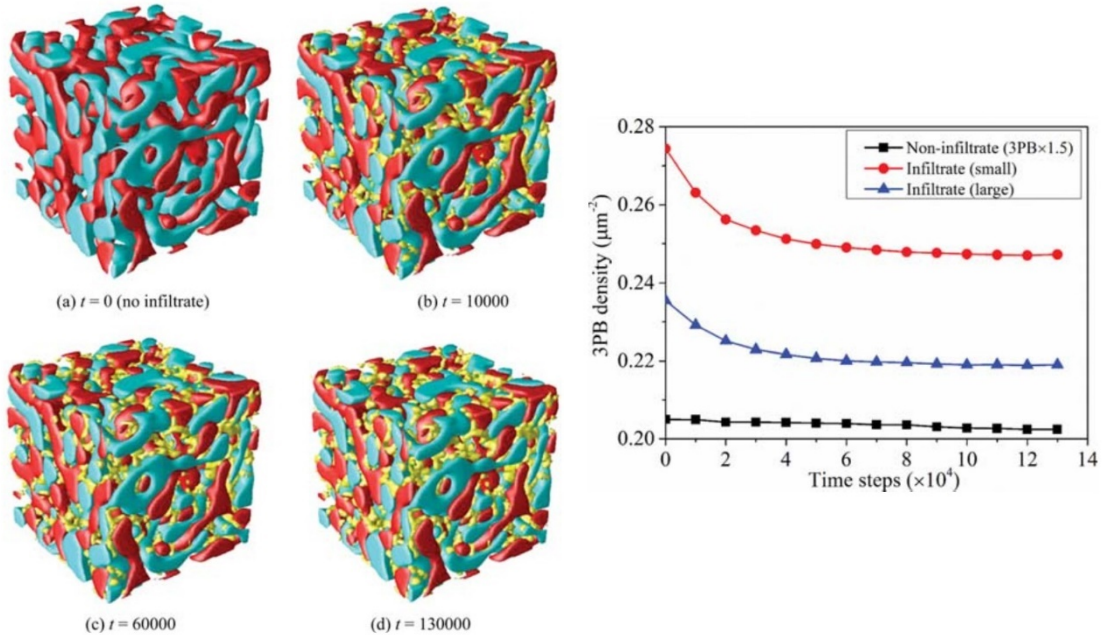


Figure 18. (Left) Temporal evolution of three-phase cathode microstructures infiltrated by nanoparticles (their sizes are around 50–100 nm after 1.3 x $10^5$ time steps, t). The red, green, transparent, and yellow color represents YSZ, LSM, pore, and infiltrate phase, respectively [32]. (Right) Comparison of the calculated 3PB density of backbone and infiltrated cathode as a function of time steps (with the values of 3PB density for non-infiltrated cathode electrostatic discharge multiplied by 1.5) [32].

## Summary and Outlook

In this report, we discussed important developments over the last few decades in microstructural science that allow for precise characterization of the local chemistry and structure at site-specific locations using analytical TEM, and for 3-D microstructures to be reconstructed. Advances in specimen preparation methods were also presented, focusing on FIB and laser milling for SOFC applications.

Building on these, a variety of recent studies related to the SECA program were used as examples of characterizing and understanding microstructures with a forward-looking perspective. In other words, these examples demonstrate that future integrated physical and computational experiments will afford predictive descriptions of SOFC degradation modes. For example, the Cr degradation investigations not only isolated the primary electrochemical problem but showed that, in aggressive poisoning environments, the degradation in LSM-based cathodes is highly non-uniform, indicating that electrochemical activity is clearly heterogeneous.

We discussed the primary focus of literature investigations of 3-D phase distributions in SOFCs, primarily focused on in-house prepared cells that have high uniformity. From these smaller volume areas, mostly from FIB-SEM, the average microstructure and average performance seem to be well correlated. Capturing non-uniformity and correlating it to local performance, is less well studied. However, a few examples are given that address phase and crystallographic distributions, indicating that capturing and analyzing features far from the mean is now becoming possible. 3-D XCT over a range of length scales are discussed to address homogeneity issues and their impact on SOFC models using reconstructed microstructures. We also addressed the crystallographic heterogeneities in SOFCs using 2-D and 3-D EBSD information to address grain size heterogeneities and microstructural energetics. Only small volumes have been reconstructed in 3-D to date, but it was shown that one can address crystallographic preferences of specific interfaces and phases, as well as the energetic driving forces for microstructural evolution, essential components in computational models that are rapidly improving. Lastly, a recent phase field model and the output of a host of computational investigations were presented, including both a three-phase cathode and an infiltrated three-phase cathode. Though these models were homogeneous (random initial structures), they can be applied to large more heterogeneous systems.

The important takeaway points are as follows:

- Modern microstructural characterization tools allow for full 3-D reconstructions of complex systems over a range of length scales with a range of spatial and temporal resolutions. It is possible to populate the complete crystallographic, phase, and energy landscape for SOFCs, with an appropriate set of samples to be explored.
- Commercial SOFCs are likely, for cost-related reasons, to be more heterogeneous than the typical cells prepared in-house by research outfits. For commercial cells purchased and used in SECA programs (InDEC and MSRI), the volume required to capture the average is larger than the typical FIB-SEM volume, as shown in the nano-XCT work herein, and reflected in the EBSD work. However, new methods are capable of addressing such large volumes and quantitatively analyzing the heterogeneities.
- Computational tools are ready to be informed by and benchmarked against real SOFC samples, especially targeting how the nature of heterogeneities impacts SOFC performance and degradation. By implementing the computational codes with proper structural heterogeneities and energetic/diffusive driving forces, structural evolution will be linked to computational performance throughout a real cell.

These takeaway points indicate that the outlook is very positive for capturing and modeling SOFC performance using realistic and heterogeneous microstructures. Currently, FIB-SEM methods are migrating from traditional ion sources for removal of material to so-called plasma-FIB methods and femto-second laser ablation methods, both which can be combined with EBSD to generate 30 nm resolution over volumes on the order of hundreds of microns in the same time as experiments discussed herein. Improvements in synchrotron beam lines and lab-scale X-ray sources will further increase the resolution and field of view for XCT. Computational

power is rapidly accelerating such that the questions previously off the table, so far as quantitatively addressing them, are quickly coming to the realm of accessibility. The rapidity with which these questions are addressed and with which the methods become generally available depends on the cohesiveness with which the various physical and computational programs move forward in a connected fashion.

## References


[1] N. Q. Minh and T. Takahashi, *Science and Technology of Ceramic Fuel Cells*. Elsevier, 1995.

[2] S. Singhal, "Advances in solid oxide fuel cell technology," *Solid State Ionics*, vol. 135, no. 1, pp. 305–313, Nov. 2000.

[3] P. Singh and N. Q. Minh, "Solid oxide fuel cells: Technology status," *International Journal of Applied Ceramic Technology*, vol. 1, no. 1, pp. 5–15, 2004.

[4] S. P. S. Badwal, S. Giddey, C. Munnings, and A. Kulkarni, "Review of Progress in High Temperature Solid Oxide Fuel Cells," *Journal of the Australian Ceramic Society*, vol. 50, no. 1, pp. 23–37, 2014.

[5] S. C. Singhal, "Solid oxide fuel cells for power generation," *Wiley Interdisciplinary Reviews: Energy and Environment*, 2014.

[6] L. Helmick, S. J. Dillon, K. Gerdes, R. Gemmen, G. S. Rohrer, S. Seetharaman, and P. A. Salvador, "Crystallographic Characteristics of Grain Boundaries in Dense Yttria-Stabilized Zirconia," *International Journal of Applied Ceramic Technology*, vol. 8, no. 5, pp. 1218–1228, Sep. 2011.

[7] L. Helmick, "Microstructural Characterization of Solid Oxide Fuel Cell Cathode Materials," *PhD Thesis, Carnegie Mellon University*, pp. 1–226, 2010.

[8] T. A. Cruse, B. J. Ingram, M. Krumpelt, S. Wang, and P. A. Salvador, "Effects of cell operating conditions on degradation by chromium," in *TMS Annual Meeting Supplemental Proceedings Volume Materials Processing and Properties*, TMS, 2008, pp. 573–579.

[9] M. Krumpelt, T. A. Cruse, B. J. Ingram, J. L. Routbort, S. Wang, P. A. Salvador, and G. Chen, "The Effect of Chromium Oxyhydroxide on Solid Oxide Fuel Cells," *J Electrochem Soc*, vol. 157, no. 2, pp. B228–B233, 2010.

[10] S. Wang, T. A. Cruse, M. Krumpelt, B. J. Ingram, and P. A. Salvador, "Microstructural Degradation of (La,Sr)$MnO_3$/YSZ Cathodes in Solid Oxide Fuel Cells with Uncoated E-Brite Interconnects," *J Electrochem Soc*, vol. 158, no. 2, p. B152, 2011.

[11] G. J. Nelson, W. M. Harris, J. J. Lombardo, J. R. Izzo Jr., W. K. S. Chiu, P. Tanasini, M. Cantoni, J. Van herle, C. Comninellis, J. C. Andrews, Y. Liu, P. Pianetta, and Y. S. Chu, "Comparison of SOFC cathode microstructure quantified using X-ray nanotomography and focused ion beam–scanning electron microscopy," *Electrochem Commun*, vol. 13, no. 6, pp. 586–589, Jun. 2011.

[12] J. R. Wilson, W. Kobsiriphat, R. Mendoza, H.-Y. Chen, J. M. Hiller, D. J. Miller, K. Thornton, P. W. Voorhees, S. B. Adler, and S. A. Barnett, "Three-dimensional reconstruction of a solid oxide fuel cell anode," *Nat Mater*, vol. 5, no. 7, pp. 541–544, Jun. 2006.

[13] D. Gostovic, J. R. Smith, D. P. Kundinger, K. S. Jones, and E. D. Wachsman, "Three- Dimensional Reconstruction of Porous LSCF Cathodes," *Electrochem Solid St*, vol. 10, no. 12, pp. B214–B217, 2007.

[14] D. Gostovic, N. J. Vito, K. A. O'Hara, K. S. Jones, and E. D. Wachsman, "Microstructure and Connectivity Quantification of Complex Composite Solid Oxide Fuel Cell Electrode Three-Dimensional Networks," *Journal of the American Ceramic Society*, vol. 94, no. 2, pp. 620–627, Nov. 2010.

[15] N. S. K. Gunda, H.-W. Choi, A. Berson, B. Kenney, K. Karan, J. G. Pharoah, and S. K. Mitra, "Focused ion beam-scanning electron microscopy on solid-oxide fuel-cell electrode: Image analysis and computing effective transport properties," *J Power Sources*, vol. 196, no. 7, pp. 3592–3603, Apr. 2011.

[16] J. R. Wilson, M. Gameiro, K. Mischaikow, W. Kalies, P. W. Voorhees, and S. A. Barnett, "Three-Dimensional Analysis of Solid Oxide Fuel Cell Ni-YSZ Anode Interconnectivity," *Microsc Microanal*, vol. 15, no. 1, pp. 71–77, Jan. 2009.

[17] N. Vivet, S. Chupin, E. Estrade, T. Piquero, P. L. Pommier, D. Rochais, and E. Bruneton, "3-D Microstructural characterization of a solid oxide fuel cell anode reconstructed by focused ion beam tomography," *J Power Sources*, vol. 196, no. 18, pp. 7541–7549, Sep. 2011.

[18] E. A. Wargo, A. C. Hanna, A. Çeçen, S. R. Kalidindi, and E. C. Kumbur, "Selection of representative volume elements for pore-scale analysis of transport in fuel cell materials," *J Power Sources*, vol. 197, pp. 168–179, Jan. 2012.

[19] P. R. Shearing, J. Golbert, R. J. Chater, and N. P. Brandon, "3-D reconstruction of SOFC anodes using a focused ion beam lift-out technique," *Chemical Engineering Science*, vol. 64, no. 17, pp. 3928–3933, Sep. 2009.

[20] H. Iwai, N. Shikazono, T. Matsui, H. Teshima, M. Kishimoto, R. Kishida, D. Hayashi, K. Matsuzaki, D. Kanno, M. Saito, H. Muroyama, K. Eguchi, N. Kasagi, and H. Yoshida, "Quantification of SOFC anode microstructure based on dual beam FIB-SEM technique," *J Power Sources*, vol. 195, no. 4, pp. 955–961, Feb. 2010.

[21] P. R. Shearing, J. Gelb, and N. P. Brandon, "X-ray nano computerised tomography of SOFC electrodes using a focused ion beam sample-preparation technique," *J Eur Ceram Soc*, vol. 30, no. 8, pp. 1809–1814, May 2012.

[22] J. Joos, T. Carraro, A. Weber, and E. Ivers-Tiffee, "Reconstruction of porous electrodes by FIB/SEM for detailed microstructure modeling," *J Power Sources*, vol. 196, no. 17, pp. 7302–7307, Sep. 2011.

[23] S. J. Dillon, L. Helmick, H. M. Miller, L. Wilson, R. Gemman, R. V. Petrova, K. Barmak, G. S. Rohrer, and P. A. Salvador, "The Orientation Distributions of Lines, Surfaces, and Interfaces around Three-Phase Boundaries in Solid Oxide Fuel Cell Cathodes," *Journal of the American Ceramic Society*, vol. 94, no. 11, pp. 4045–4051, 2011.

[24] J. Laurencin, R. Quey, G. Delette, H. Suhonen, P. Cloetens, and P. Bleuet, "Characterisation of Solid Oxide Fuel Cell Ni-8YSZ substrate by synchrotron X-ray nano-tomography: from 3-D reconstruction to microstructure quantification," *J Power Sources*, vol. 198, pp. 182–189, Jan. 2012.

[25] J. R. Smith, A. Chen, D. Gostovic, D. Hickey, D. Kundinger, K. L. Duncan, R. T. DeHoff, K. S. Jones, and E. D. Wachsman, "Evaluation of the relationship between cathode microstructure and electrochemical behavior for SOFCs," *Solid State Ionics*, vol. 180, no. 1, pp. 90–98, 2009.

[26] N. Shikazono, D. Kanno, K. Matsuzaki, H. Teshima, S. Sumino, and N. Kasagi, "Numerical Assessment of SOFC Anode Polarization Based on Three-Dimensional Model Microstructure Reconstructed from FIB-SEM Images," *J Electrochem Soc*, vol. 157, no. 5, p. B665, 2010.

[27] J. R. Wilson, J. S. Cronin, A. T. Duong, S. Rukes, H.-Y. Chen, K. Thornton, D. R. Mumm, and S. Barnett, "Effect of composition of (La0.8Sr0.2MnO3–Y2O3-stabilized ZrO2) cathodes: Correlating three-dimensional microstructure and polarization resistance," *J Power Sources*, vol. 195, no. 7, pp. 1829–1840, Apr. 2010.

[28] Q. Liu, S. Bhattacharya, L. Helmick, S. P. Donegan, A. D. Rollett, G. S. Rohrer, and P. A. Salvador, "Crystallography of Interfaces and Grain Size Distributions in Sr-Doped LaMnO3," *Journal of the American Ceramic Society*, vol. 97, no. 8, pp. 2623–2630, Aug. 2014.

[29] J. H. Kim, W. K. Liu, and C. Lee, "Multi-scale solid oxide fuel cell materials modeling," *Computational Mechanics*, vol. 44, no. 5, pp. 683–703, Oct. 2009.

[30] H.-Y. Chen, H.-C. Yu, J. S. Cronin, J. R. Wilson, S. A. Barnett, and K. Thornton, "Simulation of coarsening in three-phase solid oxide fuel cell anodes," *J Power Sources*, vol. 196, no. 3, pp. 1333–1337, 2011.

[31] Q. Li, L. Liang, K. Gerdes, and L.-Q. Chen, "Phase-field modeling of three-phase electrode microstructures in solid oxide fuel cells," vol. 101, no. 3, p. 033909, 2012.

[32] L. Liang, Q. Li, J. Hu, S. Lee, K. Gerdes, and L.-Q. Chen, "Phase field modeling of microstructure evolution of electrocatalyst-infiltrated solid oxide fuel cell cathodes," *Journal of Applied Physics*, vol. 117, no. 6, pp. 065105–8, Feb. 2015.

## **Modeling Cathodes of Solid Oxide Fuel Cells** *by Paul A. Salvador (Carnegie Mellon University)*


### Summary

Over the past few decades, activity in the field of modeling basic scientific processes and complex engineered systems has seen an incredible expansion and generated an impressive set of advances in understanding and capabilities. Still, we have yet to realize the full promise of modeling for SOFCs. The challenge is, of course, the incredible complexity of the SOFC, which requires models to capture electrochemical and transport processes across widely varying temporal and spatial scales, and to couple together the individual processes into a coherent whole. Though the task is formidable, should an appropriate scale-bridging multi-physics models be developed, the design and optimization of efficient, durable, cost-effective SOFCs would be revolutionized.

In this report we break down the challenge to modeling the SOFC cathode, in which a significant portion of the SOFC loss occurs in operation and, therefore, represents a large reward to SOFC design if successful. First we describe the modeling challenge, and break the issues into ab initio models of energetics, microstructural models of coupled transport equations, and micro-kinetic models and continuum descriptions of SOFC behavior.

We focus largely on the first area, because ab initio modeling of electrochemistry on complex oxides is maturing at an impressive rate. Specifically, we first describe the relative facility of screening thermodynamic properties as functions of chemistry and strain, briefly addressing the methodologies required for cathodes. Next, these energies are built into full-scale defect models and compared favorably to known cathode defect chemistry in operational conditions. From there we discuss computation of transition state energies and their utility in predicting (modeling) reaction pathways and transport parameters (exchange and diffusion coefficients). Throughout, we demonstrate how one can use large-scale data sets to generate simple descriptors of performance. All of this data can ultimately be provided upward to coarser scale models, though some scale-bridging work is needed, and that has not seen much growth.

The area of full-scale microstructural modeling of electrochemical properties is in its beginning stages, but it should allow the description of both average performance and the local deviations from average in cathodes, holding great promise in the isolation of degradation mechanisms. We present some initial reports on these areas. In contrast, phase field models of microstructural evolution are well developed in other areas of science, and we present their applications to microstructural evolution of bare and infiltrated cathodes. These results together indicate that performance and evolution can ultimately be coupled in full-scale 3-D models.

The area of continuum modeling SOFCs is, in contrast to the prior areas, relatively mature. We describe newer approaches that include microstructural properties in effective medium models, which aim to describe the relative importance of all competitive electrochemical and

transport pathways. These coarser scale models also hold promise to describing durability if one can model the behavior of heterogeneities throughout the large volume of the cathode over which boundary conditions (thermodynamic and electrochemical) vary considerably. In each case, we describe the recent work and allude to the promise of the near-term future.

## Introduction

SOFCs are, at their core, a conceptually simple device that converts chemical energy to electrical energy via the controlled electrochemical oxidation of a fuel [1–8]. The overall reaction mechanism of an individual SOFC is shown in Figure 1 [9]. An SOFC has two electrodes sandwiching an oxide ion ($O^{2-}$) conducting electrolyte and an outer circuit connecting the two electrodes. Diatomic oxygen gas ($O_2$) is reduced to oxide ions within the cathode using electrons from the circuit; the ions transport across the electrolyte to the anode. In the anode, the fuel ($H_2$ in Figure 1) is oxidized ($H^+$), releasing electrons to the outer circuit, and reacts with the oxide ions to form the oxidation product ($H_2O$). The efficient conversion of fuels to electricity is the attractive feature driving fuel cell development [1-8].

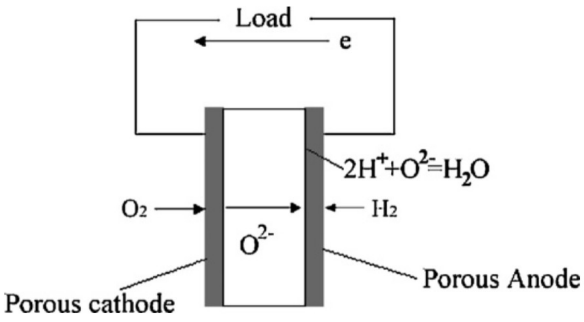


Figure 1. A schematic of an SOFC operating on hydrogen fuel (from [9]).

SOFCs have been known since the mid-1800s but have not yet gained traction as commercially viable large-scale energy conversion devices [1–8]. This is because, in reality, they are complex, highly engineered systems that require optimization of (and between) macro- and micro- and atomic-scale physical processes in a multi-component, complex geometrical system. Much of the design and optimization process has been carried out empirically over the hundred plus years of investigations. Such investigations have brought SOFCs to the precipice of commercialization, but the strict requirements on performance over the expected lifetimes at reasonable costs (required to impact the commodity electricity market) still pose a challenge. In the last few decades, however, computational modeling has been developed that promises new directions for improved optimization of fuel cells [9–16], both individually at every scale and across scales. Computations promise to open design avenues by exploring performance space more quickly than experiments can, as well as generating underlying understanding of

scientific and material trends. This is especially true in the degradation and lifetime areas, because it is nearly impossible to run 5–10 yr tests in operational conditions since accelerated tests are known to promote processes not active in operational conditions [1–8], and the timescale is not efficient in the design cycle.

SOFCs are essentially electrochemical transport devices, which require transport of mass, charge, and heat. Mechanistically, these transport processes range across both temporal and spatial scales [9–20], and they are coupled to each other in various fashions. In time, they range from femtoseconds to several years, depending on the nature of the transport and the driving forces. In space, they range from sub-angstrom electronic processes to centimeter scale transport through the entire cell (and larger if one considers systems) [9, 12, 16–20]. As such, complete modeling of SOFCs requires one to model individual processes at their relevant temporal and spatial scales, to bridge across these scales, and to couple together the individual processes into a coherent whole.

A host of modeling and simulation platforms exist that are appropriate to tackling optimization of SOFCs. Figure 2 plots some of the relevant modeling platforms versus (on the horizontal axis) the time and length scales that can be resolved [12]. The location of the platform on the vertical axis represents the computational cost (time). The length scales of the important features in an SOFC are plotted schematically at the base of Figure 2 [12]. There is not one single appropriate modeling approach to capture SOFC performance and/or design.

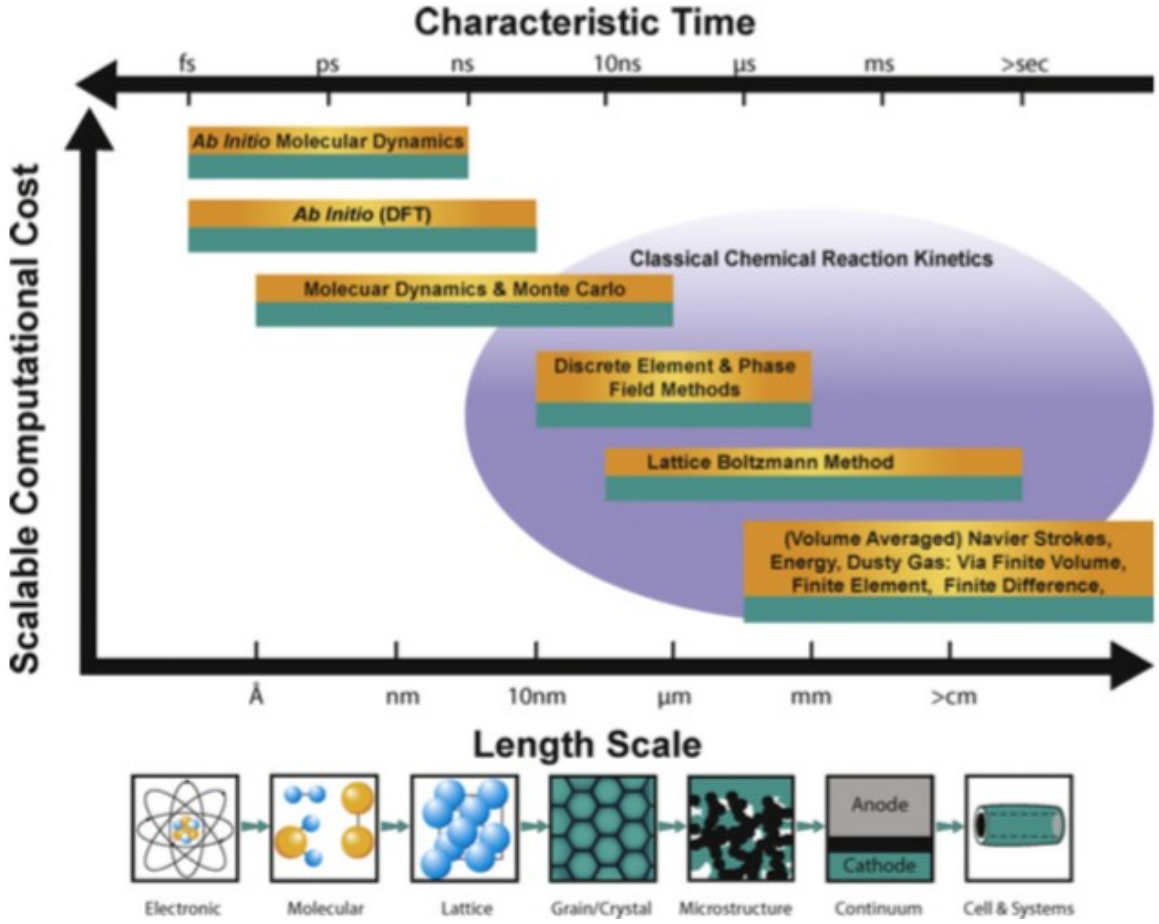


Figure 2. A plot of several SOFC modeling methods with regard to their computational cost versus the time and length scales that can be resolved (from [12]).

Several excellent reviews [9–19] are available that cover modeling at different scales for SOFCs. Though there is much work still to be done at the individual process level, the near-term modeling challenges are in bridging the time and length scales (often called scale bridging) and coupling different processes together (often called multi-physics modeling). Should an appropriate scale-bridging multi-physics model be developed, the design and optimization of efficient, durable, cost-effective SOFCs would be revolutionized. This is essentially the holy grail of modern engineering: computational design integrated with experimental verification of inputs, models, and predictions, to accelerate technological development.

In this report, we discuss modeling electrochemical processes within the cathode of an SOFC. The cathode is a two- or three-phase material that is responsible for carrying out the oxygen reduction reaction (ORR), which involves gas, ion, and electron transport [9, 13, 21, 22]. Gas transports to the electrochemically active sites through pores, and ions and electrons can

travel through one or two solid phases, depending on the cathode design. Schematics of how the ORR proceeds locally at the cathode/electrolyte interface are shown in Figure 3(a–c) for different cathodes [21]. A scanning electron microscopy (SEM) image of a porous two solid phase composite is shown in Figure 3(d), giving an idea to the realistic length scales in commercial SOFCs. Recent studies have identified that up to 80% of total fuel cell efficiency loss is due to cathode polarization caused by sluggish ORR kinetics [1]. In other words, improved understanding, modeling, and design of SOFC cathodes offers a large return on SOFC optimization. This requires an improved understanding of chemical reaction kinetics using appropriate models (see purple oval of Figure 2). What is clear, as will be seen later, is that various pathways compete at the local levels at all length scales, which renders modeling cathode performance not just a matter of getting a single sub-process correct, but of generating details of the ensemble of processes and appropriately integrating them.

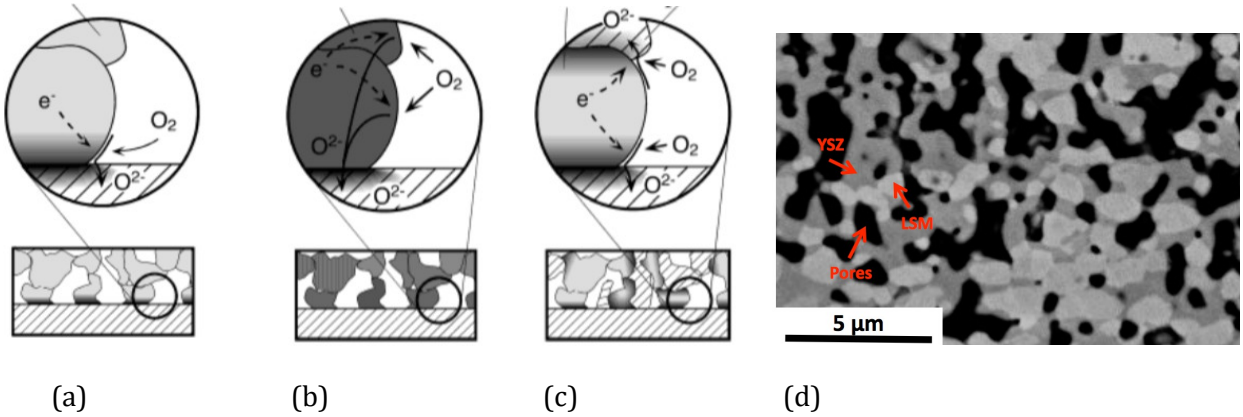


Figure 3. (a-c) Schematics of the ORR in common cathode configurations: (a) a porous electronic conductor oxide; (b) porous mixed conductor; (c) porous two-phase composite [21]. (d) a back-scattered electrons image from a porous two-phase composite (YSZ = yttria stabilized zirconia, LSM = lanthanum strontium manganese oxide).

In this report, we present some of the recent work on modeling SOFC cathodes across the relevant time and length scales. We break these down similarly to other researchers [9–20, 23]. First we present work using ab initio density functional theory, highlighting some of the important results of late. Then we look at micro-structural scale modeling of cathodes using multi-physics to capture performance and phase field modeling to capture evolution of microstructures. Finally, we discuss micro-kinetic reaction pathway models that govern the ORR from a measurable cell and other continuum level descriptions of cathode performance. The goal is to give a snapshot of modeling possibilities to motivate continued development of models, especially into the scale-bridging and commercially important sector of degradation modeling. Of course, to tackle these latter challenges, one must first demonstrate successes at the individual processes steps. We will focus on the ab initio and microstructural models, because these promise to bridge upwards to the micro-kinetics/continuum models. We should

note that we will focus on results from modeling rather than the details of models or modeling methods themselves.

## Ab initio Density Functional Theory

Perhaps some of the most impressive advances in modeling over the past 20 years have been in the area of ab initio modeling of complex oxides, especially perovskites. Technique developments, computational advances, and closer interactions and verification with physical experimentation has greatly improved the applicability of modeling to real world problems (including impressive predictive powers) and increased the sophistication of problems being tackled using ab initio modeling. The real attraction of ab initio modeling of SOFCs has to do with its ability to isolate and provide an energetic value for specific states (adsorption, defect formation, etc.). Considering the complexity of the ORR in SOFCs, involving multiple potential pathways (see Figure 3) that often have many sub-steps that can be rate limiting (see the section on continuum modeling), such information is incredibly important. Experimentally, many of the relevant values are challenging or impossible to access directly, especially energetics of surface processes in operational conditions. As ab initio models produce energetic values that predict/model relevant properties and processes, their values can be used to improve microstructural or continuum level models. Also, property trends and descriptors of performance can be extracted from ab initio studies, even using materials or physical states that are difficult to access (but relevant to generating understanding), which promise accelerated material development. These ideas are discussed further below.

A small sub-set of references on ab initio modeling of interest to SOFC work is given here: [11–13, 20, 24–50]. Within those references are a host of more foundational works for the interested reader (the literature is quite expansive). The primary ab initio model used for complex oxides is density functional theory (DFT), whether the modeling is focused on computing dielectric, magnetic, electronic, catalytic, or structural properties. DFT provides an energy value (essentially something like the total energy of the electrons in the system) for the model under consideration, and the energy value is dependent on both the model and the functional employed in the computations. As with all experimentation (whether physical or computational), one must understand the uncertainties in values and the appropriateness of adopting a determined value outside its applicability. More importantly, there are several known challenges in using DFT to model materials of relevance to SOFC cathodes. Ni-, Mn-, Co-, and Fe-containing oxides are known as strongly correlated electron systems, and a variety of functionals and additional parameters (such as the U parameter) have been developed to improve the model outputs for such correlated electron systems (which the assumptions in DFT generally have difficulty handling). Some of this will be briefly discussed below.

The range of parameters modeled with DFT spans the electronic structure and phase stability of bulk materials; the surface energies and preferred surface termination and reconstructions of specific surfaces; the bulk and surface defect formation energies; the transition state energies underlying transport and reaction processes; strain effects on many of these energies; molecular interactions with surfaces; and much more. Here we highlight some

examples that move beyond individual determinations of specific values (which was carried out in the early days of ab initio measurements) and focus on broad data sets generating predictive trends, expansive models generating full thermodynamic models of materials, determination of transition state values to parameterize transport properties, and mining massive data sets to generate fundamental descriptors that predict the utility of new materials as SOFC cathode components. The chosen examples are not meant to be exhaustive, rather we find them to be exciting examples of how ab initio modeling is tackling important issues in SOFC cathode science. The goal is to establish the maturity and robustness of ab initio methods such that they can serve as the finest scale modeling of SOFCs, serving as a foundation on which the coarser scale models can be improved.

**Energetics of Fundamental Processes and Performance Descriptors**

One of the more robust uses of DFT is in the determination of energies for fundamental processes, such as vacancy formation energies or adsorption energies. In the area of materials design, one aims to generate descriptors that can be used for screening potential new materials. In the area of catalysis on metal surfaces, there are simple models (such as the *d*-band center) that relate the surface composition, surface structure, and electronic structure of metals and alloys to their reactivity (such as adsorption energies), including how strain or coverage modify reactivity. With the maturation of DFT in perovskite oxides, it is now possible to generate such descriptors for cathode activity, though one needs to survey a large compositional space across a large computational space of comparable DFT quantities. Kitchin's group has explored the role of a large number of material and computational parameters on the bulk and surface properties of perovskite oxides [27, 29, 51] to extract some descriptors. Here we focus on the trends.

In the left panel of Figure 4, the dissociative surface oxygen adsorption energy and surface vacancy formation energies are plotted as a function of *d*-band filling (i.e., *B*-cation in the $ABO_3$ perovskite) for both $LaBO_3$ and $SrBO_3$ series [29]. The figure exhibits reactivity trends based on the number of *d*-electrons of the *B* atom. The reactivity energetics of both families of perovskites mostly display a systematic linear scaling with the number of *d*-electrons of the *B* atom, except when the *d*-band of the *B* atom is empty ($LaScO_3$ and $SrTiO_3$). While the surface oxygen adsorption is more favored on $LaBO_3$ surfaces, $SrBO_3$ surfaces offer easier formation of surface oxygen vacancies [29]. This suggests that the effect of the oxidation state depends on the type of reactivity, and that some optimization may occur in mixed systems. However, because these energies are correlated, they cannot be independently modified for these materials.

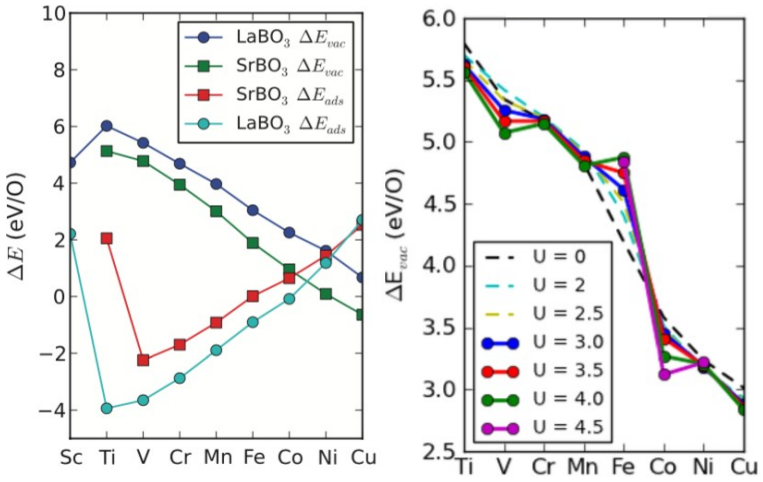


Figure 4. (Left) Perovskite reactivity trends of surface oxygen adsorption and vacancy formation relative to the number of *d*-electrons of the *B* atom [29]. (Right) Bulk vacancy formation energy using different U values relative to the number of *d*-electrons of the *B* atom in La*B*$O_3$ [27].

A set of bulk oxygen vacancy formation energies is plotted in the right panel of Figure 4 [27] for La*B*$O_3$, this time using different values of the Hubbard *U* correction term. What is clear from this plot is that the Hubbard *U* term, which is important to properly capture electron correlation effects, modifies the systematic trend from the *U*=0 case (*U* was zero in the calculations done in the prior study). There are particularly large effects for *B*=V, Fe, and Co, where the relative ordering with their neighbors can be reversed (see V-Cr, Fe-Mn, and Co-Cu). Unfortunately, choosing the correct *U* is usually done by fitting computations to specific experimental properties one hopes to accurately model, and is done on a material to material basis. However, Curnan and Kitchin used self-consistent computational approach to determine an appropriate *U* value for each composition [27], an approach that seems promising to generate self-consistent trends that capture electron correlation effects more accurately. Nevertheless, care must be applied in interpreting and applying outputs in these correlated electron systems.

One area of interest in SOFC design is understanding the role of strain in performance, because thin film studies have shown that strained films have very different transport and electronic properties when compared to bulk materials or relaxed films [52–54]. Because strain modifies the local volume and bonding environments, one expects the energies to be perturbed. The role of strain on properties is relatively straightforward to explore using DFT, as it is straightforward to constrain the volume in different fashions and compute the energy. The strain dependence of the surface oxygen vacancy formation energy ($E_{vac}$ [O]) (a) La*B*$O_3$ (001) and (b) Sr*B*$O_3$ (001) surfaces is shown in Figure 5 [29]. The vacancy formation energies are expressed as differences relative to the vacancy formation energy of an unstrained surface. The effect of compressive strain generally lowers the oxygen vacancy formation energy, and

tensile strain generally increases the oxygen vacancy formation energy. The mechanism of strain-modulated reactivity was correlated to strain-induced changes in the *d*-band width and *d*-band center [29], in approximate agreement with a rectangular band model. However, relaxation effects at the surface significantly affect the quantitative agreement with the simple model, and have significant effects on the trends observed in reactivity. The potential impact of *U* values on the trends remains to be seen. However, these high-throughput models generate incredible amounts of data (presented here is a small fraction of the papers, as is true with the other studies discussed below).

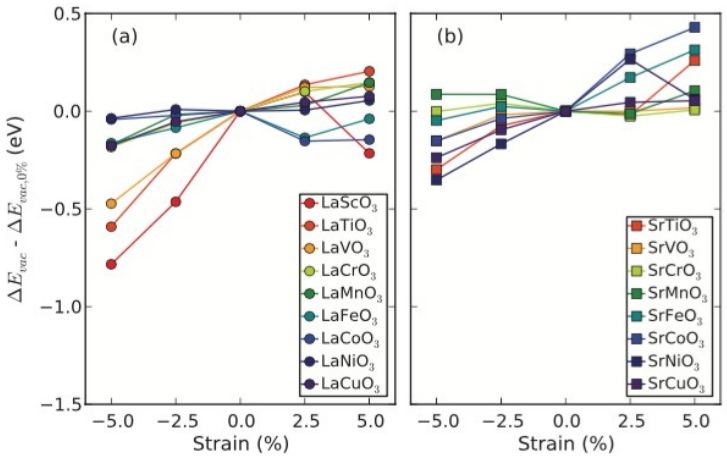


Figure 5. Strain dependence of the surface oxygen vacancy formation energy ($E_{vac}$ [O]) of α–$BO_2$ terminated (a) La$BO_3$ (001) and (b) Sr$BO_3$ (001) surfaces strained to ±5, ±2.5 and 0% of the DFT equilibrium volume. The vacancy formation energies are expressed as differences relative to the vacancy formation energy of an unstrained surface [29].

Morgan's group has been pioneering the use of DFT to model important parameters associated with reactivity of SOFCs [24, 28, 30, 34, 39, 41, 42], including the generation of descriptors for performance [30]. Again, the descriptor approach searches for a functional relationship between a simple calculated property and catalytic activity. Morgan's group searched for an electronic structure descriptor for the ORR activity of electron-rich perovskite cathodes and found that the energetic location of the bulk *p*-band center was a descriptor with strong positive correlations to many relevant ORR properties. Two such correlations between calculated *p*-band centers and experimentally determined properties are shown in Figure 6. On the left is a plot of the area specific resistance (ASR) measured experimentally versus the *p*-band center determined computationally. The ASR is a characteristic resistance describing the contribution to the cell impedance from the cathode ORR and it is therefore a measure of the catalyst's overall ORR activity, including both surface

and bulk kinetic processes [30]. On the right is a similar plot of the oxygen surface exchange measured experimentally versus the *p*-band center determined computationally. Incorporation of oxygen in the cathode surface is considered to play a fundamental role in the SOFC ORR, and *k** values correlate with ORR activity. In both cases, strong positive correlations are observed, even though these parameters are lump parameters (involving many fundamental sub-steps).

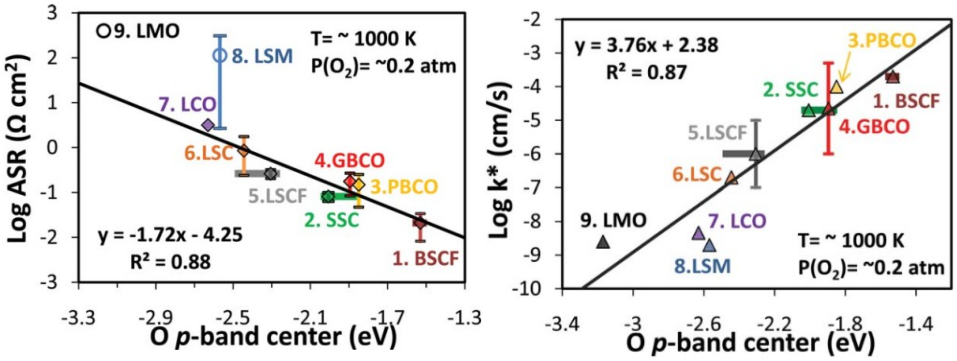


Figure 6. Experimental (left) ASR at ≈1000 K and (right) surface exchange coefficients (*k**) measured under $P(O_2)$ = 0.2–1.0 bar at T ≈ 1000 K vs. the calculated bulk O p-band center of perovskites. Experimental ASR and *k** data come from references given in [30]. The range of the calculated O p-band centers are represented with horizontal bars [30].

All of the above results imply that bulk calculations of materials, which generate the shape and location of the *p*-bands (oxygen) and *d*-bands (metal), may predict the performance of new materials. While the *p*-band center model fit the surface exchange properties better than the *d*-band center model [30], the *d*-band model fit underlying fundamental processes well [27, 29, 51]. It may be that both descriptors are valid for different processes, or that one is preferred. More experiments are needed to differentiate between these hypotheses.

**Ab-initio Modeling of High-Temperature Defect Chemistry**

Even though Sr-doped $LaMnO_3$ has been intensely investigated experimentally, there is considerable disagreement in the values of fundamental parameters of interest in modeling. For example, extracting the defect reaction enthalpies from experimental measurements of non-stoichiometry leads to a significant spread in the value of the thermodynamic parameters. Another way to state this is that many models can fit the experimental data, and the adjustable parameters have a wide spread in values, depending on the model. Morgan's group used a combination of ab initio and empirical models to describe the non-stoichiometry of the well-studied $LaMnO_3$ system [28]. The model explicitly calculates the reaction enthalpies and entropies with ab initio methods in the solid phase, while empirical values were used to model

$O_2$ gas. The upper panel of Figure 7 shows the results of the $\Delta G_{rxn}$ vs. $P(O_2)$ at T = 1000 K for 12 defect reactions. The defect reactions are given in Kröger-Vink notation using a small polaron model. To generate a full defect model, reactions where $\Delta G_{rxn}$ was low over some range of $P(O_2)$ (12, 9, 1, and 2, which are depicted with thick lines) were considered. Ultimately, the model included reactions 1, 2, and 12 (reaction 9 requires an A-site vacancy, whose populations are low, so it was excluded).

The lower left panel of Figure 7 compares the non-stoichiometry of the model derived using ab initio energies to the measured values reported elsewhere ([55] and [56]). A very good fit is obtained between this ab initio model and the experimental data [28]. This provides a set of ab initio based defect reaction energies that can be used for accurate modeling of the LMO system, greatly reducing the uncertainty in the key defect reaction energies for this material. Although the non-stoichiometry fit well, the electronic and ionic transport properties based from this model were less accurate. However, an empirical modification to the temperature dependent charge disproportionation energy could be used to tune the model predictions such that both the oxygen tracer diffusion activation barrier and the oxygen non-stoichiometry vs. $P(O_2)$ was in good agreement with the experimental values. The non-stoichiometry of the modified model is compared with the measured values in the lower right panel of Figure 7. These fits are similarly good (but the diffusion values are better) to the pure ab initio model. This framework for modeling defect thermodynamics initiated from ab initio calculations will help resolve and understand defect chemistry of many complex oxide systems [28], while providing self-consistent computational values of thermodynamic quantities to micro-scale and continuum level modeling efforts.

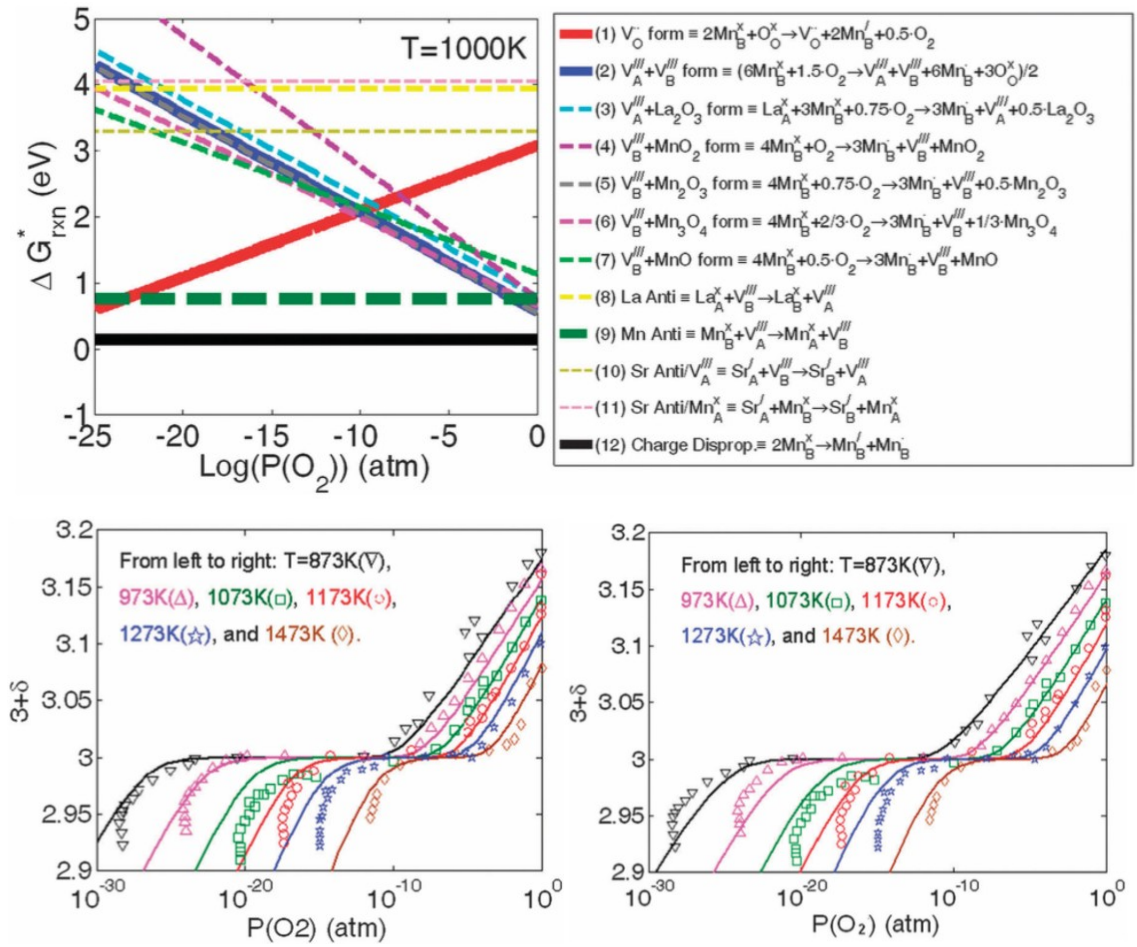


Figure 7. (Top) 12 defect reaction free energies calculated vs. P(O2) at T = 1000 K. (Bottom) Predictions of LaMnO3 oxygen non-stoichiometry vs. P(O2) based on a defect model using (left) ab initio defect energetics (solid lines) and (right) the same but with modified temperature dependent charge disproportionation energies. The defect model includes reaction (1), reaction (2), and reaction (12) [28]. The experimental points are from [55] and [56].

**Transition State Theory and Rate Constants**

Our examples above focused on the use of ab initio methods to compute fundamental energetics of defect species, to generate descriptors of performance, and to construct comprehensive defect models built by combining several individually computed reaction energies. However, transport and reaction processes are often limited by the barriers that exist between two distinct stable states. In this section we describe the use of ab initio models to calculate these barriers, as well as to incorporate the barrier energies into kinetic descriptors of reaction and transport. Modeling of transition state theories for catalysis is widely done in metals, and complex oxides are now coming up to speed.

Maier and co-workers have been very active in the development and application of ab initio modeling to understand SOFC cathodes (see for example references [11, 37, 40, 46, 47] and the further references within their thorough review [11]). In particular, they have extensively modeled the surfaces of $LaMnO_3$ [46, 47] and the oxygen incorporation reactions [11, 37] (among other things). The black lines in Figure 8 show the energetic landscape computed with DFT for one of the possible multi-step reaction pathways for oxygen exchange (incorporation), which includes molecular adsorption (exothermic) and dissociation (on a native surface) of the molecular oxygen species to two $O^-$ surface species (with a computed barrier of 0.6 eV). Incorporation occurs when a surface vacancy and $O^-$ species meet. Their results indicate that surface vacancies have a lower barrier for migration (0.7 eV) than do $O^-$ species (2.0 eV). Thus, the oxygen vacancies migrate until they approach the $O^-$, and incorporation of $O^-$ into a neighboring vacancy is a barrier-free process. This step can be rate limiting because the number of oxygen vacancies is very low for $LaMnO_3$ [11, 37].

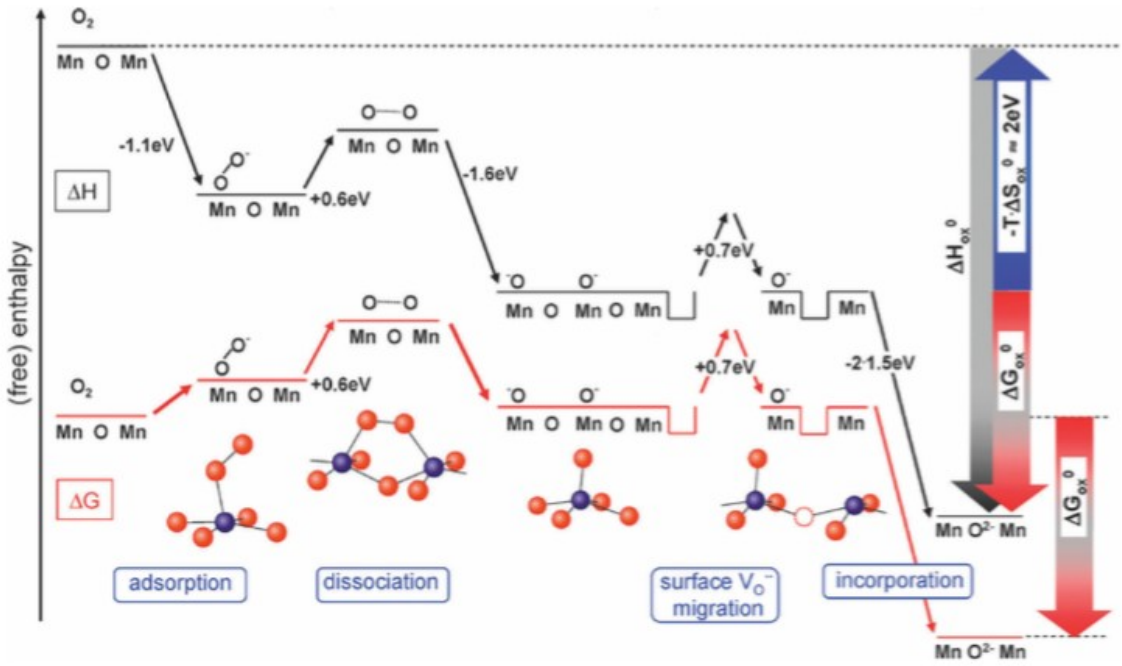


Figure 8. One potential reaction pathway for oxygen incorporation into $LaMnO_3$. The black line shows the electronic energy profile (ΔH); the red line corresponds to a semi-quantitative free energy profile (ΔG) [11, 37].

The picture described above does not include the strongly negative entropic contributions to oxygen incorporation (exchange), which arise from loss of translational/rotational degrees of freedom of the $O_2$ molecule, primarily on adsorption [11, 37]. The red lines in Figure 8 correspond to a (semi-quantitative) estimate of the Gibbs free energy profile. Similar approaches were carried out for

different reaction pathways [11, 37]. These models are similar to the semi-quantitative models of defect chemistry discussed above. They can be used to determine both the concentrations of oxygen vacancies and adsorbate coverage in different conditions. Reaction rates were estimated as a function of the concentration of molecular adsorbates and surface oxygen vacancies, based on the energies of the $O^-$ intermediates, corresponding adsorbate coverages, and reaction barriers (combined with standard attempt frequencies) [11, 37]. The rate of different pathways are shown in different planes in Figure 9: the pink/violet planes correspond to the pathway shown in Figure 8. The black lines represent expected values for $La_{0.8}Sr_{0.2}MnO_{3-d}$ (LSM) in high $pO_2$s, and the rate limiting step is the approach of surface vacancy to the nearly immobile $O^-$. Both the vacancy concentration and mobility are predicted to be decisive in this region (it is near the cusp in the plane). The authors used the same plot to extrapolate where $La_{0.58}Sr_{0.4}Co_{0.2}Fe_{0.8}O_{3-\delta}$ (LSCF) would be expected to exist in this plot (red lines), demonstrating that a different rate limiting step is at work [11, 37]. Much of these observations are in line with experimental work.

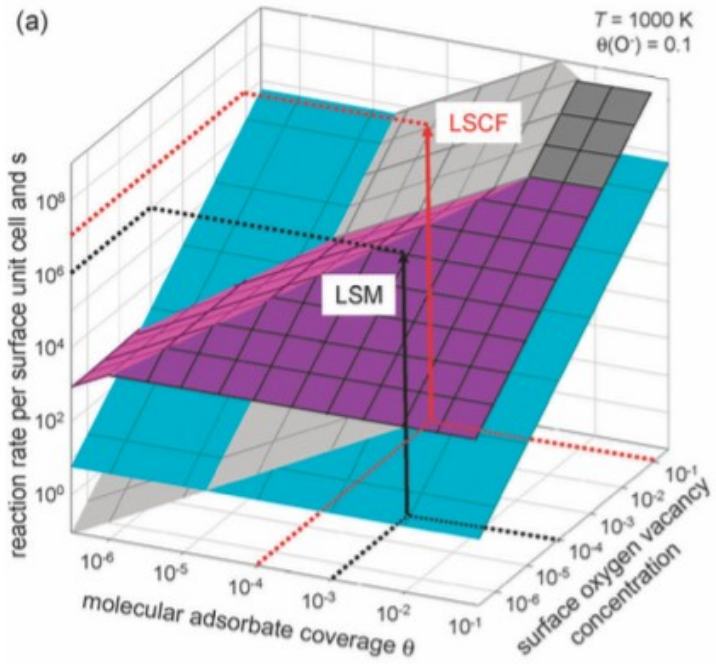


Figure 9. An estimate of the reaction rates for the alternative reaction pathways (different color planes) of oxygen incorporation on the LSM (based on DFT energies for intermediates and barriers). The adsorbate coverage and surface vacancy concentration are given as molar fractions. The black line indicates the LSM path, and the red represents an extrapolation for LSCF [11, 37].

As with the ab initio models of defect chemistry, a coherent picture of reactivity (incorporation or exchange) can be built up from a large computational foundation, assuming the computations are self consistent and the thermodynamic models are complete (even if the gas phase is empirically or semi-quantitatively treated). One can compute individually a range of reaction pathways and sub-processes, and integrate them into a cohesive whole that no longer has an individual value or solution, but a range of solutions that depend quantitatively and consistently on computed parameters of the model. Integrating these solution libraries into for micro-scale and continuum-level models will capture the complexity of the ORR much more accurately, especially with regard to spatially varying performance associate with degradation in SOFCs.

Liu's group at Georgie Tech has also widely implemented ab initio models to understand the performance of SOFC cathodes, especially $LaMnO_3$ based cathodes (see [13, 20, 45, 57] and reference therein). Here we highlight their work related to the current discussion. Whereas the last example related to using DFT to model surface exchange (*k*) reactions using transition state theory, Liu's group did similar work to model diffusion in LSM based materials. Figure 10 describes the results of DFT modeling oxygen diffusion in the (110) plane (highlighted in Figure 10 [a]) in LSM. The trajectory of the oxygen (or vacancy) is shown in Figure 10 (b). The energy of the initial ($O_1$), final ($O_2$), and intermediate states are shown in Figure 10(c). The computed migration barrier was found to be lower than experimental activation energies of activation energies of secondary ion mass spectrometry diffusion. The authors computed an activation energy (Ea) that was equal to the sum of the migration barrier with the vacancy formation energy, and this yielded satisfactory agreement for several different materials. The important aspect of using ab initio computations is that the separate components of experimental processes can be de-coupled, hopefully generating a more complete understanding of the physical processes, as well as affording new design criteria.

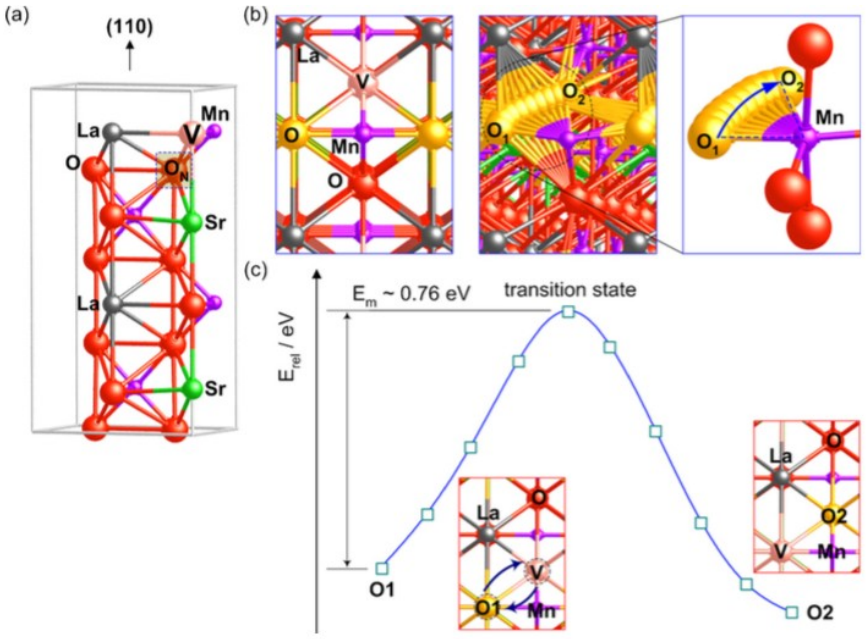

Figure 10. (a,b) Illustration of LSM (110) structures (a), the surface model and (b) bulk before and after ionic conduction. V and $O_N$ (N = 1 or 2) are, respectively, an oxygen vacancy and the nearest neighboring oxygen to V. (c) Trajectory and energy of oxygen ion conduction through LSM. $O_1$ and $O_2$ are the initial and final states of the oxygen [13, 20].

Along these lines, the authors then computed the energetics of oxygen interactions on (100) surfaces of a range of cathode materials, as well as the diffusion barriers (similar to above). Figure 11 plots the activation energy for diffusion versus the oxygen adsorption energies (averaged as adsorption energies of superoxo- and peroxo-like species on B cations) [13]. A strong correlation exists between the two values. The best cathodes ($La_{0.5}Sr_{0.5}CoO_{3-\delta}$ and $Sm_{0.5}Sr_{0.5}CoO_{3-\delta}$) exhibit both weak oxygen binding and low barriers to diffusion. This shows that a variety of correlations and predictive descriptors can be uncovered, aiding rational design of new materials. It is not necessary to have a single descriptor, as we have already seen that the ORR in cathodes is complex. It is interesting to observe the strong correlation in many computed parameters and the existence of a few strong correlations between properties and underlying descriptors. At this point they provide multiple avenues for materials design to move and propose new tests computationally and experimentally.

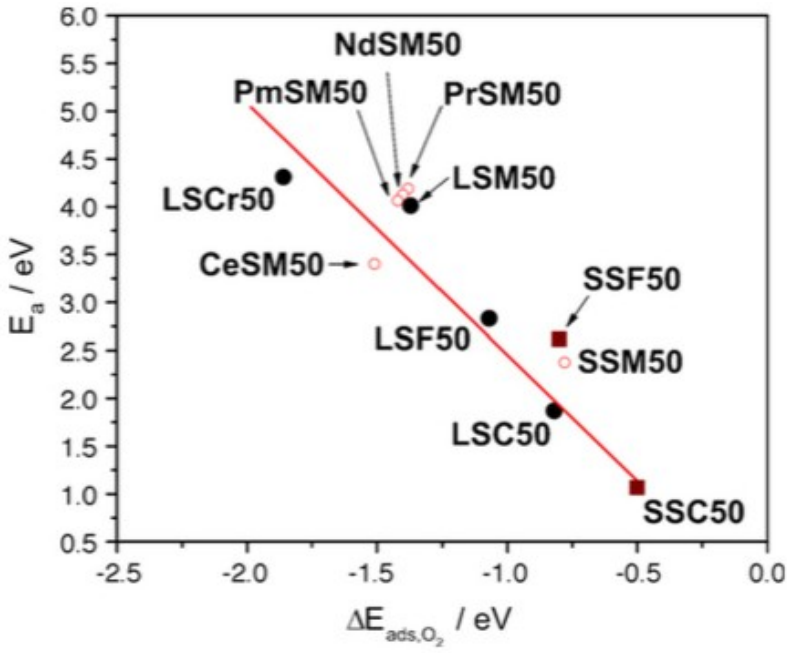


Figure 11. Comparison of adsorption energies $E_{ads,O2}$ versus diffusion barriers $E_a$ of oxygen ions through the MIEC bulk phases. $E_{ads,O2}$ is the averaged adsorption energies of superoxo- and peroxo-like species on B cations [13].

This limited set of recent observations in ab initio modeling highlights the maturity and robustness of such methods to model that atomic scale and fundamental electronic aspects of electrochemistry and transport in SOFCs. It is hard not to be excited about ab initio models from just this set of data. The challenge that remains to the ab initio models is to generate this fundamental data for the entire ensemble of reaction mechanisms, surfaces, and transitions states. For example, are the special surfaces focused on herein (specific [100] terminations) sufficient or meaningful for accurate predictions of transport and reaction pathways? This comes down to our ability to solve larger ensemble data sets. To some extent this could be solved by populating force field models of molecular dynamics (which we are not treating here) and directly solving for effective transport parameters based on the ensemble properties, but force models are still questionable in complex oxides. In the short term, ab initio values should be included in 3-D microstructural models and continuum level models, compared to experimental results and improved from there. These initial observations are promising, but the complexity of SOFC microstructures will require generation of much more data to precisely capture the physics. What is less clear is to what level of precision must we model SOFCs to capture accurately their performance and to modify efficiently the design of SOFCs to improve durability and market attractiveness? It seems likely that coarser-scale models can be used to establish the sensitivity of the SOFC performance to parameter variations at the scale that ab initio methods can tackle.

## 3-D Microstructural Modeling of SOFCs

### Modeling Electrochemistry

Recently, there has been a host of experimental efforts to reconstruct 3-D depictions of fuel cell electrodes [58–65], because the intrinsic reliability and durability of SOFCs is tied closely to the distribution of microstructural features generated during manufacture and to their evolution in operational conditions. Quantifying the distribution of microstructural features over a three-dimensional volume that captures all relevant physical properties and at different stages of operation is, therefore, essential to the development of predictive models of SOFC performance.

One example of a reconstructed volume of a $La_{0.58}Sr_{0.4}Co_{0.2}Fe_{0.8}O_{3-\delta}$ (LSCF) cathode is shown in Figure 12(left) [66]. Usually, one calculates average microstructural parameters, such as phase fractions, surface areas, triple phase boundaries (TPBs), etc. from these reconstructed volumes. One can also compute connectivity and tortuosity parameters, though a variety of approaches can be used to determine them. When the values are to be used to understand transport, it is convenient to determine the values by simulating transport through the networks. For example, the tortuosity of a transport path through the volume can be calculated by simulating transport under a specified driving force and comparing the simulated transport value to the effective medium model of interest. An example of one finite element model simulating transport under a 1V driving force is shown in Figure 12(right), which depicts the potential distribution through the tortuous LSCF path [66]. The effective transport tortuosity was ultimately calculated from the transport model, and then this value can be used in coarser

scale models. Figure 12(right) illustrates how one can map transport properties in 3-D on real fuel cells, which is the long-term goal in electrochemical models.

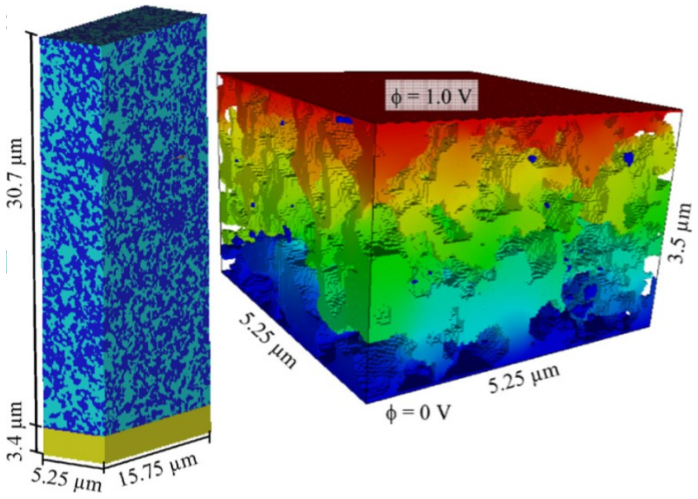


Figure 12. (Left) A 3-D reconstruction (based on focused ion beam SEM experiments) of a porous LSCF cathode [66]. (Right) The potential distribution inside the reconstructed microstructure using finite element modeling [66].

Using this same reconstruction, the same group developed a multi-physics model that computed the electrochemical performance of the LSCF cathode [67]. Since this is one of the first 3-D models of electrochemical performance, they also compared the 3-D model to a similar continuum level (1D) model that incorporated the 3-D microstructural features into the effective medium theory (the details are described in the paper [67]). The 3-D model included oxygen diffusion in the gas phase, oxygen ion diffusion in the bulk phase, surface exchange on the interface gas/mixed conducting electrode material, and charge transfer at the interface electrolyte–electrode material [67]. The oxygen molar fraction in the pores of the cathode operated at 800 °C, re-plotted in Figure 13 here, for 5 different slices through the cross section of the cathode (the tops of the images are the top air-side of the cathode and the bottoms are the interface with the electrolyte). These images demonstrate that the overall performance at each 2-D slice is similar, but the details vary owing to local variations. These cathodes were relatively homogenous cathodes, and commercial cathodes are expected to have larger-scale heterogeneities. As such, it will be interesting to model how local heterogeneities perturb performance and potentially lead to spatially varying degradation [68, 69].

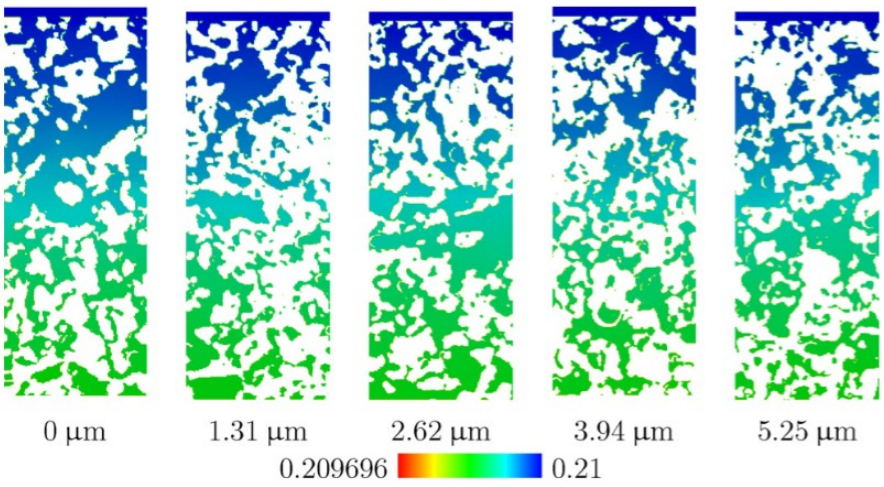


Figure 13. Oxygen molar fraction in pores at 800 °C. The slice location is shown below each image, and the width (height) of each slice is 5.25 (14) µm [67].

The electrochemical performance of the 3-D model was compared to a well-established 1D model [70], using microstructural parameters from the 3-D microstructure as inputs in the 1D model. The comparison with the asymptotic 1D model was done by comparing two separate performance indexes. The first characterized the extension of the active zone into the electrode, described as the characteristic length (this is the length where the exponential current distribution has decayed by 1/e). The second index was the cathodic area specific resistance ($ASR_{cat}$). Both comparisons were made over a range of temperatures. The results of these comparisons are shown in Figure 14.

The difference between the two models is of the order of 12% for the characteristic length and of 5% for the $ASR_{cat}$ (at the highest temperature). These observations confirm that cathodes with homogeneous mixed ionic/electronic conducting (MIEC) microstructures can be modeled with coarser scale 1D models, as long as the coarse-scaled model is properly calibrated to the details of the real microstructure [67]. The future in this area is to investigate inhomogeneous microstructures and to map spatially and to quantify distributions of electrochemical properties in inhomogeneous microstructures. Similar comparisons are needed between inhomogeneous 3-D microstructural and continuum level models as were done above for the homogeneous case. Finally, coupling of the evolution and property models will allow for local polarizations to drive locally varying evolution. Such models require larger volume experimental data sets to be collected, and for large scale computations to be implemented on these computationally expensive/stiff problems.

Comparison characteristic distance for 3D model and 1D model.

| $T$ [°C] | 3D model | 1D model | Ratio 1D/3D |
|---|---|---|---|
| | $\delta$ [μm] | $\delta$ [μm] | $\delta$(1D)/$\delta$(3D) |
| 600 | 0.77 | 0.67 | 0.87 |
| 650 | 0.82 | 0.72 | 0.88 |
| 700 | 0.88 | 0.78 | 0.88 |
| 750 | 0.94 | 0.83 | 0.88 |
| 800 | 0.99 | 0.87 | 0.88 |

Comparison $ASR_{cat}$ for 3D model and 1D model.

| $T$ [°C] | 3D model $ASR_{cat}$ [$\Omega$ cm$^2$] | 1D model $ASR_{cat}$ [$\Omega$ cm$^2$] | Ratio 1D/3D $ASR_{cat}$(1D)/$ASR_{cat}$(3D) |
|---|---|---|---|
| 600 | 0.614 | 0.616 | 1.003 |
| 650 | 0.188 | 0.188 | 1.000 |
| 700 | 0.074 | 0.074 | 1.000 |
| 750 | 0.033 | 0.032 | 0.970 |
| 800 | 0.019 | 0.018 | 0.947 |

Figure 14. Comparison at different temperatures of the characteristic distance (top) and the ASR (bottom) for a 3-D model and a 1-D model [67].

**Modeling Microstructural Evolution**

The inherent complexity of SOFC cathode microstructures coupled to the aggressive operational environments mean that one expects microstructural evolution to occur over their expected lifetimes. The computational models of electrochemistry on 3-D microstructures show their electrochemical performance compares well to physical experiments. This gives promise that models soon will capture the electrochemical properties of SOFCs over large enough volumes to describe heterogeneous electrodes in commercial SOFCs. Models of microstructural evolution [15, 71–73] will help us understand how architectural degradation proceeds, and local electrochemical properties evolve, during long-term exposure in specific operational conditions.

Recently, phase field models were developed to describe electrode microstructures (including electrode-, electrolyte-, pore-, and infiltrate-phases) in SOFCs [72]. The driving force for microstructure evolution is the decrease in total interfacial boundary energy. The most important physical parameters in the model are the gradient energy coefficients ($\kappa^{\#}$ for the $i^{th}$ phase) and the kinetic mobilities (of atoms and grain boundaries). Examples of how the equilibrium TPB contact angles (using 2-D simulations) vary for three sets of gradient energy coefficients of the solid phases are shown in Figure 15. Thus far, the actual gradient coefficients (and the kinetic mobilities) for SOFC electrode materials have not been physically measured or computed from models. Future integrated physical and computational experiments will allow for models to be informed using accurate data properly validated for specific systems of interest. The result will be predictive models of electrochemical performance over time. Most importantly, one needs to know if the gradient coefficients (or

mobilities) vary with electrochemical loading, if one is to capture the long-term local degradation accurately.

The temporal 3-D microstructural evolution is shown in Figure 16 (left) for phase volumes of 30% electrode (electron channel), 30% electrolyte (ion channel), 40% pore (gas channel) [72]. These began as a randomly disordered microstructure, but phase coalescence occurs and is controlled by the interparticle diffusion through microstructure. Over time, the experimental microstructural changes seem to be slowing down. The simulated microstructures are similar to experimental ones.

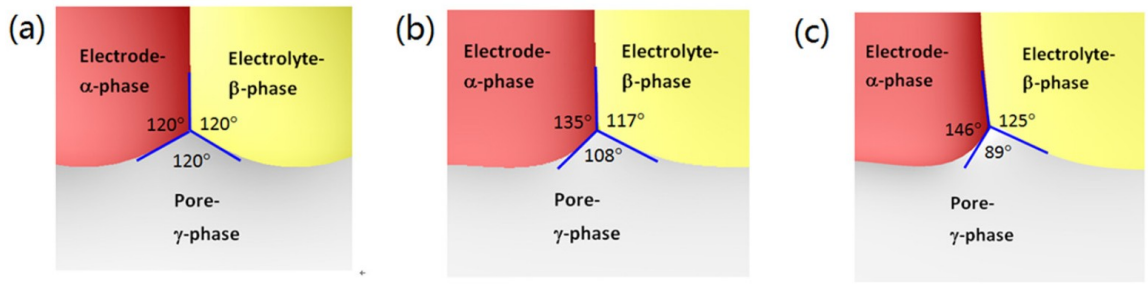


Figure 15. Equilibrium contact angles at triple junctions for three sets of gradient energy coefficients $\kappa^{\$,}$ ($\kappa^{\%}$) = (a) 2.5 (2.5), (b) 1.5 (3.5), and (c) 0.5 (5.5) [72].

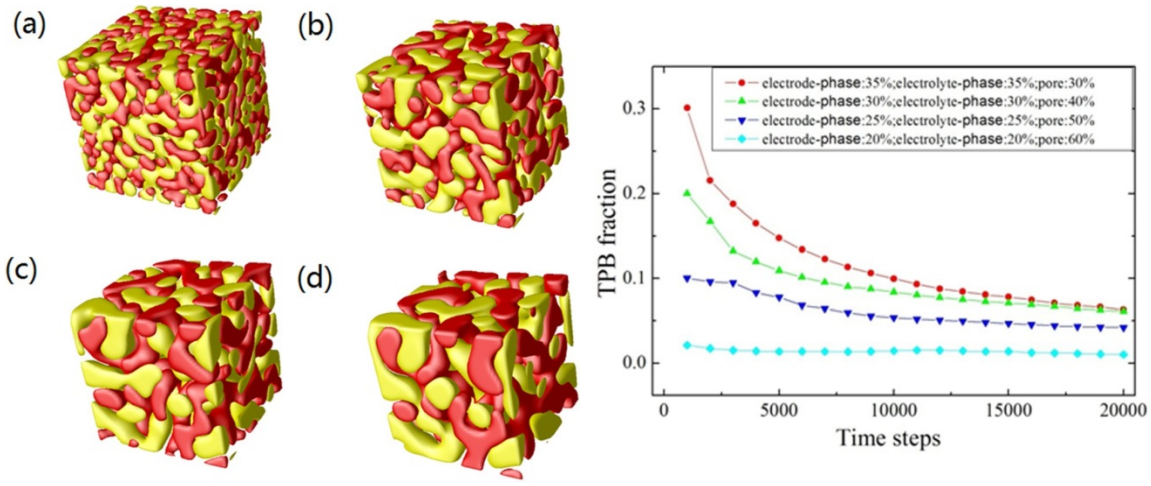


Figure 16. (Left) Temporal microstructural evolution in a three-phase SOFC electrode system at time step: (a) 1,000, (b) 5,000, (c) 10,000, and (d) 20,000. The electrode phase, electrolyte phase, and pore phase are represented in red, yellow, and transparent (volume fractions are 30%, 30%, and 40%, respectively). (Right) Temporal evolution of TPB fraction for different three-phase volume fractions with $ % the fixed gradient coefficient $\kappa''$ ($\kappa''$) = (a) 1.5 (3.5) (Figure 15[b]) [72].

Figure 16(right) shows the temporal evolution of TPB fraction for different three-phase volume fractions in SOFC electrodes. In the early stages, one observes a rapid decrease of the TPB, for all phase fractions. Over time, the TPB fractions seem to stabilize. These values are given for a specific set of energetic and kinetic parameters, which can be validated for specific systems using experimental comparisons. Interestingly, the magnitude of TPB fraction shows a significant dependence on the three-phase volume fraction. The significance of this should be emphasized with respect to the heterogeneities observed in phase distributions and TPBs in commercial SOFCs [59]. Since the phase volumes clearly affect evolution of microstructural features and electrochemical properties, coupling these together will require a concerted effort, especially if local heterogeneities exist in real SOFCs. The important point to emphasize is that the missing piece of the puzzle is the integration of experiments and computations to address the coupled evolution problem, capturing the relevant information for specific heterogeneous systems.

Recently, the phase field model developed for three-phase cathode microstructures was extended to include an infiltrate phase of nanoparticles [71]. First, a three-phase LSM/YSZ cathode backbone microstructure was generated (for phase volumes of 33% electrode [electron channel], 33% electrolyte [ion channel], 34% pore [gas channel]), where the particle size was ≈1 μm. Then, small nuclei of infiltrate phase with particle sizes around 5 nm (small) or 10 nm (large) were randomly placed on the LSM and YSZ surfaces (with twice as much on YSZ as on LSM, and volume fractions the same for small and large particles). The temporal evolution of the small infiltrate system is shown in Figure 17(left), where the nanoparticles have coarsened to ≈50–100 nm after $1.3 \times 10^5$ time steps. Figure 17(right), shows a comparison of TPB density for non-infiltrated and infiltrated cathodes with different initial infiltrate particle sizes (infiltrates were considered to be the same as the electrode phase (LSM). The initial TPBs are in accordance with intuition. The model shows that the TPB density drops significantly owing to infiltrate coarsening at the initial stage, but stabilize over time. In all cases tested, the infiltrated cathode retained a high TPB length throughout the "operational lifetime", and always exhibited higher TPB densities than the as-fabricated cathode backbone. The smaller infiltrate particles give better cathode performance for a certain amount of infiltrate. What is of major interest now is to simulate the electrochemical performance of these infiltrated cathodes using models similar to those described above.

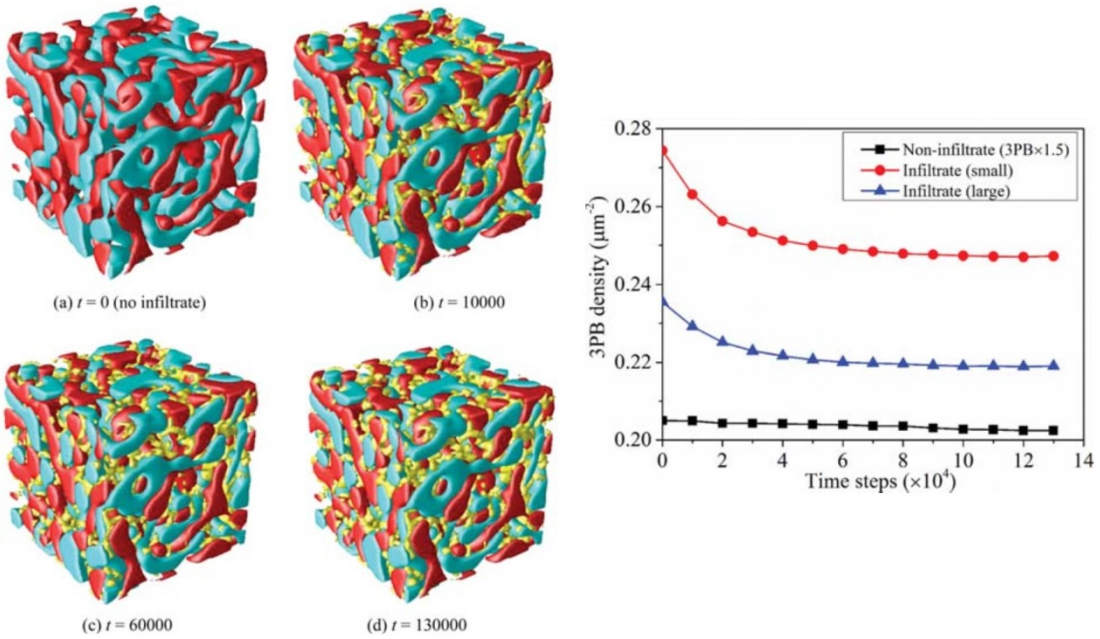


Figure 17. (Left) Temporal evolution of three-phase cathode microstructures infiltrated by nanoparticles (their sizes are around 50–100 nm after 1.3 x $10^5$ time steps, *t*). The red, green, transparent, and yellow color represents YSZ, LSM, pore, and infiltrate phase, respectively [71]. (Right) Comparison of the calculated TPB density of backbone and infiltrated cathode as a function of time steps (with the values of TPB density for non-infiltrated cathode electrostatic discharge multiplied by 1.5) [71].

## Micro-kinetic and Continuum Level Modeling of SOFC Cathodes

This area of modeling is relatively mature with respect to methods discussed above. The concepts in these models are to solve (usually in 1-D) the coupled differential equations describing some sub-set of reaction and transport pathways that capture the ORR in cathodes, and to compare the model to some subset of experimental observations, or to carry out sensitivity analyses comparing predicted performance over a range of values for model parameter. Upon comparison of models with observations, some sort of conclusion concerning the specific pathways is attempted. Several interesting review papers exist that describe these micro-kinetics and continuum level models (which also can bridge beyond the cathode to the full fuel cell operation) [9, 10, 14–18, 2–23]. S e e [9, 21, 22] for some reviews concerning only cathode modeling. Briefly, we paraphrase the summary concerning such modeling from the most recent of these reviews [9]. First off, the oxygen reduction mechanism in the cathode of an SOFC is complex and the exact reaction mechanisms remain an active area of debate. First off, there is no consensus on the reaction steps or intermediate species. Many sub-reactions have been used to describe reasonably the ORR, and these include distinct oxygen species appearing in one or more steps. Second, because the ORR can be divided into these several sub-steps of electrochemistry and transport, the rate-limiting step remains unclear. Furthermore, the rate-limiting step may vary in different operational conditions. While improved correlations are being made between models and observations, it is becoming

increasingly clear that one reaction pathway/rate-limiting step may not be sufficient to model the complex cathode behavior. Third, the reaction zone itself is unclear. In Figure 3, we showed several different overall zones, being at the TPBs at the cathode/electrolyte interface, the surfaces of the cathode in the near the electrolyte region, or TPBs in the cathode in the near electrolyte region. For simplicity of design and interpretation of experiments, we generally try to isolate the preferred path/zone. However, models with two charge-transfer pathways co-existing demonstrate each path contributes and competes for dominance under different operation conditions. Fourth, and last, realistic geometrical and microstructural parameters are needed to accurately model real cathodes using simplified models, as already alluded to in the last section. Many prior models ignored or adjusted such parameters. The perceived success of researchers using these different models indicates that (1) such models can capture the properties of SOFC cathodes but (2) the solution space is difficult to winnow down owing to the large number of adjustable parameters in any given model. Before addressing paths to overcoming these challenges to accurate full-scale SOFC cathode models, we present one of these micro-kinetics models that highlights the multiple pathways possible in a given cathode.

The group at NETL and WVU developed a micro-scale dynamic continuum model of a porous composite LSM–YSZ cathode (built from conceptually similar earlier models [74–79]) that incorporates a full composite cathode, where the LSM/YSZ interface is randomly distributed according to the underlying cathode microstructure [80]. A schematic of the porous composite cathode is shown in Figure 18, with pore phase percolation existing in the unrepresented third dimension. The ion-conducting and electron-conducting phases were intermingled and the TPBs were distributed throughout the electrode allowing reactions to occur throughout the electrode. A variety of surface and bulk reactions were considered, shown in Figure 18. The model permits simultaneous 2PB and TPB (i.e., 3PB) pathways for the ORR.

Figure 19 plots profiles of local overpotential and the corresponding local volumetric charge transfer rates (through the thickness of the cathode) at an applied over-voltage of 0.3 V for (a) 2PB and (b) TPB pathways [80]. Both figures indicate that local over-potentials intensify from the cathode surface to the active interface (though in some cases other shapes were observed). The local volumetric 2PB and TPB charge transfer rates are higher at the active interface, as expected. The charge transfer rates are high enough and far away from the active interface such that the entire cathode thickness is electrochemically active, similar to what is known for real cathodes. TPB charge transfer rates are dominant over 2PB rates, but the apparent overpotential for the 2PB mechanism is higher (owing to a higher activation for the 2PB mechanism).

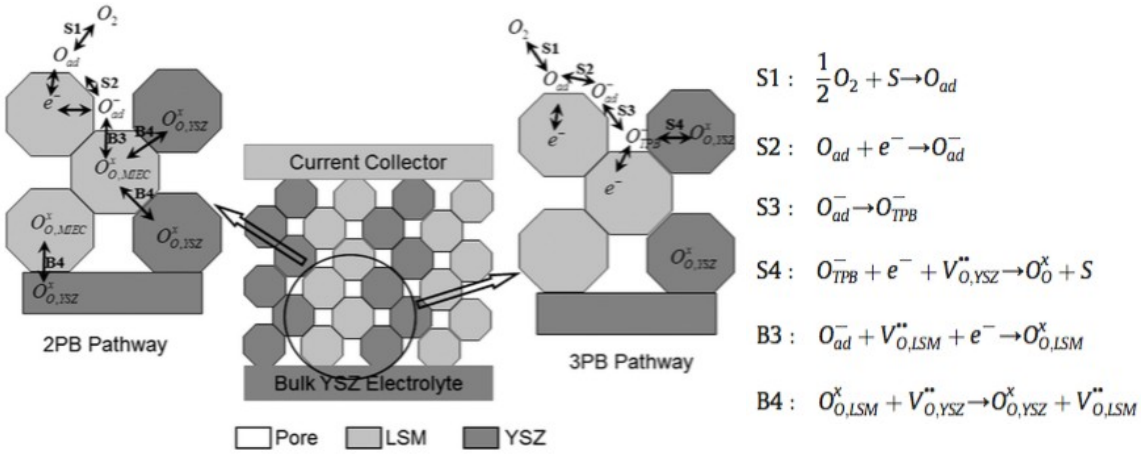


Figure 18. Schematic representation of the composite cathode and the reaction mechanisms for 2 PB and TPB (3PB) pathways of oxygen reduction on LSM–YSZ [80].

The model was run using a range of different parameters, as discussed in [80]. Because the entire active cathode participated in electrochemistry, a sensitivity analysis was done to determine the effect of cathode thickness on the polarization curve (as shown in Figure 20). The model predicts that total current density asymptotically increases with thickness, thus the existence of an optimum thickness is captured by the model beyond which no appreciable performance increase can be achieved. The optimal value of thickness depends on the microstructural parameters chosen [80].

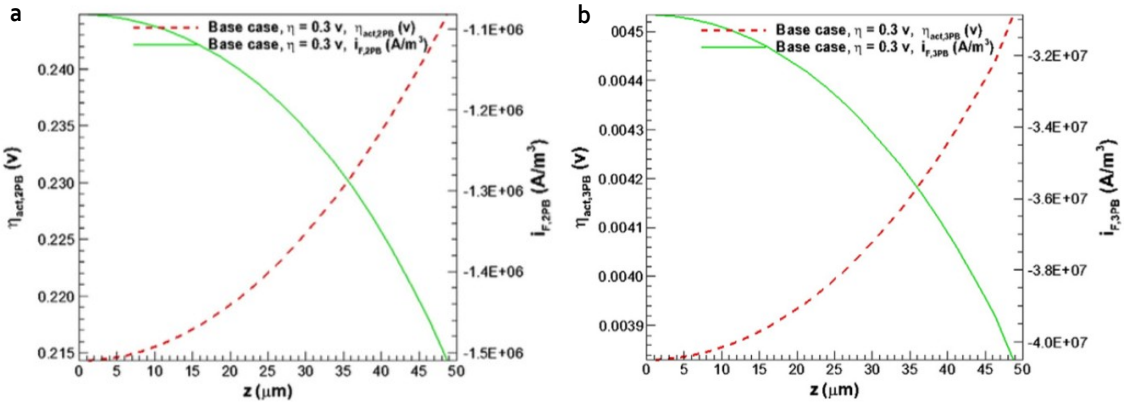


Figure 19. Profiles of local overpotential and the corresponding local volumetric charge transfer rates at an applied over-voltage of 0.3 V for (a) 2PB and (b) TPB pathways [80].

The point of presenting this model was to demonstrate (1) that more than one pathway can simultaneously contribute to the cathode performance, (2) that each pathway has several contributing sub-processes that require accurate thermodynamic and kinetic parameters, and

(3) that the electrochemical properties are microstructurally dependent and electrochemistry is distributed throughout the cathode itself. In other words, the quality of the micro-kinetic continuum level models is dependent on information that can be generated from ab initio and 3-D microstructural models. Even though the coarse-scale models continue to add sophistication and have low computational costs, they are inherently limited by the quality of the underlying parameters. These continuum models are attractive to explore cell level inhomogeneities and to bridge to the CFD style full SOFC models, but first they will need to be bridged to the finer scale models described earlier.

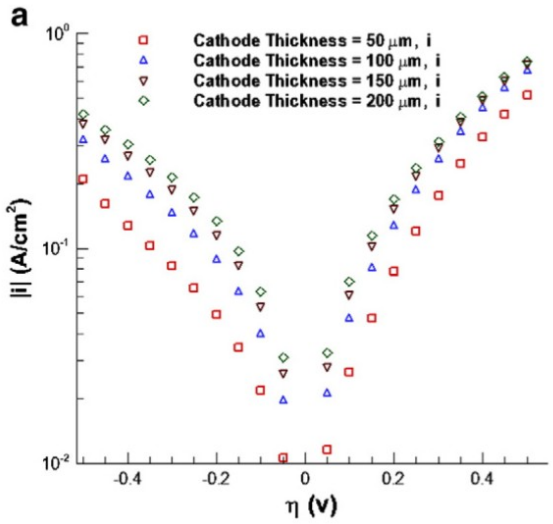


Figure 20. Effect of cathode thickness on polarization curve of model [80].

## Summary and Outlook

In this report, we discussed exciting approaches to modeling SOFCs cathodes. First, we presented the grand challenge of developing models that can capture the full complexity of cathode electrochemistry and transport. Despite the complexity, the payoff to SOFC design and optimization could be revolutionary.

Then we presented an overview and recent promising results in the areas of ab initio modeling. These included calculation of thermodynamic formation energies, which were coupled to free energy models to predict defect chemistry at high temperatures. Next recent work in transition state energy calculations were coupled to kinetic models to predict transport parameters of different materials. Throughout, correlations of calculated energies and electronic descriptors to transport parameters were presented, which hold promise for screening potential materials without extensive testing required for many materials. Ultimately, these results indicate that it is possible to generate thermodynamic and kinetic parameters required for coarser scale models.

3-D microstructural modeling was presented next. Such modeling provides important metrics to be fed to continuum effective medium models, such as tortuosity etc. More recently, models that capture the full scale multi-physics on real SOFC microstructures have been developed and it was demonstrated that they capture performance accurately, when compared to accepted 1D models. These hold promise to capture local variations in property, potentially capture degradation. To go along with this, phase field modeling of microstructural evolution was discussed. Together, these two sets can capture performance over time and can be used to inform coarser scale models as to how local volumes evolve if there are local heterogeneities in cells (which there are).

Finally, we briefly presented new directions in micro-kinetic modeling that build from similar microstructural information described in the 3-D modeling section. The results demonstrate that multiple paths exist when a complete set of micro-kinetic models are included, and the relative contribution is related to material, microstructural, geometrical, and electrochemical operational parameters. This result reinforces the complexity of the challenge in modeling SOFCs, and the necessity of increasing the accuracy of model parameters at the lower levels, and to expand coarse-scale situations to probe heterogeneous cathode systems.

Taken together, the results are extremely promising for SOFC cathode modeling. Within each of the areas, advanced models are arising that provide accurate descriptions of physical behavior. Despite the advances within each area, it is clear that oxygen reduction and transport mechanisms in SOFC cathodes require models to be integrated across these areas. In other words, the models appear to be mature enough that scale bridging methods and multi-scale models are ripe for development. With advances in computational power, the outlook is very exciting in modeling SOFCs, and the quest toward computational design integrated with experimental verification for the acceleration of SOFC deployment in markets will succeed in the not too distant future.

## References


[1] V. S. Bagotsky, *Fuel Cells: Problems and Solutions*: Wiley, 2012.

[2] L. Blum, W. A. Meulenberg, H. Nabielek, and R. Steinberger-Wilckens, "Worldwide SOFC technology overview and benchmark," *International Journal of Applied Ceramic Technology,* vol. 2, pp. 482-492, 2005.

[3] P. Singh and N. Q. Minh, "Solid Oxide Fuel Cells: Technology Status," *Int. J. Appl. Ceram. Technol.,* vol. 1, pp. 5-15, 2004.

[4] O. Yamamoto, "Solid Oxide Fuel Cells: Fundamental Aspects and Prospects,"*Electrochimica Acta,* vol. 45, pp. 2423-2435, 2000.

[5] S. C. Singhal, "Advances in Solid Oxide Fuel Cell Technology," *Solid State Ionics,* vol. 135, pp. 305-313, 2000.

[6] S. C. Singhal, "Science and Technology of Solid-Oxide Fuel Cells," *MRS Bulletin,* vol. 25, pp. 16-21, 2000.

[7] A. Hammou and J. Guindet, "Solid Oxide Fuel Cells," in *The CRC Handbook of Solid State Electrochemistry*, ed: CRC Press, 1997, pp. 407-443.

[8] N. Q. Minh and T. Takahashi, *Science and Technology of Ceramic Fuel Cells*. New York: Elsevier, 1995.

[9] Y. H. Li, R. Gemmen, and X. B. Liu, "Oxygen reduction and transportation mechanisms in solid oxide fuel cell cathodes," *Journal of Power Sources,* vol. 195, pp. 3345-3358, 2010.

[10] M. Garcia-Camprubi, S. Izquierdo, and N. Fueyo, "Challenges in the electrochemical modelling of solid oxide fuel and electrolyser cells," *Renewable & Sustainable Energy Reviews,* vol. 33, pp. 701-718, 2014.

[11] M. M. Kuklja, E. A. Kotomin, R. Merkle, Y. A. Mastrikov, and J. Maier, "Combined theoretical and experimental analysis of processes determining cathode performance in solid oxide fuel cells," *Physical Chemistry Chemical Physics,* vol. 15, pp. 5443-5471, 2013.

[12] K. N. Grew and W. K. S. Chiu, "A review of modeling and simulation techniques across the length scales for the solid oxide fuel cell," *Journal of Power Sources,* vol. 199, pp. 1- 13, 2012.

[13] Y. Choi, M. C. Lin, and M. Liu, "Rational design of novel cathode materials in solid oxide fuel cells using first-principles simulations," *Journal of Power Sources,* vol. 195, pp. 1441-1445, 2010.

[14] M. Andersson, J. L. Yuan, and B. Sunden, "Review on modeling development for multiscale chemical reactions coupled transport phenomena in solid oxide fuel cells," *Applied Energy,* vol. 87, pp. 1461-1476, 2010.

[15] J. H. Kim, W. K. Liu, and C. Lee, "Multi-scale solid oxide fuel cell materials modeling,"*Computational Mechanics,* vol. 44, pp. 683-703, 2009.

[16] S. Kakac, A. Pramuanjaroenkij, and X. Y. Zhou, "A review of numerical modeling of solid oxide fuel cells," *International Journal of Hydrogen Energy,* vol. 32, pp. 761-786, 2007.

[17] V. M. Janardhanan and O. Deutschmann, "Modeling of Solid-Oxide Fuel Cells,"*Zeitschrift für Physikalische Chemie,* vol. 221, pp. 443-478, 2007.

[18] M. Peksen, A. Al-Masri, R. Peters, L. Blum, and D. Stolten, "3D Multiscale-Multiphysics SOFC Modelling Status at the Institute of Electrochemical Process Engineering, FZ Julich," *ECS Transactions,* vol. 68, pp. 2861-2866, 2015.

[19] A. Smirnov, A. Burt, and I. Celik, "Multi-physics simulations of fuel cells using multi-component modeling," *Journal of Power Sources,* vol. 158, pp. 295-302, 2006.

[20] M. L. Liu, M. E. Lynch, K. Blinn, F. M. Alamgir, and Y. Choi, "Rational SOFC material design: new advances and tools," *Materials Today,* vol. 14, pp. 534-546, 2011.

[21] S. B. Adler, "Factors Governing Oxygen Reduction in Solid Oxide Fuel Cell Cathodes,"*Chemical Reviews,* vol. 104, pp. 4791-4843, 2004.

[22] J. Fleig, "Solid oxide fuel cell cathodes: Polarization mechanisms and modeling of the electrochemical performance," *Annual Review of Materials Research,* vol. 33, pp. 361- 382, 2003.

[23] K. Wang, D. Hissel, M. C. Pera, N. Steiner, D. Marra, M. Sorrentino*, et al.*, "A Review on solid oxide fuel cell models," *International Journal of Hydrogen Energy,* vol. 36, pp. 7212-7228, 2011.

[24] Y.-L. Lee and D. Morgan, "Ab initio defect energetics of perovskite (001) surfaces for solid oxide fuel cells: A comparative study of $LaMnO_3$ versus $SrTiO_3$ and $LaAlO_3$," *Physical Review B,* vol. 91, 2015.

[25] M. Youssef and B. Yildiz, "Predicting self-diffusion in metal oxides from first principles: The case of oxygen in tetragonal $ZrO_2$," *Physical Review B,* vol. 89, pp. 024105-6, 2014.

[26] H. Luo, Y. Shin, Y. Yu, D. Cetin, K. Ludwig, U. Pal*, et al.*, "Predicting oxygen vacancy non-stoichiometric concentration in perovskites from first principles," *Applied Surface Science,* vol. 323, pp. 65-70, 2014.

[27] M. T. Curnan and J. R. Kitchin, "Effects of Concentration, Crystal Structure, Magnetism, and Electronic Structure Method on First-Principles Oxygen Vacancy Formation Energy Trends in Perovskites," *Journal Of Physical Chemistry C,* vol. 118, pp. 28776-28790, 2014.

[28] Y.-L. Lee and D. Morgan, "Ab initio and empirical defect modeling of $LaMnO_{3+/-\delta}$ for solid oxide fuel cell cathodes," *Physical Chemistry Chemical Physics,* vol. 14, pp. 290- 302, 2012.

[29] S. A. Akhade and J. R. Kitchin, "Effects of strain, d-band filling, and oxidation state on the surface electronic structure and reactivity of 3d perovskite surfaces," *The Journal of Chemical Physics,* vol. 137, p. 084703, 2012.

[30] Y.-L. Lee, J. Kleis, J. Rossmeisl, Y. Shao-Horn, and D. Morgan, "Prediction of solid oxide fuel cell cathode activity with first-principles descriptors," *Energy & Environmental Science,* vol. 4, pp. 3966-3970, 2011.

[31] A. Kushima, D. Parfitt, A. Chroneos, B. Yildiz, J. A. Kilner, and R. W. Grimes, "Interstitialcy diffusion of oxygen in tetragonal $La_2CoO_{4+\delta}$," *Physical Chemistry Chemical Physics,* vol. 13, pp. 2242-2249, 2011.

[32] W. A. Harrison, "Origin of Sr segregation at $La_{1-x}Sr_xMnO_3$ surfaces," *Physical Review B,* vol. 83, 2011.

[33] J. W. Han and B. Yildiz, "Enhanced one dimensional mobility of oxygen on strained $LaCoO_3$(001) surface," *Journal Of Materials Chemistry,* vol. 21, pp. 18983-8, 2011.

[34] W. Donner, C. Chen, M. Liu, A. J. Jacobson, Y.-L. Lee, M. Gadre*, et al.*, "Epitaxial Strain-Induced Chemical Ordering in $La_{0.5}Sr_{0.5}CoO_{3-\delta}$ Films on $SrTiO_3$," *Chemistry Of Materials,* vol. 23, pp. 984-988, 2011.

[35] A. Chroneos, B. Yildiz, A. Tarancón, D. Parfitt, and J. A. Kilner, "Oxygen diffusion in solid oxide fuel cell cathode and electrolyte materials: mechanistic insights from atomistic simulations," *Energy & Environmental Science,* vol. 4, pp. 2774-16, 2011.

[36] Z. Cheng, J.-H. Wang, Y. Choi, L. Yang, M. C. Lin, and M. Liu, "From Ni-YSZ to sulfur-tolerant anode materials for SOFCs: electrochemical behavior, in situ characterization, modeling, and future perspectives," *Energy & Environmental Science,* vol. 4, pp. 4380-30, 2011.

[37] Y. A. Mastrikov, R. Merkle, E. Heifets, E. A. Kotomin, and J. Maier, "Pathways for Oxygen Incorporation in Mixed Conducting Perovskites: A DFT-Based Mechanistic Analysis for (La,Sr)$MnO_{3-\delta}$," *Journal of Physical Chemistry C,* vol. 114, pp. 3017-3027, 2010.

[38] A. Kushima, S. Yip, and B. Yildiz, "Competing strain effects in reactivity of $LaCoO_3$ with oxygen," *Physical Review B,* vol. 82, p. 115435, 2010.

[39] Y.-L. Lee and D. Morgan, "Prediction of Surface Oxygen Vacancy Concentrations of $(La_{1-x}Sr_x)MnO_3$," *ECS Transactions,* vol. 25, pp. 2769-2774, 2009.

[40] Y. A. Mastrikov, E. Heifets, E. A. Kotomin, and J. Maier, "Atomic, electronic and thermodynamic properties of cubic and orthorhombic $LaMnO_3$ surfaces," *Surface Science,* vol. 603, pp. 326-335, 2009.

[41] Y.-L. Lee, D. Morgan, J. Kleis, and J. Rossmeisl, "Ab initio Defect Energetics in $LaBO_3$ Perovskite Solid Oxide Fuel Cell Materials," presented at the 216th ECS Meeting, 2009.

[42] Y.-L. Lee, J. Kleis, J. Rossmeisl, and D. Morgan, "Ab initio energetics of $LaBO_3$(001) (B=Mn, Fe, Co, and Ni) for solid oxide fuel cell cathodes," *Physical Review B,* vol. 80, p. 224101, 2009.

[43] Y.-L. Lee, J. Kleis, J. Rossmeisl, and D. Morgan, "Ab initio energetics of $LaBO_3$(001) (B=Mn , Fe, Co, and Ni) for solid oxide fuel cell cathodes," *Physical Review B,* vol. 80, p. 224101, 2009.

[44] F. Lallet, N. Olivi-Tran, and L. J. Lewis, "Interface energies of (100)(YSZ) and (111)(YSZ) epitaxial islands on (0001)(alpha-$Al_2O_3$ substrates from first principles," *Physical Review B,* vol. 79, 2009.

[45] Y. Choi, M. C. Lin, and M. Liu, "Computational Study on the Catalytic Mechanism of Oxygen Reduction on $La_{0.5}Sr_{0.5}MnO_3$ in Solid Oxide Fuel Cells," *Angewandte Chemie International Edition,* vol. 46, pp. 7214-7219, 2007.

[46] R. A. Evarestov, E. A. Kotomin, Y. A. Mastrikov, D. Gryaznov, E. Heifets, and J. Maier, "Comparative density-functional LCAO and plane-wave calculations of LaMnO3 surfaces," *Physical Review B,* vol. 72, p. 214411, 2005.

[47] R. A. Evarestov, E. A. Kotomin, D. Fuks, J. Felsteiner, and J. Maier, "Ab Initio Calculations of the $LaMnO_3$ Surface Properties," *Applied Surface Science,* vol. 238, pp. 457-463, 2004.

[48] G. Ballabio, M. Bernasconi, F. Pietrucci, and S. Serra, "Ab Initio of Yttria-Stabilized Cubic Zirconia Surfaces," *Physical Review B,* vol. 70, p. 075417, 2004.

[49] G. Stapper, M. Bernasconi, N. Nicoloso, and M. Parrinello, "Ab Initio Study of Structural and Electronic Properties of Yttria-Stabilzed Cubic Zirconia," *Physical Review B,* vol. 59, pp. 797-810, 1999.

[50] S. Gennard, F. Cora, and C. R. A. Catlow, "Comparison of the bulk and surface properties of ceria and zirconia by ab initio investigations," *J Phys Chem B,* vol. 103, pp. 10158-10170, 1999.

[51] S. A. Akhade and J. R. Kitchin, "Effects of strain, d-band filling, and oxidation state on the bulk electronic structure of cubic 3d perovskites," *Journal of Chemical Physics,* vol. 135, 2011.

[52] L. Yan and P. A. Salvador, "Substrate and Thickness Effects on the Oxygen Surface Exchange of $La_{0.7}Sr_{0.3}MnO_3$ Thin Films," *ACS Applied Materials and Interfaces,* vol. 4, pp. 2541-2550, 2012.

[53] L. Yan, B. Kavaipatti, K.-C. Chang, H. You, and P. A. Salvador, "Microstructural effects on the oxygen exchange kinetics of La0. 7Sr0. 3MnO3 thin films," *ECS Transactions,* vol. 35, pp. 2063--2075, 2011.

[54] L. Yan, K. R. Balasubramaniam, S. Wang, H. Du, and P. A. Salvador, "Effects of crystallographic orientation on the oxygen exchange rate of $La_{0.7}Sr_{0.3}MnO_3$ thin films," *Solid State Ionics,* vol. 194, pp. 9-16, 2011.

[55] J. Mizusaki, N. Mori, H. Takai, Y. Yonemura, H. Minamiue, H. Tagawa*, et al.*, "Oxygen nonstoichiometry and defect equilibrium in the perovskite-type oxides $La_{1-x}Sr_xMnO_{3+\delta}$," *Solid State Ionics,* vol. 129, pp. 163-177, 2000.

[56] K. Kamata, T. Nakajima, T. Hayashi, and T. Nakamura, "Nonstoichiometric Behavior and Phase-Stability of Rare-Earth Manganites at 1200 °C . 1. $LaMnO_3$," *Materials Research Bulletin,* vol. 13, pp. 49-54, 1978.

[57] Y. Choi, D. S. Mebane, M. C. Lin, and M. Liu, "Oxygen Reduction on LaMnO3-Based Cathode Materials in Solid Oxide Fuel Cells," *Chemistry of Materials,* vol. 19, pp. 1690- 1699, 2007.

[58] Y. L. Liu, K. Thyden, M. Chen, and A. Hagen, "Microstructure degradation of LSM-YSZ cathode in SOFCs operated at various conditions," *Solid State Ionics,* vol. 206, pp. 97- 103, 2012.

[59] S. Dillon, L. Helmick, H. Miller, L. Wilson, R. Gemman, R. Petrova, *et al.*, "The Orientation Distributions of Lines, Surfaces, and Interfaces around Three-Phase Boundaries in Solid Oxide Fuel Cell Cathodes," *Journal of the American Ceramic Society,* vol. 94, pp. 4045-4051, 2011.

[60] L. Helmick, "Microstructural Characterization of Solid Oxide Fuel Cell Cathode Materials," Ph.D., Materials Science and Engineering, Carnegie Mellon University, Pittsburgh, 2010.

[61] D. Gostovic, K. A. O'Hara, N. J. Vito, E. D. Wachsman, and K. S. Jones, "Multiple Length Scale Characterization of Doped Lanthanum Manganite Composite Cathodes," *ECS Transactions,* vol. 16, pp. 83-93, 2009.

[62] J. R. Izzo, Jr., A. S. Joshi, K. N. Grew, W. K. S. Chiu, A. Tkachuk, S. H. Wang, *et al.*, "Nondestructive reconstruction and analysis of SOFC anodes using X-ray computed tomography at sub-50 nm resolution," *J. Electrochem. Soc.,* vol. 155, pp. B504-B508, 2008.

[63] J. R. Wilson, W. Kobsiriphat, R. Mendoza, H.-Y. Chen, T. Hines, J. M. Hiller, *et al.*, "Three dimensional reconstruction of solid oxide fuel cell electrodes using focused ion beam - scanning electron microscopy," *ECS Trans.,* vol. 7, pp. 1879-1887, 2007.

[64] J. R. Wilson, W. Kobsiriphat, R. Mendoza, H.-Y. Chen, J. M. Hiller, D. J. Miller, *et al.*, "Three-Dimensional Reconstruction of a Solid-Oxide Fuel-Cell Anode," *Nature Materials,* vol. 5, pp. 541-544, 2006.

[65] J. Joos, T. Carraro, A. Weber, and E. Ivers-Tiffee, "Reconstruction of porous electrodes by FIB/SEM for detailed microstructure modeling," *Journal of Power Sources,* vol. 196, pp. 7302-7307, 2011.

[66] J. Joos, T. Carraro, A. Weber, and E. Ivers-Tiffée, "Reconstruction of porous electrodes by FIB/SEM for detailed microstructure modeling," *Journal of Power Sources,* vol. 196, pp. 7302-7307, 2011.

[67] T. Carraro, J. Joos, B. Ruger, A. Weber, and E. Ivers-Tiffee, "3D finite element model for reconstructed mixed-conducting cathodes: I. Performance quantification," *Electrochimica Acta,* vol. 77, pp. 315-323, 2012.

[68] S. Wang, T. A. Cruse, M. Krumpelt, B. J. Ingram, and P. A. Salvador, "Microstructural Degradation of (La,Sr)$MnO_3$/YSZ Cathodes in Solid Oxide Fuel Cells with Uncoated E- brite Interconnects," *Journal of the Electrochemical Society,* vol. 158, pp. B152-B158, 2011.

[69] M. Krumpelt, T. A. Cruse, B. J. Ingram, J. L. Routbort, S. Wang, P. A. Salvador, *et al.*, "The Effect of Chromium Oxy-hydroxide on Solid Oxide Fuel Cells," *Journal of the Electrochemical Society,* vol. 157, pp. B228-B233, 2010.

[70] S. B. Adler, J. A. Lane, and B. C. H. Steele, "Electrode kinetics of porous mixed- conducting oxygen electrodes," *Journal of the Electrochemical Society,* vol. 143, pp. 3554-3564, 1996.

[71] L. Y. Liang, Q. Li, J. M. Hu, S. Lee, K. Gerdes, and L. Q. Chen, "Phase field modeling of microstructure evolution of electrocatalyst-infiltrated solid oxide fuel cell cathodes," *Journal of Applied Physics,* vol. 117, p. 065105, 2015.

[72] Q. Li, L. Y. Liang, K. Gerdes, and L. Q. Chen, "Phase-field modeling of three-phase electrode microstructures in solid oxide fuel cells," *Applied Physics Letters,* vol. 101, p. 033909, 2012.

[73] H.-Y. Chen, H.-C. Yu, J. S. Cronin, J. R. Wilson, S. A. Barnett, and K. Thornton, "Simulation of coarsening in three-phase solid oxide fuel cell anodes," *Journal of Power Sources,* vol. 196, pp. 1333-1337, 2011.

[74] X. J. Chen, S. H. Chan, and K. A. Khor, "Simulation of a composite cathode in solid oxide fuel cells," *Electrochimica Acta,* vol. 49, pp. 1851-1861, 2004.

[75] S. H. Chan, X. J. Chen, and K. A. Khor, "Cathode micromodel of solid oxide fuel cell," *Journal of the Electrochemical Society,* vol. 151, pp. A164-A172, 2004.

[76] J. Deseure, Y. Bultel, L. Dessemond, and E. Siebert, "Theoretical Optimisation of a SOFC Composite Cathode," *Electrochimica Acta,* vol. 50, pp. 2037-2046, 2005.

[77] M. Gong, R. S. Gemmen, D. S. Mebane, K. Gerdes, and X. Liu, "Simulation of Surface- Potential Driven ORR Kinetics on SOFC Cathode with Parallel Reaction Pathways," *Journal Of The Electrochemical Society,* vol. 161, pp. F344-F353, 2013.

[78] M. Y. Gong, R. S. Gemmen, and X. B. Liu, "Modeling of oxygen reduction mechanism for 3PB and 2PB pathways at solid oxide fuel cell cathode from multi-step charge transfer," *Journal of Power Sources,* vol. 201, pp. 204-218, 2012.

[79] G. W. Coffey, J. S. Hardy, L. R. Pederson, P. C. Rieke, and E. C. Thomsen, "Oxygen reduction activity of lanthanum strontium nickel ferrite," *Electrochemical and Solid State Letters,* vol. 6, pp. A121-A124, 2003.

[80] S. Pakalapati, K. Gerdes, H. Finklea, M. Gong, X. Liu, and I. Celik, "Micro scale dynamic modeling of LSM/YSZ composite cathodes," *Solid State Ionics,* vol. 258, pp. 45-60, 2014.

## **Thin Films and Solid Oxide Fuel Cell Cathodes** *by Paul A. Salvador (Carnegie Mellon University)*


### Summary

Over the past few decades, incredible advances have been made in the preparation of thin films of complex oxides, especially with respect to controlling their crystalline quality, microstructures, thicknesses, and surface morphologies, as well as patterning them to specific shapes. The vast majority of research and development of complex oxide films focuses on electronic, magnetic, and photonic materials and devices, but a recent proliferation of their use has occurred in the energy sector. Thin films offer routes to understanding basic materials and device properties, especially those concerning electrochemically active surfaces, and avenues to improved materials.

In this report, we focus on how thin film research has been used to investigate electrochemical properties of SOFC cathode materials. The overarching goal of this work is to isolate important features in the bulk or surface of the cathode that control the oxygen reduction reaction (ORR), which is related to the overpotential of the cathode. Specifically, this report will discuss recent experimental work that unravels both surface structures and properties of thin film cathodes, as well as their relation to the underlying chemical and microstructural states. The overwhelming importance of the surface chemistry and microstructure indicates that a host of controllable parameters can modify electrochemical properties of a given material, but also implies that the even more extensive quantitative characterization of structure and properties is required to control all parameters in SOFC design. We integrate discussions of the challenges associated with translating the understanding gained in thin film experiments to SOFC technology.

Initially, thin films were used as proxies for bulk materials to determine materials properties, such as conductivities or surface exchange properties. The vast majority of cathode film research still focuses unraveling basic materials properties. We use examples of electrical conductivity relaxation (ECR) measurements on $La_{0.7}Sr_{0.3}MnO_3$ (LSM) thin films, in which orientation, strain, dislocation density, and planar boundary density, all impact the measured time constants and effective surface exchange values. Variations in the observed surface exchange values and activation energies are significant, even though the material does not vary in many cases. We discuss this with respect to observations in the literature for other materials and to the application of such data to SOFC design.

Patterning films into microelectrodes was pursued as the next step in understanding the ORR, aiming to differentiate between specific electrochemical reaction pathways. We will briefly review this work, discussing again the impact of SOFC microstructures on the results. Additionally, we present some work on extracting other basic materials parameters from patterned electrodes, such as the surface oxygen diffusivity.

Methods to interrogate the surface structure and properties of thin films have also made incredible progress in the past decade. In particular, the use of X-ray methods at synchrotron light sources have afforded new insights into electrochemically active surfaces in conditions similar to those of operation. Also, advances in scanning probe methodologies, have allowed similar investigations to be made on the local level. Much of the work carried out has been to measure surface chemistry and surface electronic structure, aiming to find correlations to understand performance or degradation of SOFCs. We will discuss how both of these methods have been used on thin films samples to investigate surface segregation and electronic properties of SOFC cathodes.

## Introduction

SOFCs are of interest because they can generate electrical power directly from electrochemical fuel oxidation in an efficient and environmentally friendly fashion [1–3]. The general operation is schematized (at the cell level) in Figure 1. Oxygen gas is reduced in the cathode, being converted to $O^{2-}$, which transport through the cathode and electrolyte into the anode where they react with fuel, such as $H_2$, to form combustion products, $H_2O$ and electrons. The device functions primarily through chemical conversion and transport, and the efficiency of the device is closely linked to the losses required to achieve electrocatalysis and transport (both between and within the distinct phases of the device) at a given current density [1–3]. These losses are related to surface and bulk properties of the component phases, as well as the microstructure, distribution, and physical dimensions of the phases and cell components. Having the performance being related to so many parameters renders the optimization of SOFCs a rather complex problem. Moreover, any component phase must satisfy very strict stability and compatibility criteria [1–3], both in operation and processing conditions. Nevertheless, when SOFCs are operated at specific current densities/voltages, the oxygen incorporation (or uptake) process can contribute significantly to the losses of the cell, limiting the performance of the SOFCs.

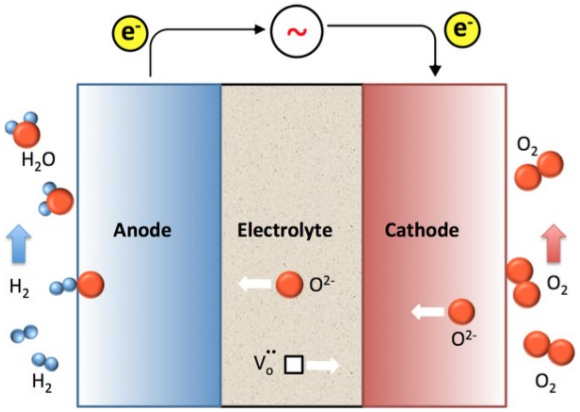


Figure 1. Schematic of the SOFC during operation. Hydrogen fuel on the anode side and oxygen gas on the cathode side are separated by a dense electrolyte layer that conducts $O^{2-}$. Electrons transfer through the outside circuit for electricity generation (from [4]).

The cathode in SOFCs is responsible for the ORR, as well as transport of oxide ions to and incorporation into the electrolyte. Recent studies have identified that, at intermediate temperatures (600–800 °C), up to 80% of total fuel cell efficiency loss is due to cathode polarization caused by the sluggish ORR kinetics [5]. Therefore, optimizing the ORR kinetics in SOFC cathodes is one of the key challenges to improving the energy conversion efficiency of SOFCs over a broad range of operational conditions[6–8]. However, because of the complex nature of the ORR and the difficulties associated with investigating the ORR in the aggressive SOFC operating conditions, the exact ORR mechanisms are only beginning to be understood [6, 9–11].

Bulk properties of many cathode materials are well studied in ceramic forms, such as electronic and ionic conductivities, thermal stabilities and phase compatibilities [1, 2, 8, 11], and the performance of modern SOFC cathodes is within acceptable limits. But, as SOFCs move toward market deployment, their optimization is driven by achieving specific performances at lower costs to manufacture with decreased degradation rates. Generally speaking, the limitations in designing highly active cathodes for oxygen incorporation arise now from the lack of direct correlations between surface/interface chemistry/structure and performance of SOFC cathode materials over the appropriate ranges SOFC operational conditions [12]. The goals of the fundamental science program in thin film cathodes investigations is to support SOFC development by unraveling the basic mechanisms of ORR and improving our understanding of parameters that control surface activity. In this report, we discuss how thin film materials and advanced experimental approaches are moving us toward these goals.

The complexity of understanding the ORR, which involves the interaction of gaseous oxygen transported in the pores, electrons transported in an electronic conductor (the cathode in the

image), and oxide ions (or vacancies) in an ion conductor (the cathode and electrolyte in the image), is illustrated in Figure 2. Several basic reaction/transport pathways exist for the ORR on a cathode material (a, b) and a host of sub-steps exist for any of these paths (c). The so-called triple phase boundary (TPB) path includes surface diffusion of oxygen species and oxide ion incorporation at the TPB, while the (b) the bulk path is based on oxygen incorporations at the surface and bulk diffusion across a mixed ionic/electronic conductor (MIEC). Some sub-steps related to the bulk path are shown in (c), highlighting simply the complexity of adsorption, dissociation, charge transfer, surface diffusion, adatom incorporation, and bulk diffusion. For the TPB path, surface adsorption, surface diffusion, and maximizing TPB quantities should optimize performance. In the bulk path, optimizing all steps in the surface exchange of oxygen between the bulk and gas, as well as diffusion to the electrolyte are important.

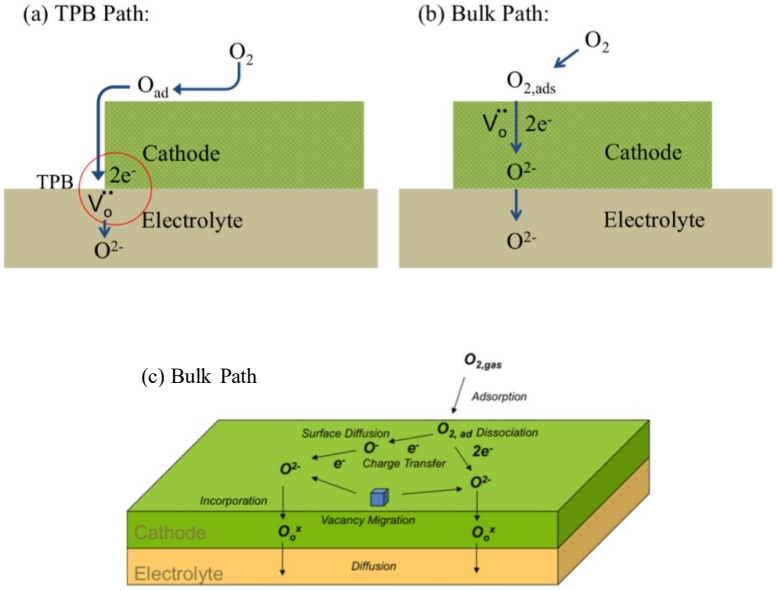


Figure 2. (a,b) Schematics of two different oxygen transport pathways in SOFC cathodes: (a) The TPB path is considered important for poor ionic conductors (such as LSM) while (b) the bulk path is considered important for MIECs (such as LSCF or LSC). (c) A schematic illustrating potential intermediate species and reaction substeps in the ORR at cathode surface (from [13]).

Two major options exist for improving the cathode performance by specifically targeting the oxygen incorporation process: changing the component solid materials or adding yet another material (a catalyst) to the existing frameworks [1–3, 14]. In general, both of these are tantamount to improving the overall surface reactivity while maintaining the bulk properties of existing cathodes. Two major transport parameters [15] are defined for cathode materials: the surface exchange coefficient $k$ and the bulk diffusion coefficient $D$. Both relate the flux of oxygen to the driving forces, $k$ at the surface and $D$ through the bulk. Using ceramics, it is difficult to disentangle the two parameters, with accurate measurements of $D$ being easier to obtain than of $k$ [15]. The best way to access accurate measurements of $k$ is to move to a

sample geometry in which diffusion is much faster than exchange, and thin films are ideal geometries for this. As shown in Figure 3(a), using the chemical exchange and diffusion coefficients, the important geometrical parameter is the length $D/k$. For most cathode materials, this in on the order of microns, which means that very thin samples are required.

The thickness of thin films can be varied easily from sub-nanometer (one unit cell of LSM is ≈0.4 nm) to hundreds of nanometers [16–22]. Such dense film overlayers are ideal for measuring the bulk path, as there are no TPBs; this is discussed in the section on surface exchange. Moreover, such films can be patterned to remove well-defined portions of the film, exposing well-defined electrolyte surface and quantities of TPBs (relative to the surface area and thickness of the film).

Patterned films give access to investigating the relative importance of the TPB and bulk pathways [23, 24], which will be discussed briefly in the section on patterned electrodes. Because the thin film has a well-defined surface and flat surface morphologies, a variety of modern surface tools can provide structural, chemical, and morphological understanding of the surface, as well as electronic property mapping (discussed in the section on surface segregation and heterogeneities). This report will present work from thin film cathode investigations that uncover some important complexities to the surface properties of SOFC cathodes, and project their relevance to SOFC design.

The primary issue related to the use of thin films as model SOFC cathodes is that the thin film length scale is much smaller than the micron-length scale of real SOFC materials. However, it has been shown that, by infiltrating active materials onto a porous cathode or electrolyte backbone [25–28], the electrochemical performance of SOFCS could be significantly enhanced. Normally, the infiltration materials are in the form of nanoparticles [26] or the dense film structure [27], with a dimension of less than 100 nm [29], as illustrated in Figure 3(b). Thin film research speaks directly to the performance of such infiltrates, in addition to the earlier discussed attributes.

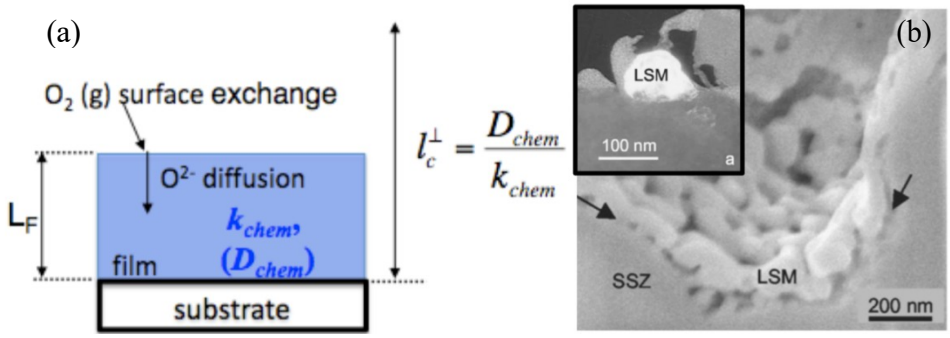


Figure 3. (a) Schematic illustrating how thin films isolate surface control to the ORR: $L_F$ is the film thickness, $k_{chem}$ is the surface chemical exchange coefficient, *D*chem is the bulk chemical diffusion coefficient, and $l_c$ is a characteristic critical thickness (from [4]). (b) An SEM image of an LSM infiltrated porous scandia-stabilized zirconium (SSZ) cathode of an anode-supported SOFC (Figures are from [14]).

## Controlling Structural Aspects in Thin Films

The primary arguments given above for using thin films imply that the main difference between bulk material and thin films is simply their geometries. In other words, thin films appear to be good proxies for bulk materials while they isolate surface features in experiments. Using this assumption, thin film preparation and characterization methods need to achieve and demonstrate the proper crystal structure and stoichiometry having a given thickness and surface roughness. It is relatively straightforward to achieve such a film using modern methods. In spite of the implication, thin films often diverge from their bulk counterparts because the micro-, defect-, and surface-structures of films vary significantly from bulk materials. Furthermore, these structures can depend strongly on the growth parameters, substrate type and orientation, and film thickness. While this calls into question a direct correlation of film properties to bulk materials, it offers a number of controllable parameters that potentially impact transport and electrocatalytic properties. The latter is exciting from both a fundamental scientific perspective and for future SOFC design, because observations show very strong dependencies of the transport properties on these parameters.

It is of interest to differentiate between expected micro-, defect-, and surface-structures, and briefly describe how one can measure these values. Here we will delineate three basic types of films used in the SOFC experiments: epitaxial films on isostructural substrates, textured films on non-isostructural substrates, and random polycrystalline films. The latter are most similar to bulk ceramics, though films often have much smaller grains. These polycrystalline films are expected to have higher grain boundary populations than bulk, and are expected to have all possible surface orientations. Such films provide very little control for investigating surface properties. On the other end of the spectrum are epitaxial films on isostructural substrates, schematized in Figure 4 (left).

Epitaxial films grow with an identical orientation (and aligned unit cells) to that of the isostructural substrate. Most SOFC cathodes are derivatives of the perovskite structure, and a number of commercially available single crystal substrates can be used. Furthermore, one can control the surface orientation to explore the anisotropic properties of materials.

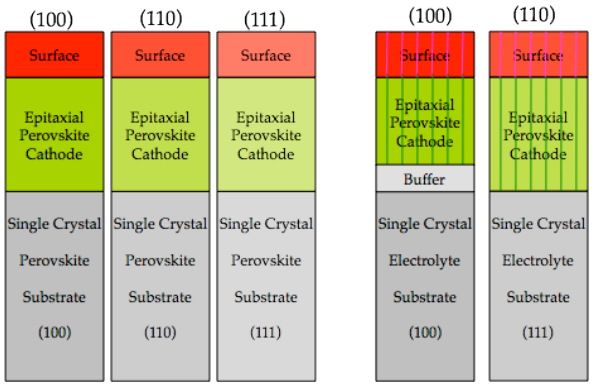


Figure 4. Schematics of film structures for (left three) epitaxial films and (right two) textured films. In each, the grey layer(s) represents the substrate, the green layer represents the bulk of the film, and the red layer represents the surface, Dark green vertical lines in the textured films represent variant boundaries (special kinds of grain boundaries). The different shades represent different orientations.

Unfortunately, most commercial substrates do not conduct ions well, so they are not good electrolytes on which to test electrochemical performance. yttria-stabilized zirconia (YSZ) single crystals are also available in different orientations. But, since the underlying crystal structures (fluorite and perovskite) have significant mismatches, most cathode perovskite films on YSZ are best described as textured: all crystallites are oriented similarly with respect to the substrate crystal, but have high densities of closely related orientation variants and low-angle grain boundaries.

The traditional approach to identifying phase, orientation, texture (or epitaxy), and thickness (or growth rate) is through X-ray diffraction (XRD), and characterizing surface roughness is through atomic force microscopy. These are non-destructive experiments. Figure 5 shows several XRD scans from a textured LSM (110) film on YSZ (111). Only ($hh$0) peaks of a perovskite are observed in the $\theta$-$2\theta$ scans in (a), indicating a $<110>_{LSM}$ || $<111>_{YSZ}$ [30, 31]. $\phi$ scans from the same film registered for the film {200} and substrate {220} planes are shown in (b). The $\phi$ scans support the existence of 6 degenerate variants having $<111>_{LSM}$ || $<011>_{YSZ}$ [32]. The question is: do the boundaries between the individual variants affect transport properties?

The film surface morphology and surface features were characterized by AFM [32], shown in Figure 6. The surface of the 600 nm thick film is fairly smooth, though rougher than epitaxial films on isostructural substrates, with a roughness of ≈3 nm; the total surface area calculated is very close to the projected scanning area within a 1–2% variation. The as-deposited film has a uniform surface with small grain-shaped surface features that coarsen after post-annealing for

24 hr. The estimated grain size from AFM images are 100 (150) nm for 850 (900) °C. These surface features are shown later to impact transport, so having control over the grain size is important in establishing their role.

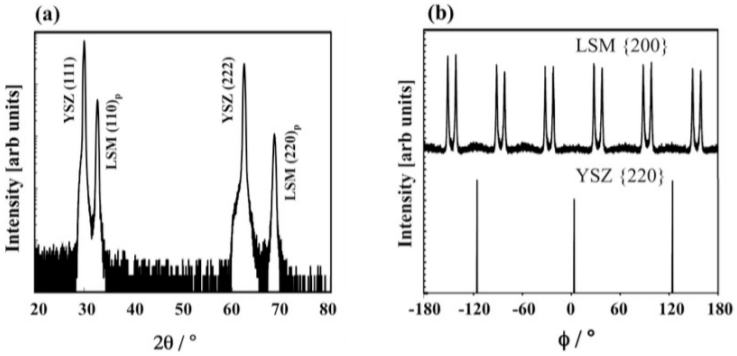


Figure 5. XRD patterns for 600 nm thick LSM films on YSZ (111) substrates: (a) $\theta-2\theta$ scans for (*hh*0) film peaks and (*hhh*) for substrate peaks; (b) $\phi$ scan for {200} LSM peaks and {220} YSZ peaks [32].

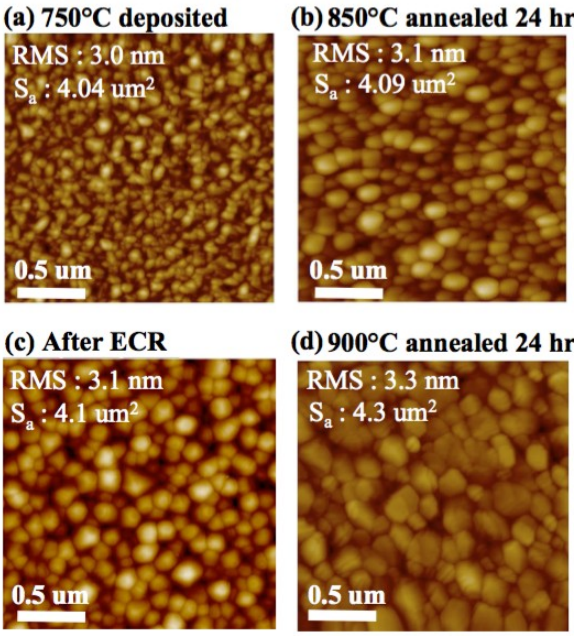


Figure 6. AFM images of 600 nm thick LSM (110) film on YSZ (111) substrates, the values of (root mean square) roughness and total surface area of the 2 µm by 2 µm scanning area are given in the images; the black and white color scale for all images are from 0 nm to 20 nm: (a) as-deposited film; (b) for the films annealed at 850 °C for 24 hr annealing; (c) for the films annealed at 850 °C for 24 hr annealing after ECR measurements; (d) for the films annealed at 900 °C for 24 hr annealing [32].

In epitaxial films, one does not expect variant boundaries of this type owing to the much-improved lattice match. However, the structural state is still significantly impacted from the bulk material. This depends on thickness and annealing conditions. For extremely thin films, the films become strained owing to the energy penalty required to create misfit dislocations to relax the misfit strain. The strain can be tailored using different substrates, but it is known to significantly impact point defect and compositional segregation, and more recently the intrinsic transport parameters of materials. Depending on the mismatch and kinetics of relaxation, films can be strained anywhere from tens of nm to hundreds of nm in thickness. Once dislocation generation occurs, the film relaxes by propagation of dislocations to the interface, though whether the dislocation remains isolated or bundles into sub-grain boundaries in not easy to know, though both lead to a decrease in the perfect alignment of crystal planes, resulting in a broadening of the XRD $\omega$ scans. In contrast, strained films have narrow rocking curves that are displaced in $\omega$ angle owing to uniform strains. This is evident in Figure 7, where the strained 50 nm films have narrow rocking curves (FWHM values) shifted from each other on different substrates (the film on NdGaO3 [NGO] is in compression and that on SrTiO3 [STO] is in tension), while the thicker films have broader rocking curves at a similar $\omega$ angle [16]. The FWHM broadening is primarily ascribed to an increase in inhomogeneous strains around dislocations, whose threading components intersect the surface and impact transport. The main point here is the experiments can quantify features associated with crystalline quality.

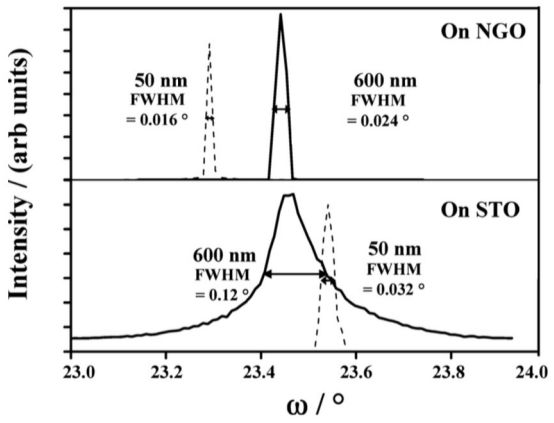


Figure 7. XRD rocking curves of 50 and 600 nm LSM films on different substrates: (upper) (002) peak of LSM films on NGO; (lower) (002) peak of LSM films on STO. FWHM of each peak was marked in the plot [16].

The issue with XRD, as described above, is that one obtains the average state of the film, but cannot directly assess the spatial distribution of defects. New methods in scanning electron microscopy (SEM) developed in the semiconductor communities are being applied to defect analysis in cathode thin films [13, 33]. Electron channeling contrast imaging

(ECCI) has recently been shown to be effective at mapping planar defects in strained thin films, including anti-phase boundaries (APBs), and dislocations in films of different states of relaxation [13, 33]. Example images are shown in Figure 8 [13, 33]. The images in (a) and (b) are from a strained 50 nm thick (110) LSM film that is coherently strained to the substrate. The imaging conditions in (a) highlight the meandering APBs present in the film at low-densities—low enough to not significantly impact the net transport properties. Using the imaging conditions in (b), the APBs vanish and a low-number of dislocation can be imaged ($\approx 6 \times 10^6$ cm$^{-2}$). A 600 nm thick, partially relaxed film is shown in (c), highlighting dislocations again. The contrast is high but uniformly distributed indicating the dislocations are uniformly distributed (not widely separated into grain boundaries), but their density is so high they are difficult to independently resolve: the density is $\geq 10^9$ cm$^{-2}$ in (c). Since ECCI is non-destructive and carried out in the SEM, it offers straightforward complementary non-destructive tool for film characterization before and after property measurements.

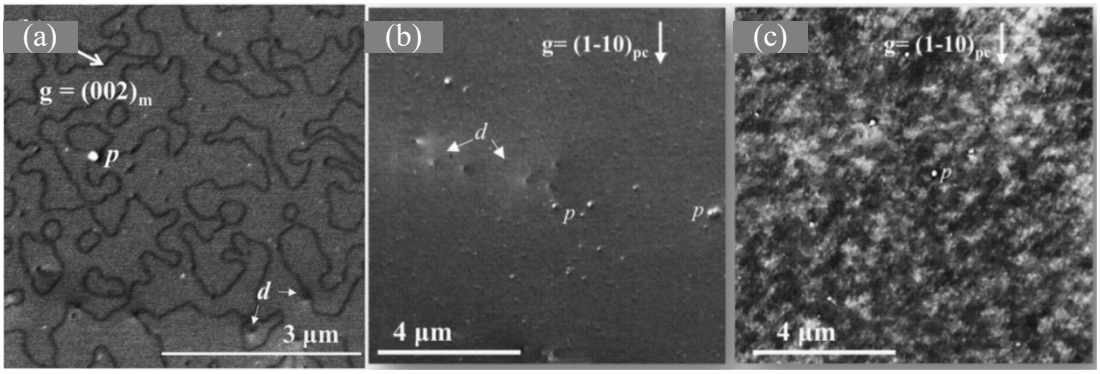


Figure 8. ECCI micrographs showing (a)APBs [33], (b) dislocations in a strained LSM (110) film on STO, and (c) dislocations in relaxed LSM. The dislocation density is $\approx 6 \times 10^6$ in (b) and $\geq 10^9$ cm$^{-2}$ in (c) [13, 33].

It should be noted that, although the APBs (a coherent planar fault) shown in (a) did not appear to impact transport, other coherent planar faults (of higher densities) were observed to impact transport for LSM films on NGO substrates [13]. The coherent planar faults do not significantly impact the XRD and AFM images described above. They can be imaged using destructive transmission electron microscopy (TEM) methods, depending on their distribution and alignment.

The main points to take from this discussion of thin films relative to their use in cathode studies are as follows: (1) Films, and other supported layers of similar dimensions, can differ significantly in their structure from their bulk counterparts. (2) A variety of traditional and novel non-destructive methods can be used to interrogate the structural state of the film, including the spatial mapping of extended defects. The micro-, defect-, and surface-structures of films can be controlled as a function of the substrate, thickness, and annealing. (4) Extensive structural characterization and comparison between films of varied defect structures are required to make meaningful interpretations of what parameter primarily

influences the transport properties. This latter point will be reinforced in the next section on surface exchange measurements, briefly considered in the patterned electrode studies, and reinforced again in the surface segregation studies.

## Thin Films and Surface Exchange

Samples with well-defined geometries, such as dense pellets [34–37], thin films [38–40], and patterned microelectrodes [23, 24, 41–45], are well suited to the study of fundamental ORR kinetics, owing to the simplified analysis and the ability to separate effectively $k$ and $D$. In particular, progress made on thin films and microelectrodes allows for the isolation of the surface exchange processes. Commonly employed methods for investigating the ORR kinetics are: (1) oxygen tracer gas exchange combined with secondary ion mass spectrometry (SIMS) [46–51] ($k^*$), (2) electrical conductivity relaxation (ECR) [52–58] ($k_{chem}$), and (3) electrochemical impedance spectroscopy (EIS) methods [38, 42–44, 59–61] ($k_q$). Quantitative differences between these measurements are well understood [15]. If the surface exchange reaction was insensitive to micro-, defect-, and surface-structures, measurements would be relatively easy to equate between sample geometry and measurement method (including variations in the oxygen pressures and temperatures). The point of this discussion is that the condition is not upheld: the transport properties are measurably sensitive to details of the micro-, defect-, and surface-structures.

The first clue to the importance of micro-, defect-, and surface-structures to exchange properties is indicated by the range of values observed for given materials when measured in different forms or by different groups. Figure 9 plots surface exchange values of the LSC $(La,Sr)CoO_3$ system on both bulk samples (blue data) and thin film electrodes (orange) [62]. It can be seen that measured $k^*$ values deviate by ≈3 orders of magnitude, and also have different activation energies (slope). These vast differences imply no single $k$ value that truly represents LSC.

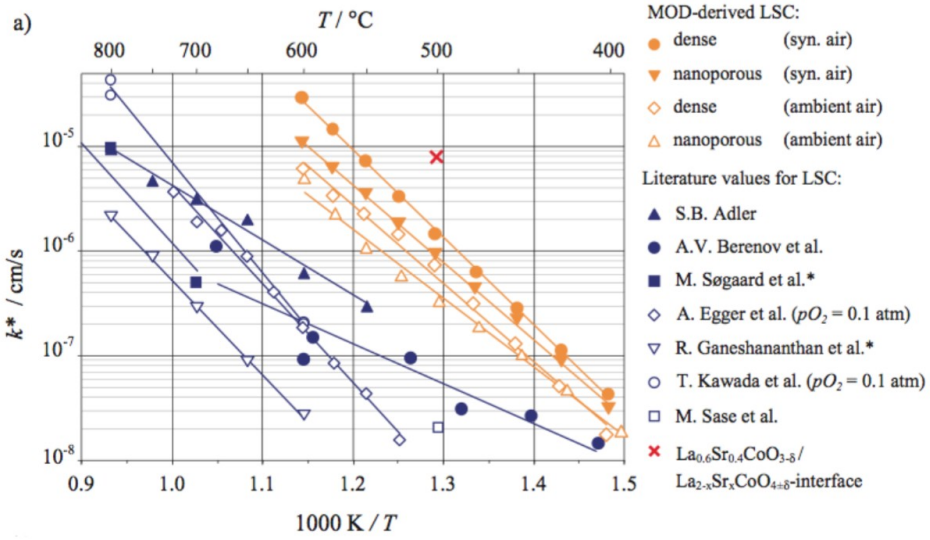


Figure 9. k* values of LSC bulk and thin films. Figure from Hayd et al. [62].

Plots with such scattered $k$ or $D$ values are common for other compositions as well. Figure 10 plots $k^*$ and $k_q$ collected on bulk and thin film LSM electrodes [49, 61, 63–65] for polycrystalline ceramics and thin films, as well as surface exchange from grains and grain boundaries. Figure 11 plots the temperature dependence of surface exchange coefficient $k_{chem}$ of LSM (100) and (110) surfaces [4]. The activation energies ($E_a$) of $k_{chem}$ from various microstructural features are marked, including the strained and relaxed epitaxial films and textured films discussed above in the structural discussion. All of the films in Figure 11 were made by a single person using the same equipment in a single laboratory.

In general, up to 7 orders of magnitude differences in $k$ values have been measured on nominally the same composition, which arise from variations in experimental conditions, geometries, and material micro-, defect-, and surface-structures. The challenges lies in how to accurately quantify the surface exchange rate with respect to all of the variables, and later how to integrate this into SOFC design. Using the examples from Figure 11, we will discuss in more detail the manner in which strain and extended defects perturb the measured surface exchange. A microstructural model was proposed to explain the observed $k_{chem}$ dependence on substrate [16], film thickness, and temperature for epitaxial LSM films involving (1) the native dislocation-free surface and (2) the surface/bulk region around a dislocation that intersects the surface. Schematics of the limiting cases expected from the proposed model are given in Figure 12, for a film of thickness $L_F$.

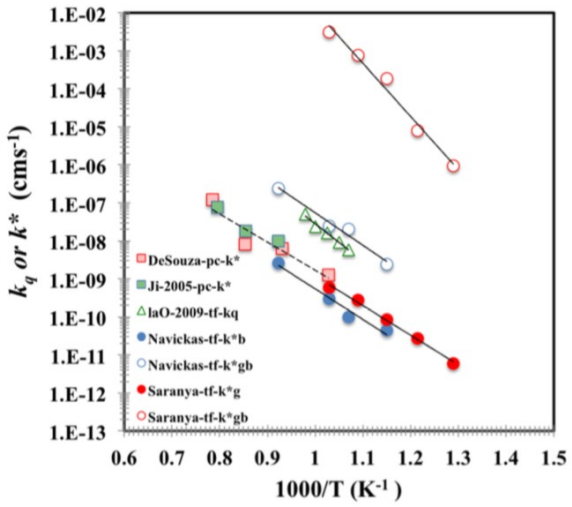


Figure 10. Values of $k^*$ and $k_q$ collected on bulk and thin film LSM electrodes [49, 61, 63–65]. The "pc", "tf", "g", and "gb" represent polycrystalline thin films, surface exchange on grains and surface exchange on grain boundaries [13].

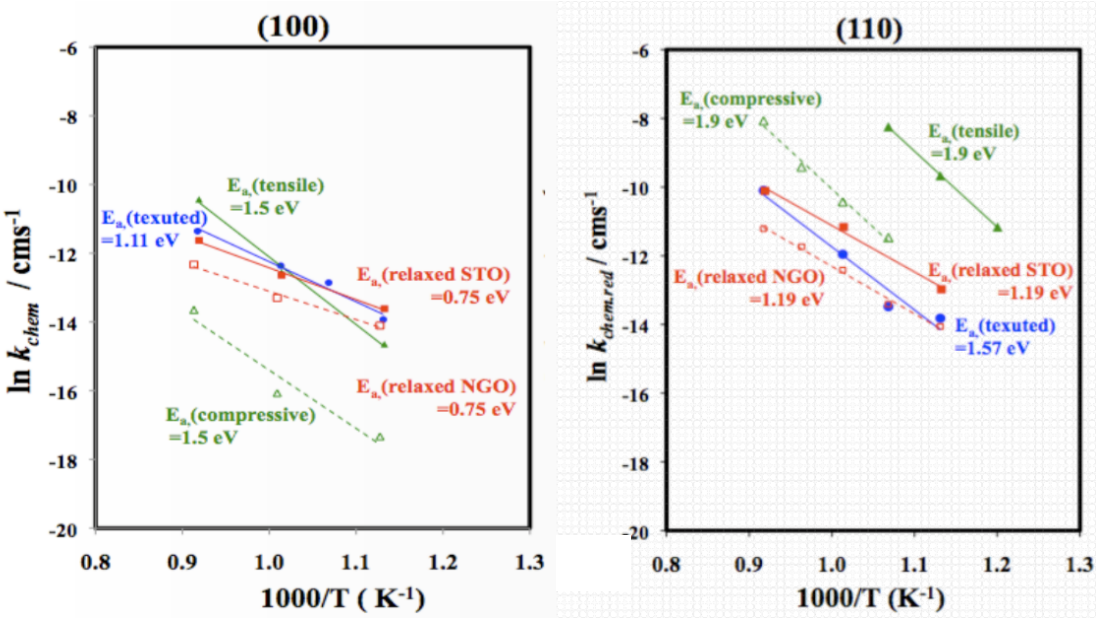


Figure 11. Temperature dependency of surface exchange coefficient kchem of LSM (100) and(110) surfaces. The activation energies (Ea) of kchem from various microstructural features are marked [4].

In Figure 12(a), a schematic of surface exchange is given for the native dislocation-free surface. The total flux of oxygen, $J_T$ (atoms/cm$^2$), is related to the flux across the native surface, $J_S$

(atoms/cm$^2$). This flux is a function of strain, where LSM on STO (NGO) is in biaxial tension (compression). The rocking curve widths shown in Figure 7 corroborate the low number of dislocations in the strained films. A schematic of measured flux versus inverse temperature for these surfaces are shown in Figure 12(b) (similar to what was measured). When the films relax, a largely dislocation-mediated process, threading dislocations intersect the native surface and propagate across the film thickness. For films in which the dislocation density is large enough, the entire film can exchange with the gas phase through a dislocation mediated mechanism (Figure 12[e],) a schematic of surface exchange is given for the dislocation-mediated surface. The thick gray surface indicates the portion of the surface that contributes to this path and dislocations are shown as vertical dashed lines. The total flux of oxygen, $J_T$, is now related to the flux across the surface with intersecting dislocations, $J_D$ (atoms/cm$^2$). The film with a lower dislocation content has a lower surface exchange, but the activation energies are again similar (which were observed to be near 0.7 eV [16]). When both pathways contribute, the values and activation energies are intermediate [16, 66]. The contribution of each path also varies with temperature, in a complicated fashion [16].

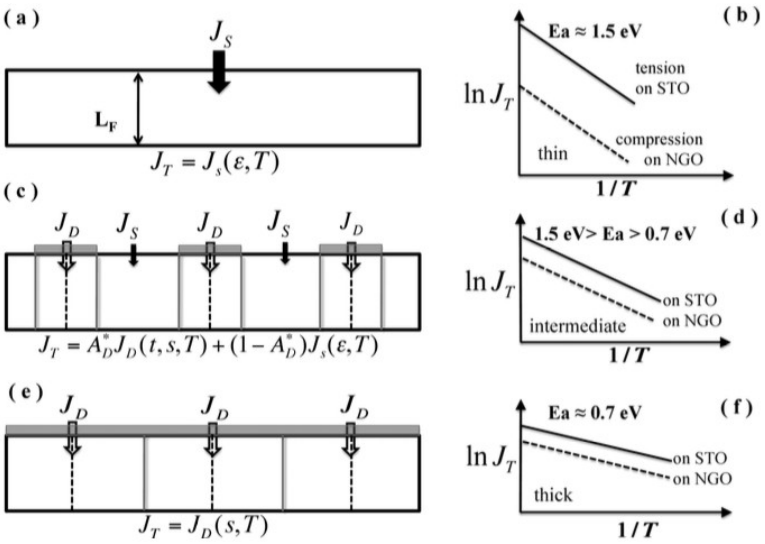


Figure 12. Schematics (a,c,e) of the flux of oxygen during ECR on films. (a) Only the native surface contributes, (c) both the native surface and dislocations (vertical dashed lines) contribute, and (e) only the dislocations contribute. The region of the surface (bulk) that each dislocation affects is marked by a gray horizontal (vertical) line. Schematic plots of the corresponding flux (which is proportional to $k_{chem}$) versus inverse temperature are given in b, d, and f for the surfaces shown respectively in a, c, and e [16].

A similar microstructural model was proposed to explain the observations for textured LSM films that exhibited two distinct contributions to surface exchange [32]. A columnar grain structure is depicted in Figure 13(a), with a shaded active volume for an individual grain on the lower right. In Figure 13(b) and (c), two different oxygen exchange paths exist through the grain center ($k_{grain}$) or via the grain boundaries ($k_{gb}$), with different relative amounts. Again, the different paths have different activation energies and $k$ values at any given

temperature. Also, the relative contribution of each path is temperature and grain-sized dependent [4, 32].

A similar conclusion, with strong quantitative modeling of several data sets, was observed for $k^*$ in LSM textured films [63]. The combination of computational modeling and experimental data carried out in [63] will become the norm in making strong quantitative conclusions for the relative contribution of the different pathways. Combining microstructural characterization with such modeling will allow for extrication of the defect and native properties from films with controlled variations in structural features, and this will allow for improved design of materials. The point is not to dismay at the 7 orders of magnitude variations in transport parameters in different samples of similar material, but to generate data sets with appropriate samples having controlled microstructural features, to ensure an appropriate number of observations to disentangle the role of each pathway. Then one can design improved SOFC cathodes with optimized structures.

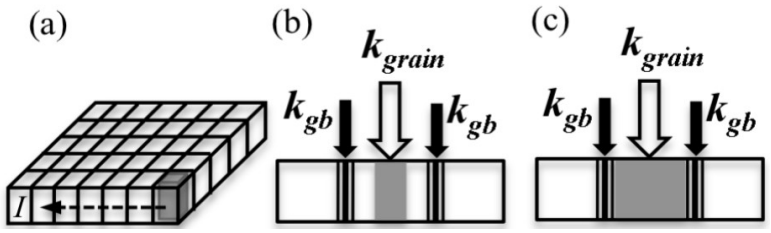


Figure 13. (a) Schematic of grain boundary networks inside a textured film. (b, c) Two oxygen flux pathways with different contributions: an intrinsic surface/grain path and a variant/grain boundary path. The relative contribution varies with temperature and grain size [4, 32].

## Patterned Electrode Thin Films

In addition to using blanket films supported on a substrate, as described above, cathode researchers have used micro-patterned electrodes to explore the relative role of TPBs on electrochemical activity. Fleig et al. [24] have conducted a nice review on the use of circular microelectrodes to establish well-defined geometry-dependent experiments, to minimize the importance of ohmic drops, and to avoid the necessity of a reference electrode [24]. We give a few examples of reports to highlight the utility of this approach, when combined with electrochemical impedance spectroscopy (EIS), to extract a fundamental understanding of material behavior.

Examples of these micro-patterned electrodes are shown in Figure 14(a) and (b). As seen in (a), many electrodes can be fabricated on a single film, which allows for good quality statistical studies or investigating many observations of irreversible processes [24]. Other groups have used mesh-type electrodes, one such type is shown in Figure 14(c) and (d) [67]. The well-defined geometries and ability to pattern ranges of geometries allows for quantitative mechanistic studies when reaction paths and rate-limiting steps have strong

correlations with geometry [24]. These patterned electrodes are then investigated using IES, and models are fit to extract materials parameters.

The electrode polarization resistance at 800 °C for LSM is plotted versus the diameter of the microelectrode in Figure 15, at (a) -300 mV cathodic bias and (b) +300 mV anodic bias. The slope of ≈-2 in (a) and ≈-1 in (b) indicates the mechanistic pathway is a function of the area and perimeter, respectively, in the different conditions. In other words, the pathways shown in Figure 2 (and reproduced in Figure 15[c] and [d]), vary with polarization. It is believed (from such measurements) that the current along the surface path can be expected to be slightly higher than that of the bulk path (in low polarizations) [24].

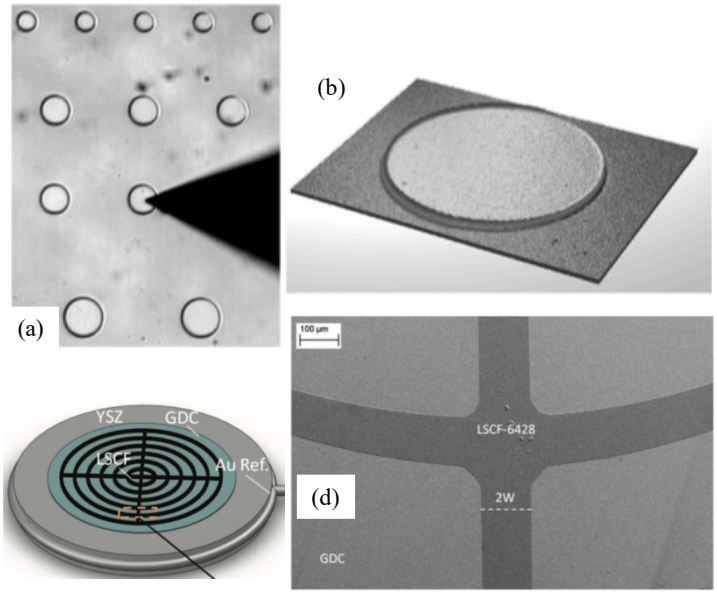


Figure 14. (a) Optical microscope image of LSM microelectrodes of different size on a YSZ single crystal (with a contact probe about 60 µm at the tip) [24], [12]. (b) Interferometry image of a 100 nm thick LSCF microelectrode on YSZ (100 µm diameter) [24]. (c) A patterned cathode with a YSZ electrolyte, a sputtered $Gd_{0.1}Ce_{0.9}O_{1.95}$ barrier layer (blue), and an LSCF-6428 pattern [67]. (d) An SEM image of pattern such as in (c) with $l_{TPB}$ = 50 $cm^{-1}$ [67].

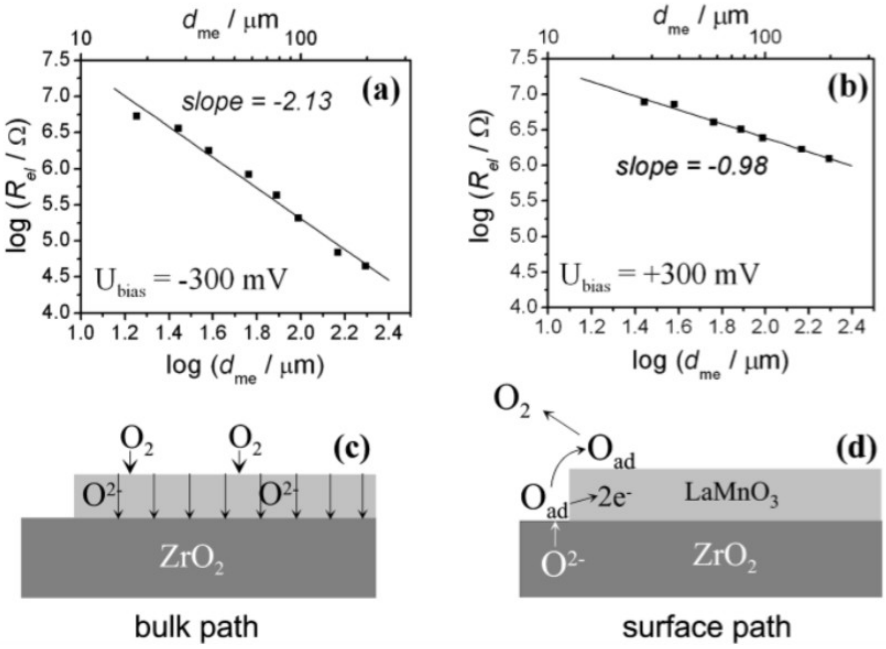


Figure 15. Electrode polarization resistance of LSM *vs.* its diameter at ≈800 °C for (a) a cathodic dc bias of –300 mV and (b) an anodic dc bias of +300 mV. Also, sketches illustrating the path of the ORR for (c) cathodic bias and (d) strong anodic bias (from [24]).

Patterned electrodes like those shown in Figure 14(c) and (d) were used to control the TPB length ($l_{TPB}$) while maintaining the surface area constant in 500 nm thick $La_{0.6}Sr_{0.4}Co_{0.8}Fe_{0.2}O_{3-d}$ (LSCF) films, and then measured with EIS. The EIS results of these electrodes were consistent with the ORR reaction being co-limited between diffusion and surface exchange [67]. Equivalent circuits were fit to the EIS data, and the inverse of the characteristic resistance was shown to be linear function of $l_{TPB}$, indicating the importance of the TPB path. However, since the inverse characteristic resistance did not extrapolate to zero at $l_{TPB}$ =0, the bulk path also contributed to the performance. Then, a reaction pathway model was fit to the extracted EIS parameters and underlying transport parameters were determined, notably the ratio of the surface diffusion (which is difficult to measure) to the bulk diffusion (v) and the surface exchange rate (related to the exchange coefficient described previously). These values are plotted versus partial pressure of oxygen ($pO_2$) for various temperatures in Figure 16 (a) and (b) respectively. While the surface exchange rate was nearly $pO_2$ independent, the ratio of diffusivities implied the surface diffusivity was increasingly important as the $pO_2$ increased [67].

These results imply that both reaction pathways and basic materials parameters can be extracted simultaneously from well-designed experiments using patterned electrodes. What is equally important is results from patterned electrodes further support that the reaction process in SOFC cathodes is complex, and multiple paths compete closely with one another, including the bulk and TPB paths, as well as whether or not one is surface or bulk limited, or

whether the surface is diffusion or exchange limited. Disentangling all of the contributions requires further experiments to properly populate computational models incorporating microstructure into the SOFC cathode, over all operating conditions (temperature [*T*], $pO_2$, polarization, etc.).

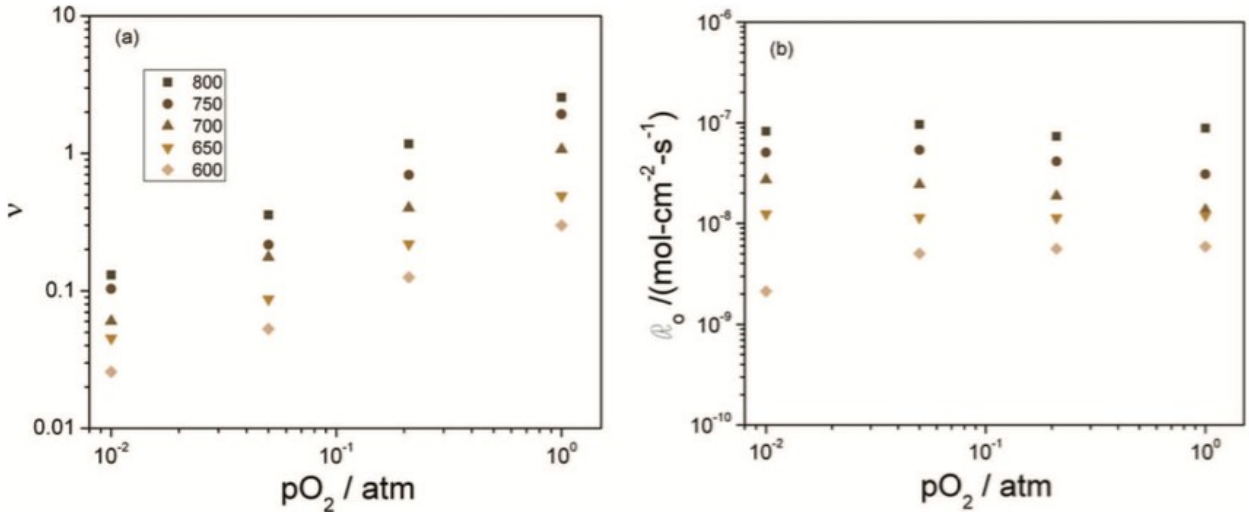


Figure 16. Transport parameters of LSCF extracted from EIS results at 800 °C in different $pO_2$ values. The sample was a patterned electrode having $l_{TPB}$ = 430 $cm^{-1}$. v represents the ratio of the surface diffusion value to the bulk diffusion and $R_O$ represents the surface exchange rate (see reference [67]).

A couple of caveats are required regarding the discussion of the last two sections. First, the films investigated as patterned electrodes are typically textured films with significant grain boundary densities. As was discussed with respect to Figure 13, the grain boundaries contribute significantly to the surface exchange response, which varies with temperature and their density. It is of interest to understand how the extended defect populations in patterned electrodes affect the observed electrochemical transport. Second, the surface exchange measurements do not touch upon the effects of polarization. An important question is: do local parameters such as surface exchange (or its sub-steps) vary with polarization similar to what is observed in the pathways? A hint at this answer is given in the next section, which demonstrates that surface chemistry is a strong function of polarization.

## Surface Segregation and Heterogeneities

Either example of thin films, the blanket overlayers or patterned microelectrodes can be further addressed with surface-sensitive probes. Such probes afford an understanding of surface crystal structure (through diffraction), surface morphology (through reflectance or scanning probes), and electronic structure (through spectroscopy or current-voltage characteristics). The challenge to surface science is to develop tools that allow for such

information to be obtained in near or real operating conditions. In this section, we give examples of tools developed over the last decade to address these issues.

Fister et al. [18] used synchrotron-based total reflection X-ray fluorescence (TXRF) measurements to monitor the depth-dependent composition of LSMO films at temperatures ranging from 25 to 900 °C and $pO_2$ from 0.15 to 150 Torr. These conditions are quite similar to those used to determine surface exchange at no bias, as were the films (being strained epitaxial films). The Sr content in the first 2 nm of the film is plotted in Figure 17(a) versus $pO_2$ at different temperatures for a 16 nm (100) LSM thin film on $DyScO_3$. It is clear there is always some Sr-enrichment at the surface in this film (and others reported therein [18]). This had been previously reported in the literature, using various ex-situ measurements near room temperature. Here it is apparent that the surface composition varies with temperature and $pO_2$ (though less so with temperature as $pO_2$ increased). The excess Sr composition at the surface is plotted versus temperature in Figure 17(b). Linear fits versus inverse temperature were used to extract the enthalpy of segregation at different partial pressures, which are shown in Figure 17(c), which captures the thermodynamic driving force for segregation (without bias).

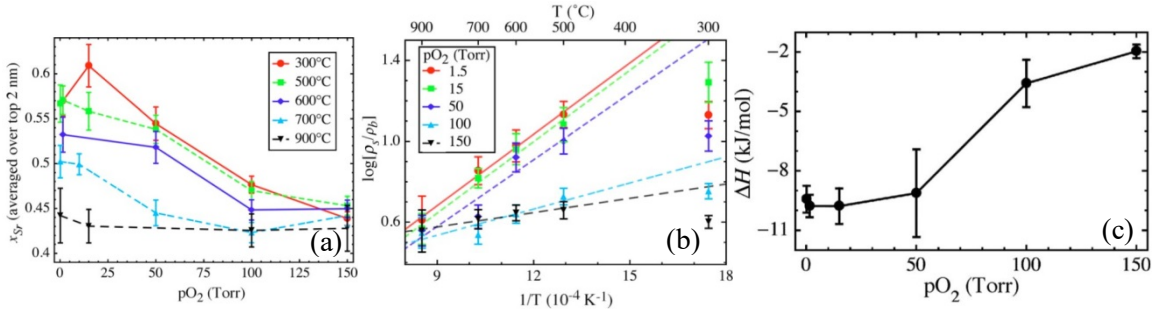


Figure 17. (a) Sr surface concentration vs $pO_2$ at $T$ = 300 – 900 °C. (b) Sr surface enrichment as a function inverse temperature for a variety of oxygen partial pressures (the ratio is of the Sr/La ratio integrated over the first 2 nm over the bulk value. The lines are linear fits. (c) Enthalpy of Sr surface segregation as a function of $pO_2$ [18].

Another example that illustrates the dynamic nature of the surface and its relation to environmental conditions is shown in Figure 18, which depicts real time TXRF data for a LSCF film in two different gas compositions at 800 °C: (a) one containing 30% $CO_2$ and one without $CO_2$ [68]. The data is plotted as the ratio of the Sr-content to the sum of the Sr- and La-content as a function of X-ray beam incident angle. The signal volume increases as the X-ray beam angle increases, and data is averaged over increasing depths into the film. The vertical line indicates the critical angle for total reflection, which is most surface sensitive. On annealing, the as-deposited films experience a Sr-enrichment at the surface (smallest angles) in both atmospheres, but the time to reach the steady state is much faster in the $CO_2$ containing gas.

This was believed to arise because $SrCO_3$ phases form on the surface, in the $CO_2$ atmosphere, which increase the driving force for Sr to enrich the surface.

In fact, most studies of surface chemistry at elevated temperatures in SOFC cathode like conditions, whether on epitaxial or textured films and whether a bias is applied or not, support the concept of a dynamic surface structure having a composition that differs from the bulk. Furthermore, the surface state depends on orientation and/or texture, as many (110) textured films develop large islands of Sr-rich (or other alkaline earth elements) phases (oxides or carbonates or hydroxides, depending on the atmosphere) that form at high temperatures but can resorb at lower temperatures [69]. In addition, the surface state depends on polarization [70], as surface charges result in migration of charged species in the cathodes [69, 71]. Usually, the time constant to obtain steady state in the surface cation composition is larger than that required for the oxygen profile, but the latter will depend on the surface composition over time. Thus, when the polarization varies across the surface, so should the surface composition. Therefore the challenge to modeling SOFCs precisely, is to capture all levels of this dynamic nature over time, especially with regard to degradation potentially associated with surface phases or decreased local activity. Of course, an important question is also: how precise must models be to capture SOFC performance over time? For many performance criteria, we don't know.

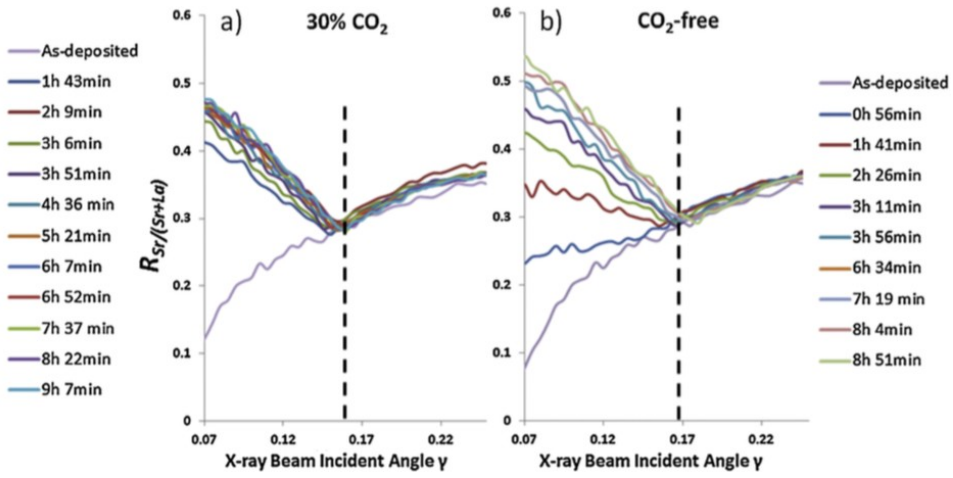


Figure 18. Real-time TXRF data for LSCF-6428 plotted as the ratio Sr/(Sr + La) versus X-ray beam incident angle. The plots are from data collected at 800 °C in (a) 30% $CO_2$, 21% $O_2$, and 49% $N_2$ and (b) 21% $O_2$ and 79% $N_2$ [68].

While synchrotron-based X-ray experiments provide powerful examples of probing surface structure and composition in operating conditions, access to them is limited and experimental time is precious. Developing laboratory-scale experimentation is critical to generating the amount of observations/data needed to understand the complex behavior of cathodes. A variety

of ex-situ surface sensitive probes are well-known in surface science, which are primarily ultra-high vaccum (UHV)-based methods. Because the surfaces are so dynamic in operating conditions, correlating ex-situ UHV observations to SOFC conditions are challenging, though many important fundamental insights are obtained. Yildiz's group [17, 71–73] has been deploying an in-situ approach combining surface sensitive probes of electronic structure and chemical state, specifically combining scanning tunneling microscopy/spectroscopy (STM/STS) and Auger electron spectroscopy AES, at relatively high temperatures and in non-UHV conditions to model cathode surfaces closely to the reaction environment of operational SOFC cathodes.

An example of this combined approach is shown in Figure 19 [17] using a 50 nm thick (110) LSM textured film on YSZ (111) (with as similar morphology to those shown in Figure 6). The room temperature STS data are shown in (a), which exhibit semiconducting behavior with a gap of 2.6 eV. However, when the temperature is raised, above 400 °C, the film exhibits metallic behavior (gapless) [17]. The STS continues to evolve with temperature, first increasing in current density at a given voltage and then decreasing again. Thus, the electronic structure undergoes a dramatic change at lower temperatures, and then a more gradual but continual evolution with increasing temperature. The surface compositions determined from AES are plotted in Figure 19(c) as cation fractions and in (d) as ratios of (La+Sr) to Mn (which is ≈1 in the bulk). The results revealed Sr-enrichment on the surfaces from 500 to 700 °C, which accompanies the decrease in tunneling conductance in STS. This suggests that the *A*-site rich and Mn-poor surfaces are less active for electron exchange for LSM. Once again, a complex and dynamic interplay occurs between composition and properties as a function of ambient conditions in the cathode material.

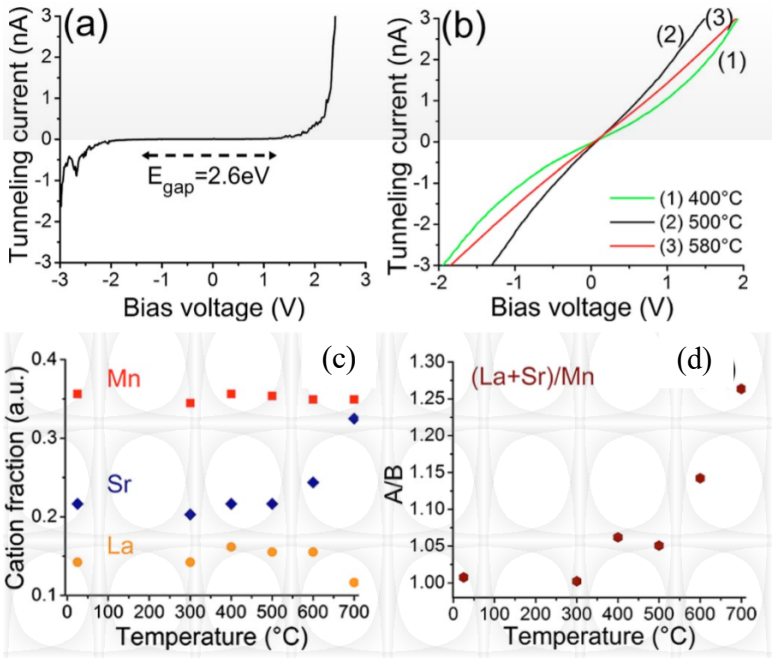


Figure 19. Tunneling current spectra acquired on the surface of the 50-nm-thick LSM at (a) room temperature and (b) 400, 500, and 580 °C [17]. (c,d) Temperature-dependent surface concentrations from AES in $10^{-6}$ mbar oxygen reported as (c) cation fractions and (d) (La+Sr) /Mn ratios [17].

As described previously, epitaxial films differ from textured films in the types of extended defects and overall strain states. Biaxial strains of several percent can be supported in epitaxial thin films and this is known to impact the low-temperature magneto-electric properties, as well as the surface exchange properties [13, 16, 66, 72, 73]. Figure 20(left) shows the STS results (plotted as dI/dV vs V, which is indicative of the electronic density of states) at room temperature in UHV for an LSM film in compressive strain (LSM/LAO) and another in tensile strain (LSM/STO). Both exhibit semiconductor-like behavior, but the gaps are significantly different (as are the density of states outside the gap regions). The film in compression has a smaller gap and larger density of states than the film in tension. Figure 20 (right) shows similar STS plots (though the scales are different) at 500 °C in $10^{-3}$ mbar $O_2$ for the same films. As for the textured films, the gap is lost in both of these strained epitaxial films. What is even more interesting, is that the relative density of states flips from the low-temperature case: the film in tension has a larger density of state than the film in compression. Again, the surface properties are observed to be dynamic and complex in response to external stimuli, varying substantially between low-temperature UHV environments and near operational conditions. These films are similar to the films discussed for surface exchange in Figure 12, where epitaxial films in tension had higher surface exchanges than films in tension [16]. Perhaps the electronic density of state differences contribute to the variations in surface exchange [74].

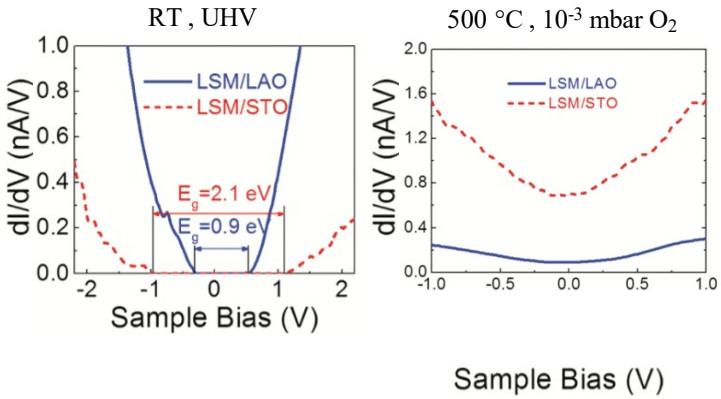


Figure 20. (a) Tunneling spectra on compressive strained LSM on $LaAlO_3$ (blue, solid line) and tensile strained LSM on STO (red, dashed line), showing the energy gap, Eg, for both samples at room temperature in ultra-high vacuum. (b) The band gap obtained from the density functional calculations of total density of states of LSM as a function of strain [72].

Figure 21 [71] illustrates some of the competing effects that drive surface segregation (which modifies properties) in $LaMnO_3$ films, though similar effects are expected and observed in other cathode materials. The size of the mismatch of the dopant cation is found to correlate with preferred segregation, but is influenced by $pO_2$. A smaller size mismatch between the host and dopant cations suppresses segregation. The chemical expansion (contraction) of the doped $LaMnO_3$ in the low (high) oxygen pressures alters the dopant misfit and modifies the strain energy (segregation driving force). This explanation is depicted in the left panel. However, redistributions of charged defects causes other charged defects to respond. The space charge region is influenced by the external conditions, such as polarization, and the charge carrier density in the cathode (screening ability). The right panel illustrates this with respect to the driving force for dopant diffusion to the surface as a function of $pO_2$ [71]. These collected results demonstrate the power of new experimental methods, using thin films SOFC cathodes, to unravel what actors contribute to cathode performance, but also highlight the need to develop probes functional in operational conditions to fully de-convolute the complex behavior of SOFC cathodes materials.

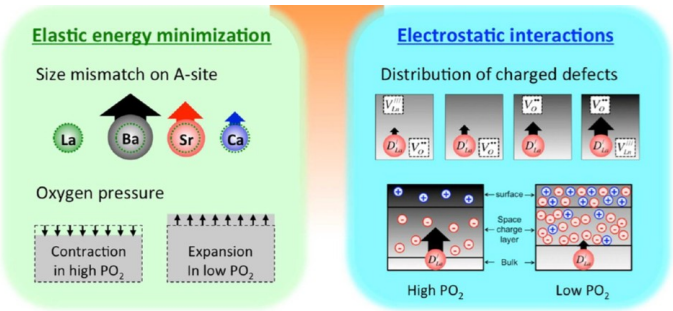


Figure 21. Illustration of the mechanisms that drive dopant segregation to the surface of $LnMnO_3$ [71].

## Summary and Outlook

In this report, we discussed important developments over the last few decades in using thin film cathodes to investigate fundamental aspects that contribute to cathode performance in SOFCs. We especially reviewed relevant results to the SECA cathode program, attempting to integrate the understanding generated from a range of experiments.

First, it is clear that details of the micro-, defect-, and surface-structures of SOFC cathodes directly impact parameters relevant to the ORR. In particular, strain, orientation, dislocations, grain/variant/other planar boundaries, and TPB, all modify the local ORR. Because these can be controlled and quantified in a reasonable fashion using thin films, research will continue along the lines described above. Moreover, the number and types of defects obtainable in thin films are often much greater than in bulk materials, which is another benefit to their use in basic investigations. The question to SOFC developers is how to incorporate the positive outcomes from thin film research into commercially viable SOFCs. The most likely connection is through surface modification methods, such as infiltration.

Second, most measurements made on thin films demonstrate that multiple pathways are actively competing in oxygen reduction. As such the rate-limiting step, or the fractional contributions of different pathways, varies as a function of the external conditions and local microstructure. Similarly, the surface composition and electronic structure vary with external conditions and local microstructure. The complex and dynamic nature of the surface is fascinating for science, but challenging to digest for SOFC designers. The work on thin film SOFC cathodes does not solve any of the design problems as of yet, but hints that many materials parameters exist to improve oxygen reduction throughout the cathode; more parameters ultimately means more potential design space.

Third, because the surfaces and properties are dynamic with temperature, pressure, bias, composition, and local microstructure, over precisely the variable operational conditions, length scales, and defect states that exist in complex SOFC cathodes, a full understanding of the local performance (which is likely coupled to local degradation modes) can only be achieved through further experimentation in which these parameters can be controlled and investigated. The challenge is no longer how to control the local surface state, as much of the thin film work discussed above demonstrates is possible. The challenge is now twofold: first, one must recognize the importance of the microstructure within the cathode phase (not just the TPB

content) and accurately characterize it; second, continued improvements must be made in surface science tools that can characterize SOFC cathodes in operational conditions. The experiments described above (TXRF, STM/S) demonstrate the need to continue moving surface science from UHV to the extreme environments in SOFCs. Ultimately, detailed fundamental parameters measured over a range of near operational conditions can be fed into computational models that can assist in the design of improved SOFC cathodes.

## References


[1] N. Q. Minh and T. Takahashi, *Science and Technology of Ceramic Fuel Cells*. New York: Elsevier, 1995.

[2] S. C. Singhal, "Advances in Solid Oxide Fuel Cell Technology," *Solid State Ionics,* vol. 135, pp. 305-313, 2000.

[3] P. Singh and N. Q. Minh, "Solid Oxide Fuel Cells: Technology Status," *Int. J. Appl. Ceram. Technol.* , vol. 1, pp. 5-15, 2004.

[4] L. Yan, "Investigation of the Oxygen Surface Exchange Properties of $La_{0.7}Sr_{0.3}MnO_3$ Thin Films by Electrical Conductivity Relaxation Measurements," Ph.D., Materials Science and Engineering, Carnegie Mellon University, Pittsburgh, 2011.

[5] V. S. Bagotsky, *Fuel Cells: Problems and Solutions*: Wiley, 2012.

[6] S. B. Adler, "Factors Governing Oxygen Reduction in Solid Oxide Fuel Cell Cathodes," *Chemical Reviews,* vol. 104, pp. 4791-4843, 2004.

[7] D. J. L. Brett, A. Atkinson, N. P. Brandon, and S. J. Skinner, "Intermediate temperature solid oxide fuel cells," *Chemical Society Reviews,* vol. 37, pp. 1568-1578, 2008.

[8] A. J. Jacobson, "Materials for Solid Oxide Fuel Cells," *Chemistry of Materials,* vol. 22, pp. 660-674, 2010.

[9] M. M. Kuklja, E. A. Kotomin, R. Merkle, Y. A. Mastrikov, and J. Maier, "Combined theoretical and experimental analysis of processes determining cathode performance in solid oxide fuel cells," *Physical Chemistry Chemical Physics,* vol. 15, pp. 5443-5471, 2013.

[10] J. Fleig, "Solid Oxide Fuel Cell Cathodes: Polarization Mechanisms and Modeling the Electrochemical Performance," *Annu. Rev. Mater. Res.,* vol. 33, pp. 361-82, 2003.

[11] C. W. Sun, R. Hui, and J. Roller, "Cathode materials for solid oxide fuel cells: a review," *Journal of Solid State Electrochemistry,* vol. 14, pp. 1125-1144, 2010.

[12] J. Fleig, H. Kim, J. Jamnik, and J. Maier, "Oxygen Reduction Kinetics of Lanthanum Manganite (LSM) Model Cathodes: Partial Pressure Dependence and Rate-Limiting Steps," *Fuel Cells,* vol. 8, pp. 330-337, 2008.

[13] M. Yan, "Defect Analysis and Microstructural Effects on the Surface Exchange Properties of $La_{0.7}Sr_{0.3}MnO_{3-\delta}$ (LSM) Epitaxial Thin Films," Ph.D., Materials Science and Engineering, Carnegie Mellon University, Pittsburgh, 2015.

[14] T. Z. Sholklapper, V. Radmilovic, C. P. Jacobson, S. J. Visco, and L. C. D. Jonghe, "Synthesis and stability of a nanoparticle-infiltrated solid oxide fuel cell electrode," *Electrochem. Solid-State Lett.,* vol. 10, pp. B74–B76, 2007.

[15] J. Maier, *Physical Chemistry of Ionic Materials Ions and Electrons in Solids*: John Wiley & Sons, 2004.

[16] L. Yan and P. A. Salvador, "Substrate and Thickness Effects on the Oxygen Surface Exchange of $La_{0.7}Sr_{0.3}MnO_3$ Thin Films," *ACS Applied Materials and Interfaces,* vol. 4, pp. 2541-2550, 2012.

[17] K. Katsiev, B. Yildiz, K. Balasubramaniam, and P. A. Salvador, "Electron tunneling characteristics on $La_{0.7}Sr_{0.3}MnO_3$ thin-film surfaces at high temperature," *Applied Physics Letters,* vol. 95, p. 092106, 2009.

[18] T. T. Fister, D. D. Fong, J. A. Eastman, P. M. Baldo, M. J. Highland, P. H. Fuoss*, et al.*, "In situ characterization of strontium surface segregation in epitaxial $La_{0.7}Sr_{0.3}MnO_3$ thin films as a function of oxygen partial pressure," *Applied Physics Letters,* vol. 93, p. 151904, Oct 13 2008.

[19] H. Du, P. J. Fisher, M. Skowronski, P. A. Salvador, and O. Maksimov, "Growth and structural characterization of epitaxial $Ba_{0.6}Sr_{0.4}TiO_3$ films deposited on $REScO_3(110)$ (RE = Dy, Gd) substrates using pulsed laser deposition," *Journal of Crystal Growth,* vol. 310, pp. 1991-1998, Apr 2008.

[20] P. A. Salvador, A. M. Haghiri-Gosnet, B. Mercey, M. Hervieu, and B. Raveau, "Growth and magnetoresistive properties of $(LaMnO_3)_m(SrMnO_3)_n$ superlattices," *Applied Physics Letters,* vol. 75, pp. 2638-2640, Oct 25 1999.

[21] B. Mercey, P. A. Salvador, W. Prellier, T. D. Doan, J. Wolfman, J. F. Hamet*, et al.*, "Thin film deposition: a novel synthetic route to new materials," *Journal of Materials Chemistry,* vol. 9, pp. 233-242, Jan 1999.

[22] P. A. Salvador, T. D. Doan, B. Mercey, and B. Raveau, "Stabilization of $YMnO_3$ in a perovskite structure as a thin film," *Chemistry of Materials,* vol. 10, pp. 2592-2595, Oct 1998.

[23] J. Fleig, "Microelectrodes in solid state ionics," *Solid State Ionics,* vol. 161, pp. 279-289, 2003.

[24] J. Fleig, F. S. Baumann, V. Brichzin, H. R. Kim, J. Jamnik, G. Cristiani*, et al.*, "Thin film microelectrodes in SOFC electrode research," *Fuel Cells,* vol. 6, pp. 284-292, 2006.

[25] P. Seungdoo, J. G. Raymond, and M. V. John, "Tape Cast Solid-Oxide Fuel Cells for the Direct Oxidation of Hydrocarbons," *Journal of The Electrochemical Society,* vol. 148, pp. A443-A447, 2001.

[26] Z. S. Tal, L. Chun, P. J. Craig, J. V. Steven, and C. D. J. Lutgard, "LSM-Infiltrated Solid Oxide Fuel Cell Cathodes," *Electrochemical and Solid-State Letters,* vol. 9, pp. A376- A378, 2006.

[27] M. E. Lynch, L. Yang, W. Qin, J.-J. Choi, M. Liu, K. Blinn*, et al.*, "Enhancement of $La_{0.6}Sr_{0.4}Co_{0.2}Fe_{0.8}O_{3-delta}$ durability and surface electrocatalytic activity by $La_{0.85}Sr_{0.15}MnO_{3+/-delta}$ investigated using a new test electrode platform," *Energy & Environmental Science,* vol. 4, pp. 2249-2258, 2011.

[28] J. San Ping and W. Wei, "Fabrication and Performance of GDC-Impregnated (La,Sr)$MnO_3$ Cathodes for Intermediate Temperature Solid Oxide Fuel Cells," *Journal of The Electrochemical Society,* vol. 152, pp. A1398-A1408, 2005.

[29] Z. S. Tal, R. Velimir, P. J. Craig, J. V. Steven, and C. D. J. Lutgard, "Synthesis and Stability of a Nanoparticle-Infiltrated Solid Oxide Fuel Cell Electrode," *Electrochemical and Solid-State Letters,* vol. 10, pp. B74-B76, 2007.

[30] D. Mori, H. Oka, Y. Suzuki, N. Sonoyama, A. Yamada, R. Kanno*, et al.*, "Synthesis, Structure, and Electrochemical Properties of Epitaxial Perovskite La0.8Sr0.2CoO3 Film on YSZ Substrate," *Solid State Ionics,* vol. 177, pp. 535-540, 2006.

[31] D. Mori, H. Oka, Y. Suzuki, A. Yamada, R. Kanno, N. Imanishi*, et al.*, "Synthesis, Structure and Electrochemical Properties of Epitaxial Perovskite Films Deposited on YSZ Substrate " *ECS Transactions,* vol. 7, pp. 749-756, 2007.

[32] L. Yan, B. Kavaipatti, K.-C. Chang, H. You, and P. A. Salvador, "Microstructural effects on the oxygen exchange kinetics of La0. 7Sr0. 3MnO3 thin films," *ECS Transactions,* vol. 35, pp. 2063--2075, 2011.

[33] M. Yan, M. D. Graef, Y. N. Picard, and P. A. Salvador, "Electron channeling contrast imaging of anti-phase boundaries in coherently strained $La_{0.7}Sr_{0.3}MnO_3$ thin films on (110)-oriented $SrTiO_3$," *Applied Physics Letters,* vol. 107, p. 041601, 2015.

[34] F. H. van Heuveln, H. J. M. Bouwmeester, and F. P. F. van Berkel, "Electrode Properties of Sr-Doped $LaMnO_3$ on Yttria-Stabilized Zirconia," *Journal of The Electrochemical Society,* vol. 144, pp. 126-133, 1997.

[35] J. Van Herle, A. J. McEvoy, and K. R. Thampi, "A study on the $La_{1-x}Sr_xMnO_3$ oxygen cathode," *Electrochimica Acta,* vol. 41, pp. 1447-1454, 1996.

[36] W. Wang and S. P. Jiang, "A mechanistic study on the activation process of (La,Sr)$MnO_3$ electrodes of solid oxide fuel cells," *Solid State Ionics,* vol. 177, pp. 1361-1369, 2006.

[37] H. Kamata, A. Hosaka, J. Mizusaki, and H. Tagawa, "High temperature electrocatalytic properties of the SOFC air electrode $La_{0.8}Sr_{0.2}MnO_3$/YSZ," *Solid State Ionics,* vol. 106, pp. 237-245, 1998.

[38] A. Endo, M. Ihara, H. Komiyama, and K. Yamada, "Cathodic reaction mechanism for dense Sr-doped lanthanum manganite electrodes," *Solid State Ionics,* vol. 86-88, pp. 1191-1195, 1996.

[39] A. Endo, H. Fukunaga, C. Wen, and K. Yamada, "Cathodic reaction mechanism of dense $La_{0.6}Sr_{0.4}CoO_3$ and $La_{0.81}Sr_{0.09}MnO_3$ electrodes for solid oxide fuel cells," *Solid State Ionics,* vol. 135, pp. 353-358, 2000.

[40] I. Tsutomu, H. Tatsunori, U. Yoshiharu, O. Zempachi, and T. Zen-ichiro, "Preparation of Perovskite-Type $La_{1-x}Sr_xMnO_3$ Films by Vapor-Phase Processes and Their Electrochemical Properties," *Journal of The Electrochemical Society,* vol. 145, pp. 1999- 2004, 1998.

[41] K. Erik, S. M. David, D. Rupak, C. Charles, and L. Meilin, "Characteristic Thickness for a Dense $La_{0.8}Sr_{0.2}MnO_3$ Electrode," *Electrochemical and Solid-State Letters,* vol. 8, pp. A592-A595, 2005.

[42] V. Brichzin, J. Fleig, H. U. Habermeier, G. Cristiani, and J. Maier, "The geometry dependence of the polarization resistance of Sr-doped $LaMnO_3$ microelectrodes on yttria- stabilized zirconia," *Solid State Ionics,* vol. 152-153, pp. 499-507, 2002.

[43] V. Brichzin, J. Fleig, H. U. Habermeier, and J. Maier, "Geometry Dependence of Cathode Polarization in Solid Oxide Fuel Cells Investigated by Defined Sr-Doped $LaMnO_3$ Microelectrodes," *Electrochemical and Solid-State Letters,* vol. 3, pp. 403-406, 2000.

[44] J. Fleig, H. R. Kim, J. Jamnik, and J. Maier, "Oxygen Reduction Kinetics of Lanthanum Manganite (LSM) Model Cathodes: Partial Pressure Dependence and Rate-Limiting Steps," *Fuel Cells,* vol. 8, pp. 330-337, 2008.

[45] J. Fleig and J. Maier, "The polarization of mixed conducting SOFC cathodes: Effects of surface reaction coefficient, ionic conductivity and geometry," *Journal of the European Ceramic Society,* vol. 24, pp. 1343-1347, 2004.

[46] C. C. Kan, H. H. Kan, F. M. Van Assche, E. N. Armstrong, and E. D. Wachsman, "Investigating oxygen surface exchange kinetics of $La_{0.8}Sr_{0.20}MnO_{3-delta}$ and $La_{0.6}Sr_{0.4}Co_{0.2}Fe_{0.8}O_{3-delta}$ using an isotopic tracer," *Journal of the Electrochemical Society,* vol. 155, pp. B985-B993, 2008.

[47] C. C. Kan and E. D. Wachsman, "Isotopic-switching analysis of oxygen reduction in solid oxide fuel cell cathode materials," *Solid State Ionics,* vol. 181, pp. 338-347, 2010.

[48] R. A. De Souza and J. A. Kilner, "Oxygen transport in $La_{1-x}Sr_xMn_{1-y}Co_yO_{3\pm delta}$ perovskites: Part II. Oxygen surface exchange," *Solid State Ionics,* vol. 126, pp. 153-161, 1999.

[49] R. A. De Souza, J. A. Kilner, and J. F. Walker, "A SIMS study of oxygen tracer diffusion and surface exchange in $La_{0.8}Sr_{0.2}MnO_{3+delta}$," *Materials Letters,* vol. 43, pp. 43-52, 2000.

[50] T. Horita, K. Yamaji, N. Sakai, Y. Xiong, T. Kato, H. Yokokawa*, et al.*, "Imaging of oxygen transport at SOFC cathode/electrolyte interfaces by a novel technique," *Journal of Power Sources,* vol. 106, pp. 224-230, 2002.

[51] T. Horita, K. Yamaji, N. Sakai, H. Yokokawa, T. Kawada, and T. Kato, "Oxygen reduction sites and diffusion paths at $La_{0.9}Sr_{0.1}MnO_{3-x}$/yttria-stabilized zirconia interface for different cathodic overvoltages by secondary-ion mass spectrometry," *Solid State Ionics,* vol. 127, pp. 55-65, 2000.

[52] L. Chen, C. L. Chen, and A. J. Jacobson, "Electrical conductivity relaxation studies of oxygen transport in epitaxial $YBa_2Cu_3O_{7-delta}$ thin films," *Ieee Transactions on Applied Superconductivity,* vol. 13, pp. 2882-2885, 2003.

[53] X. Chen, S. Wang, Y. L. Yang, L. Smith, N. J. Wu, B. I. Kim*, et al.*, "Electrical conductivity relaxation studies of an epitaxial $La_{0.5}Sr_{0.5}CoO_{3-delta}$ thin film," *Solid State Ionics,* vol. 146, pp. 405-413, 2002.

[54] J. E. ten Elshof, M. H. R. Lankhorst, and H. J. M. Bouwmeester, "Oxygen exchange and diffusion coefficients of Strontium-Doped Lanthanum Ferrites by Electrical Conductivity Relaxation," *Journal of the Electrochemical Society,* vol. 144, pp. 1060-1067, 1997.

[55] L. M. v. d. Haar, M. W. d. Otter, M. Morskate, H. J. M. Bouwmeester, and H. Verweij, "Chemical Diffusion and Oxygen Surface Transfer of $La_{1-x}Sr_xCoO_{3-d}$ Studied with Electrical Conductivity Relaxation," *Journal of the Electrochemical Society,* vol. 149, p. J41, 2002.

[56] G. Kim, S. Wang, A. J. Jacobson, and C. L. Chen, "Measurement of oxygen transport kinetics in epitaxial $LaNiO_{4+delta}$ thin films by electrical conductivity relaxation," *Solid State Ionics,* vol. 177, pp. 1461-1467, Jul 2006.

[57] A. Rivera, J. Santamarı, and C. Leo, "Electrical conductivity relaxation in thin-film yttria-stabilized zirconia," *Applied Physics Letters,* vol. 78, p. 610, 2001.

[58] B. Lu. Yan, Balasubramaniam, S. Wang, H. Du, and P. Salvador, "Electrical Conductivity Relaxation Study of Solid Oxide Fuel Cell Cathodes using Epitaxial (001)- Oriented Strontium-Doped Lanthanum Manganite Thin Films," *Mat. Res. Soc. Symp. Proc.,* vol. 1255, 2010.

[59] M. Junichiro, S. Takatoshi, and T. Hiroaki, "A Chemical Diffusion-Controlled Electrode Reaction at the Compact $La_{1-x}Sr_xMnO_3$/Stabilized Zirconia Interface in Oxygen Atmospheress," *Journal of The Electrochemical Society,* vol. 143, pp. 3065-3073, 1996.

[60] G. J. la O' and Y. Shao-Horn, "Thickness Dependence of Oxygen Reduction Reaction Kinetics on Strontium-Substituted Lanthanum Manganese Perovskite Thin-Film Microelectrodes," *Electrochemical and Solid State Letters,* vol. 12, pp. B82-B85, 2009.

[61] G. J. la O', B. Yildiz, S. McEuen, and Y. Shao-Horn, "Probing oxygen reduction reaction kinetics of Sr-doped $LaMnO_3$ supported on $Y_2O_3$-stabilized $ZrO_2$," *Journal of the Electrochemical Society,* vol. 154, pp. B427-B438, 2007.

[62] J. Hayd, H. Yokokawa, and E. Ivers-Tiffee, "Hetero-Interfaces at Nanoscaled (La,Sr)$CoO_3$-delta Thin-Film Cathodes Enhancing Oxygen Surface-Exchange Properties," *Journal of the Electrochemical Society,* vol. 160, pp. F351-F359, 2013.

[63] E. Navickas, T. M. Huber, Y. Chen, W. Hetaba, G. Holzlechner, G. Rupp*, et al.*, "Fast oxygen exchange and diffusion kinetics of grain boundaries in Sr-doped $LaMnO_3$ thin films," *Physical Chemistry Chemical Physics,* vol. 17, pp. 7659-7669, 2015.

[64] A. M. Saranya, D. Pla, A. Morata, A. Cavallaro, J. Canales-Vazquez, J. A. Kilner*, et al.*, "Engineering Mixed Ionic Electronic Conduction in $La_{0.8}Sr_{0.2}MnO_{3+d}$ Nanostructures through Fast Grain Boundary Oxygen Diffusivity," *Advanced Energy Materials,* vol. 5, p. 1500377, 2015.

[65] Y. Ji, J. A. Kilner, and M. F. Carolan, "Electrical properties and oxygen diffusion in yttria-stabilised zirconia (YSZ)-$La_{0.8}Sr_{0.2}MnO_{3+/-delta}$ (LSM) composites," *Solid State Ionics,* vol. 176, pp. 937-943, 2005.

[66] L. Yan, K. R. Balasubramaniam, S. Wang, H. Du, and P. A. Salvador, "Effects of crystallographic orientation on the oxygen exchange rate of $La_{0.7}Sr_{0.3}MnO_3$ thin films," *Solid State Ionics,* vol. 194, pp. 9-16, 2011.

[67] L. J. Miara, S. N. Basu, U. B. Pal, and S. Gopalan, "2D Numerical Model for Identification of Oxygen Reduction Reaction Mechanisms in Patterned Cathodes of $La_{0.6}Sr_{0.4}Co_{0.2}Fe_{0.8}O_3$-delta," *Journal of the Electrochemical Society,* vol. 159, pp. F419- F425, 2012.

[68] Y. Yu, H. Luo, D. Cetin, X. Lin, K. Ludwig, U. Pal*, et al.*, "Effect of atmospheric $CO_2$ on surface segregation and phase formation in $La_{0.6}Sr_{0.4}Co_{0.2}Fe_{0.8}O_{3-delta}$ thin films," *Applied Surface Science,* vol. 323, pp. 71-77, 2014.

[69] P. Fuoss, K.-C. Chang, and H. You, "In situ X-ray studies of film cathodes for solid oxide fuel cells," *Journal of Electron Spectroscopy and Related Phenomena,* vol. 190, pp. 75- 83, 2013.

[70] A. K. Huber, M. Falk, M. Rohnke, B. Luerssen, L. Gregoratti, M. Amati*, et al.*, "In situ study of electrochemical activation and surface segregation of the SOFC electrode material La0.75Sr0.25Cr0.5Mn0.5O3 +/-delta," *Physical Chemistry Chemical Physics,* vol. 14, pp. 751-758, 2012.

[71] W. Lee, J. W. Han, Y. Chen, Z. H. Cai, and B. Yildiz, "Cation Size Mismatch and Charge Interactions Drive Dopant Segregation at the Surfaces of Manganite Perovskites," *Journal of the American Chemical Society,* vol. 135, pp. 7909-7925, 2013.

[72] H. Jalili, J. W. Han, Y. Kuru, Z. H. Cai, and B. Yildiz, "New Insights into the Strain Coupling to Surface Chemistry, Electronic Structure, and Reactivity of $La_{0.7}Sr_{0.3}MnO_3$," *Journal of Physical Chemistry Letters,* vol. 2, pp. 801-807, 2011.

[73] A. Kushima, S. Yip, and B. Yildiz, "Competing strain effects in reactivity of $LaCoO_3$ with oxygen," *Physical Review B,* vol. 82, p. 115435, 2010.

[74] M. Kubicek, A. Limbeck, T. Fromling, H. Hutter, and J. Fleig, "Relationship between Cation Segregation and the Electrochemical Oxygen Reduction Kinetics of $La_{0.6}Sr_{0.4}CoO_{3-delta}$ Thin Film Electrodes," *Journal of the Electrochemical Society,* vol. 158, pp. B727-B734, 2011.